Theoretische Physik

Radiative corrections for the direct detection of neutralino dark matter and its relic density

Inaugural-Dissertation

zur Erlangung des Doktorgrades

der Naturwissenschaften im Fachbereich Physik

der Mathematisch-Naturwissenschaftlichen Fakultät

der Westfälischen Wilhelms-Universität Münster

vorgelegt von

Patrick Norbert Steppeler

aus Gütersloh

– 2016 –

„Das Unendliche!" Törleß kannte das Wort aus dem Mathematikunterrichte. Er hatte sich nie etwas Besonderes darunter vorgestellt. Es kehrte immer wieder; irgend jemand hatte es einst erfunden, und seither war es möglich, so sicher damit zu rechnen wie nur mit irgend etwas Festem. Es war, was es gerade in der Rechnung galt; darüber hinaus hatte Törleß nie etwas gesucht. Und nun durchzuckte es ihn wie mit einem Schlage, daß an diesem Worte etwas furchtbar Beunruhigendes hafte.

– Robert Musil

Kurzfassung

In dieser Arbeit werden supersymmetrische Einschleifenkorrekturen der starken Wechsel-wirkung zur elastischen Streuung vom leichtesten Neutralino an Nukleonen berechnet. Die Rechnung wird im Detail beschrieben und erfolgt in voller Allgemeinheit innerhalb des Minimal Supersymmetrischen Standardmodells (MSSM). Um hierbei auf das etablierte Verfahren der Tensorreduktion zurückgreifen zu können, ist es notwendig, diese Methode für verschwindende Gram-Determinanten zu stabilisieren. Anschließend werden die Strah-lungskorrekturen auf eine effektive Feldtheorie abgebildet, welche auf dem skalaren Opera-tor $\bar{\chi}\chi\bar{q}q$ und dem axialen Vektoroperator $\bar{\chi}\gamma_5\gamma_\mu\chi\bar{q}\gamma_5\gamma^\mu q$ beruht. Diese Abbildung erfolgt an der hohen Skala $\mu_{\text{high}} \sim 1000$ GeV, während die zugehörigen nuklearen Matrixelemente an der niedrigen Skala $\mu_{\text{low}} \sim 5$ GeV definiert sind. Um beide Skalen zu verknüpfen, wird das Laufen der effektiven Operatoren und der assoziierten Wilson-Koeffizienten in Form von Renormierungsgruppengleichungen berücksichtigt.

Das leichteste Neutralino gilt als kanonisches Beispiel für ein schwach wechselwirken-des, massives Teilchen, aus welchen die dunkle Materie bestehen könnte. Um die Exis-tenz derartiger Teilchen zu überprüfen, werden derzeit Experimente zu ihrem direkten Nachweis durchgeführt. Diese basieren auf der Wechselwirkung von dunkler Materie mit Nukleonen. Die führenden Beiträge zum spinunabhängigen, beziehungsweise spinabhän-gigen Neutralino-Nukleon Wirkungsquerschnitt werden durch die oben genannten effek-tiven Operatoren beschrieben. Die Berechnung der zugehörigen Strahlungskorrekturen entspricht einer Reduktion der theoretischen Unsicherheit und ermöglicht eine genauere Bestimmung der Eigenschaften des Neutralinos im Falle eines positiven Signals sowie das Setzen von robusteren Ausschlussgrenzen im Falle negativer Befunde.

Des Weiteren werden Strahlungskorrekturen zu Annihilations- und Koannihilations-prozessen von Gauginos in Quarks berechnet, wobei der Fokus erneut auf supersym-metrischen Einschleifenkorrekturen der starken Wechselwirkung liegt. In vielen Szenarien des MSSM tragen diese Prozesse führend zum in der Boltzmann-Gleichung auftretenden (Ko)Annihilationswirkungsquerschnitt bei. Die Boltzmann-Gleichung ermöglicht es, die Reliktdichte der Neutralinos zu bestimmen, d. h. ihre gegenwärtige Menge vorherzusagen.

Diese Vorhersage ist experimentell überprüfbar und somit von großer phänomenologi-scher Bedeutung. Genaue Messungen der Temperaturfluktuationen der kosmischen Mikro-wellenhintergrundstrahlung ermöglichen eine präzise Bestimmung der Reliktdichte. Durch einen Vergleich der theoretischen Vorhersage mit dem experimentellen Befund können große Bereiche des Parameterraums des MSSM ausgeschlossen werden. Um dabei die ex-perimentelle Präzision bestmöglich auszunutzen, ist es notwendig, theoretische Unsicher-heiten zu minimieren und die genannten Strahlungskorrekturen zu berücksichtigen.

Die Strahlungskorrekturen zur elastischen Neutralino-Nukleon Streuung und zur zu-gehörigen Reliktdichte sind in das numerische Paket `Dark matter at next-to-leading order` implementiert worden. Mithilfe dieses Programms wird eine phänomenologische Untersuchung durchgeführt und der Einfluss der Strahlungskorrekturen analysiert. Dabei zeigt sich, dass die Reliktdichte der Neutralinos oftmals nicht nur von einem, sondern

von einer Vielzahl von Gaugino (Ko)Annihilationsprozessen abhängt. Die berechneten Strahlungskorrekturen führen zu einer relativen Verschiebung der Reliktdichte von bis zu 10%, was die experimentelle Unsicherheit ($\pm 2\%$ für das 1σ-Konfidenzintervall) signifikant übersteigt und deutlich macht, dass diese Korrekturen bei einer Identifikation des kosmologisch bevorzugten Parameterbereichs des MSSM berücksichtigt werden sollten. Zusätzlich wird der Zusammenhang zwischen der Reliktdichte und den Neutralino-Nukleon Wirkungsquerschnitten untersucht. Im spinunabhängigen Fall führt die Berücksichtigung der Strahlungskorrekturen zu einer relativen Verschiebung von etwa $+14\%$ gegenüber einer Rechnung auf Bornniveau. Diese Verschiebung ist vergleichbar mit gegenwärtigen nuklearen Unsicherheiten, welche die Vorhersage ebenfalls beeinflussen. Der spinabhängige Wirkungsquerschnitt ist noch größeren Veränderungen unterworfen und wird durch Strahlungskorrekturen um bis zu -50% verschoben.

Abstract

In this thesis we calculate supersymmetric one-loop corrections of the strong interaction to elastic neutralino-nucleon scattering. The calculation is described in detail and performed in full generality within the Minimal Supersymmetric Standard Model (MSSM). In order to benefit from the well-established tensor reduction method, we have to stabilise the latter for vanishing Gram determinants. Afterwards the radiative corrections are matched onto an effective field theory based on the scalar operator $\bar{\chi}\chi\bar{q}q$ and the axial-vector operator $\bar{\chi}\gamma_5\gamma_\mu\chi\bar{q}\gamma_5\gamma^\mu q$. This matching procedure is performed at the high scale $\mu_{\mathrm{high}} \sim 1000$ GeV, whereas the associated nuclear matrix elements are defined at the low scale $\mu_{\mathrm{low}} \sim 5$ GeV. To link both scales, the running of the effective operators and their corresponding Wilson coefficients is taken into account via renormalisation group equations

The lightest neutralino can be considered as a canonical example for a weakly interacting, massive particle which could constitute dark matter. To verify the existence of such particles, so-called direct detection experiments are conducted currently. These are based on the interaction between dark matter and nucleons. The leading contributions to the spin-independent and spin-dependent neutralino-nucleon cross sections are governed by the effective operators mentioned above, respectively. The calculation of the associated radiative corrections corresponds to a reduction of the theoretical uncertainty and permits to identify neutralino properties more reliably in case of positive findings and to set more robust exclusion bounds in case of negative findings.

Furthermore, we calculate radiative corrections to annihilation and coannihilation processes of gauginos into quarks, where we focus again on supersymmetric one-loop corrections of the strong interaction. These processes contribute dominantly to the (co)annihilation cross section entering the Boltzmann equation in many scenarios of the MSSM. The Boltzmann equation allows to determine the neutralino relic density, i.e. to predict their present abundance.

This prediction can be checked experimentally and is thus of great phenomenological relevance. Measurements of the temperature fluctuations of the cosmic microwave background permit to determine the relic density precisely. Comparing the theoretical prediction with the experimental finding allows to exclude large fractions of the MSSM parameter space. In order to maximally benefit from the experimental precision, it is necessary to minimise theoretical uncertainties and to include the aforementioned radiative corrections.

The radiative corrections to the elastic neutralino-nucleon scattering and the corresponding relic density have been implemented into the numerical package `Dark matter at next-to-leading order`. With the help of this program, we perform a phenomenological investigation and analyse the impact of the radiative corrections. It turns out that the neutralino relic density depends not on a single but a multitude of gaugino (co)annihilation processes in parallel quite often. The calculated radiative corrections lead to a relative shift of the relic density of up to 10%, which is significantly larger than the experimental uncertainty ($\pm 2\%$ at the 1σ confidence level) and demonstrates that these corrections

should be included when identifying the cosmologically preferred region of the MSSM. Moreover, we investigate the relation between the relic density and the neutralino-nucleon cross sections. In the spin-independent case, the inclusion of radiative corrections leads to a relative shift roughly $+14\%$ in comparison to a tree-level calculation. This shift is comparable to typical recent nuclear uncertainties, which influence the prediction as well. The spin-dependent cross section is subject to even larger shifts and modified by up to -50% by radiative corrections.

Table of contents

List of figures

List of tables

List of publications

The work on this thesis has contributed to the following publications and proceedings:

- HERMANN, Björn; KLASEN, Michael; KOVAŘÍK, Karol; MEINECKE, Moritz; STEPPELER, Patrick: One-loop corrections to gaugino (co)annihilation into quarks in the MSSM. In: *Physical Review D* **89** (2014), p. 114012

- HARZ, Julia; HERMANN, Björn; KLASEN, Michael; KOVAŘÍK, Karol; MEINECKE, Moritz; STEPPELER, Patrick: *Precision predictions for supersymmetric dark matter.* 2014. - http://arxiv.org/abs/1408.4960

- HARZ, Julia; HERMANN, Björn; KLASEN, Michael; KOVAŘÍK, Karol; STEPPELER, Patrick: *Precise Prediction of the Dark Matter Relic Density within the MSSM.* 2015. - http://arxiv.org/abs/1510.06295

- HARZ, Julia; HERMANN, Björn; KLASEN, Michael; KOVAŘÍK, Karol; STEPPELER, Patrick: *Interplay of gaugino (co)annihilation processes in the context of a precise relic density calculation.* 2015. - http://arxiv.org/abs/1510.09104

- HARZ, Julia; HERMANN, Björn; KLASEN, Michael; KOVAŘÍK, Karol; STEPPELER, Patrick: Theoretical uncertainty of the supersymmetric dark matter relic density from scheme and scale variations. In: *Physical Review D* **93** (2016), p. 114023

- KLASEN, Michael; KOVAŘÍK, Karol; STEPPELER, Patrick: SUSY-QCD corrections for the direct detection of neutralino dark matter and correlations with the relic density. To be published in: *Physical Review D* (2016)

- HARZ, Julia; HERMANN, Björn; KLASEN, Michael; KOVAŘÍK, Karol; STEPPELER, Patrick: *Predicting the neutralino relic density in the MSSM more precisely.* 2016. - http://arxiv.org/abs/1609.04998

The author presented the project at the following occasions:

- FRÜHJAHRSTAGUNG DER DEUTSCHEN PHYSIKALISCHEN GESELLSCHAFT
  March 2014, Mainz, Germany

- IDENTIFICATION OF DARK MATTER
  June 2014, Amsterdam, Netherlands

- PLANCK CONFERENCE
  May 2015, Ioannina, Greece

- INVITED SEMINAR AT NIKHEF
  July 2015, Amsterdam, Netherlands

1. Introduction

Mankind has marvelled at the stars and wondered about their nature and origin for thousands of years. In the course of time, this wondering has inspired mythology, enabled nautical navigation and became a distinct field of science, namely astronomy. Apart from that, we are unalteredly awed by stellar distances and the sheer eternalness of stars.

Given their heavy impact on our cultural history, there is a touch of irony in the fact, that stars seem to make up only a small fraction of the matter content of the universe and that we got originally aware of this by studying stellar motions (cf. [1–3]). According to recent cosmological observations, so-called *dark matter* outnumbers usual baryonic matter by a factor of five (cf. [4]). Even though the existence of dark matter is experimentally well confirmed nowadays, almost nothing is known about its nature and the identification of dark matter remains one of the biggest unsolved problems of modern physics.

A popular and consistent explanation for dark matter is based on the existence of *weakly interacting massive particles* (WIMPs) which are supposed to stream through the universe in large numbers. This hypothesis has led to a fruitful intertwining of cosmology and particle physics – the most extreme possible pairing in terms of involved length scales. Assuming that dark matter consists of WIMPs, their quantity, the so-called *relic density*, can be inferred from a multipole analysis of the cosmic microwave background. The most recent measurement is given by the Planck satellite and allows to determine the relic density with a relative error of only $\pm 2\%$ at the 1σ confidence level (cf. [5, 6]). In contrast, little is known about WIMP qualities like its mass or associated interactions. To gather such information and to confirm the existence of WIMPs, so-called *direct detection* experiments are executed (see e.g. [7, 8]). These experiments aim at observing WIMPs directly by detecting the nuclear recoil of a rare WIMP-nucleus interaction.

The *Standard Model of particle physics* does not include any suitable WIMP candidate and has to be extended to explain dark matter. A theoretical well motivated example for such an extension is given by *Supersymmetry* (SUSY) – a new symmetry between bosons and fermions. Incorporating SUSY in its minimal form leads to the *Minimal Supersymmetric Standard Model* (MSSM), which includes numerous additional particles. The lightest neutralino $\tilde{\chi}_1^0$ is one of those particles and turns out to be a good WIMP candidate if the conservation of a new quantum number called R-parity is postulated.

Within this thesis we adopt the MSSM, assume the lightest neutralino to account for dark matter and perform precision calculations affecting its predicted quality and quantity. On the one hand, we calculate radiative corrections to the neutralino-nucleon cross sections. These cross sections are essential when translating the (positive or negative) findings of a direct detection experiment on the MSSM. Including radiative corrections to the neutralino-nucleon cross sections corresponds to a reduction of the theoretical uncertainty, which in turn allows to determine the neutralino qualities more reliably in case of positive findings or to set more robust exclusion bounds in case of negative findings. On the other hand, we calculate radiative corrections to neutralino and chargino (co)annihilation into quarks. In many scenarios of the MSSM, these processes contribute dominantly to the

(co)annihilation cross section entering the *Boltzmann equation*. Solving the Boltzmann equation permits to predict the relic density. This prediction may then be compared with the experimental value deduced from the Planck data. In order to fully benefit from the experimental precision and to reliably identify the cosmological preferred region of the MSSM parameter space, theoretical uncertainties have to be minimised and radiative corrections to the (co)annihilation cross section have to be included.

This thesis is organised as follows: The subsequent chapter 2 is devoted to Supersymmetry. We sketch the basic idea of SUSY and present its main motivation. After a brief summary of the SUSY algebra, we argue that SUSY can not be realised exactly and discuss possible SUSY breaking mechanisms. Moreover, we introduce the MSSM and specify its particle content. In chapter 3 we turn from microscopic length scales and elementary particles to cosmological length scales and dark matter. We collect and discuss experimental evidence for the existence of dark matter. Afterwards we present and analyse the most common explanatory models. Out of these models, we favour the aforementioned WIMP hypothesis and assume the lightest neutralino to be the WIMP candidate.

Chapter 4 can be considered as the analytical core part of this thesis. We present the basic idea of direct detection and illustrate the composition of the corresponding detection rate. This rate includes the neutralino-nucleon cross sections, which can be calculated in the framework of *effective field theory*. We perform a full $\mathcal{O}(\alpha_s)$ *matching calculation* of the full and effective theory, where the former is given by the MSSM and the latter consists of the dominant four-fermion operators $\bar{\chi}\chi\bar{q}q$ and $\bar{\chi}\gamma_5\gamma_\mu\chi\bar{q}\gamma_5\gamma^\mu q$. To the knowledge of the author, this calculation has not been done before. Moreover, we detail the *running* of these effective operators and their associated Wilson coefficients, i.e. we describe their evolution from the high scale $\mu_{\text{high}} \sim 1000$ GeV down to the low scale $\mu_{\text{low}} \sim 5$ GeV. We continue with the discussion of the Boltzmann equation and the prediction of the neutralino relic density in chapter 5. To render this prediction more precisely, a full $\mathcal{O}(\alpha_s)$ calculation of neutralino and chargino (co)annihilation into quarks has been performed. We illustrate this calculation and comment on the main difficulties.

The analytic results of chapters 4 and 5 have been implemented in the numerical package `Dark matter at next-to-leading order` (`DM@NLO`, cf. [9]). This package, its main functionalities and chronological development, is presented in chapter 6. Thereafter we use `DM@NLO` for a phenomenological study in chapter 7. More precisely, we analyse the impact of the radiative corrections calculated in chapter 5 on the cosmological preferred region of the MSSM parameter space. In addition, we combine these calculations with those of chapter 4 to precisely predict the neutralino-nucleon cross sections for a given MSSM scenario. We finally conclude in chapter 8.

Remarks on the conventions, useful mathematical relations and technical details of methods relevant for the calculation in chapter 4 are presented separately in the appendices A to H. The reasons for this outsourcing are twofold: On the one hand, we aim at better legibility of the main part, especially for those already familiar with the technical machinery or more interested in phenomenology. On the other hand, readers particularly interested in technical details can directly access the respective self-contained appendix. We stress that chapter F includes additional original work. This chapter deals with *dimensional regularisation*, a well-known procedure to identify and isolate poles from divergent integrals. The associated tensor reduction method fails in case of vanishing Gram determinants, which occur naturally for zero relative velocity between incoming particles. This situation is encountered in chapter 4 and an alternative solution is worked out in detail.

2. Supersymmetry

What is the essence, the most fundamental property of a physical theory? A possible answer to this profound question could be: The essence of any physical theory is its underlying mathematical structure which in turn is defined by its symmetries.

Regarding symmetries as fundamental principles of nature has proven very fruitful in particle physics. Historical examples include the so-called *eightfold way* introduced by Murray Gell-Mann to organise mesons into octets and the *Higgs mechanism*, which gives rise to the masses of the weak gauge bosons [10]. Mathematically spoken, the former is based on a conserved $SU(3)$ flavour symmetry and the latter on a spontaneously broken $SU(2) \times U(1)$ gauge symmetry. Both of these findings are included in the *Standard Model* (SM) of particle physics, our recent and extraordinarily successful physical theory of the microscopic world.

Nevertheless, the SM has its shortcomings. In this chapter we illustrate some of these shortcomings and motivate the introduction of yet another symmetry – namely *Supersymmetry* (SUSY) – to compensate for them. We briefly discuss the corresponding SUSY algebra and sketch why and how SUSY is broken. Afterwards we present the *Minimal Supersymmetric Standard Model* (MSSM) and its particle content. This is of interest as the aim of this thesis are precision calculations within the MSSM (cf. chapters 4 and 5). We finally present the so-called phenomenological MSSM (pMSSM), which can be considered as a handy version of the MSSM including less free parameters. More detailed introductions to SUSY can be found in e.g. [11–14].

2.1. Basic idea and motivation of Supersymmetry

The introduction of Supersymmetry into particle physics is usually accredited to Julius Wess and Bruno Zumino [15, 16]. Note that although Wess and Zumino were the first to construct a consistent supersymmetric Lagrangian, SUSY was mentioned in quite different contexts several times before, see e.g. [17–19].

The basic idea of SUSY is to connect bosonic and fermionic degrees of freedom. More precisely, we introduce one[1] additional generator $\mathcal{Q}$ which transforms bosons into fermions and vice versa.

$$\mathcal{Q} \left| \text{boson} \right\rangle = \left| \text{fermion} \right\rangle \quad \text{and} \quad \mathcal{Q} \left| \text{fermion} \right\rangle = \left| \text{boson} \right\rangle. \tag{2.1}$$

The inclusion of SUSY has far reaching consequences. A direct result is that the numbers of bosonic and fermionic degrees of freedom are equal. Interestingly, SUSY also affects some of the shortcomings of the Standard Model, which we discuss in the following subsections.

---

[1] In this thesis we restrict ourselves to the MSSM, which belongs to the class of so-called $\mathcal{N} = 1$ SUSY models. Hence, we introduce only one SUSY generator $\mathcal{Q}$.
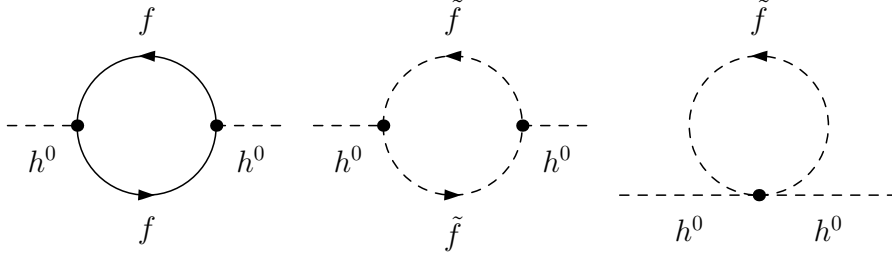
Figure 2.1.: Standard Model fermionic correction (left) and supersymmetric bosonic corrections (middle and right) to the Higgs mass

2.1.1. Hierarchy problem

We start with the analysis of the so-called *hierarchy problem* [20–22]. The hierarchy problem basically raises the question why the weak interaction is about 10^{32} times stronger than gravity. From a more technical point of view, this problem becomes manifest in radiative corrections to the Higgs mass m_{h^0}. Within the Standard Model, the Higgs self-energy is subject to radiative corrections including fermions f as shown on the left of figure 2.1. The most important contribution stems from the heaviest fermion, the top quark. Assuming that the Standard Model is valid up to a high scale Λ_{high} and using a cut-off method to *regularise* the divergent integral (cf. chapter F), we see that these radiative corrections are quadratically divergent, i.e. that they are proportional to $\Lambda_{\mathrm{high}}^2$. If the Standard Model is valid as long as quantum gravity effects are negligible, we can identify the high scale with the Planck scale $\Lambda_{\mathrm{Planck}} \sim 10^{19}$ GeV.

In contrast to that, the Higgs boson has recently been found experimentally and its mass has been measured to be around 125 GeV [23, 24]. What happened with the tremendous radiative corrections? The answer is that they vanish in the process of *renormalisation* (cf. chapter G). Even though renormalisation offers a consistent and technically solid solution to this dilemma, it seems to be *unnatural* that the Higgs mass is not only very sensitive to the Planck scale but that this dependence is somehow cancelled with incredible precision order by order in perturbation theory.

The introduction of SUSY offers an alternative solution to the hierarchy problem. Due to the transformation given in (2.1), every fermion of the Standard Model is accompanied by a supersymmetric bosonic partner, a so-called sfermion $\tilde{f}$. These sfermions lead to radiative corrections to the Higgs mass as well, the relevant diagrams are shown in the middle and on the right of figure 2.1. Interestingly, the contributions from these diagrams precisely cancel the quadratic divergence mentioned before. Having included SUSY, the final result depends only logarithmically on the high scale Λ_{high} and the original hierarchy problem is solved.

2.1.2. Unification of gauge couplings

One or maybe even the greater goal of physics is to describe nature with as little formulae as possible. In order to reduce the theoretical machinery, it has proven fruitful to find a common description for seemingly disconnected phenomena. Historical examples include the unification of electricity and magnetism to electromagnetism by James Clerk Maxwell or the unification of electromagnetic and weak interactions to the electroweak Standard

Model by Sheldon Lee Glashow, Mohammad Abdus Salam and Steven Weinberg [25, 26]. Following this path, the next logical step would be the unification of electroweak and strong interactions, i.e. to embed both in one, large simple gauge group like e.g. $SU(5)$ [27]. Such theories are usually called *grand unified theories* (GUTs).

An essential feature of any GUT is the *unification of gauge couplings* at some high energy scale Λ_{GUT} [28]. For energies larger than Λ_{GUT}, strong and electroweak interactions are unified and only one microscopic interaction remains. This unification can be investigated in detail with so-called *renormalisation group equations* (RGEs, cf. section G.4), which determine the value of physical parameters at a given energy. Within the Standard Model, the three gauge couplings approach each other but do not meet at a specific point.

This outcome is modified by SUSY. The additional supersymmetric particles contribute to the RGEs and allow for a unification of the gauge couplings at $\Lambda_{\mathrm{GUT}} \sim 10^{16}$ GeV. As SUSY is in no sense tailored to optimise the running of gauge couplings, this result is quite remarkable.

2.1.3. Dark matter

According to recent cosmological observations, the dominant matter component of the universe is so-called *dark matter*, a non-luminous, non-baryonic, massive form of matter whose origin and nature has not been identified yet. A popular hypothesis states that dark matter consists of weakly interacting massive particles (WIMPs). However, there is no suitable WIMP within the Standard Model. This fact can be interpreted in two ways. On the one hand, one might assume that the Standard Model is complete, i.e. that there are no additional non-SM particles. According to this assumption, the WIMP hypothesis has proven false. On the other hand, one might stick to the WIMP hypothesis and conclude that at least one additional non-SM particle has to exist. Taking into account that there are several other known shortcomings of the Standard Model, the second option is commonly preferred.

When introducing SUSY, a whole zoo of new supersymmetric partner particles is created. It turns out that in particular the neutralino $\tilde{\chi}_1^0$, which is the lightest supersymmetric particle (LSP) in many scenarios of the MSSM, is a suitable WIMP. This means that in contrast to the SM, SUSY offers a consistent explanation for dark matter. More details on dark matter are given in chapter 3.

2.1.4. Haag-Łopuszański-Sohnius theorem

Another, more formal motivation for SUSY is given by the *Haag-Łopuszański-Sohnius theorem* [29]. This theorem states that the most general symmetry a non-trivial quantum field theory can possess, is an internal gauge symmetry paired with external Poincaré symmetry and extended by SUSY. The Standard Model is an example for a non-trivial quantum field theory. As gauge and Poincaré symmetry are realised, it seems natural to expect that SUSY is realised as well.

A crucial condition for the Haag-Łopuszański-Sohnius theorem to hold is the anticommutativity of the SUSY generators. If these generators would commute, i.e. if they would be of bosonic rather than fermionic character, no additional non-trivial symmetry can be constructed. This is covered by the *Coleman-Mandula* theorem [30].

Having presented the main motivation for introducing SUSY, we stress that this motivation is originally of rather formal, mathematical character. The fact that SUSY gives

rise to a rich phenomenology and can e.g. explain dark matter additionally, is the reason for the sustained attractivity of this approach. Nevertheless, no explicit experimental evidence for the realisation of SUSY in nature has been found yet.

2.2. SUSY algebra

In this section, we present the *SUSY algebra* which has been worked out in the context of the Haag-Łopuszański-Sohnius theorem [29]. The SUSY algebra extends the *Poincaré algebra* given by

$$[P_\mu, P_\nu] \quad = \quad 0. \tag{2.2}$$

$$[M_{\mu\nu}, P_\rho] \quad = \quad i(g_{\nu\rho}P_\mu - g_{\mu\rho}P_\nu). \tag{2.3}$$

$$[M_{\mu\nu}, M_{\rho\sigma}] \quad = \quad i(g_{\mu\sigma}M_{\nu\rho} + g_{\nu\rho}M_{\mu\sigma} - g_{\mu\rho}M_{\nu\sigma} - g_{\nu\sigma}M_{\mu\rho}). \tag{2.4}$$

Here P_μ denotes the generator of space-time translations and $M_{\mu\nu}$ the generator of Lorentz transformations. In order to write down the SUSY algebra in compact form, we introduce the *generalised Pauli matrices* σ^μ and $\bar{\sigma}^\mu$ which are defined via

$$\sigma^\mu = (\mathbb{1}, \sigma^i) \quad \text{and} \quad \bar{\sigma}^\mu = (\mathbb{1}, -\sigma^i), \tag{2.5}$$

where σ^i denotes the usual *Pauli matrices*.

$$\sigma^1 = \begin{pmatrix} 0 & 1 \\ 1 & 0 \end{pmatrix}, \quad \sigma^2 = \begin{pmatrix} 0 & -i \\ i & 0 \end{pmatrix} \quad \text{and} \quad \sigma^3 = \begin{pmatrix} 1 & 0 \\ 0 & -1 \end{pmatrix}. \tag{2.6}$$

Furthermore, we define

$$\sigma^{\mu\nu} = \frac{i}{2}(\sigma^\mu \bar{\sigma}^\nu - \sigma^\nu \bar{\sigma}^\mu) \quad \text{and} \quad \bar{\sigma}^{\mu\nu} = \frac{i}{2}(\bar{\sigma}^\mu \sigma^\nu - \bar{\sigma}^\nu \sigma^\mu). \tag{2.7}$$

We decompose the spinorial generator $\mathcal{Q}$ into two *Weyl components* $\mathcal{Q}_a$ with $a = 1, 2$ (cf. chapter E). Undotted indicies stand for the $(\frac{1}{2}, 0)$ representation and dotted indices for the $(0, \frac{1}{2})$ representation of the homogeneous Lorentz group. SUSY generators of both representations are linked via $\bar{\mathcal{Q}}_{\dot{a}} = \mathcal{Q}_a^\dagger$. Using this nomenclature, we can write down the SUSY algebra as

$$\{\mathcal{Q}_a, \bar{\mathcal{Q}}_{\dot{b}}\} \quad = \quad 2(\sigma^\mu)_{a\dot{b}}P_\mu \quad \text{and} \quad \{\bar{\mathcal{Q}}^{\dot{a}}, \mathcal{Q}^b\} = 2(\bar{\sigma}^\mu)^{\dot{a}b}P_\mu. \tag{2.8}$$

$$\{\mathcal{Q}_a, \mathcal{Q}_b\} \quad = \quad \{\bar{\mathcal{Q}}^{\dot{a}}, \bar{\mathcal{Q}}^{\dot{b}}\} = 0. \tag{2.9}$$

$$[M_{\mu\nu}, \mathcal{Q}_a] \quad = \quad -\frac{1}{2}(\sigma_{\mu\nu})_a{}^b \mathcal{Q}_b \quad \text{and} \quad [M_{\mu\nu}, \bar{\mathcal{Q}}^{\dot{a}}] = -\frac{1}{2}(\bar{\sigma}_{\mu\nu})^{\dot{a}}{}_{\dot{b}} \bar{\mathcal{Q}}^{\dot{b}}. \tag{2.10}$$

$$[\mathcal{Q}_a, P_\mu] \quad = \quad [\bar{\mathcal{Q}}^{\dot{a}}, P_\mu] = 0. \tag{2.11}$$

The consequences of this highly abstract algebra are quite counterintuitive. According to (2.8), transforming e.g. a fermion into a boson and back into a fermion is linked with a space-time translation. However, in order to meet phenomenological requirements, it has proven useful to extend this algebra even further by imposing an additional $U(1)$ symmetry. If R denotes the generator of this new symmetry, we have

$$[\mathcal{Q}_a, R] = \mathcal{Q}_a \quad \text{and} \quad [\mathcal{Q}_{\dot{a}}, R] = -\mathcal{Q}_{\dot{a}}. \tag{2.12}$$

As R is a bosonic generator, the Coleman-Mandula theorem holds and R commutes with the generators of the Poincaré algebra, i.e.

$$[P_\mu, R] = [M_{\mu\nu}, R] = 0. \tag{2.13}$$

2.3. Soft SUSY breaking

In the last section we have formally introduced SUSY and disregarded any experimental finding, which we try to make good for at this point. Remember that SUSY transformations as given by (2.1) only modify the spin of the considered particle. SUSY is an external symmetry and does not affect gauge symmetry. There are no new interactions introduced and any SUSY particle possesses the very same quantum numbers as its partner particle – except for spin. In particular, both particles have the same mass as the mass operator $-P^2$ commutes with the SUSY generator $\mathcal{Q}$ according to (2.11). Hence, if SUSY is an exact symmetry of nature, there should exist light and even massless supersymmetric partners of e.g. the electron and the gluon, respectively. These particles would have been easily detected long ago. Therefore, SUSY has to be a *broken symmetry*.

The trick is to break SUSY *softly*, i.e. in such a way that its original benefits persist. In particular, softly broken SUSY has to be renormalisable and shall solve the hierarchy problem. Soft SUSY breaking is included by adding suitable terms to the MSSM Lagrangian, i.e. via

$$\mathcal{L}_{\mathrm{MSSM}} = \mathcal{L}_{\mathrm{SUSY}} + \mathcal{L}_{\mathrm{soft}}. \tag{2.14}$$

In this notation, the full MSSM Lagrangian consists of a SUSY conserving part $\mathcal{L}_{\mathrm{SUSY}}$ which contains Yukawa and gauge interactions and additional SUSY violating mass terms and trilinear couplings collected in $\mathcal{L}_{\mathrm{soft}}$. The crucial point is that the latter all have positive mass dimension. An explicit expression for the full MSSM Lagrangian can be found in e.g. [13].

As we do not know if SUSY is realised at all, we can only speculate about its breaking mechanism. In practice, one parametrises this lack of knowledge by adding all possible terms which respect gauge symmetry and renormalisability. This can be interpreted as an *effective field theory* (cf. chapter H) approach. The usual assumption is that there exists a so-called hidden sector which is responsible for soft SUSY breaking at some high scale $\Lambda_{\mathrm{soft}} \gg \Lambda_{\mathrm{electroweak}} \sim 100$ GeV. The hidden sector involves heavy particles which are somehow connected with the visible SUSY sector via a messenger sector. This means that although the heavy particles of the hidden sector are absent at the electroweak scale, they leave marks affecting the visible sector. These remnants are nothing but the soft breaking terms incorporated in $\mathcal{L}_{\mathrm{soft}}$.

However, dealing with soft SUSY breaking in this manner comes with its downsides. The biggest disadvantage in comparison to unbroken SUSY is the considerably increased number of free parameters. The Standard Model of particle physics involves 19 free parameters.[2] The SUSY conserving part $\mathcal{L}_{\mathrm{SUSY}}$ modifies the Higgs sector and the higgsino mass parameter μ effectively replaces the SM Higgs boson mass m_{h^0} as a free parameter (cf. subsection 2.4.1). In contrast, soft SUSY breaking introduces 105 new independent parameters, leading to 124 free parameters in total and resulting in a large arbitrariness of the theory [31]. To handle this arbitrariness and to allow for meaningful comparisons with experimental data, so-called *phenomenological models* are introduced. We return to this issue in section 2.5.

---

[2] A possible parametrisation is given by the six quark masses m_q, the three lepton masses m_l, the Higgs mass m_{h^0}, the Higgs vacuum expectation value v, the strength of the three gauge couplings, the three mixing angles of the Cabibbo-Kobayashi-Maskawa matrix, the associated CP violating phase and the vaccum angle $\theta_{\mathrm{QCD}} = 0$ of quantum chromodynamics (QCD), which is included to avoid the strong CP problem. The Standard Model does not include non-zero neutrino masses, which would lead to three more mass terms, three additional mixing angles and one additional phase.

Some of the 105 soft breaking parameters are mass parameters. Let m_{soft} denote the largest mass parameter appearing in $\mathcal{L}_{\text{soft}}$. The corresponding terms lead to additional contributions to the Higgs self-energy proportional to m_{soft}^2. If this mass parameter is very large in comparison to the electroweak scale $\Lambda_{\text{electroweak}} \sim 100$ GeV, the Higgs mass becomes subject to large radiative corrections again and the hierarchy problem reappears. To avoid this, m_{soft} is assumed not to be substantially larger than the electroweak scale, i.e. $m_{\text{soft}} \sim 1$ TeV. As the mass splittings between the known Standard Model particles and their superpartners are determined by the mass parameters of $\mathcal{L}_{\text{soft}}$, this translates to the masses of the SUSY particles. At least the lightest SUSY particles should possess masses around m_{soft} or smaller. This line of arguments has led to the optimism that SUSY particles are observable with the Large Hadron Collider (LHC). However, since no evidence for SUSY at the TeV scale has been found yet, this theory – or at least its original motivation – is on the edge.

One might also go beyond the effective approach and wonder what the actual SUSY breaking mechanism might be, i.e. where the terms in $\mathcal{L}_{\text{soft}}$ are stemming from and how SUSY breaking is mediated into the visible sector. The most prominent examples for the latter include *gravity mediated* and *gauge mediated SUSY breaking* [32–36]. In case of gravity mediated or Planck scale SUSY breaking, the mediation is due to gravity and the resulting soft mass parameters are related to the Planck scale via

$$m_{\text{soft}} \sim \frac{\Lambda_{\text{soft}}^2}{\Lambda_{\text{Planck}}}. \tag{2.15}$$

Assuming that m_{soft} is around ~ 1 TeV, we conclude that gravity mediated SUSY breaking occurs at $\Lambda_{\text{soft}} \sim 10^{11}$ GeV. On the other hand, we have gauge mediated SUSY breaking, which bases on ordinary strong and electroweak interactions. The soft breaking terms are generated by loop diagrams including some new messenger particles of mass m_{mess}. This leads to

$$m_{\text{soft}} \sim c_L \frac{\Lambda_{\text{soft}}^2}{m_{\text{mess}}}, \tag{2.16}$$

where $c_L \sim 0.1$ denotes a loop factor including Standard Model gauge couplings. If we assume that the messenger mass is of similar size as Λ_{soft}, we deduce that gauge mediated SUSY breaking can take place at much lower energies than gravity mediated SUSY breaking, namely at $\Lambda_{\text{soft}} \sim 10^4$ GeV.

2.4. The Minimal Supersymmetric Standard Model

Having motivated and introduced SUSY on a general footing, we turn to the concrete model relevant for our studies, the *Minimal Supersymmetric Standard Model*. In brief, the MSSM can be understood as a supersymmetrised version of the Standard Model with as little new particles as possible. In particular, only one SUSY generator $\mathcal{Q}$ is introduced, which is referred to as $\mathcal{N} = 1$ SUSY. The essential features of the MSSM can be summarised as follows:

- Each gauge boson gets a supersymmetric fermionic partner. This affects all gluons g and the electroweak gauge eigenstates B, W_1, W_2 and W_3. The associated superpartners are called gluinos $\tilde{g}$, bino $\tilde{B}$ and winos $\tilde{W}_1$, $\tilde{W}_2$ and $\tilde{W}_3$.

- The Standard Model includes one Higgs doublet containing four degrees of freedom. In the course of the Higgs mechanism, three of them are "eaten up" by the weak gauge bosons rendering them massive. Afterwards one physical particle is left – the Higgs boson h^0 [10].

  If one wants to consistently implement SUSY, a second Higgs doublet has to be added as the masses of up- and down-type quarks can not be generated from the same doublet anymore [13]. Moreover, the inclusion of a second doublet avoids certain gauge anomalies [37]. The result is that from the original eight degrees of freedom five become manifest as physical particles, i.e. Higgs bosons. There is a light scalar h^0, a heavy scalar H^0, a pseudoscalar A^0 and two charged $H^\pm$ Higgs bosons. All of these Higgs bosons get supersymmetric fermionic partners, so-called higgsinos. More details on the Higgs sector of the MSSM are given in subsection 2.4.1.

  We stress that the light scalar Higgs boson has to be SM-like and possess a mass of $m_{h^0} \sim 125$ GeV, which is one of the most severe constraints on the MSSM.

- The winos $\tilde{W}_2$ and $\tilde{W}_3$ are electrically charged and possess the same quantum numbers as the charged higgsinos. These particles mix into mass eigenstates called charginos $\tilde{\chi}_k^\pm$, where $k = 1, 2$. Similarly the electrically neutral bino $\tilde{B}$, wino $\tilde{W}_1$ and the neutral higgsinos mix into so-called neutralinos $\tilde{\chi}_i^0$, where $i = 1, 2, 3, 4$. These mixings are described in subsection 2.4.2. We commonly refer to charginos and neutralinos as gauginos.

- Each quark q of the Standard Model gets supersymmetric scalar partners, so-called squarks $\tilde{q}$. As quarks consist of left- and right-handed chiral components $q_{L/R}$ which are independent degrees of freedom, there are two squarks $\tilde{q}_{L/R}$ per quark. These two squarks are interaction eigenstates, which mix into mass eigenstates $\tilde{q}_{1,2}$ as described in subsection 2.4.3. Note that the squarks themselves are spin zero particles for which chirality is not defined. The subscript L/R simply refers to the chirality of their original quark partners.

  In the same way each lepton l gets accompanied by so-called sleptons $\tilde{l}$. There are two sleptons $\tilde{l}_{L/R}$ per charged lepton (i.e. for $l = e, \mu, \tau$). In case of neutrinos, we have only one sneutrino $\tilde{\nu}_L$ per neutrino ν_L as only left-handed neutrinos exist in the Standard Model.

- The MSSM introduces a new conserved multiplicative quantum number called R-parity. The underlying symmetry is of $\mathbb{Z}_2$ type and a remnant of the $U(1)$ symmetry defined by (2.12) and (2.13). More precisely, the R-parity of a particle possessing baryon number B, lepton number L and spin S is given by

$$P_R = (-1)^{3(B-L)+2S}. \tag{2.17}$$

  The outcome is simple: Every Standard Model particle (including the additional Higgs bosons H^0, A^0 and $H^\pm$) has R-parity $+1$ and all associated SUSY partners have R-parity -1. If R-parity is conserved, baryon and lepton number violating processes are absent and SUSY introduces no new possible channels for e.g. the decay of the proton.

Table 2.1.: Particle content of the MSSM

Standard Model plus second Higgs doublet		SUSY partners	
Symbol	**Name**	**Symbol**	**Name**
u, c, t	Up quarks	$\tilde{u}_i, \tilde{c}_i, \tilde{t}_i$, where $i = 1, 2$	Up squarks
d, s, b	Down quarks	$\tilde{d}_i, \tilde{s}_i, \tilde{b}_i$, where $i = 1, 2$	Down squarks
e, μ, τ	Charged leptons	$\tilde{e}_i, \tilde{\mu}_i, \tilde{\tau}_i$, where $i = 1, 2$	Charged sleptons
ν_e, ν_μ, ν_τ	Neutrinos	$\tilde{\nu}_e, \tilde{\nu}_\mu, \tilde{\nu}_\tau$	Sneutrinos
g	Gluons	$\tilde{g}$	Gluinos
$W^\pm$	$W^\pm$ bosons	$\tilde{\chi}_k^\pm$, where $k = 1, 2$	Charginos
$H^\pm$	Charged Higgs bosons		
γ	Photon	$\tilde{\chi}_j^0$, where $j = 1, 2, 3, 4$	Neutralinos
Z^0	Z^0 boson		
h^0	Light scalar Higgs boson		
H^0	Heavy scalar Higgs boson		
A^0	Pseudoscalar Higgs boson		

Another important consequence is that SUSY particles can only interact pairwise. This implies that heavier SUSY particles may subsequently decay into lighter ones, but the lightest supersymmetric particle (LSP) can not decay and has to be stable. In typical scenarios of the MSSM, the LSP turns out to be the lightest neutralino $\tilde{\chi}_1^0$. If this particle is stable, it turns out to be a viable dark matter candidate as it is in addition uncoloured, electrically neutral and massive (cf. subsection 3.2.3).

R-parity conservation also affects the production of SUSY particles at colliders. SUSY particles can only be produced in pairs. In case of the LHC, the primarily produced particles are likely to be strongly interacting, i.e. squarks or gluinos, which quickly decay into the LSP. If the LSP is only weakly interacting as e.g. the lightest neutralino, this particle is not detectable. Hence, the typical LHC signal of a SUSY production process consists of missing energy plus jets. The latter occur necessarily during the decay processes of the coloured SUSY particles.

We finally mention that R-parity violating models are studied as well, the main phenomenological motivation being the generation of neutrino masses [38].

Having collected the main features of the MSSM, we present its particle content, i.e. its mass eigenstates in table 2.1 (inspired by [39]). The particle content of the MSSM is investigated in greater detail in the following subsections.

2.4.1. Higgs sector

We begin with the discussion of the Higgs sector of the MSSM, wherein we basically follow the extensive review [40]. As mentioned before, two Higgs doublets H_1 and H_2 have to be included in case of the MSSM. These doublets can be written as

$$H_1 \;=\; \frac{1}{\sqrt{2}} \begin{pmatrix} H_1^0 \\ H_1^- \end{pmatrix} = \frac{1}{\sqrt{2}} \begin{pmatrix} v_1 + \phi_1^0 + i\xi_1^0 \\ \phi_1^- \end{pmatrix}. \tag{2.18}$$

$$H_2 \;=\; \frac{1}{\sqrt{2}} \begin{pmatrix} H_2^+ \\ H_2^0 \end{pmatrix} = \frac{1}{\sqrt{2}} \begin{pmatrix} \phi_2^+ \\ v_2 + \phi_2^0 + i\xi_2^0 \end{pmatrix}. \tag{2.19}$$

The first Higgs doublet has hypercharge $Y = -1$ and is responsible for the mass generation of down-type quarks, whereas the second doublet has $Y = +1$ and takes care of the up-type quark masses. The neutral components of both doublets acquire non-vanishing vacuum expectation values (VEVs) in terms of

$$\langle H_1 \rangle = \frac{1}{\sqrt{2}} \begin{pmatrix} v_1 \\ 0 \end{pmatrix} \quad \text{and} \quad \langle H_2 \rangle = \frac{1}{\sqrt{2}} \begin{pmatrix} 0 \\ v_2 \end{pmatrix}. \tag{2.20}$$

These VEVs are restricted by the condition

$$v_1^2 + v_2^2 = v^2 = \frac{1}{\sqrt{2}G_F} \sim (246 \text{ GeV})^2, \tag{2.21}$$

where G_F denotes the Fermi constant. The Fermi constant has been introduced in the Fermi theory of beta decay (cf. chapter H) and can be reexpressed in terms of the weak coupling constant g_w and the $W^\pm$ boson mass $m_{W^\pm}$ as

$$G_F = \frac{\sqrt{2}g_w^2}{8m_{W^\pm}^2}. \tag{2.22}$$

Having set the absolute value of the two VEVs, their ratio remains undetermined yet. This ratio is of great phenomenological relevance and phrased $\tan\beta$, i.e.

$$\tan\beta = \frac{v_2}{v_1}. \tag{2.23}$$

The physical Higgs bosons are related to the individual components of the Higgs doublets via rotation matrices. More precisely, we have

$$\begin{pmatrix} H^0 \\ h^0 \end{pmatrix} \;=\; \begin{pmatrix} \cos\alpha & \sin\alpha \\ -\sin\alpha & \cos\alpha \end{pmatrix} \begin{pmatrix} \phi_1^0 \\ \phi_2^0 \end{pmatrix}. \tag{2.24}$$

$$\begin{pmatrix} G^0 \\ A^0 \end{pmatrix} \;=\; \begin{pmatrix} \cos\beta & \sin\beta \\ -\sin\beta & \cos\beta \end{pmatrix} \begin{pmatrix} \xi_1^0 \\ \xi_2^0 \end{pmatrix}. \tag{2.25}$$

$$\begin{pmatrix} G^\pm \\ H^\pm \end{pmatrix} \;=\; \begin{pmatrix} \cos\beta & \sin\beta \\ -\sin\beta & \cos\beta \end{pmatrix} \begin{pmatrix} \phi_1^\pm \\ \phi_2^\pm \end{pmatrix}. \tag{2.26}$$

The neutral and charged Goldstone bosons G^0 and $G^\pm$ do not correspond to physical particles but are absorbed into the longitudinal components of the massive gauge bosons [41–43].

Up to now, the Higgs sector contains six parameters: Four independent Higgs boson masses and the mixing angles α and β. However, it turns out that only two of them can be chosen independently. The conventional choice is to define $\tan\beta$ and m_{A^0} as input parameters. The other parameters can then be obtained via

$$m_{h^0,H^0}^2 = \frac{1}{2}\left(m_{A^0}^2 + m_{Z^0}^2 \mp \sqrt{(m_{A^0}^2 + m_{Z^0}^2)^2 - 4m_{A^0}^2 m_{Z^0}^2 \cos^2 2\beta}\right). \quad (2.27)$$

$$m_{H^\pm}^2 = m_{A^0}^2 + m_{W^\pm}^2. \quad (2.28)$$

$$\tan 2\alpha = \tan 2\beta \frac{m_{A^0}^2 + m_{Z^0}^2}{m_{A^0}^2 - m_{Z^0}^2}. \quad (2.29)$$

We stress that these relations only hold at tree-level and are subject to radiative corrections. These corrections are substantial as the tree-level prediction

$$
\begin{aligned}
m_{h^0}^2 &= \frac{1}{2}\left(m_{A^0}^2 + m_{Z^0}^2 - \sqrt{(m_{A^0}^2 + m_{Z^0}^2)^2 - 4m_{A^0}^2 m_{Z^0}^2 \cos^2 2\beta}\right) \\
&\leq \frac{1}{2}\left(m_{A^0}^2 + m_{Z^0}^2 - \sqrt{(m_{A^0}^2 + m_{Z^0}^2)^2 - 4m_{A^0}^2 m_{Z^0}^2}\right) \\
&= \frac{1}{2}\left(m_{A^0}^2 + m_{Z^0}^2 - \sqrt{(m_{A^0}^2 - m_{Z^0}^2)^2}\right) = m_{Z^0}^2 \quad (2.30)
\end{aligned}
$$

is clearly not fulfilled.

So far we have omitted another important and independent parameter of the Higgs sector, namely the higgsino mass parameter μ. This parameter appears in front of the two chiral superfields $\hat{H}_1$ and $\hat{H}_2$ in $\mathcal{L}_{\text{SUSY}}$. These chiral superfields can be considered as objects simultaneously including the Higgs doublets introduced in (2.19) and their SUSY equivalents, the fermionic higgsino doublets $\tilde{H}_1$ and $\tilde{H}_2$ given by

$$\tilde{H}_1 = \frac{1}{\sqrt{2}}\begin{pmatrix} \tilde{H}_1^0 \\ \tilde{H}_1^- \end{pmatrix} \quad \text{and} \quad \tilde{H}_2 = \frac{1}{\sqrt{2}}\begin{pmatrix} \tilde{H}_2^+ \\ \tilde{H}_2^0 \end{pmatrix}. \quad (2.31)$$

For more details on the superfield formalism, we refer to [13].

The higgsino mass parameter has manifold implications. Firstly – as its name suggests – it drives the masses of the higgsinos. Being a dimensionful parameter, it also appears in front of trilinear couplings, i.e. couplings between three scalar particles. Some of these couplings are relevant for the mixing of the squarks. Therefore, we reencounter μ in subsection 2.4.3, where we discuss squark mixing in greater detail. Finally, μ appears in the scalar Higgs potential.

The latter is connected with the so-called μ-problem of the MSSM, which bears some resemblance to the hierarchy problem and can be summarised as follows. μ is a SUSY preserving quantity and thus not connected to $\mathcal{L}_{\text{soft}}$ and its typical mass scale m_{soft}. The latter is assumed to be around the TeV scale in order to solve the hierarchy problem, whereas μ can be arbitrarily large, e.g. of $\mathcal{O}(\Lambda_{\text{Planck}})$. However, the scalar Higgs potential includes not only μ but a couple of soft SUSY breaking terms as well. After electroweak symmetry breaking, we want to obtain a non-vanishing VEV of $v \sim 246$ GeV. This implies that either some miraculous cancellation is going on or all parameters entering the Higgs potential should be roughly of the same order and hence μ has to be around the TeV scale as well. Within the MSSM, there is no a priori reason why μ should be that small. Possible explanations can be found in e.g. [44–46].

2.4.2. Chargino and neutralino sector

The electrically charged higgsinos $\tilde{H}_1^-$ and $\tilde{H}_2^+$ introduced in the previous subsection possess the same quantum numbers as the charged winos $\tilde{W}_2$ and $\tilde{W}_3$. These particles mix into mass eigenstates called charginos $\tilde{\chi}_k^\pm$, where $k = 1, 2$. The corresponding part of the MSSM Lagrangian reads

$$\mathcal{L}_{\text{MSSM}} \supset -(\psi^-)^T \mathcal{M}^{\tilde{\chi}^\pm} \psi^+ + \text{h. c.,} \tag{2.32}$$

where we have introduced the shorthand notation

$$\psi^+ = \begin{pmatrix} \tilde{W}_2 \\ \tilde{H}_2^+ \end{pmatrix} \quad \text{and} \quad \psi^- = \begin{pmatrix} \tilde{W}_3 \\ \tilde{H}_1^- \end{pmatrix}. \tag{2.33}$$

The chargino mass matrix includes the higgsino and wino mass parameters μ and M_2 and is given by

$$\mathcal{M}^{\tilde{\chi}^\pm} = \begin{pmatrix} M_2 & \sqrt{2} m_{W^\pm} \sin\beta \\ \sqrt{2} m_{W^\pm} \cos\beta & \mu \end{pmatrix}. \tag{2.34}$$

The aim is to diagonalise this matrix, i.e. to find the mass eigenstates. To achieve this, we introduce two unitary 2×2 chargino mixing matrices $U^{\tilde{\chi}^\pm}$ and $V^{\tilde{\chi}^\pm}$ which satisfy

$$\left(U^{\tilde{\chi}^\pm}\right)^* \mathcal{M}^{\tilde{\chi}^\pm} \left(V^{\tilde{\chi}^\pm}\right)^{-1} \overset{!}{=} \begin{pmatrix} m_1^{\tilde{\chi}^\pm} & 0 \\ 0 & m_2^{\tilde{\chi}^\pm} \end{pmatrix}. \tag{2.35}$$

Given this diagonalisation and following [11], the physical four-component Dirac chargino fields can be constructed via

$$\tilde{\chi}_i^+ = \begin{pmatrix} \chi_i^+ \\ \overline{\left(\chi_i^-\right)}^T \end{pmatrix}, \quad \text{where} \quad \chi_i^+ = V_{ij}^{\tilde{\chi}^\pm} \psi_j^+ \quad \text{and} \quad \chi_i^- = U_{ij}^{\tilde{\chi}^\pm} \psi_j^-. \tag{2.36}$$

The two chargino masses are given by

$$\begin{aligned} m_{\tilde{\chi}_{1,2}^\pm}^2 &= \frac{1}{2} \Big(M_2^2 + \mu^2 + 2 m_{W^\pm}^2 \\ &\quad \mp \sqrt{(M_2^2 + \mu^2 + 2 m_{W^\pm}^2)^2 - 4(m_{W^\pm}^2 \sin 2\beta - \mu M_2)^2} \Big). \end{aligned} \tag{2.37}$$

By convention, the first chargino is chosen to be the lighter one.

In a similar fashion, the neutral bino $\tilde{B}$, the neutral wino $\tilde{W}_1$ and the neutral higgsinos $\tilde{H}_1^0$ and $\tilde{H}_2^0$ mix into so-called neutralinos $\tilde{\chi}_i^0$, where $i = 1, 2, 3, 4$. By collecting all the aforementioned neutral fields into a vector

$$\left(\psi^0\right)^T = \begin{pmatrix} \tilde{B}, & \tilde{W}_1, & \tilde{H}_1^0, & \tilde{H}_2^0 \end{pmatrix}, \tag{2.38}$$

we can compactly write down the corresponding term of the MSSM Lagrangian as

$$\mathcal{L}_{\text{MSSM}} \supset -\frac{1}{2} \left(\psi^0\right)^T \mathcal{M}^{\tilde{\chi}^0} \psi^0 + \text{h. c.} \tag{2.39}$$

Herein the symmetric 4×4 neutralino mass matrix $\mathcal{M}^{\tilde{\chi}^0}$ is given by

$$\mathcal{M}^{\tilde{\chi}^0} = \begin{pmatrix} \mathcal{M}^{\tilde{\chi}^0}_{11} & \mathcal{M}^{\tilde{\chi}^0}_{12} & \mathcal{M}^{\tilde{\chi}^0}_{13} & \mathcal{M}^{\tilde{\chi}^0}_{14} \\ \mathcal{M}^{\tilde{\chi}^0}_{21} & \mathcal{M}^{\tilde{\chi}^0}_{22} & \mathcal{M}^{\tilde{\chi}^0}_{23} & \mathcal{M}^{\tilde{\chi}^0}_{24} \\ \mathcal{M}^{\tilde{\chi}^0}_{31} & \mathcal{M}^{\tilde{\chi}^0}_{32} & \mathcal{M}^{\tilde{\chi}^0}_{33} & \mathcal{M}^{\tilde{\chi}^0}_{34} \\ \mathcal{M}^{\tilde{\chi}^0}_{41} & \mathcal{M}^{\tilde{\chi}^0}_{42} & \mathcal{M}^{\tilde{\chi}^0}_{43} & \mathcal{M}^{\tilde{\chi}^0}_{44} \end{pmatrix}, \tag{2.40}$$

where its components read

$$\mathcal{M}^{\tilde{\chi}^0}_{11} = M_1. \qquad\qquad \mathcal{M}^{\tilde{\chi}^0}_{22} = M_2. \tag{2.41}$$

$$\mathcal{M}^{\tilde{\chi}^0}_{34} = \mathcal{M}^{\tilde{\chi}^0}_{43} = -\mu. \qquad \mathcal{M}^{\tilde{\chi}^0}_{12} = \mathcal{M}^{\tilde{\chi}^0}_{21} = \mathcal{M}^{\tilde{\chi}^0}_{33} = \mathcal{M}^{\tilde{\chi}^0}_{44} = 0. \tag{2.42}$$

$$\mathcal{M}^{\tilde{\chi}^0}_{13} = \mathcal{M}^{\tilde{\chi}^0}_{31} = -m_{Z^0} \cos\beta \sin\theta_W. \quad \mathcal{M}^{\tilde{\chi}^0}_{14} = \mathcal{M}^{\tilde{\chi}^0}_{41} = m_{Z^0} \sin\beta \sin\theta_W. \tag{2.43}$$

$$\mathcal{M}^{\tilde{\chi}^0}_{23} = \mathcal{M}^{\tilde{\chi}^0}_{32} = m_{Z^0} \cos\beta \cos\theta_W. \quad \mathcal{M}^{\tilde{\chi}^0}_{24} = \mathcal{M}^{\tilde{\chi}^0}_{42} = -m_{Z^0} \sin\beta \cos\theta_W. \tag{2.44}$$

Hence, the neutralino mass matrix includes the bino, wino and higgsino mass parameters M_1, M_2 and μ. To diagonalise the neutralino mass matrix, we introduce the 4×4 unitary neutralino mixing matrix N which is defined by

$$\begin{pmatrix} m_{\tilde{\chi}^0_1} & 0 & 0 & 0 \\ 0 & m_{\tilde{\chi}^0_2} & 0 & 0 \\ 0 & 0 & m_{\tilde{\chi}^0_3} & 0 \\ 0 & 0 & 0 & m_{\tilde{\chi}^0_4} \end{pmatrix} \overset{!}{=} N^* \mathcal{M}^{\tilde{\chi}^0} N^{-1}. \tag{2.45}$$

In this convention, the four neutralinos are ordered by mass, i.e. $m_{\tilde{\chi}^0_1} < m_{\tilde{\chi}^0_2} < m_{\tilde{\chi}^0_3} < m_{\tilde{\chi}^0_4}$. Moreover, we can introduce four-component Majorana fields via

$$\tilde{\chi}^0_i = \begin{pmatrix} \chi^0_i \\ \left(\overline{\chi^0_i}\right)^T \end{pmatrix}, \quad \text{where} \quad \chi^0_i = N_{ij}\psi^0_j. \tag{2.46}$$

2.4.3. Squark sector

As stressed earlier, we have to distinguish between squark gauge eigenstates $\tilde{q}_{L/R}$ and squark mass eigenstates $\tilde{q}_{1,2}$. The latter constitute the actual particles, whereas the former correspond to SUSY transformed quark gauge eigenstates which occur in the kinematic part of the MSSM Lagrangian in terms of

$$\mathcal{L}_{\text{MSSM}} \supset -\begin{pmatrix} \tilde{q}_L, & \tilde{q}_R \end{pmatrix}^* \mathcal{M}^{\tilde{q}} \begin{pmatrix} \tilde{q}_L \\ \tilde{q}_R \end{pmatrix} = -\begin{pmatrix} \tilde{q}_L, & \tilde{q}_R \end{pmatrix}^* \begin{pmatrix} \mathcal{M}^{\tilde{q}}_{11} & \mathcal{M}^{\tilde{q}}_{12} \\ \mathcal{M}^{\tilde{q}}_{21} & \mathcal{M}^{\tilde{q}}_{22} \end{pmatrix} \begin{pmatrix} \tilde{q}_L \\ \tilde{q}_R \end{pmatrix}. \tag{2.47}$$

The components of the squark mass matrix $\mathcal{M}^{\tilde{q}}$ are given by

$$\mathcal{M}^{\tilde{q}}_{11} = M_{\tilde{q}}^2 + (I_3 - e_q \sin^2\theta_W)\cos 2\beta\, m_{Z^0}^2 + m_q^2. \tag{2.48}$$

$$\mathcal{M}^{\tilde{q}}_{12} = \mathcal{M}^{\tilde{q}}_{21} = m_q(A_q - \mu(\tan\beta)^{-2I_3}). \tag{2.49}$$

$$\mathcal{M}^{\tilde{q}}_{22} = M_{\tilde{u}/\tilde{d}}^2 + e_q \sin^2\theta_W \cos 2\beta\, m_{Z^0}^2 + m_q^2. \tag{2.50}$$

Here $M_{\tilde{q}}^2$, $M_{\tilde{u}}^2$ and $M_{\tilde{d}}^2$ are soft breaking parameters. If the considered squark $\tilde{q}$ is of up-type, we include $M_{\tilde{u}}^2$, otherwise $M_{\tilde{d}}^2$. The weak mixing or Weinberg angle is given by θ_W. In addition, e_q denotes the electric charge of the corresponding quark in units of the elementary charge e and I_3 denotes the third component of its weak isospin. This means that we have

$$I_3 \;=\; \frac{1}{2} \quad \text{and} \quad e_q = \frac{2}{3} \quad \text{for up-type quarks.} \tag{2.51}$$

$$I_3 \;=\; -\frac{1}{2} \quad \text{and} \quad e_q = -\frac{1}{3} \quad \text{for down-type quarks.} \tag{2.52}$$

In order to arrive at the mass eigenstates, we have to diagonalise the squark mass matrix $\mathcal{M}^{\tilde{q}}$, which is accomplished by the squark mixing matrix $U^{\tilde{q}}$. More precisely, we demand

$$\begin{pmatrix} m_{\tilde{q}_1}^2 & 0 \\ 0 & m_{\tilde{q}_2}^2 \end{pmatrix} \overset{!}{=} U^{\tilde{q}} \mathcal{M}^{\tilde{q}} \left(U^{\tilde{q}} \right)^{\dagger} . \tag{2.53}$$

In this notation, the squark masses $m_{\tilde{q}_{1,2}}^2$ correspond to the eigenvalues of $\mathcal{M}^{\tilde{q}}$ and are given by

$$m_{\tilde{q}_{1,2}}^2 = \frac{1}{2} \left(\mathcal{M}_{11}^{\tilde{q}} + \mathcal{M}_{22}^{\tilde{q}} \mp \sqrt{(\mathcal{M}_{11}^{\tilde{q}} - \mathcal{M}_{22}^{\tilde{q}})^2 + 4(\mathcal{M}_{12}^{\tilde{q}})^2} \right) , \tag{2.54}$$

where we have chosen the first squark to be the lighter one. We can finally parametrise the squark mixing matrix $U^{\tilde{q}}$ as a rotation matrix, i.e. we can introduce the squark mixing angle $\theta_{\tilde{q}}$ via

$$U^{\tilde{q}} = \begin{pmatrix} \cos\theta_{\tilde{q}} & \sin\theta_{\tilde{q}} \\ -\sin\theta_{\tilde{q}} & \cos\theta_{\tilde{q}} \end{pmatrix} , \quad \text{where} \quad \tan 2\theta_{\tilde{q}} = \frac{2\mathcal{M}_{12}^{\tilde{q}}}{\mathcal{M}_{11}^{\tilde{q}} - \mathcal{M}_{22}^{\tilde{q}}} . \tag{2.55}$$

2.5. Phenomenological MSSM

In this section we return to the issue of free parameters already mentioned in section 2.3. The inclusion of soft SUSY breaking in its most general form leads to 105 new parameters. Fortunately, not all of them are completely unrestricted. In fact, many of these parameters affect Standard Model precision observables via loop corrections and are therefore strongly constrained. This is especially true for SUSY induced flavour changing neutral currents or new sources of CP violation. In order to incorporate these constraints and to reduce the amount of free parameters, phenomenological models are introduced.

Our numerical studies presented in chapter 7 are performed within the so-called *phenomenological MSSM* (pMSSM) as described in [47]. This model is based on the following three assumptions:

- No new sources of CP violation

- No flavour changing neutral currents

- First and second generation universality

Taking these postulations into account, only 19 free parameters remain. These parameters are collected and described in table 2.2. Remember that the Higgs mass $m_{h^0} \sim 125$ GeV

Table 2.2.: Parameters of the pMSSM

Parameter	Description
$\tan\beta$	Ratio of the two vacuum expectation values v_2 and v_1 as discussed in subsection 2.4.1 and defined in (2.23)
μ	Higgsino mass parameter as discussed in subsection 2.4.1
m_{A^0}	Pole mass of the pseudoscalar Higgs boson A^0
M_1	Bino mass parameter, appearing e.g. in (2.41)
M_2	Wino mass parameter, appearing e.g. in (2.34) and (2.41)
M_3	Gluino mass parameter
$M_{\tilde{q}_{1,2}}$ and $M_{\tilde{q}_3}$	Squark mass parameters, correspond to $M_{\tilde{q}}$ in (2.48) for the first two and third generation, respectively
$M_{\tilde{u}_{1,2}}$ and $M_{\tilde{u}_3}$	Up squark mass parameters, correspond to $M_{\tilde{u}}$ in (2.50) for the first two and third generation, respectively
$M_{\tilde{d}_{1,2}}$ and $M_{\tilde{d}_3}$	Down squark mass parameters, correspond to $M_{\tilde{d}}$ in (2.50) for the first two and third generation, respectively
$M_{\tilde{l}_{1,2}}$ and $M_{\tilde{l}_3}$	Slepton mass parameters, analogs of $M_{\tilde{q}_{1,2}}$ and $M_{\tilde{q}_3}$ in slepton mass matrix
$M_{\tilde{e}_{1,2}}$ and $M_{\tilde{e}_3}$	Slepton mass parameters, analogs of $M_{\tilde{u}_{1,2}}$ and $M_{\tilde{u}_3}$ in slepton mass matrix
A_t, A_b and A_τ	Trilinear couplings of stops, sbottoms and staus

is not a free parameter anymore and has to be reproduced by the pMSSM, which reduces its valid parameter space.

However, within this thesis and the `DM@NLO` project (cf. chapter 6), we eliminate eight more parameters and work with a simplified version of the pMSSM consisting of only eleven free parameters. This is achieved by the following suppositions:

- The slepton sector is of minor phenomenological interest for our studies and parametrised by a common mass parameter $M_{\tilde{l}} := M_{\tilde{l}_{1,2}} = M_{\tilde{l}_3} = M_{\tilde{e}_{1,2}} = M_{\tilde{e}_3}$.

- The first two generation of squarks are described by a common mass parameter, i.e. $M_{\tilde{q}_{1,2}} = M_{\tilde{u}_{1,2}} = M_{\tilde{d}_{1,2}}$.

- The third generation of squarks is described by two independent mass parameters, namely $M_{\tilde{u}_3}$ and $M_{\tilde{q}_3} = M_{\tilde{d}_3}$.

- All trilinear couplings except for A_t are set to zero, i.e. $A_b = A_\tau = 0$.

All in all, we are left with the following eleven parameters defining our pMSSM setup:

$$\tan\beta, \mu, m_{A^0}, M_1, M_2, M_3, M_{\tilde{q}_{1,2}}, M_{\tilde{q}_3}, M_{\tilde{u}_3}, M_{\tilde{l}} \quad \text{and} \quad A_t. \tag{2.56}$$

3. Phenomenology of dark matter

More than 80 years ago, curious astronomical observations indicated the existence of an additional, non-luminous form of matter, so-called *dark matter* [1]. Since then, further evidence has been found by many independent experiments operating on a vast range of length scales and by now, the field of dark matter has become mature. The ongoing experimental effort is impressive and includes the most sensitive detectors ever built [7, 8]. Thanks to measurements of the cosmic microwave background, the amount of dark matter is known with percent precision [4–6]. Review articles on dark matter are appearing frequently to keep track of this rapidly evolving field, cf. e.g. [39, 48–51]. Textbooks for scientists and many popular science books for a broader audience are available, see e.g. [52–55]. People are even starting to investigate the subject of dark matter from a historical and sociological perspective [56]. Despite all this progress, the true nature of dark matter is still unknown and identifying it remains one of the biggest open problems for modern physics.

In this chapter we basically address two questions: Why do we believe dark matter actually exists and what could it be? We are not aiming for completeness and just stress the most essential aspects. Parts of the following are inspired by [57]. Similar chapters can be found in almost every recent PhD thesis related to dark matter phenomenology, see e.g. [58–64].

3.1. Evidence for the existence of dark matter

3.1.1. Dynamics of the coma cluster

Although there were other, earlier observations (cf. [49, 65–67]), Fritz Zwicky is probably the most famous pioneer of dark matter. In 1933 he investigated the redshifts of galaxies, which were referred to as "extragalactic nebulae" at that time [1]. Zwicky applied the virial theorem of classical mechanics on the coma cluster, assuming that it had reached mechanical equilibrium. The virial theorem directly connects the averaged kinetical and potential energy through

$$\bar{E}_{\text{kin}} = -\frac{1}{2}\bar{E}_{\text{pot}}.$$
(3.1)

Moreover, he estimated the total amount of luminous matter to $M \sim 1.6 \cdot 10^{42}$ kg and the radius of the cluster to $R \sim 10^{22}$ m, which allowed him to calculate the averaged potential energy via

$$\bar{E}_{\text{pot}} = -\frac{3}{5}G\frac{M^2}{R},$$
(3.2)

where G denotes the gravitational constant. Given this result, he was able to infer the averaged kinetical energy and hence averaged velocity to $\sqrt{\bar{v^2}} \sim 80$ km/s. When comparing this value with the one obtained from his redshift measurements, he found serious
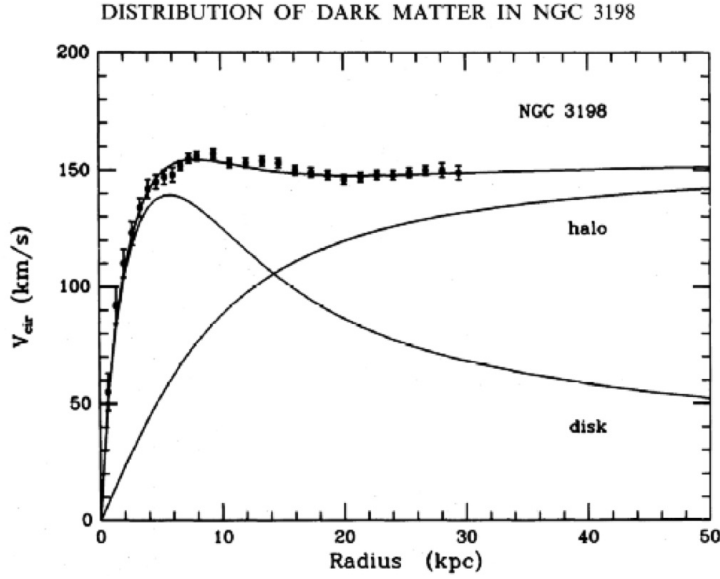
Figure 3.1.: Rotation curve of the galaxy NGC 3198

disagreement, the latter being much larger. He concluded that there must be an additional, non-luminous matter component which he omitted when estimating M: "Falls sich dies bewahrheiten sollte, würde sich also das überraschende Resultat ergeben, dass dunkle Materie in sehr viel größerer Dichte vorhanden ist als leuchtende Materie" [1].

3.1.2. Rotation curves

The next essential observation in the field of dark matter was made by Vera Rubin and W. Kent Ford Jr. roughly fourty years later. Rubin and Ford determined the rotation velocities v_{rot} of stars orbiting their galactic centers by measuring the redshift of the stars [2, 3]. Following Newtonian mechanics, this velocity is given by

$$v_{\text{rot}}(R) = \sqrt{\frac{GM(R)}{R}},$$ (3.3)

where R denotes the distance to the corresponding galactic center. The mass profile $M(R)$ is assumed to be spherically symmetric and reads

$$M(R) = 4\pi \int_0^R \mathrm{d}r\, r^2 \rho(r).$$ (3.4)

For large r, the mass density $\rho(r)$ should decrease heavily as most stars are populating the inner regions of the galaxy. Hence, $M(R)$ becomes almost constant for large R and the rotation velocities should fall proportional to $1/\sqrt{R}$ in complete analogy to the rotation velocities of the planets orbiting the sun.

Interestingly, no such behaviour was found in the experimental data as exemplarily shown in figure 3.1 (taken from [68]), where the spiral galaxy NGC 3198 has been investigated. The upper line labelled 'NGC 3198' represents the actual measurement. The rotation velocities stay basically constant for large distances to the galactic center. The
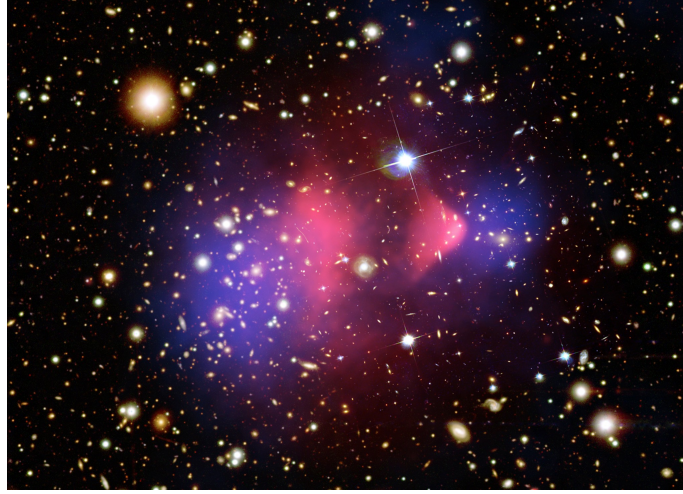
Figure 3.2.: Distribution of interstellar gas (shown in red) confronted with information obtained from gravitational lensing (shown in blue) in the bullet cluster

lower curve labelled 'disk' corresponds to the argumentation given above and shows the expected but not observed $1/\sqrt{R}$ decline for large radial distances. We stress that this discrepancy between theory and experiment has been found in dozens of galaxies.

Taking these measurements seriously, there are basically two ways how to resolve the dilemma. The first option is to reconsider and modify the underlying theory, namely Newtonian mechanics. This sounds drastically but has been worked out in detail. We return to this point in subsection 3.2.1. The second, commonly preferred option is to conclude that one of the ingoing assumptions is not fulfilled. The experimental observations can be brought into agreement with Newtonian mechanics when adjusting the mass profile. More precisely, we assume that a halo of dark matter surrounds each galaxy. This halo extends to much larger radii than the luminous part of the galaxy. Its impact on the resulting rotation velocity is illustrated by the curve labelled 'halo' in figure 3.1. Superposing the effects of the disk galaxy and the dark matter halo, we obtain the observed curve.

3.1.3. The bullet cluster

The cluster 1E 0657-558, usually referred to as *the bullet cluster*, consists of two galaxy clusters which collided about 100 million years ago. It is located in the constellation Carina and led to an "empirical proof" of the existence of dark matter [69]. Let us briefly recapitulate the main findings of this paper and ignore its paradoxal title.

The bullet cluster is depicted in figure 3.2 (taken from [70]). The two original clusters have passed each other without major losses and are located in the midst of the blue areas. The clusters themselves are directly observable as they emit visible light. We see that the left cluster is much larger than the right one.

Both clusters consist not only of galaxies which in turn consist of stars and planets but also of interstellar gas. The interstellar gas is usually the dominant baryonic matter component and emits X-rays, which can be easily detected. The corresponding regions are those marked red in figure 3.2. We see that the interstellar gas has noticed the collision. Electromagnetic friction processes slowed it down and separated it from the galaxy clusters.
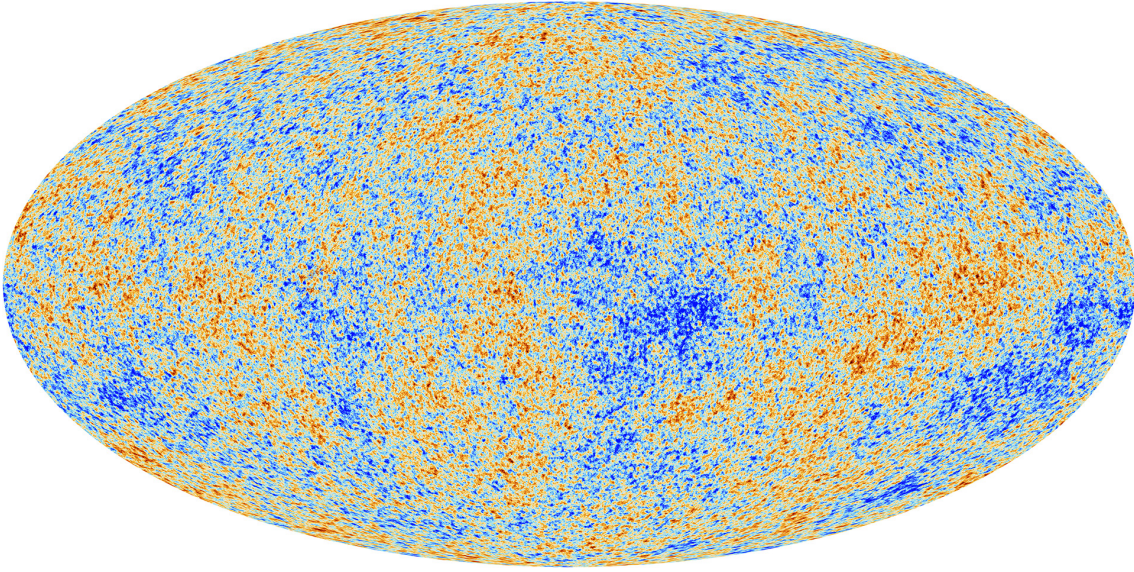
Figure 3.3.: Temperature anisotropies of the cosmic microwave background measured by the Planck satellite

The blue regions correspond to those of the highest mass density. These regions have been determined via weak gravitational lensing and coincide with the regions of the clusters themselves although the interstellar gas is the dominant baryonic matter component.

Similar to the previous subsections, we end up with the conclusion that there must be more than just ordinary baryonic matter to explain the observation. More precisely, we postulate that both of the original clusters are surrounded by dark matter halos. In contrast to the interstellar gas, these halos stick to their corresponding clusters during the collision and surpass each other unhinderedly as dark matter does not interact electromagnetically.

3.1.4. Cosmic microwave background

So far we have gathered strong qualitative evidence that dark matter exists but its actual amount is only vaguely guessable. This situation has changed in the past decades due to the measurement of the *cosmic microwave background (CMB)*.

The CMB can be seen as an afterglow of the big bang and its sheer existence is an essential prediction of the big bang theory. It arose when the universe got transparent, i.e. when matter and radiation decoupled. At that time, the universe was about 380000 years old and had a temperature of roughly 3000 K. The CMB should be of black body nature and spatially homogeneous, the latter being explained by an inflationary epoch of the early universe. Moreover, the CMB should possess tiny temperature fluctuations which lead to the clumping of matter and the formation of galaxies during the evolution of the universe.

All of these predictions were confirmed by the Cosmic Background Explorer (COBE) in 1992 [71]. The black body temperature was found to be $T = 2.7$ K and the inhomogeneities have shown up at $\mathcal{O}(10^{-5})$ K. To obtain further information on the CMB and in particular its anisotropies, two successive missions were launched, namely the Wilkinson Microwave

Anisotropy Probe (WMAP) [4] and the Planck satellite [5, 6]. A full sky map of the temperature anisotropies measured by the Planck satellite is shown in figure 3.3 (taken from [72]).

One can perform a sophisticated multipole analysis of these anisotropies and try to reproduce the obtained spectrum by a cosmological model. This fit is usually performed for the so-called ΛCDM model, which can be considered as the recent cosmological standard model [73]. The ΛCDM model is based on a flat universe obeying a Friedmann-Lemaître-Robertson-Walker metric. Its dynamic is dominantly driven by the eponymous dark energy and cold dark matter content, which are abbreviatory denoted Λ and CDM, respectively. The model contains six free parameters in total. We are mainly interested in the baryonic and cold dark matter densities, which were found to be

$$\Omega_{\mathrm{b}}h^2 = 0.02205 \pm 0.00028 \quad \text{and} \quad \Omega_{\mathrm{CDM}}h^2 = 0.1199 \pm 0.0027, \tag{3.5}$$

respectively [5]. Here h denotes the present Hubble expansion rate H in units of 100 km s^{-1} Mpc^{-1}. The densities are given in terms of the critical density

$$\rho_{\mathrm{c}} = \frac{3H^2}{8\pi G}. \tag{3.6}$$

In these units a density of one corresponds to a perfectly flat universe. Within the ΛCDM model, the amount of dark energy is fixed by the condition that the universe is flat, i.e. that all contributing densities add up to one. For any more details on the CMB and the aforementioned multipole analysis we refer to [74–76].

3.1.5. Numerical N-body simulations

As discussed in the previous subsections, valuable cosmological information can be extracted from the CMB and its anisotropies. The obtained knowledge can be used as a starting point for another validity check of the ΛCDM model. More precisely, the temperature anisotropies and corresponding density fluctuations can be implemented as initial conditions in numerical *N-body simulations*, which aim at simulating the structure formation of the universe. Examples for such projects are the Millennium and the Bolshoi simulation [77, 78].

The central finding of all these simulations is that structure formation is dominantly driven by dark matter. As dark matter interacts gravitationally but not electromagnetically, it starts to clump earlier than baryonic matter which gets driven apart by radiation. Therefore, dark matter amplifies initial density fluctuations and forms so-called dark gravitational centres which also attract ordinary baryonic matter. In case of the Millennium simulation, the amount of dark matter was chosen to be

$$\Omega_{\mathrm{DM}}h^2 = 0.1092445. \tag{3.7}$$

Given this input, typical cosmological structures including galaxies, clusters of galaxies and voids could be numerically reproduced. Moreover, smaller structures like galaxies formed earlier than larger structures like clusters, which is in agreement with cosmological observations.

Apart from confirming the ΛCDM model and the importance of its dark matter component, N-body simulations lead to a second insight. The dark matter component should be mainly cold, i.e. heavy and moving non-relativistically. Otherwise, gravitational centres

get washed out again and structure formation follows the opposite direction, i.e. larger structures form earlier than smaller structures. On the other hand, a small portion of warm or hot dark matter is preferred to avoid more detailed discrepancies between the simulations and reality. One example for such a discrepancy is the so-called *missing satellite problem* [79, 80]. Structure formations basing solely on cold dark matter lead to a hierarchical formation of structures and give rise to many small scale structures like dwarf galaxies and dark matter subhalos. Although these objects exist in reality as well, their observed number is much smaller than the one predicted by simulations basing solely on cold dark matter.

3.2. Dark matter candidates

3.2.1. Modified Newtonian mechanics

We are now turning to possible explanations of the phenomena described in the previous section. The first option is to deny that dark matter exists and that these observations point to shortcomings of the underlying theory, namely Newtonian mechanics. In 1983 Mordehai Milgrom published his *modified version of Newtonian mechanics* (MOND) [81]. The main motivation of this theory is to explain the observed rotation curves (cf. subsection 3.1.2) without adding an additional dark matter component.

The basic assumption of MOND is that Newtons second law $\vec{F} = m\vec{a}$ is only valid for large accelerations $\vec{a}$. Large refers to accelerations which we encounter in daily life as e.g. the gravitational acceleration on earth. The postulated, more general form also valid for small circular accelerations present in the outer regions of a galaxy reads

$$\vec{F} = m\vec{a}\mu\left(\frac{a}{a_0}\right), \tag{3.8}$$

where a_0 denotes a new constant of nature and $a = |\vec{a}|$. The function $\mu(x)$ is a priori not uniquely defined but has to fulfill the limits $\mu(x \gg 1) = 1$ and $\mu(x \ll 1) = x$. Typical choices for this function include

$$\mu(x) = \frac{x}{1+x} \quad \text{or} \quad \mu(x) = \frac{x}{\sqrt{1+x^2}}. \tag{3.9}$$

Let m denote the mass of a star orbiting its galactic center at a distance R and $M(R)$ the mass profile of the galaxy as given in (3.4). Using modified Newtonian dynamics, we can determine the rotation velocity of the star to

$$\frac{GmM(R)}{R^2} = m\frac{a^2}{a_0} \quad \Leftrightarrow \quad \frac{a_0 GM(R)}{R^2} = \frac{v^4}{R^2} \quad \Leftrightarrow \quad v = \sqrt[4]{a_0 GM(R)}. \tag{3.10}$$

Due to the fact that the mass profile is almost constant for large R, we obtain a constant rotation velocity for stars in the outer galactic regions as found experimentally. Hence, MOND is able to explain the observed rotation curves successfully and reproduces Newtonian mechanics in the limit of large accelerations.

Moreover, Jacob Bekenstein was able to generalise MOND into a relativistic theory in 2004 [82, 83]. This theory is usually referred to as *tensor-vector-scalar gravity (TeVeS)*

and can be understood as an alternative to general relativity. In TeVeS, the usual metric tensor[3] $\eta_{\mu\nu}$ is replaced by

$$\tilde{\eta}_{\mu\nu} = (\eta_{\mu\nu} + v_\mu v_\nu)e^{-2\phi} - v_\mu v_\nu e^{2\phi}, \qquad (3.11)$$

which includes an additional vector v_μ and an additional scalar ϕ. An introduction to TeVeS can be found in [84].

Nevertheless, MOND and its relativistic counterpart TeVeS suffer from several deficits. The probably most serious counter-argument for these theories are the findings of the bullet cluster (cf. subsection 3.1.3). When investigating the bullet cluster in the TeVeS scheme, alternative formulae for weak gravitational lensing have to be applied which slightly modify the result. However, the main outcome remains unchanged: The dominant matter component as indicated by gravitational lensing does not coincide with the interstellar gas which is the dominant baryonic matter component. Ironically, another detail of the bullet cluster can be interpreted in favour of MOND, namely its collision velocity [85].

3.2.2. Massive astronomical compact halo objects

Another possible explanation of the phenomena described in section 3.1 agrees on the need for an additional, non-luminous matter component but denies its exotic, non-baryonic nature. The assumption here is that dark matter consists of so-called *massive compact astronomical halo objects* (MACHOs). Examples for MACHOs include brown and white dwarfs, neutron stars or black holes. These objects are meant to be present in the outer regions of galaxies in large numbers and make up the dark matter halo.

Although MACHOs do not emit light themselves, they are indirectly observable via weak gravitational lensing. Whenever a MACHO passes the line of sight of a luminous object, it bends the emitted light due to its massive nature and acts as a gravitational lens. The resulting brightening of the light signal is very characteristic and can be well distinguished from other possible effects. Basing on this principle, there have been several studies looking for MACHOs, like e.g. the Expérience pour la Recherche d'Objet Sombres (EROS) experiment [86]. The EROS experiment was able to detect MACHOs in the Magellanic clouds. However, the observed number was much too small to account for the total amount of dark matter.

MACHO surveys and in particular the assumptions they are based on have been questioned recently [87]. Following this paper, limits placed on the MACHO content of the galactic halo from surveys in the Magellanic clouds are inconsistent and model-dependent and do not provide a secure basis for rejecting an all-MACHO halo.

However, there are other, more deadly counter-arguments against MACHOs as the dominant component of dark matter, namely the findings of subsections 3.1.4 and 3.1.5. The total amount of baryonic matter and hence MACHOs is strictly limited by the measurement of the CMB as given in (3.5). Moreover, MACHOs were not present in the early universe. Therefore, it is highly questionable how they should have formed dark gravitational centres and supported structure formation during that period.

---

[3]We are using $\eta_{\mu\nu}$ for the metric tensor of general relativity and $g_{\mu\nu}$ for the metric tensor of special relativity which also appears in quantum field theory.

3.2.3. Weakly interacting massive particles

The hypothesis we are following in this thesis is based on the existence of *weakly interacting massive particles* (WIMPs). These WIMPs are supposed to stream through the universe in large numbers and form dark matter halos around galaxies which explain the observations described in section 3.1.

Such a dark matter particle has to fulfill a number of conditions. First of all it should be dark, i.e. it should not interact electromagnetically. Moreover, it should also be colour neutral as it otherwise would have been detected in searches for exotic isotopes [88, 89]. As we expect the dark matter particle to be still present these days, it should be stable or at least stable with respect to the age of the universe. Finally, it should be cold, i.e. heavy and moving non-relativistically to meet the findings of N-body simulations (cf. subsection 3.1.5).

By now, the attentive reader might have noticed the biggest shortcoming of this hypothesis: There is no WIMP within the Standard Model of particle physics. The best candidate within the SM are neutrinos, which are very light and hence contribute to hot dark matter. Apart from that, neutrinos are simply not abundant enough to completely account for dark matter [48].

This leads to two possible conclusions. Either the WIMP hypothesis has proven wrong or it points towards physics beyond the Standard Model and the existence of at least one new particle. We optimistically pursue the latter option in this thesis. More precisely, we identify the dark matter particle with the lightest *neutralino* $\tilde{\chi}_1^0$, the lightest supersymmetric particle in many scenarios of the MSSM (cf. chapter 2). This particle is the canonical example for a WIMP and fulfills all the requirements listed above. We stress that the main motivation of the MSSM is not the creation of a suitable dark matter candidate but solving the hierarchy problem. The fact that the MSSM additionally gives rise to such a candidate and furthermore enables the unification of gauge couplings at high energies, makes this approach very appealing.

Another example of a WIMP with an original motivation independent of dark matter is the *axion*. From a theoretical perspective, terms violating charge and parity symmetry (CP) simultaneously are not excluded in quantum chromodynamics (QCD). However, such a violation is not observed in nature. A solution to this so-called strong CP problem is the Peccei-Quinn mechanism [90]. In the course of this mechanism, a new symmetry is introduced and broken globally. The axions appear as remnants of the broken symmetry, namely as pseudo-Goldstone bosons. For an overview of axions as a dark matter candidate, we refer to [91, 92]. Sometimes the Peccei-Quinn mechanism is combined with SUSY, which leads to yet another WIMP, namely the *axino* [93–95].

Of course there are plenty of other models which are directly motivated by dark matter, i.e. their main purpose is to generate a suitable WIMP by modifying the Standard Model as little as possible. These models are commonly referred to as minimal models, which can be traced back to [96]. Other examples for minimal models include e.g. [97, 98].

4. Calculation of neutralino-nucleon cross sections

In this chapter we introduce the concept of *direct detection of dark matter* and discuss the composition of the corresponding detection rate. Starting with the tree-level contributions, we show how to calculate radiative corrections to the four-fermion couplings between neutralinos and nucleons in detail. Including these radiative corrections permits to set more robust exclusion bounds on the MSSM parameter space in case of negative experimental findings or to identify neutralino properties more reliably in case of positive experimental findings. To be exact, we perform a full one-loop calculation in the framework of the MSSM to determine all contributions up to $\mathcal{O}(\alpha_s)$ to the kinematically unsuppressed effective operators $\bar{\chi}\chi\bar{q}q$ and $\bar{\chi}\gamma_5\gamma_\mu\chi\bar{q}\gamma_5\gamma^\mu q$ and their associated Wilson coefficients. This calculation can be seen as the core part of this thesis. To the knowledge of the author, such a systematic analysis at next-to-leading order (NLO) for a concrete and non-minimal model like the MSSM has never been done before.[4] The results of this calculations have been published in [103].

4.1. Basic idea of direct detection

The basic idea behind direct detection of dark matter is actually quite simple and was first mentioned by Edward Witten [104]. The mechanism is based on the following line of arguments:

1. We assume that there is a non-negligible local dark matter density ρ_0. Furthermore, we assume that dark matter consists (at least partially) out of weakly interacting massive particles.

2. This implies that dark matter particles stream through the earth every second. Rarely some of them weakly interact with one of the nucleons an atom, transferring a small amount of energy. We call this the *recoil energy*. The process is depicted in figure 4.1.[5]

3. If one is able to detect this recoil process and to safely exclude all other non-dark matter sources simultaneously, one has found experimental evidence for the existence of the assumed dark matter particle.

---

[4]An example for a somewhat similar study for a minimal model, namely the *inert doublet model*, can be found in [99]. A one-loop analysis for a toy model with a charged mediator has been performed in [100]. Some general remarks on loop contributions in the context of dark matter direct detection can be found in [101]. We also mention [102], where QCD corrections in the context of indirect detection are discussed.

[5]This and all other Feynman diagrams appearing in this thesis have been generated by the help of `FeynArts` [105].
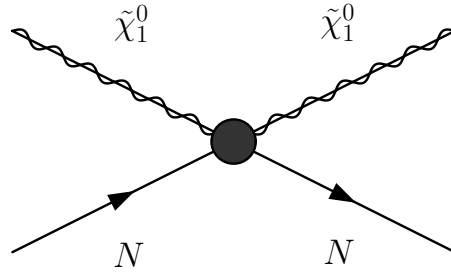
Figure 4.1.: Elastic scattering process of a neutralino $\tilde{\chi}_1^0$ and a nucleon N

The last point already names the experimental difficulties. One has to detect an event which happens very rarely and in which only a small amount of energy is transferred. Simultaneously, one has to ensure that the measured signal is actually due to dark matter and exclude all other possible sources. Therefore, the key words of every successful direct detection experiment are *sensitivity* and *background reduction.*

In practice, no indisputable positive direct detection signal has been found yet.[6] That is why the logic above is typically inverted and used to falsify or disfavour hypothetical dark matter candidates. The line of arguments is as follows:

1. We assume there is a non-negligible local dark matter density ρ_0. We postulate the existence of a concrete WIMP dark matter candidate, e.g. the lightest neutralino $\tilde{\chi}_1^0$ in a concrete scenario.

2. We calculate the hypothetical direct detection rate for the given candidate.

3. If one does not detect a dark matter recoil signal with an experiment which is otherwise sensitive and background free enough to measure it, the postulated candidate is experimentally disfavoured.

As experiments progress and increase in sensitivity, more and more candidates become disfavoured. This is precisely what has happened in the last decades. At the moment the strongest exclusion limits are set by the LUX ("Large Underground Xenon dark matter experiment") and the XENON100 experiment [7, 8]. Both of them are two phase liquid noble gas detectors working with xenon. Two comments are in order:

- The argumentation above bases on assumptions on the local dark matter density ρ_0. This astrophysical quantity is neither well understood nor directly measured. Changes in the underlying astrophysical model propagate through the whole chain of arguments and influence the final result. In e.g. [112] it has recently been shown that barred galaxies such as the milky way feature significant deviations from the standard dark matter halo model and that these deviations affect the resulting direct detection rate heavily. This makes it difficult to strictly exclude or falsify a dark matter candidate. In general, the experimental observations *disfavour* a certain dark matter candidate. A *falsification* is only possible with respect to a concrete underlying astrophysical model.

---

[6] We are not discussing the possible annual modulation signals of the CoGeNT ("Coherent Germanium Neutrino Technology") and DAMA/LIBRA ("Dark Matter Project/Large sodium iodide bulk for rare processes") experiments here. Consider e.g. [7, 8, 106–111] for this issue.

Nevertheless, people try to minimise the influence of the astrophysical quantities entering the calculation. This is usually called a *halo-independent approach*, cf. e.g. [113–117]. We also mention [118], where the influence of non-standard cosmology on direct detection is studied.

- The MSSM contains more than one hundred free parameters, giving rise to arbitrary many different scenarios. Although one can disfavour or exclude some concrete scenarios in the way discussed before, it is almost impossible to falsify the MSSM as a whole. There are MSSM scenarios which lead to nearly SM-like observables, including SUSY particles too heavy to be experimentally accessible. This is a severe problem from the philosophical point of view. "Ein empirisch-wissenschaftliches System muss an der Erfahrung scheitern können", as Karl Popper said [119]. It is not the aim of this thesis to discuss this problem but definitely something one should keep in mind. More thoughts on the philosophical aspects of dark matter can be found in [56, 120].

- If dark matter does not consist of particles (cf. section 3.2) or those particles interact only via gravity, direct detection is a futile approach. An interesting possibility for the latter has been given in [121] recently.

4.2. Composition of direct detection rate

In this section we present the standard formulae for the calculation of direct detection rates. Therein we mainly follow [122–124], i.e. we reconstruct how this rate is determined in `DarkSUSY`. Other useful introductions to this topic can be found in [52], the canonical review [39] or the corresponding part of the `micrOMEGAs` manual [125, 126].

The desired quantity is the rate of events $\mathrm{d}R$ per energy interval $\mathrm{d}E$. This differential event rate is typically expressed in terms of counts per kg and day and keV. It can be written as

$$\frac{\mathrm{d}R}{\mathrm{d}E} = \sum_i c_i \frac{\sigma_i}{2m_{\tilde{\chi}_1^0}\mu_i^2}\rho_0\eta_i. \tag{4.1}$$

The sum is over all detector nuclides i and the factor c_i is the mass fraction of the nuclear species i in the detector. In our case we assume the dark matter particle to be the lightest neutralino $\tilde{\chi}_1^0$ with mass $m_{\tilde{\chi}_1^0}$. Let m_i denote the mass of the nucleus of species i. Then μ_i describes the neutralino-nucleus reduced mass defined via

$$\mu_i = \frac{m_{\tilde{\chi}_1^0}m_i}{m_{\tilde{\chi}_1^0} + m_i}. \tag{4.2}$$

The local dark matter density is described by ρ_0. Before using the canonical value of 0.3 GeV/cm^3, one should calculate the neutralino relic density to ensure that its value is in agreement with the experimental constraints and that the neutralinos can solely account for dark matter (cf. chapter 5). η_i contains the integration over the dark matter velocity $\vec{v}$ relative to the detector.

$$\eta_i = \int_{v_{\mathrm{min},i}}^{v_{\mathrm{esc}}} \mathrm{d}^3v \frac{f(\vec{v})}{v} \quad \text{with} \quad v_{\mathrm{min},i} = \sqrt{\frac{m_i E}{2\mu_i^2}}. \tag{4.3}$$

The lower integration limit $v_{\min,i}$ is given by the minimal neutralino velocity which can cause a recoil energy E. Note that the formula for $v_{\min,i}$ given above holds only in the non-relativistic limit. The upper integration limit is fixed by the galactic escape speed $v_{\rm esc}$, which is usually set to 544 km/s. Faster particles are not gravitationally bound in the milky way. More details on the integration limits can be found in [127–129]. $f(\vec{v})$ is the local velocity distribution, which is typically assumed to be Maxwellian. However, recent studies have unveiled that this simplification might not describe the situation properly, see e.g. [130–132].

All the particle physics is comprised in the cross section for elastic neutralino-nucleus scattering σ_i, where we distinguish between *spin-independent* (SI) and *spin-dependent* (SD) processes. The origin of these two kinds of interaction becomes more clear on the microscopic level in the next section when we study the effective four-fermion coupling between neutralinos and quarks. Spin-independent interactions are mainly due to scalar or vector couplings, whereas spin-dependent interactions stem from axial-vector or tensor couplings.

The spin-independent cross section can be written as

$$\sigma_i^{\rm SI} = \frac{\mu_i^2}{\pi} \left| Z_i g_p^{\rm SI} + (A_i - Z_i) g_n^{\rm SI} \right|^2 |F_i^{\rm SI}(Q_i)|^2, \tag{4.4}$$

where $F_i^{\rm SI}(Q_i)$ is the spin-independent structure function for the nucleus i depending on the momentum transfer $Q_i = \sqrt{2 m_i E}$. It can be understood as the Fourier transform of the nucleon density and is normalised to $F_i^{\rm SI}(0) = 1$. As default, the form factor $F_i^{\rm SI}(Q_i)$ is taken to be of Helm form in `DarkSUSY` [123]. We have to take the structure function into account because the nuclei i are no fundamental particles. Instead each of them consists of several nucleons. More precisely, the nucleus i consists of Z_i protons and $A_i - Z_i$ neutrons, where Z_i is its atom and A_i is its mass number. To enable a comparison of direct detection results independent of the detector material and technology, the experimental collaborations typically publish constraints on the cross section between the dark matter particle and a single nucleon[7] N, which simply reads

$$\sigma_N^{\rm SI} = \frac{\mu_N^2}{\pi} \left| g_N^{\rm SI} \right|^2. \tag{4.5}$$

Here the neutralino-nucleus reduced mass μ_i is replaced by the neutralino-nucleon reduced mass μ_N in complete analogy. The nucleon masses m_N are given by

$$m_p = 0.9383 \text{ GeV} \quad \text{and} \quad m_n = 0.9396 \text{ GeV}. \tag{4.6}$$

The effective spin-independent four-fermion couplings between neutralinos and protons p or neutrons n are denoted $g_p^{\rm SI}$ and $g_n^{\rm SI}$. They can be determined via

$$g_N^{\rm SI} = \sum_q \langle N | \bar{q} q | N \rangle \alpha_q^{\rm SI}, \tag{4.7}$$

where the nucleon index N stands either for proton or neutron and the sum is over all quarks q. Just like nuclei, nucleons are no elementary particles. They are made of valence

---

[7]At this point it is typically assumed that the interaction strength of neutralinos is the same for protons and neutrons. This is not necessarily fulfilled in a non-minimal model like the MSSM. Therefore, we keep our calculations general and differ between protons and neutrons.

Table 4.1.: Scalar coefficients f_{Tq}^N used in different codes

Scalar coefficient	DM@NLO	DarkSUSY	micrOMEGAs 2.4.1	micrOMEGAs 4.2.5
f_{Tu}^p	0.0208	0.023	0.023	0.0153
f_{Tu}^n	0.0189	0.019	0.018	0.0110
f_{Td}^p	0.0411	0.034	0.033	0.0191
f_{Td}^n	0.0451	0.041	0.042	0.0273
$f_{Ts}^p = f_{Ts}^n$	0.043	0.14	0.26	0.0447
$f_{Tc}^p = f_{Tb}^p = f_{Tt}^p$	0.0663	0.0595	0.0507	0.0682
$f_{Tc}^n = f_{Tb}^n = f_{Tt}^n$	0.0661	0.0592	0.0504	0.0679

quarks, virtual sea quarks and virtual gluons. On the microscopic level, the interaction between nucleons and neutralinos is actually an interaction between these elementary particles and neutralinos. The spin-independent interaction between quarks and neutralinos is denoted α_q^{SI}. The next sections demonstrate in detail how to determine it. The quark matrix element $\langle N|\bar{q}q|N\rangle$ can be qualitatively understood as the probability to find a quark q in the nucleon N. We write it as

$$\langle N|m_q\bar{q}q|N\rangle = f_{Tq}^N m_N, \tag{4.8}$$

where m_N denotes the nucleon mass and m_q the quark mass. The scalar coefficients f_{Tq}^N are determined experimentally or via lattice QCD. We point out that especially f_{Ts}^N is affected by experimental uncertainties, which mainly stem from the determination of the pion-nucleon sigma term [133–135]. We use the values in agreement with [136–138]. These values differ from those implemented in DarkSUSY or micrOMEGAs [139, 140], which we list for comparison in table 4.1. The drastic differences in f_{Ts}^N illustrate the aforementioned uncertainty quite well. As demonstrated in [141], the factors f_{Tq}^N of the heavy quarks are linked to those of the light quarks via

$$f_{Tc}^N = f_{Tb}^N = f_{Tt}^N = \frac{2}{27}\left(1 - \sum_{q=u,d,s} f_{Tq}^N\right). \tag{4.9}$$

The spin-dependent cross section can be casted into the form

$$\sigma_i^{\text{SD}} = \frac{4\mu_i^2}{2J+1}\left(|g_p^{\text{SD}}|^2 S_{\text{pp},i}(Q_i) + |g_n^{\text{SD}}|^2 S_{\text{nn},i}(Q_i) + |g_p^{\text{SD}} g_n^{\text{SD}}| S_{\text{pn},i}(Q_i)\right), \tag{4.10}$$

where J denotes the nuclear spin. The main difference in comparison to (4.4) is that there are three spin structure functions $S_{\text{pp},i}(Q_i)$, $S_{\text{nn},i}(Q_i)$ and $S_{\text{pn},i}(Q_i)$ which come with the contributions of the proton, the neutron and the interference term. Previously we had just one global structure function $F_i^{\text{SI}}(Q_i)$. More details on the structure functions can be found in [142] and [143]. The spin-independent cross section between the neutralino and a single nucleon N reads

$$\sigma_N^{\text{SD}} = \frac{3\mu_N^2}{\pi}|g_N^{\text{SD}}|^2. \tag{4.11}$$
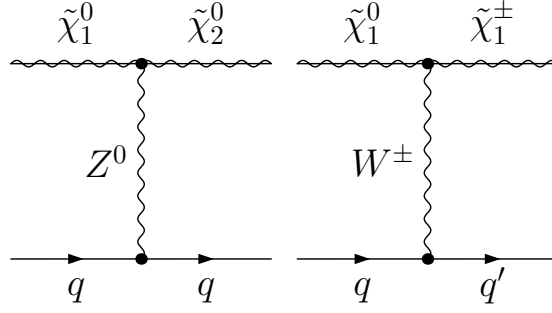
Figure 4.2.: Example processes for inelastic neutralino scattering

Note that the prefactor four of (4.10) has turned into three. This is due to the evaluation of the spin structure functions in the case of a single nucleon [123].

Analogously to the spin-independent case, the effective spin-dependent four-fermion couplings between neutralinos and protons p or neutrons n are denoted g_p^{SD} and g_n^{SD}. They are given by

$$g_N^{\mathrm{SD}} = \sum_{q=u,d,s} (\Delta q)_N \alpha_q^{\mathrm{SD}}. \tag{4.12}$$

In contrast to the spin-independent case, we sum only over the light quarks u, d and s as they mainly determine the nucleon spin.[8] $(\Delta q)_N$ can be seen as the fraction of the nucleon spin carried by the quark q. More precisely, it describes the second moment of the polarised quark density and is related to the nucleon spin vector s_μ via

$$\langle N|\bar{q}\gamma_\mu\gamma_5 q|N\rangle = 2s_\mu(\Delta q)_N. \tag{4.13}$$

We choose the default values of `micrOMEGAs` for the polarised quark densitites. Note the isospin symmetry, i.e. $(\Delta u)_p = (\Delta d)_n$ and $(\Delta d)_p = (\Delta u)_n$.

$$(\Delta u)_p = (\Delta d)_n = 0.842. \quad (\Delta d)_p = (\Delta u)_n = -0.427. \quad (\Delta s)_p = (\Delta s)_n = -0.085. \tag{4.14}$$

We discuss the spin-dependent interaction between quarks and neutralinos α_q^{SD} in detail in the next sections. A few remarks are in order:

- In the way presented here, the direct detection rate factorises into a particle physics and an astrophysics part, which nicely simplifies the calculation.

$$\frac{\mathrm{d}R^{\mathrm{SI/SD}}}{\mathrm{d}E} = \sum_i c_i \underbrace{\frac{\sigma_i^{\mathrm{SI/SD}}}{2m_{\tilde{\chi}_1^0}\mu_i^2}}_{\text{Particle physics}} \underbrace{\rho_0\eta_i}_{\text{Astrophysics}}. \tag{4.15}$$

We stress that this only holds true in the non-relativistic limit, where the cross section σ_i is independent of the neutralino velocity.

- In the following we treat only elastic scattering processes. Within elastic scattering processes the total kinetic energy is conserved and the external particles stay the same. In principle one could also think of inelastic processes as shown in figure 4.2.

---

[8]Although it was recently claimed that bottom quarks may also contribute to the spin-dependent interaction [144].
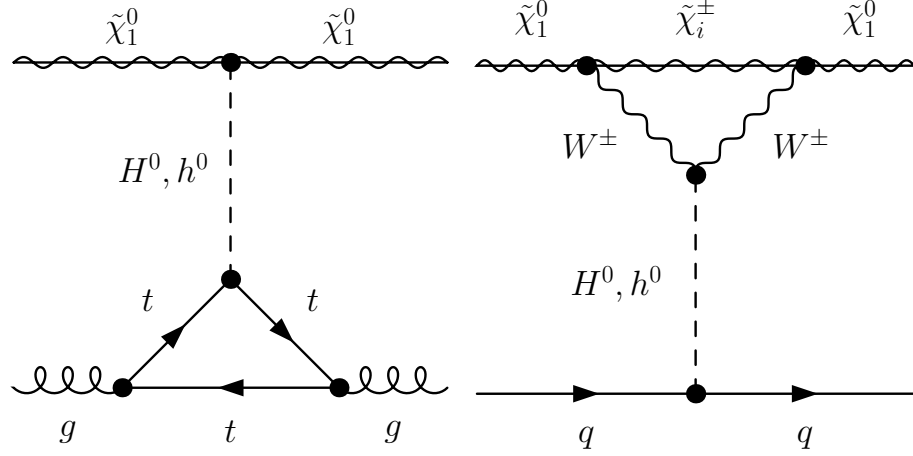
Figure 4.3.: Example processes for neutralino-gluon interaction at one-loop (left) and an electroweak correction to the neutralino-quark four-fermion coupling (right)

Inelastic dark matter nucleus scattering was considered as a possibility to explain the annual modulation signal observed by the DAMA experiment [58, 107, 145, 146]. However, as dark matter nucleus scattering occurs in the non-relativistic regime, inelastic processes are only relevant for very small mass splittings δ between the dark matter particle and its partner. In the cases shown in figure 4.2 this partner is the second neutralino $\tilde{\chi}_2^0$ or the chargino $\tilde{\chi}_1^+$. More concretely, the mass splitting has to fulfill the kinematical constraint $\delta < \beta^2 \mu_i/2$, where μ_i denotes the reduced mass for a nucleus i as given in (4.2) and β is the relative velocity between the neutralino and the nucleus in natural units [145]. For neutralino and nucleus masses of $\mathcal{O}(100 \text{ GeV})$ and velocities β of $\mathcal{O}(10^{-3})$ we obtain mass splittings δ of $\mathcal{O}(10 \text{ keV})$.

Mass degeneracies between the neutralino and other gauginos or stops can provide efficient coannihilation mechanisms (cf. subsection 5.2.2) which in turn lead to the correct relic density as demonstrated in e.g. [147–150]. In these publications, a mass degeneracy refers to splittings of $\mathcal{O}(10 \text{ GeV})$. Even smaller mass splittings lead to an additional enhancement of the coannihilation processes and a relic density way too small. Therefore, mass splittings of $\mathcal{O}(10 \text{ keV})$ can be regarded as unnatural, at least in standard scenarios of the MSSM. Nevertheless, it might be interesting to include inelastic scattering processes in other models.

- The central quantities of the next sections are α_q^{SI} and α_q^{SD}, the so-called *Wilson coefficients* for the neutralino-quark interaction. As stated in the beginning of this chapter, we determine all contributions up to $\mathcal{O}(\alpha_s)$ in the framework of the MSSM to these coefficients and the corresponding operators.

Besides the valence and virtual sea quarks, there are also virtual gluons inside the nucleons. As gluons interact only via the strong and neutralinos only via the weak interaction, they can not interact at tree-level. Nevertheless, exchange processes can occur at NLO, e.g. via a top quark triangle coupling to the gluons and a Higgs boson which in turn couples to the neutralinos as depicted on the left-hand side of figure 4.3. In this way the virtual gluons also contribute to the direct detection rate. These contributions have been calculated in [151] and [152] by Manuel Drees

31

and Mihoko Nojiri and are already included in `DarkSUSY`. The results were partially recalculated and extended by Junji Hisano et al. in [153–155]. The impact of the gluonic corrections is usually negligible if the top squark is much heavier than the neutralino and the top quark together, i.e. if $(m_t + m_{\tilde{\chi}_1^0})^2 \ll m_{\tilde{t}_1}^2$.

- Apart from radiative corrections due to the strong interaction, there are also electroweak corrections to α_q^{SI} and α_q^{SD}. Selected contributions have been calculated by Junji Hisano et al. in [156, 157]. An example process of this work is depicted on the right-hand side of figure 4.3. Note that these calculations do not allow for a general neutralino admixture and are based on further simplifying approximations. Parts of these corrections were recalculated in [129], where some serious disagreement has been found. Further electroweak corrections including Higgs boson or sfermion loops can be found in [158] and [159]. We also mention the recommendable article [160], which gives a detailed and general introduction to the theoretical framework behind dark matter direct detection and comments on the inclusion of electroweak corrections. In addition, the aforementioned gluonic contributions are discussed.

- Including the NLO contributions to the Wilson coefficients α_q^{SI} and α_q^{SD} means to improve on the precision from the particle physics point of view. Although this is certainly desirable, we should not forget that the direct detection rate contains a lot of other quantities as well, each coming with its very own uncertainty. The astrophysical and nuclear uncertainties can easily account for a total factor of three or four [132, 133, 161].

4.3. Tree-level contributions

In this section we determine the tree-level contributions to the Wilson coefficients α_q^{SI} and α_q^{SD}. We present the calculations in great detail to exemplify the procedure in general. By doing this, we set the basis for the more complicated loop calculations. Furthermore, a step by step calculation of this kind is rarely found in the literature, which is why this section might prove useful on its own. These calculations have first been carried out by Kim Griest [162–164].[9] A recommendable introduction to the topic is given in [165]. Our calculation is performed in a pragmatic and pedagogic fashion, starting from the basics. The underlying *effective field theory* formalism is introduced meanwhile and illustrated separately in chapter H.

The four relevant tree-level processes are shown in figure 4.4. We have t-channel Higgs exchanges, a t-channel Z^0 exchange and squark processes occuring in the s- and u-channel. We label these processes T1, T2, T3 and T4. The arrows on the scalar squark lines shall indicate the electric and colour flow. Majorana fermions like the neutralino are represented by a straight and a wavy line.[10] The squark processes are calculated for a general squark $\tilde{q}_i$. When including these contributions, we sum over $i = 1, 2$.

---

[9]In contrast to our calculations, all squark mixing effects were neglected by Griest.

[10]Although gluinos are Majorana fermions as well, the usual convention is to draw a straight and a cycled line in this case.
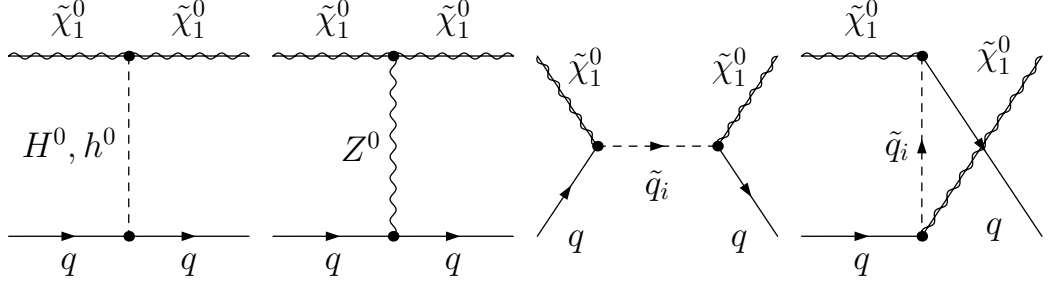
Figure 4.4.: Tree-level contributions to the neutralino-quark four-fermion coupling

4.3.1. T1: Higgs contributions

The simplest contribution to the Wilson coefficient α_q^{SI} stems from the t-channel Higgs processes depicted in the left of figure 4.4. Using the kinematical conventions given in section A.3, we can write down the amplitude as

$$i\mathcal{M}_{\mathrm{T1}} = \left[\bar{u}(p_1)i\boxed{1}u(p_a)\right]\frac{i}{t-m_\phi^2}\left[\bar{u}(p_2)i\boxed{2}u(p_b)\right], \tag{4.16}$$

where ϕ stands for h^0 or H^0. We use the notation of [166] for the couplings. Without any loss of generality, each scalar or pseudoscalar coupling can be written as

$$i\boxed{j} = i(c_j^L P_L + c_j^R P_R), \tag{4.17}$$

where we introduced the *chirality projectors* P_L and P_R.

$$P_L = \frac{\mathbb{1}-\gamma_5}{2} \quad \text{and} \quad P_R = \frac{\mathbb{1}+\gamma_5}{2}. \tag{4.18}$$

Properties of the fifth gamma matrix γ_5 are listed in chapter C. The coefficients c_j^L and c_j^R are complex numbers. In the considered case we have pure scalar couplings, so we write $c_1^L = c_1^R = g_{\phi\tilde{\chi}_1^0\tilde{\chi}_1^0}$ for the Higgs-neutralino and $c_2^L = c_2^R = g_{\phi qq}$ for the Higgs-quark coupling.[11] Concrete expressions for these and other couplings of the MSSM can be found in [11, 62, 167]. This simplifies the amplitude to

$$\mathcal{M}_{\mathrm{T1}} = -\frac{g_{\phi\tilde{\chi}_1^0\tilde{\chi}_1^0}g_{\phi qq}}{t-m_\phi^2}\left[\bar{u}(p_1)u(p_a)\right]\left[\bar{u}(p_2)u(p_b)\right]. \tag{4.19}$$

This almost completes our first tree-level calculation. To read off the Wilson coefficient, we have to identify the *spinors* $\bar{u}(p_1), u(p_a), \bar{u}(p_2)$ and $u(p_b)$ with their corresponding *spinor fields* $\bar{\chi}, \chi, \bar{q}$ and q (cf. section D.3), which leads to

$$\mathcal{M}_{\mathrm{T1}} = \underbrace{-\frac{g_{\phi\tilde{\chi}_1^0\tilde{\chi}_1^0}g_{\phi qq}}{t-m_\phi^2}}_{\text{Wilson coefficient}}[\bar{\chi}\chi][\bar{q}q]. \tag{4.20}$$

---

[11]The latter coupling has to be treated with special care as described in subsection G.5.1.

Table 4.2.: Most common four-fermion operators and their resulting interaction

Effective operator	Name	Resulting interaction
$[\bar{\chi}\chi][\bar{q}q]$	Scalar type	SI
$[\bar{\chi}\gamma_\mu\chi][\bar{q}\gamma^\mu q]$	Vector type	SI
$[\bar{\chi}\gamma_{\mu\nu}\chi][\bar{q}\gamma^{\mu\nu}q]$	Tensor type	SD
$[\bar{\chi}\gamma_5\gamma_\mu\chi][\bar{q}\gamma_5\gamma^\mu q]$	Axial-vector type	SD
$[\bar{\chi}\gamma_5\chi][\bar{q}\gamma_5 q]$	Pseudoscalar type	Strongly Suppressed

In terms of an *effective Lagrangian*, we have arrived at an effective four-fermion interaction of *scalar type*. Scalar interactions are spin-independent. At tree-level, the Wilson coefficient is just the remaining factor in front, which gives us the first contribution to α_q^{SI}.

$$\alpha_{q,\mathrm{T1}}^{\mathrm{SI}} = -\frac{g_{\phi\tilde{\chi}_1^0\tilde{\chi}_1^0}g_{\phi qq}}{t - m_\phi^2}. \tag{4.21}$$

In the non-relativistic limit we have $t \ll m_\phi^2$. This limit is performed and the Mandelstam variable is dropped in the standard approach to obtain a velocity-independent Wilson coefficient.

One might ask oneself why there is no contribution from the pseudoscalar Higgs A^0. The calculation is mainly analogous, the only difference being $c_1^L = -c_1^R = g_{A^0\tilde{\chi}_1^0\tilde{\chi}_1^0}$ and $c_2^L = -c_2^R = g_{A^0qq}$, which means we have pure pseudoscalar couplings. We end up with

$$\mathcal{M}_{A^0} = -\frac{g_{A^0\tilde{\chi}_1^0\tilde{\chi}_1^0}g_{A^0qq}}{t - m_\phi^2}[\bar{\chi}\gamma_5\chi][\bar{q}\gamma_5 q] \tag{4.22}$$

and arrive at an effective four-fermion coupling of *pseudoscalar type*. This kind of interaction is kinematically strongly suppressed in the non-relativistic limit. Therefore, we neglect all contributions stemming from the pseudoscalar Higgs.[12]

Which effective operators lead to spin-dependent or -independent interactions and which of them are kinematically suppressed is a non-trivial question. It is studied in detail in chapter six of [169], which is a highly recommendable reference for this topic. We collect the main results for the most common effective operators in table 4.2. The tensor $\gamma^{\mu\nu}$ appearing therein is defined via

$$\gamma^{\mu\nu} = \frac{i}{2}[\gamma^\mu, \gamma^\nu] = \frac{i}{2}(\gamma^\mu\gamma^\nu - \gamma^\nu\gamma^\mu). \tag{4.23}$$

All other effective operators occuring at NLO are kinematically suppressed [129, 169, 170]. For the beginning we focus on the NLO contributions to the kinematically unsuppressed operators listed above. Actually, the situation simplifies even further as we deal with neutralinos, which are Majorana fermions. In case of Majorana fermions, there are no vector or tensor contributions, the operators $\bar{\chi}\gamma_\mu\chi$ and $\bar{\chi}\gamma_{\mu\nu}\chi$ vanish exactly [129, 171]. This is explicitly proven in chapter E. Therefore, we only consider effective operators of scalar and axial-vector type, which is in agreement with [134].

---

[12]Although it is demonstrated in [168] that pseudoscalar couplings can be important under specific circumstances.

4.3.2. T2: Z^0 contribution

We continue with the calculation of the Z^0 t-channel process, which is the second process shown in figure 4.4. The amplitude is very similar to the previous one. The topological difference is that we are dealing with a vector instead of a scalar propagator. Using the *Feynman gauge*[13] we obtain

$$
\begin{aligned}
i\mathcal{M}_{\text{T2}} &= \left[\bar{u}(p_1)i\gamma^\mu\boxed{1}u(p_a)\right]\frac{-ig_{\mu\nu}}{t-m_{Z^0}^2}\left[\bar{u}(p_2)i\gamma^\nu\boxed{2}u(p_b)\right] \\
\Leftrightarrow \mathcal{M}_{\text{T2}} &= \frac{1}{t-m_{Z^0}^2}\left[\bar{u}(p_1)\gamma^\mu\boxed{1}u(p_a)\right]\left[\bar{u}(p_2)\gamma_\mu\boxed{2}u(p_b)\right].
\end{aligned}
\tag{4.24}
$$

Similarly as before, the couplings are written generically as

$$
i\gamma^\mu\boxed{1} = i\gamma^\mu(c_1^L P_L + c_1^R P_R) = i\gamma^\mu(g_{Z^0\tilde{\chi}_1^0\tilde{\chi}_1^0}^L P_L + g_{Z^0\tilde{\chi}_1^0\tilde{\chi}_1^0}^R P_R).
\tag{4.25}
$$

$$
i\gamma^\nu\boxed{2} = i\gamma^\nu(c_2^L P_L + c_2^R P_R) = i\gamma^\nu(g_{Z^0qq}^L P_L + g_{Z^0qq}^R P_R).
\tag{4.26}
$$

Performing the calculation steps of the previous subsection, this amplitude leads to four different effective operators, namely the vector type $[\bar{\chi}\gamma_\mu\chi][\bar{q}\gamma^\mu q]$, the axial-vector type $[\bar{\chi}\gamma_5\gamma_\mu\chi][\bar{q}\gamma_5\gamma^\mu q]$ and two mixed type structures $[\bar{\chi}\gamma_5\gamma_\mu\chi][\bar{q}\gamma^\mu q]$ and $[\bar{\chi}\gamma_\mu\chi][\bar{q}\gamma_5\gamma^\mu q]$. The mixed type structures are kinematically suppressed[14] and the vector type interaction vanishes for Majorana fermions. We are left with the axial-vector contribution which can be written as

$$
\mathcal{M}_{\text{T2}} = \frac{c_1^R - c_1^L}{2}\frac{c_2^R - c_2^L}{2}\frac{1}{t-m_{Z^0}^2}[\bar{\chi}\gamma_5\gamma_\mu\chi][\bar{q}\gamma_5\gamma^\mu q]
\tag{4.27}
$$

and read off the first spin-dependent contribution to the Wilson coefficient α_q^{SD}.

$$
\alpha_{q,\text{T2}}^{\text{SD}} = \frac{c_1^R - c_1^L}{2}\frac{c_2^R - c_2^L}{2}\frac{1}{t-m_{Z^0}^2}.
\tag{4.28}
$$

4.3.3. T3 and T4: Squark contributions

The remaining tree-level contributions are those due to the squark processes depicted on the right in figure 4.4. It is important to differ between the first coupling with the ingoing quark and outgoing squark and the second one with outgoing quark and ingoing squark.

$$
i\boxed{1} = i(c_1^L P_L + c_1^R P_R) = i(g_{\tilde{\chi}_1^0 q\tilde{q}_i}^L P_L + g_{\tilde{\chi}_1^0 q\tilde{q}_i}^R P_R).
\tag{4.29}
$$

$$
i\boxed{2} = i(c_2^L P_L + c_2^R P_R) = i(g_{\tilde{\chi}_1^0 \tilde{q}_i q}^L P_L + g_{\tilde{\chi}_1^0 \tilde{q}_i q}^R P_R).
\tag{4.30}
$$

---

[13]Within the so-called R_ξ gauge, the propagator of a weak gauge boson possessing four-momentum p_μ and mass m can be written as $\frac{-i}{p^2-m^2}\left(g_{\mu\nu} - (1-\xi)\frac{p_\mu p_\nu}{p^2}\right)$. Due to the vector nature of the particle, we encounter the two Lorentz indices μ and ν. In addition, ξ denotes a gauge parameter which can be arbitrarily chosen. The Feynman gauge corresponds to the choice $\xi = 1$, which simplifies the propagator to $\frac{-ig_{\mu\nu}}{p^2-m^2}$. The disadvantage of the Feynman gauge is that in contrast to e.g. the unitary gauge, unphysical particles such as Goldstone bosons have to be included explicitly (cf. e.g. [172–174]). However, in the present context we omit all contributions stemming from the pseudoscalar Goldstone boson G^0 as they are kinematically strongly suppressed.

[14]The effects of these kinds of operators are discussed in [175]. They turn out to be irrelevant for the MSSM but can be interesting for other models with dark matter candidates in the GeV range.

We start with the s-channel and write the amplitude as

$$
\begin{aligned}
i\mathcal{M}_{\text{T3}} &= \left[\bar{v}(p_a)i\boxed{1}u(p_b)\right]\frac{i}{s-m_{\tilde{q}_i}^2}\left[\bar{u}(p_2)i\boxed{2}v(p_1)\right] \\
\Leftrightarrow \mathcal{M}_{\text{T3}} &= \frac{-1}{s-m_{\tilde{q}_i}^2}\left[\bar{v}(p_a)\boxed{1}u(p_b)\right]\left[\bar{u}(p_2)\boxed{2}v(p_1)\right].
\end{aligned}
\tag{4.31}
$$

We identify the spinors $\bar{v}(p_a), u(p_b), \bar{u}(p_2)$ and $v(p_1)$ with their corresponding spinor fields $\bar{\chi}, q, \bar{q}$ and χ and obtain four different operators.

$$
\begin{aligned}
\mathcal{M}_{\text{T3}} = \frac{-1}{s-m_{\tilde{q}_i}^2}&\left(\frac{c_1^R+c_1^L}{2}\frac{c_2^R+c_2^L}{2}\underbrace{[\bar{\chi}q][\bar{q}\chi]}_{\text{Scalar type}}+\frac{c_1^R-c_1^L}{2}\frac{c_2^R-c_2^L}{2}\underbrace{[\bar{\chi}\gamma_5 q][\bar{q}\gamma_5\chi]}_{\text{Pseudoscalar type}}\right. \\
&\left.+\frac{c_1^R+c_1^L}{2}\frac{c_2^R-c_2^L}{2}\underbrace{[\bar{\chi}q][\bar{q}\gamma_5\chi]}_{\text{Mixed type}}+\frac{c_1^R-c_1^L}{2}\frac{c_2^R+c_2^L}{2}\underbrace{[\bar{\chi}\gamma_5 q][\bar{q}\chi]}_{\text{Mixed type}}\right).
\end{aligned}
\tag{4.32}
$$

If we neglect the mixed type operators, we are left with a scalar type and a pseudoscalar type operator.

$$
\mathcal{M}_{\text{T3}} = \frac{-1}{s-m_{\tilde{q}_i}^2}\left(\frac{c_1^R+c_1^L}{2}\frac{c_2^R+c_2^L}{2}\underbrace{[\bar{\chi}q][\bar{q}\chi]}_{\text{Scalar type}}+\frac{c_1^R-c_1^L}{2}\frac{c_2^R-c_2^L}{2}\underbrace{[\bar{\chi}\gamma_5 q][\bar{q}\gamma_5\chi]}_{\text{Pseudoscalar type}}\right).
\tag{4.33}
$$

The situation seems to be familiar, but in contrast to the previous cases the spinor fields are in wrong order. There is always a neutralino spinor field contracted with a quark spinor field. We have to rearrange the spinor fields before we can read off the Wilson coefficients. This procedure is called *Fierz transformation*. As this process is central for our calculations, we devote the whole chapter D to it. We transform $[\bar{\chi}q][\bar{q}\chi]$ and $[\bar{\chi}\gamma_5 q][\bar{q}\gamma_5\chi]$ according to table D.4.

$$
\begin{aligned}
[\bar{\chi}q][\bar{q}\chi] &= -\frac{1}{4}[\bar{\chi}\chi][\bar{q}q]-\frac{1}{4}[\bar{\chi}\gamma_\mu\chi][\bar{q}\gamma^\mu q]-\frac{1}{8}[\bar{\chi}\gamma_{\mu\nu}\chi][\bar{q}\gamma^{\mu\nu}q] \\
&+ \frac{1}{4}[\bar{\chi}\gamma_5\gamma_\mu\chi][\bar{q}\gamma_5\gamma^\mu q]-\frac{1}{4}[\bar{\chi}\gamma_5\chi][\bar{q}\gamma_5 q].
\end{aligned}
\tag{4.34}
$$

$$
\begin{aligned}
[\bar{\chi}\gamma_5 q][\bar{q}\gamma_5\chi] &= -\frac{1}{4}[\bar{\chi}\chi][\bar{q}q]+\frac{1}{4}[\bar{\chi}\gamma_\mu\chi][\bar{q}\gamma^\mu q]-\frac{1}{8}[\bar{\chi}\gamma_{\mu\nu}\chi][\bar{q}\gamma^{\mu\nu}q] \\
&- \frac{1}{4}[\bar{\chi}\gamma_5\gamma_\mu\chi][\bar{q}\gamma_5\gamma^\mu q]-\frac{1}{4}[\bar{\chi}\gamma_5\chi][\bar{q}\gamma_5 q].
\end{aligned}
\tag{4.35}
$$

Now that the spinor fields are in correct order, we can proceed as before. The vector and tensor type interactions vanish for Majorana fermions and the pseudoscalar type interactions are kinematically suppressed. This simplifies the transformation to

$$
[\bar{\chi}q][\bar{q}\chi] = -\frac{1}{4}[\bar{\chi}\chi][\bar{q}q]+\frac{1}{4}[\bar{\chi}\gamma_5\gamma_\mu\chi][\bar{q}\gamma_5\gamma^\mu q].
\tag{4.36}
$$

$$
[\bar{\chi}\gamma_5 q][\bar{q}\gamma_5\chi] = -\frac{1}{4}[\bar{\chi}\chi][\bar{q}q]-\frac{1}{4}[\bar{\chi}\gamma_5\gamma_\mu\chi][\bar{q}\gamma_5\gamma^\mu q].
\tag{4.37}
$$

We insert these results in (4.33) and obtain

$$
\begin{aligned}
\mathcal{M}_{\mathrm{T3}} \;=\;& \frac{1}{16(s - m_{\tilde{q}_i}^2)}\Bigg(\Big((c_1^R + c_1^L)(c_2^R + c_2^L) + (c_1^R - c_1^L)(c_2^R - c_2^L)\Big)[\bar{\chi}\chi][\bar{q}q] \\
&+ \Big(-(c_1^R + c_1^L)(c_2^R + c_2^L) + (c_1^R - c_1^L)(c_2^R - c_2^L)\Big)[\bar{\chi}\gamma_5\gamma_\mu\chi][\bar{q}\gamma_5\gamma^\mu q]\Bigg).
\end{aligned} \tag{4.38}
$$

This expression allows us to read off the Wilson coefficients.

$$
\alpha_{q,\mathrm{T3}}^{\mathrm{SI}} \;=\; \frac{1}{16(s - m_{\tilde{q}_i}^2)}\Big((c_1^R + c_1^L)(c_2^R + c_2^L) + (c_1^R - c_1^L)(c_2^R - c_2^L)\Big). \tag{4.39}
$$

$$
\alpha_{q,\mathrm{T3}}^{\mathrm{SD}} \;=\; \frac{1}{16(s - m_{\tilde{q}_i}^2)}\Big(-(c_1^R + c_1^L)(c_2^R + c_2^L) + (c_1^R - c_1^L)(c_2^R - c_2^L)\Big). \tag{4.40}
$$

In contrast to the previous processes, the squark processes contribute to both the spin-dependent and spin-independent Wilson coefficient. Concrete expressions for the couplings can be found in [62] and [11].

The remaining tree-level process is T4, the squark u-channel depicted on the right of figure 4.4. The amplitude is given by

$$
i\mathcal{M}_{\mathrm{T4}} \;=\; [\bar{u}(p_1)i\boxed{1}u(p_b)]\frac{i}{u - m_{\tilde{q}_i}^2}[\bar{u}(p_2)i\boxed{2}u(p_a)]
$$

$$
\Leftrightarrow \mathcal{M}_{\mathrm{T4}} \;=\; \frac{-1}{u - m_{\tilde{q}_i}^2}[\bar{u}(p_1)\boxed{1}u(p_b)][\bar{u}(p_2)\boxed{2}u(p_a)]. \tag{4.41}
$$

Note that we have denoted the lower coupling with the outgoing squark as $i\boxed{1}$. In this notation the couplings $i\boxed{1}$ and $i\boxed{2}$ equal those from the s-channel as given in (4.29) and (4.30). The spinor fields corresponding to $\bar{u}(p_1), u(p_b), \bar{u}(p_2)$ and $u(p_a)$ are $\bar{\chi}, q, \bar{q}$ and χ. This brings us to

$$
\mathcal{M}_{\mathrm{T4}} = \frac{-1}{u - m_{\tilde{q}_i}^2}[\bar{\chi}\boxed{1}q][\bar{q}\boxed{2}\chi], \tag{4.42}
$$

which is exactly the same expression as before, the only difference being $s \leftrightarrow u$. The resulting Wilson coefficients are thus given by

$$
\alpha_{q,\mathrm{T4}}^{\mathrm{SI}} \;=\; \frac{1}{16(u - m_{\tilde{q}_i}^2)}\Big((c_1^R + c_1^L)(c_2^R + c_2^L) + (c_1^R - c_1^L)(c_2^R - c_2^L)\Big). \tag{4.43}
$$

$$
\alpha_{q,\mathrm{T4}}^{\mathrm{SD}} \;=\; \frac{1}{16(u - m_{\tilde{q}_i}^2)}\Big(-(c_1^R + c_1^L)(c_2^R + c_2^L) + (c_1^R - c_1^L)(c_2^R - c_2^L)\Big). \tag{4.44}
$$

The *heavy squark limit* is given by $s, u \ll m_{\tilde{q}_i}^2$. In this limit, both channels lead to the same contribution and including the u-channel can be done by doubling the s-channel contribution. Although the heavy squark limit is quite popular, it may lead to incorrect results when the aforementioned condition is nut fulfilled. As we are aware of the fact that a mass degeneracy between the lightest neutralino and the lightest stop may create an efficient mechanism to obtain the correct relict density [148–150], which in turn leads to phenomenologically relevant scenarios, we do not perform this limit in the following

and distinguish between s and u channel contributions. To be more precise, we replace the Mandelstam variables by

$$t \to 0, \qquad s \to (m_{\tilde{\chi}_1^0} + m_q)^2 \qquad \text{and} \qquad u \to (m_{\tilde{\chi}_1^0} - m_q)^2 \qquad (4.45)$$

in the non-relativistic limit, which is in agreement with [176]. We also mention [177], where the direct detection prospects in case of a mass degeneracy between the lightest neutralino and a squark are investigated. To obtain meaningful results, it has proven crucial to keep the masses in the Mandelstam variables s and u in this analysis.

This completes our calculation of Wilson coefficients at tree-level. In the next section we determine the NLO contributions and extend the basic procedure explained here. Let us sum it up by four steps.

Determination of Wilson coefficients at tree-level

1. Write down and simplify the amplitude of the fundamental process. Identify the spinors with their corresponding spinor fields.

2. Sort out irrelevant effective operators.

3. If necessary, perform a Fierz transformation.

4. Read off the desired Wilson coefficients in front of the kinematically unsuppressed operators.

4.4. Virtual corrections

In the previous section we have determined the tree-level contributions to the neutralino-quark four-fermion couplings stemming from the processes depicted in figure 4.4. These are the simplest processes of the form $\tilde{\chi}_1^0 q \to \tilde{\chi}_1^0 q$. More complicated processes arise when *virtual corrections* are included, which corresponds to allowing further interactions via e.g. the strong coupling g_s. From the technical point of view, the tree-level is just the leading order contribution of a perturbative expansion in the respective coupling constant and the virtual corrections contain the higher order terms.

In this section we calculate the $\mathcal{O}(\alpha_s)$ corrections to the leading tree-level contributions, where $\alpha_s = \frac{g_s^2}{4\pi}$. The NLO contributions are divided into propagator corrections, vertex corrections and box contributions. The propagator and vertex corrections give rise to ultraviolet divergences (cf. chapter F) which are removed by adding the corresponding counterterms (cf. chapter G).

4.4.1. Propagator corrections

We start with the simplest virtual corrections, the propagator corrections shown in figure 4.5. From left to right we label these diagrams P1, P2, P3 and P4. They are understood as insertions in the tree-level squark processes depicted on the right of figure 4.4. The details of these insertions work are discussed explicitly at the end of the subsection. As we are calculating corrections in the strong coupling constant, there are no propagator corrections to the t-channel processes which contain weakly interacting h^0, H^0 and Z^0 mediators. The following calculations are quite fundamental and have been performed
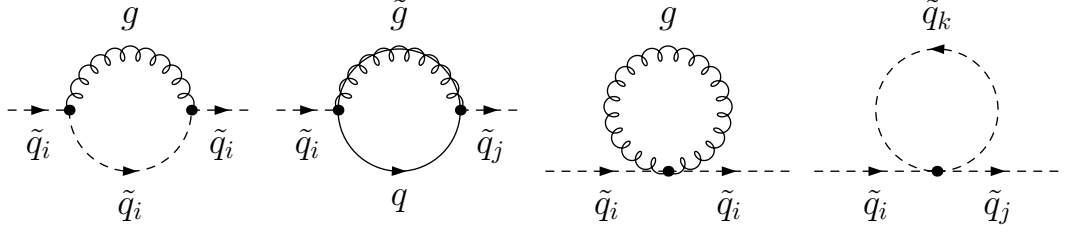
Figure 4.5.: Propagator corrections to the neutralino-quark four-fermion coupling

several times before, e.g. in [166]. Nevertheless, we discuss them in full detail to illustrate the general procedure.

Propagator correction P1

We label the incoming and outcoming four-momentum with p. The gluon carries the undetermined momentum q. The couplings are labelled $\boxed{1}$ and $\boxed{2}$, starting on the left.

$$i\boxed{1}(p_\mathrm{i}+p_\mathrm{f})^\mu = -ig_s(2p+q)^\mu. \qquad (4.46)$$
$$i\boxed{2}(p_\mathrm{i}+p_\mathrm{f})^\nu = -ig_s(2p+q)^\nu. \qquad (4.47)$$

Therein p_i denotes the initial and p_f the final squark momenta at the respective coupling. Using dimensional reduction (cf. chapter F) and inserting the colour factor $C_F = 4/3$ we obtain the amplitude

$$
\begin{aligned}
i\mathcal{M}_{\mathrm{P1}} &= C_F \mu^{4-D} \int \frac{\mathrm{d}^D q}{(2\pi)^D} i\boxed{2}(2p+q)^\nu \frac{-ig_{\mu\nu}}{q^2} i\boxed{1}(2p+q)^\mu \frac{i}{(q+p)^2 - m_{\tilde{q}_i}^2} \\
\Leftrightarrow \mathcal{M}_{\mathrm{P1}} &= -\frac{\alpha_s C_F}{4\pi} \frac{(2\pi\mu)^{4-D}}{i\pi^2} \int \mathrm{d}^D q \{\mathcal{D}_0 \mathcal{D}_1\}^{-1}(4p^2 + 4pq + q^2) \\
&= -\frac{\alpha_s C_F}{4\pi}\left(4p^2 B_0(p,0,m_{\tilde{q}_i}^2) + 4p^2 B_1(p,0,m_{\tilde{q}_i}^2) + A_0(m_{\tilde{q}_i}^2)\right). \qquad (4.48)
\end{aligned}
$$

In the intermediate step we introduced $\mathcal{D}_0 = q^2$ and $\mathcal{D}_1 = (q+p)^2 - m_{\tilde{q}_i}^2$.

Propagator correction P2

We denote the external four-momenta with p and the gluino momentum with q. Starting on the left, the couplings are given by

$$i\boxed{1} = i(c_1^L P_L + c_1^R P_R) = i(g_{\tilde{g}\tilde{q}_i q}^L P_L + g_{\tilde{g}\tilde{q}_i q}^R P_R). \qquad (4.49)$$
$$i\boxed{2} = i(c_2^L P_L + c_2^R P_R) = i(g_{\tilde{g}q\tilde{q}_j}^L P_L + g_{\tilde{g}q\tilde{q}_j}^R P_R). \qquad (4.50)$$

In the following we also need the twisted couplings

$$i\overset{\longleftrightarrow}{\boxed{1}} = i(c_1^R P_L + c_1^L P_R) \quad \text{and} \quad i\overset{\longleftrightarrow}{\boxed{2}} = i(c_2^R P_L + c_2^L P_R), \qquad (4.51)$$

which arise when commuting with a Dirac matrix. The amplitude reads

$$i\mathcal{M}_{\mathrm{P2}} = (-1)C_F \mu^{4-D} \int \frac{\mathrm{d}^D q}{(2\pi)^D} \mathrm{Tr}\left(i\boxed{2}\frac{i(\slashed{p}+\slashed{q}+m_q)}{(p+q)^2 - m_q^2}i\boxed{1}\frac{i(\slashed{q}+m_{\tilde{g}})}{q^2 - m_{\tilde{g}}}\right), \qquad (4.52)$$

where m_q and $m_{\tilde{g}}$ denote the quark and gluino mass. As we encounter a closed fermion loop, we insert an additional factor (-1) and take the trace over the whole expression. Some useful formulae for evaluating such traces are listed in chapter C. We define $\mathcal{D}_0 = q^2 - m_{\tilde{g}}^2$ and $\mathcal{D}_1 = (q+p)^2 - m_q^2$ and get

$$
\begin{aligned}
\mathcal{M}_{\mathrm{P2}} &= -\frac{C_F}{16\pi^2}\frac{(2\pi\mu)^{4-D}}{i\pi^2}\int \mathrm{d}^D q\{\mathcal{D}_0\mathcal{D}_1\}^{-1}\,\mathrm{Tr}\left(\boxed{2}(\not{p}+\not{q}+m_q)\boxed{1}(\not{q}+m_{\tilde{g}})\right) \\
&= -\frac{C_F}{16\pi^2}\frac{(2\pi\mu)^{4-D}}{i\pi^2}\int \mathrm{d}^D q\{\mathcal{D}_0\mathcal{D}_1\}^{-1}\,\mathrm{Tr}\left(\boxed{2}\overset{\leftrightarrow}{\boxed{1}}(\not{p}+\not{q})\not{q}+\boxed{2}\,\boxed{1}m_q m_{\tilde{g}}\right) \\
&= -\frac{C_F}{8\pi^2}\frac{(2\pi\mu)^{4-D}}{i\pi^2}\int \mathrm{d}^D q\{\mathcal{D}_0\mathcal{D}_1\}^{-1} \\
&\quad \left((c_2^R c_1^L + c_2^L c_1^R)(pq + q^2) + (c_2^R c_1^R + c_2^L c_1^L)m_q m_{\tilde{g}}\right) \\
&= -\frac{C_F}{8\pi^2}\Big((c_2^R c_1^L + c_2^L c_1^R)(p^2 B_1(p,m_{\tilde{g}}^2,m_q^2) + A_0(m_q^2) + m_{\tilde{g}}^2 B_0(p,m_{\tilde{g}}^2,m_q^2)) \\
&\quad + (c_2^R c_1^R + c_2^L c_1^L)m_q m_{\tilde{g}} B_0(p,m_{\tilde{g}}^2,m_q^2)\Big).
\end{aligned}
\tag{4.53}
$$

Propagator correction P3

We label the coupling as $i\boxed{1} = ic_1 g^{\mu\nu} = ig_{\tilde{q}_i\tilde{q}_i gg}g^{\mu\nu}$ and obtain the amplitude

$$
\begin{aligned}
i\mathcal{M}_{\mathrm{P3}} &= C_F\mu^{4-D}\int\frac{\mathrm{d}^D q}{(2\pi)^D}ic_1 g^{\mu\nu}\frac{-ig_{\mu\nu}}{q^2} \\
\Leftrightarrow \mathcal{M}_{\mathrm{P3}} &= C_F\frac{Dc_1}{16\pi^2}\frac{(2\pi\mu)^{4-D}}{i\pi^2}\int\mathrm{d}^D q\frac{1}{q^2} = C_F\frac{Dc_1}{16\pi^2}\underbrace{A_0(0)}_{(F.14)} = 0.
\end{aligned}
\tag{4.54}
$$

This contribution vanishes as the one-point function for the massless gluon equals zero.

Propagator correction P4

This calculation is as short as the previous one. Labelling the four-squark coupling as $i\boxed{1} = ic_1 = ig_{\tilde{q}_i\tilde{q}_j\tilde{q}_k\tilde{q}_k}$ leads to

$$
\begin{aligned}
i\mathcal{M}_{\mathrm{P4}} &= C_F\mu^{4-D}\int\frac{\mathrm{d}^D q}{(2\pi)^D}ic_1\frac{i}{q^2 - m_{\tilde{q}_k}^2} \\
\Leftrightarrow \mathcal{M}_{\mathrm{P4}} &= -C_F\frac{c_1}{16\pi^2}\frac{(2\pi\mu)^{4-D}}{i\pi^2}\int\mathrm{d}^D q\frac{1}{q^2 - m_{\tilde{q}_k}^2} = -C_F\frac{c_1}{16\pi^2}A_0(m_{\tilde{q}_k}^2).
\end{aligned}
\tag{4.55}
$$

When including this correction, we sum over both internal squark types, i.e. $k = 1, 2$.

Insertion of the propagator corrections

As mentioned before, the propagator corrections are understood as insertions in the squark tree-level processes, which is illustrated by the grey circles in figure 4.6. Note that the propagator corrections may change the squark type in general. Therefore, one has to sum over $i, j = 1, 2$ independently. In case of the propagator correction P1 there is no squark type change, only diagrams with $i = j$ are contribute. This is taken into account by the inclusion of an *Kronecker delta* δ_{ij} in the respective coupling.
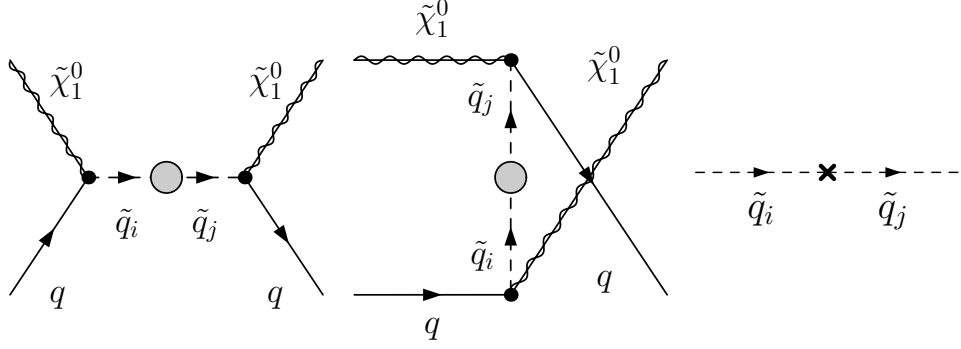
Figure 4.6.: Insertions of the propagator corrections in the tree-level diagrams (left and middle) and propagator counterterm for the neutralino-quark four-fermion coupling (right)

The final four-fermion couplings are obtained by multiplying the tree-level couplings given by (4.39) and (4.40) for the s-channel or (4.43) and (4.44) for the u-channel with the correction factors $\mathcal{M}_\mathrm{X}$ with $X \in \{\mathrm{P1, P2, P4}\}$ given by (4.48), (4.53) and (4.55) and the additional squark propagator $\frac{i}{s-m_{\tilde{q}_j}^2}$ or $\frac{i}{u-m_{\tilde{q}_j}^2}$. The final result reads

$$\alpha_{q,\mathrm{X}}^{\mathrm{SI}} = \alpha_{q,\mathrm{T3}}^{\mathrm{SI}} \frac{i\mathcal{M}_\mathrm{X}}{s-m_{\tilde{q}_j}^2} + \alpha_{q,\mathrm{T4}}^{\mathrm{SI}} \frac{i\mathcal{M}_\mathrm{X}}{u-m_{\tilde{q}_j}^2} \quad \text{and} \tag{4.56}$$

$$\alpha_{q,\mathrm{X}}^{\mathrm{SD}} = \alpha_{q,\mathrm{T3}}^{\mathrm{SD}} \frac{i\mathcal{M}_\mathrm{X}}{s-m_{\tilde{q}_j}^2} + \alpha_{q,\mathrm{T4}}^{\mathrm{SD}} \frac{i\mathcal{M}_\mathrm{X}}{u-m_{\tilde{q}_j}^2}, \tag{4.57}$$

where again $X \in \{\mathrm{P1, P2, P4}\}$.

4.4.2. Propagator counterterm

As mentioned earlier, the propagator corrections possess ultraviolet divergences. These divergences are removed via renormalisation, i.e. by a redefinition of the original parameters of the theory. In this subsection we list the needed propagator counterterm and its decomposition. For further details on the renormalisation scheme concretely implemented in `DM@NLO` we refer to chapter G and [62].

The propagator counterterm for an incoming squark $\tilde{q}_i$ of momentum p and an outgoing squark $\tilde{q}_j$ is depicted in figure 4.6. It can be casted into the form

$$\mathcal{M}_{\mathrm{PC}} = \frac{1}{2}\delta Z_{\tilde{q}}^{ij}(p^2 - m_{\tilde{q}_i}^2) + \frac{1}{2}\delta Z_{\tilde{q}}^{ji}(p^2 - m_{\tilde{q}_j}^2) - \delta_{ij}\delta m_{\tilde{q}_i}^2, \tag{4.58}$$

where $\delta Z_{\tilde{q}}^{ij}$ denotes the counterterm of the squark wave function and $\delta m_{\tilde{q}_i}^2$ denotes the counterterm for the squark mass. Note that the artificial inclusion of the squark wave function counterterm allows to separately check the ultraviolet finiteness of the propagator corrections plus counterterm and vertex corrections plus counterterms. Otherwise, only the sum of the propagator and vertex corrections and associated counterterms would be ultraviolet finite. Of course this artificial inclusion does not alter the final result as the dependence on $\delta Z_{\tilde{q}}^{ij}$ exactly cancels when adding the propagator and vertex counterterms.
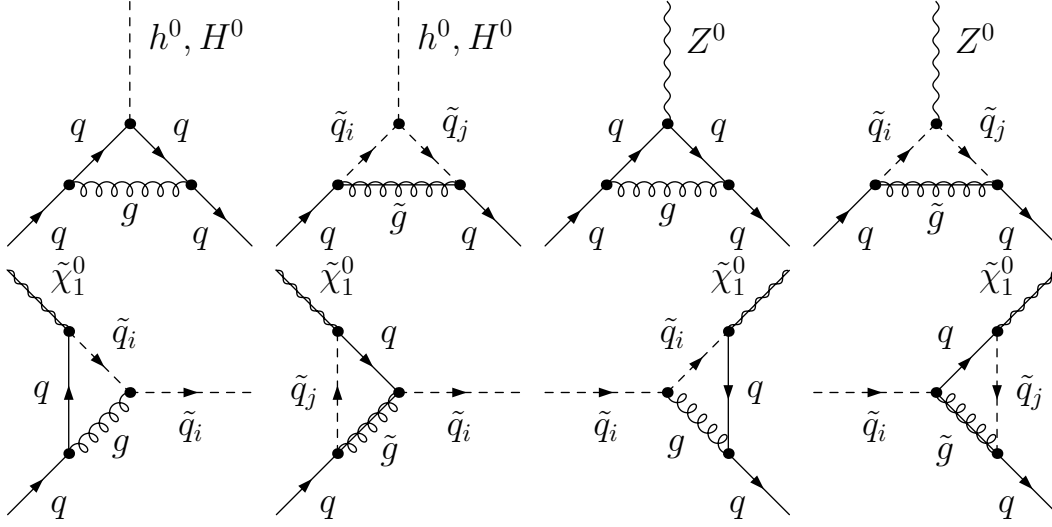
Figure 4.7.: Vertex corrections to the neutralino-quark four-fermion coupling

The insertion of the propagator counterterm in the tree-level diagrams works analogously to the insertion of the propagator corrections. More precisely, we have

$$\alpha_{q,\mathrm{PC}}^{\mathrm{SI}} = \alpha_{q,\mathrm{T3}}^{\mathrm{SI}} \frac{i\mathcal{M}_{\mathrm{PC}}}{s - m_{\tilde{q}_j}^2} + \alpha_{q,\mathrm{T4}}^{\mathrm{SI}} \frac{i\mathcal{M}_{\mathrm{PC}}}{u - m_{\tilde{q}_j}^2} \quad \text{and} \tag{4.59}$$

$$\alpha_{q,\mathrm{PC}}^{\mathrm{SD}} = \alpha_{q,\mathrm{T3}}^{\mathrm{SD}} \frac{i\mathcal{M}_{\mathrm{PC}}}{s - m_{\tilde{q}_j}^2} + \alpha_{q,\mathrm{T4}}^{\mathrm{SD}} \frac{i\mathcal{M}_{\mathrm{PC}}}{u - m_{\tilde{q}_j}^2}. \tag{4.60}$$

4.4.3. Vertex corrections

We continue with the vertex corrections which are shown in figure 4.7. From upper left to lower right we label them V1 - V8. These corrections are understood as insertions in the corresponding tree-level processes, which is explicated at the end of this subsection. All of these calculations are performed in generic manner in [166]. We briefly reproduce the first two of them to illustrate the procedure. As before, we sum over all internal squark types when finally including these corrections.

The resulting expressions include the three-point functions C_0, C_1, C_2 and C_{00}. These functions are defined and discussed in chapter F. As we want to evaluate these functions at zero velocity transfer, the standard method of determining C_1, C_2 and C_{00} – the so-called *tensor reduction* (cf. section F.4) – breaks down. An alternative approach is worked out and presented in section F.5.
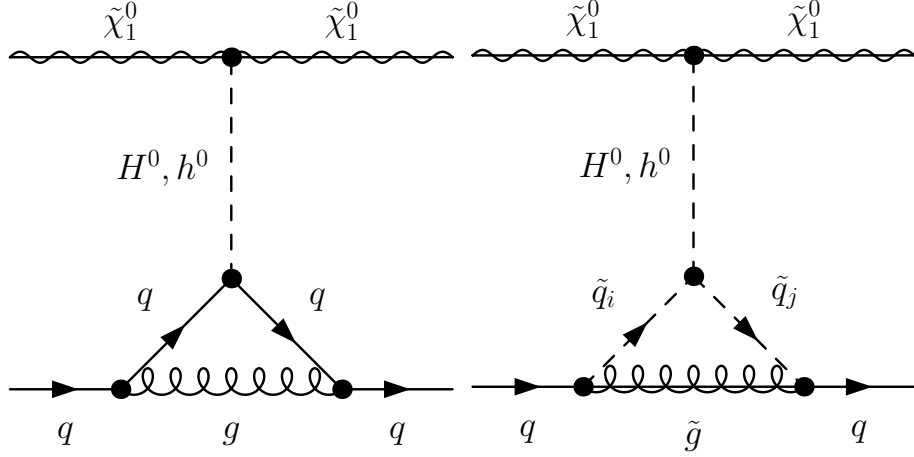
Figure 4.8.: Vertex corrections V1 (left) and V2 (right) inserted in the corresponding tree-level process T1

Vertex correction V1

We start with the gluonic correction to the tree-level process T1, namely the vertex correction V1. The corresponding diagram is shown on the left in figure 4.8. Using our usual nomenclature, we write down the amplitude as

$$
\begin{aligned}
i\mathcal{M}_{\mathrm{V1}} &= \left[\bar{u}(p_1)ig_{\phi\tilde{\chi}_1^0\tilde{\chi}_1^0}u(p_a)\right]\frac{i}{t-m_\phi^2}\frac{-ig_{\mu\nu}}{q^2}C_F\mu^{4-D}\int\frac{\mathrm{d}^Dq}{(2\pi)^D}\left[\bar{u}(p_2)(-ig_s\gamma^\mu)\right.\\
&\quad \frac{i(\not{p}_2-\not{q}+m_q)}{(p_2-q)^2-m_q^2}ig_{\phi qq}\frac{i(\not{p}_b-\not{q}+m_q)}{(p_b-q)^2-m_q^2}(-ig_s\gamma^\nu)u(p_b)\Bigg]\\
\Leftrightarrow \mathcal{M}_{\mathrm{V1}} &= \left[\bar{u}(p_1)u(p_a)\right]\frac{-g_{\phi\tilde{\chi}_1^0\tilde{\chi}_1^0}}{t-m_\phi^2}\frac{\alpha_s C_F}{4\pi}\frac{(2\pi\mu)^{4-D}}{i\pi^2}\int\mathrm{d}^Dq\\
&\quad \left[\bar{u}(p_2)\gamma^\mu\frac{\not{p}_2-\not{q}+m_q}{(p_2-q)^2-m_q^2}g_{\phi qq}\frac{\not{p}_b-\not{q}+m_q}{(p_b-q)^2-m_q^2}\gamma_\mu u(p_b)\frac{1}{q^2}\right]\\
&:= \left[\bar{u}(p_1)u(p_a)\right]\frac{-g_{\phi\tilde{\chi}_1^0\tilde{\chi}_1^0}}{t-m_\phi^2}\left[\bar{u}(p_2)I_{\mathrm{V1}}u(p_b)\right].
\end{aligned}
\tag{4.61}
$$

We compare this expression with (4.19) and note that the algebraic form is identical, the only difference is that the original coupling $g_{\phi qq}$ is replaced by the loop coupling I_{V1}. This is the central idea of the approach in [166]. The vertex corrections are calculated in a generic, modular fashion and can be regarded as couplings which are inserted in Feynman diagrams as usual. In the present case, this insertion corresponds to simply replacing $g_{\phi qq}$ in the tree-level calculation T1 by the more complicated expression I_{V1}. We continue with the evaluation of I_{V1}. Bearing in mind that it is encircled by the spinors $\bar{u}(p_2)$ and $u(p_b)$ allows us to use the Dirac equation in terms of

$$
\bar{u}(p_2)\not{p}_2 = m_q\bar{u}(p_2) \quad\text{and}\quad \not{p}_b u(p_b) = m_q u(p_b).
\tag{4.62}
$$

After some algebra we finally find the purely scalar loop coupling

$$
I_{\mathrm{V1}} = g_{\phi qq}\frac{\alpha_s C_F}{4\pi}\left(4B_0 - 2 + 4p_b p_2(C_0 + C_1 + C_2)\right),
\tag{4.63}
$$

43

where the two- and three-point functions are evaluated for the arguments $B = B(p_b - p_2, m_{\tilde{q}}^2, m_{\tilde{q}}^2)$ and $C = C(p_b, p_2, 0, m_{\tilde{q}}^2, m_{\tilde{q}}^2)$. Furthermore, we have used

$$DB_0 = (D-4)B_0 + 4B_0 = -2 + 4B_0 + \mathcal{O}(D-4) \qquad (4.64)$$

and are thus taking into account that the two-point function diverges in the limit $D \to 4$. This is explained in greater detail in section F.6. Giving some foresight, we already mention that this contribution vanishes completely after the matching procedure described in section 4.5.

Vertex correction V2

Next we consider the vertex correction V2, the supersymmetric version of V1. This process is depicted on the right in figure 4.8. We label the couplings as follows:

$$i\boxed{1} = ic_1 = ig_{\phi\tilde{\chi}_1^0\tilde{\chi}_1^0}. \qquad (4.65)$$

$$i\boxed{2} = ic_2 = ig_{\phi\tilde{q}_i\tilde{q}_j}. \qquad (4.66)$$

$$i\boxed{3} = i(c_3^L P_L + c_3^R P_R) = i(g_{\tilde{g}q\tilde{q}_i}^L P_L + g_{\tilde{g}q\tilde{q}_i}^R P_R). \qquad (4.67)$$

$$i\boxed{4} = i(c_4^L P_L + c_4^R P_R) = i(g_{\tilde{g}\tilde{q}_jq}^L P_L + g_{\tilde{g}\tilde{q}_jq}^R P_R). \qquad (4.68)$$

The coupling $i\boxed{3}$ includes the outgoing squark $\tilde{q}_i$ and the coupling $i\boxed{4}$ includes the ingoing squark $\tilde{q}_j$. Given this labelling, we obtain the amplitude

$$
\begin{aligned}
i\mathcal{M}_{V2} &= \left[\bar{u}(p_1)ig_{\phi\tilde{\chi}_1^0\tilde{\chi}_1^0}u(p_a)\right] \frac{i}{t-m_\phi^2} C_F \mu^{4-D} \int \frac{\mathrm{d}^D q}{(2\pi)^D} \\
&\quad \left[\bar{u}(p_2)i\boxed{4}\frac{i(\slashed{q}+m_{\tilde{g}})}{q^2-m_{\tilde{g}}^2}i\boxed{3}u(p_b)\right] ig_{\phi\tilde{q}_i\tilde{q}_j} \frac{i}{(p_2-q)^2-m_{\tilde{q}_j}^2} \frac{i}{(p_b-q)^2-m_{\tilde{q}_i}^2} \\
&= [\bar{u}(p_1)u(p_a)] \frac{ig_{\phi\tilde{\chi}_1^0\tilde{\chi}_1^0}}{t-m_\phi^2} \frac{C_F}{4\pi^2} \frac{(2\pi\mu)^{4-D}}{i\pi^2} \int \mathrm{d}^D q \\
&\quad \left[\bar{u}(p_2)\boxed{4}\frac{\slashed{q}+m_{\tilde{g}}}{q^2-m_{\tilde{g}}^2}\boxed{3}u(p_b)\right] \frac{g_{\phi\tilde{q}_i\tilde{q}_j}}{(p_2-q)^2-m_{\tilde{q}_j}^2} \frac{1}{(p_b-q)^2-m_{\tilde{q}_i}^2} \\
\Leftrightarrow \mathcal{M}_{V2} &:= [\bar{u}(p_1)u(p_a)] \frac{-g_{\phi\tilde{\chi}_1^0\tilde{\chi}_1^0}}{t-m_\phi^2} [\bar{u}(p_2)I_{V2}u(p_b)].
\end{aligned}
\qquad (4.69)
$$

We see that the factorisation works precisely as before. This time the tree-level coupling $g_{\phi qq}$ is replaced by the expression I_{V2} which reads

$$I_{V2} = -\frac{C_F g_{\phi\tilde{q}_i\tilde{q}_j}}{16\pi^2} \left(\boxed{4}\boxed{3}m_{\tilde{g}}C_0 - \boxed{4}\overleftrightarrow{\boxed{3}}m_q C_1 - \overleftrightarrow{\boxed{4}}\boxed{3}m_q C_2\right), \qquad (4.70)$$

where three-point functions are evaluated for the arguments $C = C(p_b, p_2, m_{\tilde{g}}^2, m_{\tilde{q}_i}^2, m_{\tilde{q}_j}^2)$. We can decompose this coupling into a left-handed and a right-handed part.

$$I_{V2} = I_{V2}^L P_L + I_{V2}^R P_R. \qquad (4.71)$$

$$I_{V2}^L = -\frac{C_F g_{\phi\tilde{q}_i\tilde{q}_j}}{16\pi^2} \left(c_4^L c_3^L m_{\tilde{g}}C_0 - c_4^L c_3^R m_q C_1 - c_4^R c_3^L m_q C_2\right). \qquad (4.72)$$

$$I_{V2}^R = -\frac{C_F g_{\phi\tilde{q}_i\tilde{q}_j}}{16\pi^2} \left(c_4^R c_3^R m_{\tilde{g}}C_0 - c_4^R c_3^L m_q C_1 - c_4^L c_3^R m_q C_2\right). \qquad (4.73)$$

It is important to note that we want to replace $g_{\phi qq}$ in (4.19) by another completely scalar expression to reobtain the scalar operator $[\bar{\chi}\chi][\bar{q}q]$. Hence, the correct replacement is $g_{\phi qq} \to 1/2(I_{V2}^R + I_{V2}^L)$. In contrast to that, the replacement $g_{\phi qq} \to 1/2(I_{V2}^R - I_{V2}^L)$ would lead to a different operator, namely $[\bar{\chi}\chi][\bar{q}\gamma_5 q]$ which is kinematically suppressed.

From now on we just list the final results needed for our vertex corrections. These results stem originally from [166]. A `Mathematica` script was used to transfer them from LaTeX to `Fortran` and to relabel the variables. Furthermore, we just list the left-handed parts of the loop couplings. The right-handed parts always follow by the substitution $L \leftrightarrow R$.

Vertex correction V3

The gluonic correction to the tree-level process T2 leads to a loop coupling

$$
\begin{aligned}
I_{V3}^L \;=\; & \frac{\alpha_s C_F}{4\pi} \left(2(C_1 + C_2)c_1^R m_q^2 \right. \\
+ \; & c_1^L(-1 + 2B_0 - 4C_{00} + 4p_b p_2(C_0 + C_1 + C_2) + 2(C_1 + C_2)m_q^2)\big),
\end{aligned} \quad (4.74)
$$

where the two- and three-point functions possess the arguments $B = B(p_b - p_2, m_q^2, m_q^2)$ and $C = C(p_b, p_2, 0, m_q^2, m_q^2)$. The coupling

$$
i\gamma^\mu \boxed{1} = i\gamma^\mu(c_1^L P_L + c_1^R P_R) = i\gamma^\mu(g_{Z^0 qq}^L P_L + g_{Z^0 qq}^R P_R) \quad (4.75)
$$

connects the quarks and the Z^0. As it is the case for the vertex correction V1, this correction vanishes after the matching procedure.

Vertex correction V4

This vertex correction is the supersymmetric version of V3. We find the compact expression

$$
I_{V4}^L \;=\; \frac{2C_F}{16\pi^2} C_{00} c_1 c_2^L c_3^R. \quad (4.76)
$$

The arguments of the C_{00} function are $C = C(p_b, p_2, m_{\tilde{g}}^2, m_{\tilde{q}_i}^2, m_{\tilde{q}_j}^2)$. The first coupling represents the coupling between the squarks and the Z^0. We write it as

$$
i\boxed{1}(p_i + p_f)_\mu = ic_1(p_b + p_2 - 2q)_\mu = ig_{Z^0 \tilde{q}_i \tilde{q}_j}(p_b + p_2 - 2q)_\mu, \quad (4.77)
$$

where p_i denotes the initial, incoming and p_f the final, outgoing squark momentum. The remaining two couplings couple a quark, a squark and a gluino, the difference being that the second coupling contains an ingoing and the third coupling an outgoing quark.

$$
\begin{aligned}
i\boxed{2} \;&=\; i(c_2^L P_L + c_2^R P_R) = i(g_{\tilde{g}q\tilde{q}_i}^L P_L + g_{\tilde{g}q\tilde{q}_i}^R P_R). \quad (4.78) \\
i\boxed{3} \;&=\; i(c_3^L P_L + c_3^R P_R) = i(g_{\tilde{g}\tilde{q}_j q}^L P_L + g_{\tilde{g}\tilde{q}_j q}^R P_R). \quad (4.79)
\end{aligned}
$$

We stress once more that this is just the part of the loop coupling relevant for our calculation. There are other terms as well, but these terms generate different Lorentz structures and lead to kinematically suppressed operators.

Vertex correction V5

The loop coupling for the vertex correction V5 reads

$$
\begin{aligned}
I_{\text{V5}}^{L}(s) \;=\; & -\frac{\alpha_s C_F}{4\pi}\Bigg(2(C_0 + C_1 + C_2)c_1^R m_q m_{\tilde{\chi}_1^0} \\
& - c_1^L(B_0 - 4p_a p_b C_2 + 2(C_0 - C_2)m_q^2 + 2C_1 m_{\tilde{\chi}_1^0}^2)\Bigg),
\end{aligned}
\tag{4.80}
$$

where the two- and three-point functions are evaluated for the arguments $B = B(p_a + p_b, m_{\tilde{q}_i}^2, 0)$ and $C = C(p_a, p_b, m_q^2, m_{\tilde{q}_i}^2, 0)$. The coupling

$$
i\,\boxed{1} = i(c_1^L P_L + c_1^R P_R) = i(g_{\tilde{\chi}_1^0 q \tilde{q}_i}^L P_L + g_{\tilde{\chi}_1^0 q \tilde{q}_i}^R P_R)
\tag{4.81}
$$

connects the neutralino, the incoming quark and the outgoing squark. This kinematic configuration holds true for the s-channel process, i.e. the insertion in the tree-level T3. However, we also want to insert this loop coupling in the u-channel process, i.e. the tree-level T4. In this case we have to replace $p_a \leftrightarrow -p_1$ and obtain

$$
\begin{aligned}
I_{\text{V5}}^{L}(u) \;=\; & -\frac{\alpha_s C_F}{4\pi}\Bigg(2(C_0 + C_1 + C_2)c_1^R m_q m_{\tilde{\chi}_1^0} \\
& - c_1^L(B_0 + 4p_1 p_b C_2 + 2(C_0 - C_2)m_q^2 + 2C_1 m_{\tilde{\chi}_1^0}^2)\Bigg),
\end{aligned}
\tag{4.82}
$$

where the two- and three-point functions are now evaluated for the arguments $B = B(-p_1 + p_b, m_{\tilde{q}_i}^2, 0)$ and $C = C(-p_1, p_b, m_q^2, m_{\tilde{q}_i}^2, 0)$.

Vertex correction V6

The gluino vertex correction to the squark processes T3 and T4 leads to a bit more lengthy loop coupling. We find

$$
\begin{aligned}
I_{\text{V6}}^{L}(s) \;=\; & \frac{C_F}{16\pi^2}\Bigg(-c_1^R\big(C_2 c_3^L c_2^R m_q + c_2^L(m_{\tilde{g}}(C_0 + C_2)c_3^L + (C_0 + C_1 + C_2)c_3^R m_q)\big)m_{\tilde{\chi}_1^0} \\
& - c_1^L\big(c_3^R m_q(m_{\tilde{g}}C_1 c_2^R + (C_0 + C_1)c_2^L m_q) \\
& + c_3^L(m_{\tilde{g}}C_0 c_2^L m_q + c_2^R(B_0 + C_1 m_q^2 + C_2 m_{\tilde{\chi}_1^0}^2 + C_0 m_{\tilde{q}_j}^2)))\Bigg).
\end{aligned}
\tag{4.83}
$$

The three couplings occuring here are all given in the usual, generic form.

$$
i\,\boxed{1} \;=\; i(c_1^L P_L + c_1^R P_R) = i(g_{\tilde{\chi}_1^0 \tilde{q}_j q}^L P_L + g_{\tilde{\chi}_1^0 \tilde{q}_j q}^R P_R).
\tag{4.84}
$$

$$
i\,\boxed{2} \;=\; i(c_2^L P_L + c_2^R P_R) = i(g_{\tilde{g} q \tilde{q}_i}^L P_L + g_{\tilde{g} q \tilde{q}_i}^R P_R).
\tag{4.85}
$$

$$
i\,\boxed{3} \;=\; i(c_3^L P_L + c_3^R P_R) = i(g_{\tilde{g} q \tilde{q}_j}^L P_L + g_{\tilde{g} q \tilde{q}_j}^R P_R).
\tag{4.86}
$$

The first coupling connects the neutralino, the incoming squark $\tilde{q}_j$ and the outgoing quark, the second one the incoming quark, the outgoing squark $\tilde{q}_i$ and the gluino and the third one the incoming quark, the outgoing squark $\tilde{q}_j$ and the gluino. The two- and three-point functions possess the arguments $B = B(p_a + p_b, m_{\tilde{g}}^2, m_q^2)$ and $C = C(p_b, p_a, m_{\tilde{q}_j}^2, m_{\tilde{g}}^2, m_q^2)$. As before, the u-channel version of this loop coupling is obtained by the replacement $p_a \leftrightarrow -p_1$. As there are no momenta occuring in (4.83), the expression remains unchanged. Hence, we have $I_{\text{V6}}^{L}(s) = I_{\text{V6}}^{L}(u)$, where the two- and three-point functions are now understood as $B = B(-p_1 + p_b, m_{\tilde{g}}^2, m_q^2)$ and $C = C(p_b, -p_1, m_{\tilde{q}_j}^2, m_{\tilde{g}}^2, m_q^2)$.

Vertex correction V7

This vertex is topologically equivalent to V5, but the fermion flow is inverted. We find

$$
\begin{aligned}
I_{\text{V7}}^{L}(s) &= -\frac{\alpha_s C_F}{4\pi}\bigg(2(C_0 + C_1 + C_2)c_1^R m_q m_{\tilde{\chi}_1^0} \\
&\quad - c_1^L(B_0 - 4p_1 p_2 C_2 + 2(C_0 - C_2)m_q^2 + 2C_1 m_{\tilde{\chi}_1^0}^2)\bigg),
\end{aligned}
\tag{4.87}
$$

where $B = B(p_1 + p_2, m_{\tilde{q}_i}^2, 0)$ and $C = C(p_1, p_2, m_q^2, m_{\tilde{q}_i}^2, 0)$. The coupling

$$
i\,\boxed{1} = i(c_1^L P_L + c_1^R P_R) = i(g_{\tilde{\chi}_1^0 \tilde{q}_i q}^L P_L + g_{\tilde{\chi}_1^0 \tilde{q}_i q}^R P_R)
\tag{4.88}
$$

connects the neutralino, the outgoing quark and the incoming squark. The u-channel version of this is obtained via the substitution $p_a \leftrightarrow -p_1$. Hence, we have

$$
\begin{aligned}
I_{\text{V7}}^{L}(u) &= -\frac{\alpha_s C_F}{4\pi}\bigg(2(C_0 + C_1 + C_2)c_1^R m_q m_{\tilde{\chi}_1^0} \\
&\quad - c_1^L(B_0 + 4p_a p_2 C_2 + 2(C_0 - C_2)m_q^2 + 2C_1 m_{\tilde{\chi}_1^0}^2)\bigg),
\end{aligned}
\tag{4.89}
$$

where $B = B(-p_a + p_2, m_{\tilde{q}_i}^2, 0)$ and $C = C(-p_a, p_2, m_q^2, m_{\tilde{q}_i}^2, 0)$.

Vertex correction V8

The last vertex correction to discuss is V8. This correction equals V6 with an inverted fermion flow. We find the loop coupling

$$
\begin{aligned}
I_{\text{V8}}^{L}(s) &= \frac{C_F}{16\pi^2}\bigg(-c_1^R(C_1 c_3^L c_2^R m_q + c_2^L(m_{\tilde{g}}(C_0 + C_1)c_3^L + (C_0 + C_1 + C_2)c_3^R m_q))m_{\tilde{\chi}_1^0} \\
&\quad - c_1^L\big(c_3^R m_q(m_{\tilde{g}}C_2 c_2^R + (C_0 + C_2)c_2^L m_q) \\
&\quad + c_3^L(m_{\tilde{g}}C_0 c_2^L m_q + c_2^R(B_0 + C_2 m_q^2 + C_1 m_{\tilde{\chi}_1^0}^2 + C_0 m_{\tilde{q}_j}^2)))\bigg),
\end{aligned}
\tag{4.90}
$$

with $B = B(p_1 + p_2, m_q^2, m_{\tilde{g}}^2)$ and $C = C(p_1, p_2, m_{\tilde{q}_j}^2, m_q^2, m_{\tilde{g}}^2)$. The couplings accord with those from V6 with inverted fermion flow, i.e.

$$
i\,\boxed{1} = i(c_1^L P_L + c_1^R P_R) = i(g_{\tilde{\chi}_1^0 q \tilde{q}_j}^L P_L + g_{\tilde{\chi}_1^0 q \tilde{q}_j}^R P_R).
\tag{4.91}
$$

$$
i\,\boxed{2} = i(c_2^L P_L + c_2^R P_R) = i(g_{\tilde{g}\tilde{q}_j q}^L P_L + g_{\tilde{g}\tilde{q}_j q}^R P_R).
\tag{4.92}
$$

$$
i\,\boxed{3} = i(c_3^L P_L + c_3^R P_R) = i(g_{\tilde{g}\tilde{q}_i q}^L P_L + g_{\tilde{g}\tilde{q}_i q}^R P_R).
\tag{4.93}
$$

As usual, the loop coupling for the u-channel is obtained by the replacement $p_a \leftrightarrow -p_1$. This leads us to $I_{\text{V8}}^{L}(s) = I_{\text{V8}}^{L}(u)$ with the two-point functions $B = B(-p_a + p_2, m_{\tilde{g}}^2, m_q^2)$ and three-point functions $C = C(-p_a, p_2, m_{\tilde{q}_j}^2, m_{\tilde{g}}^2, m_q^2)$.
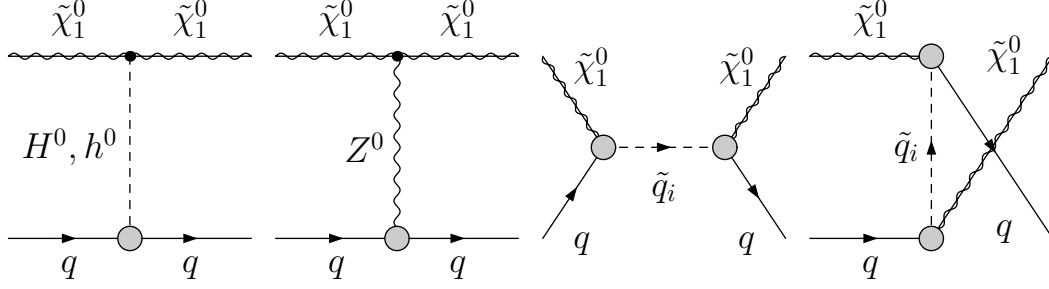
Figure 4.9.: Insertions of the vertex corrections in the tree-level diagrams

Insertion of the vertex corrections

We continue with the insertion of the vertex corrections in the corresponding tree-level processes. As already mentioned, the vertex calculations are performed in a generic, modular approach. In the end, we just replace the tree-level couplings by the corresponding loop couplings. This insertion is illustrated in figure 4.9. We stress that in case of the squark processes T3 and T4 we insert only one vertex correction at a time. Otherwise, we would get a correction of $\mathcal{O}(\alpha_s^2)$.

The calculation of the vertex corrections V1 and V2 has been performed explicitly. These contribute to the spin-independent Wilson coefficient. More precisely, we have

$$\alpha_{q,\text{V1}}^{\text{SI}} = \alpha_{q,\text{T1}}^{\text{SI}}(g_{\phi qq} \to I_{\text{V1}}) \quad \text{and} \quad \alpha_{q,\text{V2}}^{\text{SI}} = \alpha_{q,\text{T1}}^{\text{SI}}\left(g_{\phi qq} \to (I_{\text{V2}}^R + I_{\text{V2}}^L)/2\right). \tag{4.94}$$

In contrast to that, the vertex corrections V3 and V4 contribute to the spin-dependent Wilson coefficient. The replacement rules are

$$\alpha_{q,\text{V3}}^{\text{SD}} = \alpha_{q,\text{T2}}^{\text{SD}}(c_2^{R/L} \to I_{\text{V3}}^{R/L}) \quad \text{and} \quad \alpha_{q,\text{V4}}^{\text{SD}} = \alpha_{q,\text{T2}}^{\text{SD}}(c_2^{R/L} \to I_{\text{V4}}^{R/L}). \tag{4.95}$$

Just like the corresponding tree-level processes, the remaining vertex corrections V5-V8 contribute to the spin-independent and the spin-dependent Wilson coefficient. Furthermore, they can be inserted in both the s- and the u-channel processes T3 and T4. The replacement rules read

$$\alpha_{q,\text{V5}}^{\text{SI}} = \alpha_{q,\text{T3}}^{\text{SI}}(c_1^{R/L} \to I_{\text{V5}}^{R/L}(s)) + \alpha_{q,\text{T4}}^{\text{SI}}(c_1^{R/L} \to I_{\text{V5}}^{R/L}(u)). \tag{4.96}$$

$$\alpha_{q,\text{V5}}^{\text{SD}} = \alpha_{q,\text{T3}}^{\text{SD}}(c_1^{R/L} \to I_{\text{V5}}^{R/L}(s)) + \alpha_{q,\text{T4}}^{\text{SD}}(c_1^{R/L} \to I_{\text{V5}}^{R/L}(u)). \tag{4.97}$$

$$\alpha_{q,\text{V6}}^{\text{SI}} = \alpha_{q,\text{T3}}^{\text{SI}}(c_1^{R/L} \to I_{\text{V6}}^{R/L}(s)) + \alpha_{q,\text{T4}}^{\text{SI}}(c_1^{R/L} \to I_{\text{V6}}^{R/L}(u)). \tag{4.98}$$

$$\alpha_{q,\text{V6}}^{\text{SD}} = \alpha_{q,\text{T3}}^{\text{SD}}(c_1^{R/L} \to I_{\text{V6}}^{R/L}(s)) + \alpha_{q,\text{T4}}^{\text{SD}}(c_1^{R/L} \to I_{\text{V6}}^{R/L}(u)). \tag{4.99}$$

$$\alpha_{q,\text{V7}}^{\text{SI}} = \alpha_{q,\text{T3}}^{\text{SI}}(c_2^{R/L} \to I_{\text{V7}}^{R/L}(s)) + \alpha_{q,\text{T4}}^{\text{SI}}(c_2^{R/L} \to I_{\text{V7}}^{R/L}(u)). \tag{4.100}$$

$$\alpha_{q,\text{V7}}^{\text{SD}} = \alpha_{q,\text{T3}}^{\text{SD}}(c_2^{R/L} \to I_{\text{V7}}^{R/L}(s)) + \alpha_{q,\text{T4}}^{\text{SD}}(c_2^{R/L} \to I_{\text{V7}}^{R/L}(u)). \tag{4.101}$$

$$\alpha_{q,\text{V8}}^{\text{SI}} = \alpha_{q,\text{T3}}^{\text{SI}}(c_2^{R/L} \to I_{\text{V8}}^{R/L}(s)) + \alpha_{q,\text{T4}}^{\text{SI}}(c_2^{R/L} \to I_{\text{V8}}^{R/L}(u)). \tag{4.102}$$

$$\alpha_{q,\text{V8}}^{\text{SD}} = \alpha_{q,\text{T3}}^{\text{SD}}(c_2^{R/L} \to I_{\text{V8}}^{R/L}(s)) + \alpha_{q,\text{T4}}^{\text{SD}}(c_2^{R/L} \to I_{\text{V8}}^{R/L}(u)). \tag{4.103}$$
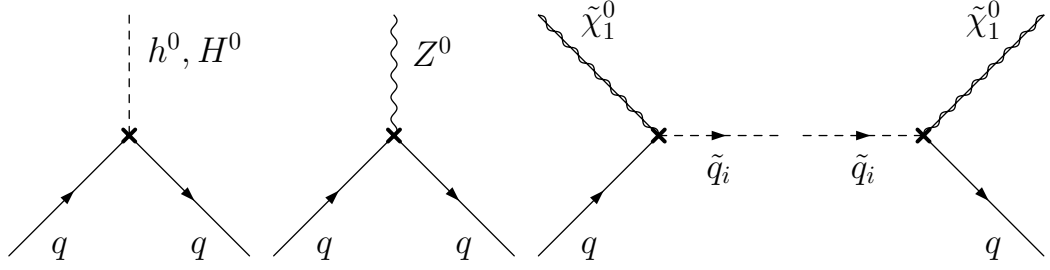
Figure 4.10.: Vertex counterterms for the neutralino-quark four-fermion coupling

4.4.4. Vertex counterterms

In the previous subsection we have demonstrated how to calculate the vertex corrections V1 to V8 and how to cast them into the loop couplings $I_{\mathrm{V1}}^{R/L}$ to $I_{\mathrm{V8}}^{R/L}$. These loop couplings replace the original tree-level couplings $g_{\phi qq}$ (for V1 and V2), $g_{Z^0 qq}$ (for V3 and V4), $g_{\tilde{\chi}_1^0 q \tilde{q}_i}$ (for V5 and V6) and $g_{\tilde{\chi}_1^0 \tilde{q}_i q}$ (for V7 and V8) as given in (4.94) to (4.103). We absorb the involved ultraviolet divergences by adding coupling counterterms in an analogous fashion. More precisely, we include a coupling counterterm for each tree-level coupling mentioned before and refer to them as $\delta g_{\phi qq}$, $\delta g_{Z^0 qq}$, $\delta g_{\tilde{\chi}_1^0 q \tilde{q}_i}$ and $\delta g_{\tilde{\chi}_1^0 \tilde{q}_i q}$. These counterterms are shown in figure 4.10.

We start with the discussion of the counterterms $\delta g_{\phi qq}$ and $\delta g_{Z^0 qq}$ which are simply given by

$$\delta g_{\phi qq}^L = g_{\phi qq}^L \left(\frac{\delta m_q}{m_q} + \frac{1}{2} \delta Z_q^L + \frac{1}{2} \delta Z_q^{R*} \right). \tag{4.104}$$

$$\delta g_{Z^0 qq}^L = g_{Z^0 qq}^L \left(\frac{1}{2} \delta Z_q^L + \frac{1}{2} \delta Z_q^{L*} \right). \tag{4.105}$$

Here δm_q denotes the counterterm for the quark mass and δZ_q the counterterm for the quark spinor field which is decomposed into its left- and right-handed part as usual. The associated right-handed parts are obtained by the replacement $L \leftrightarrow R$. We stress that the vertex correction V1 including the gluon is ultraviolet divergent, whereas its supersymmetric counterpart V2 including the gluino is ultraviolet finite. On the other hand, both of the Z^0 vertex corrections V3 and V4 are ultraviolet divergent. This is mirrored by the associated counterterms. When replacing $g_{\phi qq} \to (\delta g_{\phi qq}^R + \delta g_{\phi qq}^L)/2$ in the tree-level diagram T1, all divergent terms are of gluonic, i.e. Standard Model origin. In contrast to that, supersymmetric corrections contribute to the divergent part when replacing $c_2^{R/L} \to \delta g_{Z^0 qq}^{R/L}$ in the tree-level diagram T2. We return to this issue when matching the full theory onto the effective theory (cf. section 4.5).

The counterterms $\delta g_{\tilde{\chi}_1^0 q \tilde{q}_i}$ and $\delta g_{\tilde{\chi}_1^0 \tilde{q}_i q}$ are much lengthier and include several parameters introduced in chapter 2. In particular, we encounter the 4×4 neutralino mixing matrix N and the 2×2 squark mixing matrix $U^{\tilde{q}}$. The latter has to be renormalised and its associated counterterm reads $\delta U^{\tilde{q}}$. Having all the ingredients at hand, the counterterms

$\delta g_{\tilde{\chi}_1^0 q\tilde{q}_i}$ and $\delta g_{\tilde{\chi}_1^0 \tilde{q}_i q}$ for up-type quarks can be written as

$$
\begin{aligned}
\delta g^L_{\tilde{\chi}_1^0 q\tilde{q}_i} &= \frac{-eN_{14}^* \left(\delta m_q U_{i2}^{\tilde{q}} + m_q \delta U_{i2}^{\tilde{q}}\right)}{\sqrt{2}\sin\theta_W \sin\beta m_{W^\pm}} - \frac{\sqrt{2}e}{\sin\theta_W}\left((e_q - I_3)\tan\theta_W N_{11}^* + I_3 N_{12}^*\right)\delta U_{i1}^{\tilde{q}} \\
&\quad + \frac{1}{2}g^L_{\tilde{\chi}_1^0 q\tilde{q}_1}\delta Z_{\tilde{q}}^{1i} + \frac{1}{2}g^L_{\tilde{\chi}_1^0 q\tilde{q}_2}\delta Z_{\tilde{q}}^{2i} + \frac{1}{2}g^L_{\tilde{\chi}_1^0 q\tilde{q}_i}\delta Z_q^L.
\end{aligned} \tag{4.106}
$$

$$
\begin{aligned}
\delta g^R_{\tilde{\chi}_1^0 q\tilde{q}_i} &= \frac{-eN_{14} \left(\delta m_q U_{i1}^{\tilde{q}} + m_q \delta U_{i1}^{\tilde{q}}\right)}{\sqrt{2}\sin\theta_W \sin\beta m_{W^\pm}} + \frac{\sqrt{2}ee_q}{\cos\theta_W} N_{11}\delta U_{i2}^{\tilde{q}} \\
&\quad + \frac{1}{2}g^R_{\tilde{\chi}_1^0 q\tilde{q}_1}\delta Z_{\tilde{q}}^{1i} + \frac{1}{2}g^R_{\tilde{\chi}_1^0 q\tilde{q}_2}\delta Z_{\tilde{q}}^{2i} + \frac{1}{2}g^R_{\tilde{\chi}_1^0 q\tilde{q}_i}\delta Z_q^R.
\end{aligned} \tag{4.107}
$$

$$
\begin{aligned}
\delta g^L_{\tilde{\chi}_1^0 \tilde{q}_i q} &= \frac{-eN_{14}^* \left(\delta m_q U_{i1}^{\tilde{q}} + m_q \delta U_{i1}^{\tilde{q}}\right)}{\sqrt{2}\sin\theta_W \sin\beta m_{W^\pm}} + \frac{\sqrt{2}ee_q}{\cos\theta_W} N_{11}^*\delta U_{i2}^{\tilde{q}} \\
&\quad + \frac{1}{2}g^L_{\tilde{\chi}_1^0 \tilde{q}_1 q}\delta Z_{\tilde{q}}^{1i} + \frac{1}{2}g^L_{\tilde{\chi}_1^0 \tilde{q}_2 q}\delta Z_{\tilde{q}}^{2i} + \frac{1}{2}g^L_{\tilde{\chi}_1^0 \tilde{q}_i q}\delta Z_q^{R*}.
\end{aligned} \tag{4.108}
$$

$$
\begin{aligned}
\delta g^R_{\tilde{\chi}_1^0 \tilde{q}_i q} &= \frac{-eN_{14} \left(\delta m_q U_{i2}^{\tilde{q}} + m_q \delta U_{i2}^{\tilde{q}}\right)}{\sqrt{2}\sin\theta_W \sin\beta m_{W^\pm}} - \frac{\sqrt{2}e}{\sin\theta_W}\left((e_q - I_3)\tan\theta_W N_{11} + I_3 N_{12}\right)\delta U_{i1}^{\tilde{q}} \\
&\quad + \frac{1}{2}g^R_{\tilde{\chi}_1^0 \tilde{q}_1 q}\delta Z_{\tilde{q}}^{1i} + \frac{1}{2}g^R_{\tilde{\chi}_1^0 \tilde{q}_2 q}\delta Z_{\tilde{q}}^{2i} + \frac{1}{2}g^R_{\tilde{\chi}_1^0 \tilde{q}_i q}\delta Z_q^{L*}.
\end{aligned} \tag{4.109}
$$

For down-type quarks, these counterterms are given by

$$
\begin{aligned}
\delta g^L_{\tilde{\chi}_1^0 q\tilde{q}_i} &= \frac{-eN_{13}^* \left(\delta m_q U_{i2}^{\tilde{q}} + m_q \delta U_{i2}^{\tilde{q}}\right)}{\sqrt{2}\sin\theta_W \cos\beta m_{W^\pm}} - \frac{\sqrt{2}e}{\sin\theta_W}\left((e_q - I_3)\tan\theta_W N_{11}^* + I_3 N_{12}^*\right)\delta U_{i1}^{\tilde{q}} \\
&\quad + \frac{1}{2}g^L_{\tilde{\chi}_1^0 q\tilde{q}_1}\delta Z_{\tilde{q}}^{1i} + \frac{1}{2}g^L_{\tilde{\chi}_1^0 q\tilde{q}_2}\delta Z_{\tilde{q}}^{2i} + \frac{1}{2}g^L_{\tilde{\chi}_1^0 q\tilde{q}_i}\delta Z_q^L.
\end{aligned} \tag{4.110}
$$

$$
\begin{aligned}
\delta g^R_{\tilde{\chi}_1^0 q\tilde{q}_i} &= \frac{-eN_{13} \left(\delta m_q U_{i1}^{\tilde{q}} + m_q \delta U_{i1}^{\tilde{q}}\right)}{\sqrt{2}\sin\theta_W \cos\beta m_{W^\pm}} + \frac{\sqrt{2}ee_q}{\cos\theta_W} N_{11}\delta U_{i2}^{\tilde{q}} \\
&\quad + \frac{1}{2}g^R_{\tilde{\chi}_1^0 q\tilde{q}_1}\delta Z_{\tilde{q}}^{1i} + \frac{1}{2}g^R_{\tilde{\chi}_1^0 q\tilde{q}_2}\delta Z_{\tilde{q}}^{2i} + \frac{1}{2}g^R_{\tilde{\chi}_1^0 q\tilde{q}_i}\delta Z_q^R.
\end{aligned} \tag{4.111}
$$

$$
\begin{aligned}
\delta g^L_{\tilde{\chi}_1^0 \tilde{q}_i q} &= \frac{-eN_{13}^* \left(\delta m_q U_{i1}^{\tilde{q}} + m_q \delta U_{i1}^{\tilde{q}}\right)}{\sqrt{2}\sin\theta_W \cos\beta m_{W^\pm}} + \frac{\sqrt{2}ee_q}{\cos\theta_W} N_{11}^*\delta U_{i2}^{\tilde{q}} \\
&\quad + \frac{1}{2}g^L_{\tilde{\chi}_1^0 \tilde{q}_1 q}\delta Z_{\tilde{q}}^{1i} + \frac{1}{2}g^L_{\tilde{\chi}_1^0 \tilde{q}_2 q}\delta Z_{\tilde{q}}^{2i} + \frac{1}{2}g^L_{\tilde{\chi}_1^0 \tilde{q}_i q}\delta Z_q^{R*}.
\end{aligned} \tag{4.112}
$$

$$
\begin{aligned}
\delta g^R_{\tilde{\chi}_1^0 \tilde{q}_i q} &= \frac{-eN_{13} \left(\delta m_q U_{i2}^{\tilde{q}} + m_q \delta U_{i2}^{\tilde{q}}\right)}{\sqrt{2}\sin\theta_W \cos\beta m_{W^\pm}} - \frac{\sqrt{2}e}{\sin\theta_W}\left((e_q - I_3)\tan\theta_W N_{11} + I_3 N_{12}\right)\delta U_{i1}^{\tilde{q}} \\
&\quad + \frac{1}{2}g^R_{\tilde{\chi}_1^0 \tilde{q}_1 q}\delta Z_{\tilde{q}}^{1i} + \frac{1}{2}g^R_{\tilde{\chi}_1^0 \tilde{q}_2 q}\delta Z_{\tilde{q}}^{2i} + \frac{1}{2}g^R_{\tilde{\chi}_1^0 \tilde{q}_i q}\delta Z_q^{L*}.
\end{aligned} \tag{4.113}
$$

Note that we have included the squark wave function counterterm again. As described in subsection 4.4.2, the final result is independent of this counterterm, but the intermediate inclusion allows to separately check the ultraviolet finiteness of the propagator and vertex corrections.
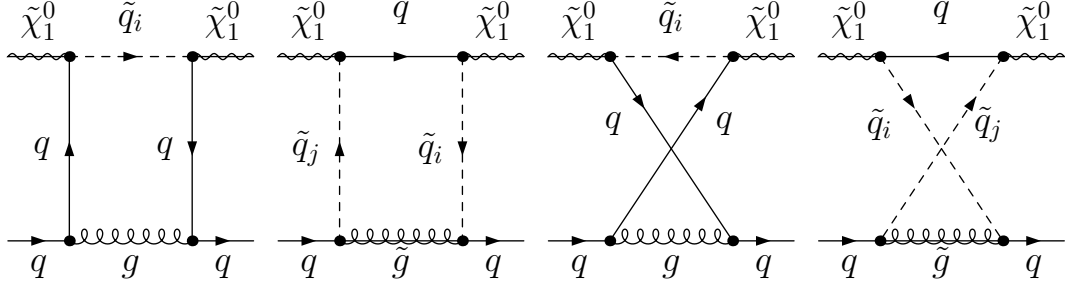
Figure 4.11.: Box contributions to the neutralino-quark four-fermion coupling

The vertex counterterms are inserted in the tree-level processes via

$$\alpha_{q,\text{VC1}}^{\text{SI}} = \alpha_{q,\text{T1}}^{\text{SI}}\left(g_{\phi qq} \to (\delta g_{\phi qq}^R + \delta g_{\phi qq}^L)/2\right). \tag{4.114}$$

$$\alpha_{q,\text{VC2}}^{\text{SD}} = \alpha_{q,\text{T2}}^{\text{SD}}(c_2^{R/L} \to \delta g_{Z^0 qq}^{R/L}). \tag{4.115}$$

$$\alpha_{q,\text{VC3}}^{\text{SI}} = \alpha_{q,\text{T3}}^{\text{SI}}(c_1^{R/L} \to \delta g_{\tilde\chi_1^0 q\tilde q_i}^{R/L}) + \alpha_{q,\text{T4}}^{\text{SI}}(c_1^{R/L} \to \delta g_{\tilde\chi_1^0 q\tilde q_i}^{R/L}). \tag{4.116}$$

$$\alpha_{q,\text{VC3}}^{\text{SD}} = \alpha_{q,\text{T3}}^{\text{SD}}(c_1^{R/L} \to \delta g_{\tilde\chi_1^0 q\tilde q_i}^{R/L}) + \alpha_{q,\text{T4}}^{\text{SD}}(c_1^{R/L} \to \delta g_{\tilde\chi_1^0 q\tilde q_i}^{R/L}). \tag{4.117}$$

$$\alpha_{q,\text{VC4}}^{\text{SI}} = \alpha_{q,\text{T3}}^{\text{SI}}(c_2^{R/L} \to \delta g_{\tilde\chi_1^0 \tilde q_i q}^{R/L}) + \alpha_{q,\text{T4}}^{\text{SI}}(c_2^{R/L} \to \delta g_{\tilde\chi_1^0 \tilde q_i q}^{R/L}). \tag{4.118}$$

$$\alpha_{q,\text{VC4}}^{\text{SD}} = \alpha_{q,\text{T3}}^{\text{SD}}(c_2^{R/L} \to \delta g_{\tilde\chi_1^0 \tilde q_i q}^{R/L}) + \alpha_{q,\text{T4}}^{\text{SD}}(c_2^{R/L} \to \delta g_{\tilde\chi_1^0 \tilde q_i q}^{R/L}). \tag{4.119}$$

4.4.5. Box contributions

In this subsection we discuss the box contributions to the neutralino-quark four-fermion coupling. In contrast to e.g. the vertex corrections, the box contributions are not contained in previous `DM@NLO` subprojects. Therefore, we present how to calculate them from scratch at this point. The corresponding Feynman diagrams are shown in figure 4.11. From left to right we refer to these box processes as B1, B2, B3 and B4. The colour algebra is the same for all four processes. More precisely, all amplitudes carry a colour factor of $C_F = 4/3$. We sum over all internal squark types when finally including these corrections.

Box B1

We start with the box B1 shown on the very left in figure 4.11. As usual, we label the initial four-momenta p_a and p_b and the final four-momenta p_1 and p_2. Starting with the neutralino-quark-squark coupling in the upper left, we clockwise label the couplings $i\boxed{1}$, $i\boxed{2}$ and $i\boxed{3}$ and $i\boxed{4}$. For the quark-gluon couplings we plug in its precise form.

$$i\boxed{1} = i(c_1^L P_L + c_1^R P_R) = i(g_{\tilde\chi_1^0 q\tilde q_i}^L P_L + g_{\tilde\chi_1^0 q\tilde q_i}^R P_R). \tag{4.120}$$

$$i\boxed{2} = i(c_2^L P_L + c_2^R P_R) = i(g_{\tilde\chi_1^0 \tilde q_i q}^L P_L + g_{\tilde\chi_1^0 \tilde q_i q}^R P_R). \tag{4.121}$$

$$i\gamma^\mu\boxed{3} = i\gamma^\mu(c_3^L P_L + c_3^R P_R) = -i\gamma^\mu g_s. \tag{4.122}$$

$$i\gamma^\nu\boxed{4} = i\gamma^\nu(c_4^L P_L + c_4^R P_R) = -i\gamma^\nu g_s. \tag{4.123}$$

We label the four-momentum of the gluon q and define it to be flowing from the right to the left. Using dimensional reduction (cf. chapter F), the amplitude can then be written

as

$$
\begin{aligned}
i\mathcal{M}_{\mathrm{B1}} &= C_F\mu^{4-D}\int\frac{\mathrm{d}^D q}{(2\pi)^D}\left[\bar{u}(p_2)i\gamma^\mu\boxed{3}\,i\frac{\slashed{q}+\slashed{p}_2+m_q}{(q+p_2)^2-m_q^2}i\boxed{2}v(p_1)\right]\left(\frac{-ig_{\mu\nu}}{q^2}\right) \\
&\quad\left(\frac{i}{(q+p_a+p_b)^2-m_{\tilde{q}_i}^2}\right)\left[\bar{v}(p_a)i\boxed{1}\,i\frac{\slashed{q}+\slashed{p}_b+m_q}{(q+p_b)^2-m_q^2}i\gamma^\nu\boxed{4}u(p_b)\right] \\
&= -i\frac{\alpha_s C_F}{4\pi}\frac{(2\pi\mu)^{4-D}}{i\pi^2}\int\mathrm{d}^D q\{\mathcal{D}_0\mathcal{D}_1\mathcal{D}_2\mathcal{D}_3\}^{-1} \\
&\quad\left[\bar{u}(p_2)\gamma^\mu(\slashed{q}+\slashed{p}_2+m_q)\boxed{2}v(p_1)\right]\left[\bar{v}(p_a)\boxed{1}(\slashed{q}+\slashed{p}_b+m_q)\gamma_\mu u(p_b)\right], \quad (4.124)
\end{aligned}
$$

where we used $\alpha_s=\frac{g_s^2}{4\pi}$ and introduced the denominators $\mathcal{D}_0,\mathcal{D}_1,\mathcal{D}_2$ and $\mathcal{D}_3$ given by

$$
\mathcal{D}_0=q^2,\ \mathcal{D}_1=(q+p_a+p_b)^2-m_{\tilde{q}_i}^2,\ \mathcal{D}_2=(q+p_2)^2-m_q^2,\ \text{and}\ \mathcal{D}_3=(q+p_b)^2-m_q^2. \quad (4.125)
$$

We can freely choose to reorder the denominators and exchange e.g. $\mathcal{D}_0\leftrightarrow\mathcal{D}_2$. What really matters is to keep track of the corresponding rotation of the arguments inside the four-point functions. This is especially important for the tensor integrals (cf. section F.4). For the choice above we get four-point functions of the form $D(p_a+p_b,p_2,p_b,0,m_{\tilde{q}_i}^2,m_q^2,m_q^2)$.

The amplitude given in (4.124) contains terms proportional to q^0,q^ρ and $q^\rho q^\sigma$ which in turn lead to the four-point functions D_0,D_ρ and $D_{\rho\sigma}$. For the definition of the tensor integrals D_ρ and $D_{\rho\sigma}$ we refer to section F.4 and in particular (F.76) and (F.77). We obtain

$$
\begin{aligned}
\mathcal{M}_{\mathrm{B1}} &= -\frac{\alpha_s C_F}{4\pi}D_0\left[\bar{u}(p_2)\gamma^\mu(\slashed{p}_2+m_q)\boxed{2}v(p_1)\right]\left[\bar{v}(p_a)\boxed{1}(\slashed{p}_b+m_q)\gamma_\mu u(p_b)\right] \\
&\quad -\frac{\alpha_s C_F}{4\pi}D_\rho\Bigg(\left[\bar{u}(p_2)\gamma^\mu\gamma^\rho\boxed{2}v(p_1)\right]\left[\bar{v}(p_a)\boxed{1}(\slashed{p}_b+m_q)\gamma_\mu u(p_b)\right] \\
&\quad +\left[\bar{u}(p_2)\gamma^\mu(\slashed{p}_2+m_q)\boxed{2}v(p_1)\right]\left[\bar{v}(p_a)\boxed{1}\gamma^\rho\gamma_\mu u(p_b)\right]\Bigg) \\
&\quad -\frac{\alpha_s C_F}{4\pi}D_{\rho\sigma}\left[\bar{u}(p_2)\gamma^\mu\gamma^\rho\boxed{2}v(p_1)\right]\left[\bar{v}(p_a)\boxed{1}\gamma^\sigma\gamma_\mu u(p_b)\right]. \quad (4.126)
\end{aligned}
$$

The next step is to simplify these expressions using the Dirac algebra presented in chapter C and the Dirac equation. In the present case we have for example

$$
\bar{u}(p_2)\slashed{p}_2=m_q\bar{u}(p_2) \qquad \text{and} \qquad \slashed{p}_b u(p_b)=m_q u(p_b). \quad (4.127)
$$

$$
\bar{v}(p_a)\slashed{p}_a=-m_{\tilde{\chi}_1^0}\bar{v}(p_a) \qquad \text{and} \qquad \slashed{p}_1 v(p_1)=-m_{\tilde{\chi}_1^0}v(p_1). \quad (4.128)
$$

We perform this calculation for the term following D_0.

$$
\left[\bar{u}(p_2)\gamma^\mu(\not{p}_2 + m_q)\boxed{2}v(p_1)\right]\left[\bar{v}(p_a)\boxed{1}(\not{p}_b + m_q)\gamma_\mu u(p_b)\right]
$$

$$
= \left[\bar{u}(p_2)\gamma^\mu\boxed{2}v(p_1)\right]\left[\bar{v}(p_a)\boxed{1}\gamma_\mu u(p_b)\right]m_q^2 + \left[\bar{u}(p_2)\gamma^\mu\not{p}_2\boxed{2}v(p_1)\right]\left[\bar{v}(p_a)\boxed{1}\gamma_\mu u(p_b)\right]m_q
$$

$$
+ \left[\bar{u}(p_2)\gamma^\mu\boxed{2}v(p_1)\right]\left[\bar{v}(p_a)\boxed{1}\not{p}_b\gamma_\mu u(p_b)\right]m_q + \left[\bar{u}(p_2)\gamma^\mu\not{p}_2\boxed{2}v(p_1)\right]\left[\bar{v}(p_a)\boxed{1}\not{p}_b\gamma_\mu u(p_b)\right]
$$

$$
= \left[\bar{u}(p_2)\gamma^\mu\boxed{2}v(p_1)\right]\left[\bar{v}(p_a)\boxed{1}\gamma_\mu u(p_b)\right]m_q^2
$$

$$
+ \left[\bar{u}(p_2)(-m_q\gamma^\mu + 2p_2^\mu)\boxed{2}v(p_1)\right]\left[\bar{v}(p_a)\boxed{1}\gamma_\mu u(p_b)\right]m_q
$$

$$
+ \left[\bar{u}(p_2)\gamma^\mu\boxed{2}v(p_1)\right]\left[\bar{v}(p_a)\boxed{1}(-m_q\gamma_\mu + 2p_{b,\mu})u(p_b)\right]m_q
$$

$$
+ \left[\bar{u}(p_2)(-m_q\gamma^\mu + 2p_2^\mu)\boxed{2}v(p_1)\right]\left[\bar{v}(p_a)\boxed{1}(-m_q\gamma_\mu + 2p_{b,\mu})u(p_b)\right].
$$

$$
= 4p_2 \cdot p_b\left[\bar{u}(p_2)\boxed{2}v(p_1)\right]\left[\bar{v}(p_a)\boxed{1}u(p_b)\right]. \tag{4.129}
$$

Interestingly, all terms of vector and axial-vector type cancel out in this case. We proceed by identifying the spinors $\bar{u}(p_2), v(p_1), \bar{v}(p_a)$ and $u(p_b)$ with their corresponding spinor fields $\bar{q}, \chi, \bar{\chi}$ and q. As usual, we keep only the relevant effective operators and obtain

$$
\begin{aligned}
4p_2 \cdot p_b[\bar{q}\boxed{2}\chi][\bar{\chi}\boxed{1}q] &= p_2 \cdot p_b(c_2^R - c_2^L)(c_1^R - c_1^L)[\bar{q}\gamma_5\chi][\bar{\chi}\gamma_5 q] \\
&+ p_2 \cdot p_b(c_2^R + c_2^L)(c_1^R + c_1^L)[\bar{q}\chi][\bar{\chi}q].
\end{aligned} \tag{4.130}
$$

Just like in the squark tree-level processes discussed in subsection 4.3.3, the spinor fields are in wrong order and we have to perform a Fierz transformation. Using table D.4 leads to

$$
\begin{aligned}
&p_2 \cdot p_b(c_2^R - c_2^L)(c_1^R - c_1^L)[\bar{q}\gamma_5\chi][\bar{\chi}\gamma_5 q] + p_2 \cdot p_b(c_2^R + c_2^L)(c_1^R + c_1^L)[\bar{q}\chi][\bar{\chi}q] \\
=\ &\frac{p_2 \cdot p_b}{4}(c_2^R - c_2^L)(c_1^R - c_1^L)\left(-[\bar{\chi}\chi][\bar{q}q] - [\bar{\chi}\gamma_5\gamma^\mu\chi][\bar{q}\gamma_5\gamma_\mu q]\right) \\
+\ &\frac{p_2 \cdot p_b}{4}(c_2^R + c_2^L)(c_1^R + c_1^L)\left(-[\bar{\chi}\chi][\bar{q}q] + [\bar{\chi}\gamma_5\gamma^\mu\chi][\bar{q}\gamma_5\gamma_\mu q]\right).
\end{aligned} \tag{4.131}
$$

Therefore, the spin-independent and spin-dependent contributions of the first term of (4.126) to α_q^{SI} and α_q^{SD} are

$$
\begin{aligned}
\alpha_q^{\text{SI}} &= \frac{\alpha_s C_F D_0 p_2 \cdot p_b}{16\pi}\left((c_2^R - c_2^L)(c_1^R - c_1^L) + (c_2^R + c_2^L)(c_1^R + c_1^L)\right) \\
&= \frac{\alpha_s C_F D_0 p_2 \cdot p_b}{8\pi}\left(c_2^R c_1^R + c_2^L c_1^L\right).
\end{aligned} \tag{4.132}
$$

$$
\begin{aligned}
\alpha_q^{\text{SD}} &= \frac{\alpha_s C_F D_0 p_2 \cdot p_b}{16\pi}\left((c_2^R - c_2^L)(c_1^R - c_1^L) - (c_2^R + c_2^L)(c_1^R + c_1^L)\right) \\
&= -\frac{\alpha_s C_F D_0 p_2 \cdot p_b}{8\pi}\left(c_2^R c_1^L + c_2^L c_1^R\right).
\end{aligned} \tag{4.133}
$$

Note that this is just the part of (4.126) proportional to D_0. The calculations for the remaining two terms including D_ρ and $D_{\rho\sigma}$ are completely analogous but much lengthier. Therefore, a `Mathematica` script was written to determine the box contributions to α_q^{SI} and α_q^{SD}. This script automatically performs the steps above. The simplification of the

amplitudes is performed with `FeynCalc` [178]. The final result for B1 in the non-relativistic limit[15] is

$$
\begin{aligned}
\alpha_{q,\text{B1}}^{\text{SI}} &= \frac{\alpha_s C_F}{8\pi} \Big((c_2^R c_1^L + c_2^L c_1^R) m_q m_{\tilde{\chi}_1^0} (-D_1 + D_{11} + D_{12} + D_{13}) \\
&+ 4c_1^L c_2^L D_{00} + c_1^L c_2^L D_{11} m_{\tilde{\chi}_1^0}^2 + 4c_1^R c_2^R D_{00} + c_1^R c_2^R D_{11} m_{\tilde{\chi}_1^0}^2 \\
&+ c_1^L c_2^L (D_1 + D_{11} + 2D_{12} + 2D_{13} + D_2 + D_{22} + 2D_{23} + D_3 + D_{33}) m_q^2 \\
&+ c_1^R c_2^R (D_1 + D_{11} + 2D_{12} + 2D_{13} + D_2 + D_{22} + 2D_{23} + D_3 + D_{33}) m_q^2 \\
&+ D_0 (c_2^L c_1^L + c_2^R c_1^R) p_2 \cdot p_b \Big). \tag{4.134}
\end{aligned}
$$

$$
\begin{aligned}
\alpha_{q,\text{B1}}^{\text{SD}} &= -\frac{\alpha_s C_F}{16\pi} \Big(-2D_1 c_1^R c_2^R m_q m_{\tilde{\chi}_1^0} + 2c_1^R c_2^L D_{00} + c_1^R c_2^L D_{11} m_{\tilde{\chi}_1^0}^2 \\
&- 2D_1 c_1^L c_2^L m_q m_{\tilde{\chi}_1^0} + 2c_1^L c_2^R D_{00} + c_1^L c_2^R D_{11} m_{\tilde{\chi}_1^0}^2 \\
&+ c_1^R c_2^L m_q^2 (2D_1 + D_{11} + 2D_{12} + 2D_{13} + 2D_2 + D_{22} + 2D_{23} + 2D_3 + D_{33}) \\
&+ c_1^L c_2^R m_q^2 (2D_1 + D_{11} + 2D_{12} + 2D_{13} + 2D_2 + D_{22} + 2D_{23} + 2D_3 + D_{33}) \\
&+ 2D_0 (c_2^R c_1^L + c_2^L c_1^R) p_2 \cdot p_b \Big). \tag{4.135}
\end{aligned}
$$

Considering the impressive length of the intermediate results, these expressions are surprisingly compact and have several interesting features. Firstly, we reencounter the terms proportional to D_0 as given in (4.132) and (4.133). We also observe two symmetries, namely $\boxed{1} \leftrightarrow \boxed{2}$ and $R \leftrightarrow L$. Moreover, we stress that only certain combinations of tensor coefficients appear. For example D_1 may appear isolated, but D_2 appears only in combination with D_3, i.e. we encounter only the sum $D_2 + D_3$. The same holds true for the combinations $D_{12} + D_{13}$ and $D_{22} + 2D_{23} + D_{33}$. The reason behind that is discussed in the context of tensor reduction for vanishing Gram determinant (cf. section F.5).

Box B2

The procedure for the gluino box B2 is completely analogous. As this box can be seen as the supersymmetric counterpart to B1, all fermions inside the loop are transformed to bosons and vice versa (cf. figure 4.11). Starting from the upper left, we clockwise label the couplings as

$$
\begin{aligned}
i\boxed{1} &= i(c_1^L P_L + c_1^R P_R) = i(g_{\tilde{\chi}_1^0 \tilde{q}_j q}^L P_L + g_{\tilde{\chi}_1^0 \tilde{q}_j q}^R P_R). \tag{4.136} \\
i\boxed{2} &= i(c_2^L P_L + c_2^R P_R) = i(g_{\tilde{\chi}_1^0 q \tilde{q}_i}^L P_L + g_{\tilde{\chi}_1^0 q \tilde{q}_i}^R P_R). \tag{4.137} \\
i\boxed{3} &= i(c_3^L P_L + c_3^R P_R) = i(g_{\tilde{g} \tilde{q}_i q}^L P_L + g_{\tilde{g} \tilde{q}_i q}^R P_R). \tag{4.138} \\
i\boxed{4} &= i(c_4^L P_L + c_4^R P_R) = i(g_{\tilde{g} q \tilde{q}_j}^L P_L + g_{\tilde{g} q \tilde{q}_j}^R P_R). \tag{4.139}
\end{aligned}
$$

---

[15]Special care is needed when sorting out irrelevant effective operators of the amplitudes of B1 and B3 in the limit $v \to 0$. It may happen that seemingly irrelevant operators become relevant in this limit. One important example is the expression $[\bar{u}(p_2)v(p_1)][\bar{v}(p_a)\not{p}_2 u(p_b)]$ which can not be simplified further in general. However, if $v = 0$ we have $p_2 = p_b$ and hence $[\bar{u}(p_2)v(p_1)][\bar{v}(p_a)\not{p}_2 u(p_b)] = [\bar{u}(p_2)v(p_1)][\bar{v}(p_a)\not{p}_b u(p_b)] = m_q[\bar{u}(p_2)v(p_1)][\bar{v}(p_a)(p_b)]$ which is nothing but the effective operator of scalar type. The results given above are correct for $v = 0$. The same calculation has been performed for $v \neq 0$ with a second `Mathematica` script. Both results are implemented in the code to allow for consistency checks. In case of the boxes B2 and B4 these problems do not occur and sorting out effective operators is relatively straightforward.

In contrast to B1, there are no vector couplings as the vector boson, the gluon, is replaced by a fermion, the gluino. The gluino momentum q is flowing from the left to the right. The amplitude reads

$$
\begin{aligned}
i\mathcal{M}_{\mathrm{B2}} &= C_F\mu^{4-D}\int\frac{\mathrm{d}^D q}{(2\pi)^D}\left[\bar{u}(p_2)i\boxed{3}i\frac{\slashed{q}+m_{\tilde{g}}}{q^2-m_{\tilde{g}}^2}i\boxed{4}u(p_b)\right]\left(\frac{i}{(q-p_b)^2-m_{\tilde{q}_j}^2}\right)\\
&\quad\left(\frac{i}{(q-p_2)^2-m_{\tilde{q}_i}^2}\right)\left[\bar{u}(p_1)i\boxed{2}i\frac{-\slashed{q}+\slashed{p}_a+\slashed{p}_b+m_q}{(-q+p_a+p_b)^2-m_q^2}i\boxed{1}u(p_a)\right]\\
&= \frac{iC_F}{16\pi^2}D_0\left[\bar{u}(p_2)\boxed{3}m_{\tilde{g}}\boxed{4}u(p_b)\right]\left[\bar{u}(p_1)\boxed{2}(\slashed{p}_a+\slashed{p}_b+m_q)\boxed{1}u(p_a)\right]\\
&\quad + \frac{i}{16\pi^2}D_\rho\Bigg(\left[\bar{u}(p_2)\boxed{3}\gamma^\rho\boxed{4}u(p_b)\right]\left[\bar{u}(p_1)\boxed{2}(\slashed{p}_a+\slashed{p}_b+m_q)\boxed{1}u(p_a)\right]\\
&\quad + \left[\bar{u}(p_2)\boxed{3}m_{\tilde{g}}\boxed{4}u(p_b)\right]\left[\bar{u}(p_1)\boxed{2}(-\gamma^\rho)\boxed{1}u(p_a)\right]\Bigg)\\
&\quad + \frac{i}{16\pi^2}D_{\rho\sigma}\left[\bar{u}(p_2)\boxed{3}\gamma^\rho\boxed{4}u(p_b)\right]\left[\bar{u}(p_1)\boxed{2}(-\gamma^\sigma)\boxed{1}u(p_a)\right],
\end{aligned}
\tag{4.140}
$$

where the four-point functions are understood as $D(-p_2, -p_b, -p_a-p_b, m_{\tilde{g}}^2, m_{\tilde{q}_i}^2, m_{\tilde{q}_j}^2, m_q^2)$. This result is transferred to the `Mathematica` program mentioned before to perform the actual evaluation. As the spinors and corresponding spinor fields are already in desired order, we can skip the Fierz transformation. The final result is

$$
\begin{aligned}
\alpha_{q,\mathrm{B2}}^{\mathrm{SI}} &= \frac{C_F}{64\pi^2}\Big(m_q m_{\tilde{g}}D_0(c_1^L c_2^L c_3^R c_4^R + c_1^L c_2^L c_3^L c_4^L + c_1^R c_2^R c_3^R c_4^R + c_1^R c_2^R c_3^L c_4^L)\\
&\quad - m_q^2\,(D_1+D_2+D_3)\,(c_1^L c_2^L c_3^R c_4^L + c_1^L c_2^L c_3^L c_4^R + c_1^R c_2^R c_3^R c_4^L + c_1^R c_2^R c_3^L c_4^R)\\
&\quad + m_{\tilde{g}}m_{\tilde{\chi}_1^0}\,(D_0+D_3)\,(c_1^R c_2^L c_3^L c_4^L + c_1^L c_2^R c_3^L c_4^L + c_1^R c_2^L c_3^R c_4^R + c_1^L c_2^R c_3^R c_4^R)\\
&\quad - m_q m_{\tilde{\chi}_1^0}(D_1+D_{13}+D_2+D_{23}+D_3+D_{33})\\
&\quad\ \ (c_1^R c_2^L c_3^L c_4^R + c_1^L c_2^R c_3^L c_4^R + c_1^R c_2^L c_3^R c_4^L + c_1^L c_2^R c_3^R c_4^L)\Big).
\end{aligned}
\tag{4.141}
$$

$$
\alpha_{q,\mathrm{B2}}^{\mathrm{SD}} = \frac{C_F}{64\pi^2}D_{00}\Big(-c_1^R c_2^L c_3^L c_4^R + c_1^L c_2^R c_3^L c_4^R + c_1^R c_2^L c_3^R c_4^L - c_1^L c_2^R c_3^R c_4^L\Big).
\tag{4.142}
$$

The spin-dependent result is really short and contains only terms proportional to D_{00}. It is symmetric under $R\leftrightarrow L$ and antisymmetric under $\boxed{1}\leftrightarrow\boxed{2}$ and $\boxed{3}\leftrightarrow\boxed{4}$. In contrast to that the spin-independent counterpart is symmetric under $R\leftrightarrow L$, $\boxed{1}\leftrightarrow\boxed{2}$ and $\boxed{3}\leftrightarrow\boxed{4}$.

Box B3

We continue with the calculation of box B3, the twisted gluon box. Starting in the upper left, the couplings are clockwise named $i\boxed{1}$, $i\boxed{2}$ and $i\boxed{3}$ and $i\boxed{4}$.

$$
i\boxed{1} = i(c_1^L P_L + c_1^R P_R) = i(g_{\tilde{\chi}_1^0\tilde{q}_i q}^L P_L + g_{\tilde{\chi}_1^0\tilde{q}_i q}^R P_R).
\tag{4.143}
$$

$$
i\boxed{2} = i(c_2^L P_L + c_2^R P_R) = i(g_{\tilde{\chi}_1^0 q\tilde{q}_i}^L P_L + g_{\tilde{\chi}_1^0 q\tilde{q}_i}^R P_R).
\tag{4.144}
$$

$$
i\gamma^\mu\boxed{3} = i\gamma^\mu(c_3^L P_L + c_3^R P_R) = -i\gamma^\mu g_s.
\tag{4.145}
$$

$$
i\gamma^\nu\boxed{4} = i\gamma^\nu(c_4^L P_L + c_4^R P_R) = -i\gamma^\nu g_s.
\tag{4.146}
$$

Note that in comparison to box B1 the couplings $\boxed{1}$ and $\boxed{2}$ are exchanged, ie. the fermion flow is inverted. The gluon carries the four-momentum q which flows from the right to the left. This leads us to the amplitude

$$
\begin{aligned}
i\mathcal{M}_{\mathrm{B3}} &= C_F \mu^{4-D} \int \frac{\mathrm{d}^D q}{(2\pi)^D} \left[\bar{u}(p_2) i\gamma^\mu \boxed{3} i \frac{\slashed{q} + \slashed{p}_2 + m_q}{(q+p_2)^2 - m_q^2} i\boxed{1} u(p_a) \right] \left(\frac{-ig_{\mu\nu}}{q^2} \right) \\
&\quad \left(\frac{i}{(q+p_2-p_a)^2 - m_{\tilde{q}_i}^2} \right) \left[\bar{u}(p_1) i\boxed{2} i \frac{\slashed{q} + \slashed{p}_b + m_q}{(q+p_b)^2 - m_q^2} i\gamma^\nu \boxed{4} u(p_b) \right] \\
&= -i\frac{\alpha_s C_F}{4\pi} D_0 \left[\bar{u}(p_2)\gamma^\mu(\slashed{p}_2 + m_q)\boxed{1} u(p_a) \right] \left[\bar{u}(p_1)\boxed{2}(\slashed{p}_b + m_q)\gamma_\mu u(p_b) \right] \\
&\quad - i\frac{\alpha_s}{4\pi} D_\rho \Big(\left[\bar{u}(p_2)\gamma^\mu \gamma^\rho \boxed{1} u(p_a) \right] \left[\bar{u}(p_1)\boxed{2}(\slashed{p}_b + m_q)\gamma_\mu u(p_b) \right] \\
&\quad + \left[\bar{u}(p_2)\gamma^\mu(\slashed{p}_2 + m_q)\boxed{1} u(p_a) \right] \left[\bar{u}(p_1)\boxed{2}\gamma^\rho \gamma_\mu u(p_b) \right] \Big) \\
&\quad - i\frac{\alpha_s}{4\pi} D_{\rho\sigma} \left[\bar{u}(p_2)\gamma^\mu \gamma^\rho \boxed{1} u(p_a) \right] \left[\bar{u}(p_1)\boxed{2}\gamma^\sigma \gamma_\mu u(p_b) \right]. \quad (4.147)
\end{aligned}
$$

The four-point functions possess the arguments $D(p_2 - p_a, p_2, p_b, 0, m_{\tilde{q}_i}^2, m_q^2, m_q^2)$. As for the gluon box B1, a Fierz transformation is necessary to rearrange the spinor fields. The final result reads

$$
\begin{aligned}
\alpha_{q,\mathrm{B3}}^{\mathrm{SI}} &= \frac{\alpha_s C_F}{8\pi} \Big((c_2^R c_1^L + c_2^L c_1^R) m_q m_{\tilde{\chi}_1^0}(-D_1 + D_{11} + D_{12} + D_{13}) \\
&\quad + 4c_1^L c_2^L D_{00} + c_1^L c_2^L D_{11} m_{\tilde{\chi}_1^0}^2 + 4c_1^R c_2^R D_{00} + c_1^R c_2^R D_{11} m_{\tilde{\chi}_1^0}^2 \\
&\quad + c_1^L c_2^L (D_1 + D_{11} + 2D_{12} + 2D_{13} + D_2 + D_{22} + 2D_{23} + D_3 + D_{33}) m_q^2 \\
&\quad + c_1^R c_2^R (D_1 + D_{11} + 2D_{12} + 2D_{13} + D_2 + D_{22} + 2D_{23} + D_3 + D_{33}) m_q^2 \\
&\quad + D_0 (c_2^L c_1^L + c_2^R c_1^R) p_2 \cdot p_b \Big). \quad (4.148) \\
\alpha_{q,\mathrm{B3}}^{\mathrm{SD}} &= -\frac{\alpha_s C_F}{16\pi} \Big(-2D_1 c_1^R c_2^R m_q m_{\tilde{\chi}_1^0} + 2c_1^R c_2^L D_{00} + c_1^R c_2^L D_{11} m_{\tilde{\chi}_1^0}^2 \\
&\quad - 2D_1 c_1^L c_2^L m_q m_{\tilde{\chi}_1^0} + 2c_1^L c_2^R D_{00} + c_1^L c_2^R D_{11} m_{\tilde{\chi}_1^0}^2 \\
&\quad + c_1^R c_2^L m_q^2 (2D_1 + D_{11} + 2D_{12} + 2D_{13} + 2D_2 + D_{22} + 2D_{23} + 2D_3 + D_{33}) \\
&\quad + c_1^L c_2^R m_q^2 (2D_1 + D_{11} + 2D_{12} + 2D_{13} + 2D_2 + D_{22} + 2D_{23} + 2D_3 + D_{33}) \\
&\quad + 2D_0 (c_2^R c_1^L + c_2^L c_1^R) p_2 \cdot p_b \Big). \quad (4.149)
\end{aligned}
$$

Thanks to the symmetry $\boxed{1} \leftrightarrow \boxed{2}$, these expressions completely agree with those for B1 given in (4.134) and (4.135). However, we stress again that the four-point functions possess different arguments than previously.

Box B4

We are left with the twisted gluino box B4 shown on the very right of figure 4.11. The couplings are given by

$$i\boxed{1} = i(c_1^L P_L + c_1^R P_R) = i(g^L_{\tilde{\chi}_1^0 q \tilde{q}_i} P_L + g^R_{\tilde{\chi}_1^0 q \tilde{q}_i} P_R). \tag{4.150}$$

$$i\boxed{2} = i(c_2^L P_L + c_2^R P_R) = i(g^L_{\tilde{\chi}_1^0 \tilde{q}_j q} P_L + g^R_{\tilde{\chi}_1^0 \tilde{q}_j q} P_R). \tag{4.151}$$

$$i\boxed{3} = i(c_3^L P_L + c_3^R P_R) = i(g^L_{\tilde{g} \tilde{q}_i q} P_L + g^R_{\tilde{g} \tilde{q}_i q} P_R). \tag{4.152}$$

$$i\boxed{4} = i(c_4^L P_L + c_4^R P_R) = i(g^L_{\tilde{g} q \tilde{q}_j} P_L + g^R_{\tilde{g} q \tilde{q}_j} P_R). \tag{4.153}$$

The gluino possesses the four-momentum q flowing from the left to the right. The amplitude is given as

$$
\begin{aligned}
i\mathcal{M}_{\text{B4}} &= C_F \mu^{4-D} \int \frac{\mathrm{d}^D q}{(2\pi)^D} \left[\bar{u}(p_2) i\boxed{3} i\frac{\slashed{q} + m_{\tilde{g}}}{q^2 - m_{\tilde{g}}^2} i\boxed{4} u(p_b) \right] \left(\frac{i}{(q - p_b)^2 - m_{\tilde{q}_j}^2} \right) \\
&\quad \left(\frac{i}{(q - p_2)^2 - m_{\tilde{q}_i}^2} \right) \left[\bar{v}(p_a) i\boxed{1} i\frac{-\slashed{q} - \slashed{p}_a + \slashed{p}_2 + m_q}{(-q - p_a + p_2)^2 - m_q^2} i\boxed{2} v(p_1) \right] \\
&= \frac{iC_F}{16\pi^2} D_0 \left[\bar{u}(p_2)\boxed{3} m_{\tilde{g}}\boxed{4} u(p_b) \right] \left[\bar{v}(p_a)\boxed{1}(-\slashed{p}_a + \slashed{p}_2 + m_q)\boxed{2} v(p_1) \right] \\
&\quad + \frac{i}{16\pi^2} D_\rho \left(\left[\bar{u}(p_2)\boxed{3}\gamma^\rho\boxed{4} u(p_b) \right] \left[\bar{v}(p_a)\boxed{1}(-\slashed{p}_a + \slashed{p}_2 + m_q)\boxed{2} v(p_a) \right] \right. \\
&\quad \left. + \left[\bar{u}(p_2)\boxed{3} m_{\tilde{g}}\boxed{4} u(p_b) \right] \left[\bar{v}(p_a)\boxed{1}(-\gamma^\rho)\boxed{2} v(p_1) \right] \right) \\
&\quad + \frac{i}{16\pi^2} D_{\rho\sigma} \left[\bar{u}(p_2)\boxed{3}\gamma^\rho\boxed{4} u(p_b) \right] \left[\bar{v}(p_a)\boxed{1}(-\gamma^\sigma)\boxed{2} v(p_1) \right]. \tag{4.154}
\end{aligned}
$$

The four-point functions are understood as $D(-p_2, -p_b, p_a - p_2, m_{\tilde{g}}^2, m_{\tilde{q}_i}^2, m_{\tilde{q}_j}^2, m_q^2)$. As it was the case for B2, a Fierz transformation is not necessary. We obtain

$$
\begin{aligned}
\alpha^{\text{SI}}_{q,\text{B4}} &= \frac{C_F}{64\pi^2} \Big(m_q m_{\tilde{g}} D_0 (c_1^L c_2^L c_3^R c_4^R + c_1^L c_2^L c_3^L c_4^L + c_1^R c_2^R c_3^R c_4^R + c_1^R c_2^R c_3^L c_4^L) \\
&\quad - m_q^2 (D_1 + D_2 + D_3)(c_1^L c_2^L c_3^R c_4^L + c_1^L c_2^L c_3^L c_4^R + c_1^R c_2^R c_3^R c_4^L + c_1^R c_2^R c_3^L c_4^R) \\
&\quad + m_{\tilde{g}} m_{\tilde{\chi}_1^0} (D_0 + D_3)(c_1^R c_2^L c_3^L c_4^L + c_1^L c_2^R c_3^L c_4^L + c_1^R c_2^L c_3^R c_4^R + c_1^L c_2^R c_3^R c_4^R) \\
&\quad - m_q m_{\tilde{\chi}_1^0}(D_1 + D_{13} + D_2 + D_{23} + D_3 + D_{33}) \\
&\quad (c_1^R c_2^L c_3^L c_4^R + c_1^L c_2^R c_3^L c_4^R + c_1^R c_2^L c_3^R c_4^L + c_1^L c_2^R c_3^R c_4^L) \Big). \tag{4.155}
\end{aligned}
$$

$$
\alpha^{\text{SD}}_{q,\text{B4}} = \frac{C_F}{64\pi^2} D_{00} \Big(-c_1^R c_2^L c_3^L c_4^R + c_1^L c_2^R c_3^L c_4^R + c_1^R c_2^L c_3^R c_4^L - c_1^L c_2^R c_3^R c_4^L \Big). \tag{4.156}
$$

These expressions equal those given in (4.141) and (4.142) for box B2, where we have to take into account different arguments for the four-point functions.
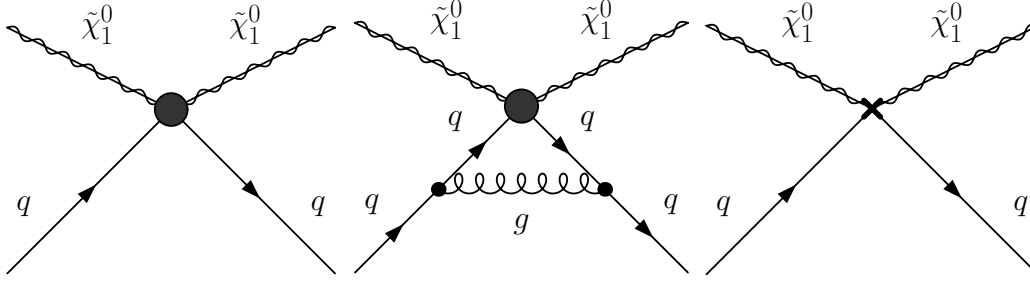
Figure 4.12.: Neutralino-quark scattering process in the effective theory at tree-level (left), including an additional gluon (middle) and including the corresponding counterterm (right)

4.5. Matching of full and effective theory

So far we have evaluated all amplitudes up to $\mathcal{O}(\alpha_s)$ relevant for the elastic scattering of neutralinos and quarks within the full theory, namely the MSSM, at the high scale $\mu_{\text{high}} \sim 1$ TeV. The next step is to map these amplitudes onto the Wilson coeffients of the effective field theory (EFT), which is illustrated in this section. In case of the tree-level calculations, we have basically already obtained the final results in section 4.3. However, in the following we repeat the matching procedure at tree-level on a more formal basis. Afterwards we use this solid footing to perform the matching procedure at NLO. A general introduction into effective field theory is given in chapter H.

4.5.1. Matching at tree-level

The effective field theory we are interested in is governed by the effective Lagrangian[16]

$$\mathcal{L}_{\text{eff}} = C_1 Q_1 + C_2 Q_2 = C_1 \bar{\chi}\chi\bar{q}q + C_2 \bar{\chi}\gamma_5\gamma_\mu\chi\bar{q}\gamma_5\gamma^\mu q. \tag{4.157}$$

It consists of only two effective operators Q_1 and Q_2 accompanied by their Wilson coefficients C_1 and C_2. As explained in section 4.3, the former operator is responsible for coherent, spin-independent interactions and the latter operator for spin-dependent interactions. Both of them lead to effective four-fermion interactions as shown on the left of figure 4.12.

The Wilson coefficients are fixed by the so-called *matching condition*. The effective theory has to reproduce the full theory at the high scale. More precisely, we demand that

$$\mathcal{M}_{\text{full}}^{\text{tree}} \overset{!}{=} \mathcal{M}_{\text{eff}}^{\text{tree}} \Leftrightarrow \mathcal{M}_{\text{T1}} + \mathcal{M}_{\text{T2}} + \mathcal{M}_{\text{T3}} + \mathcal{M}_{\text{T4}} \overset{!}{=} C_1^{\text{tree}} Q_1^{\text{tree}} + C_2^{\text{tree}} Q_2^{\text{tree}}. \tag{4.158}$$

The four tree-level amplitudes $\mathcal{M}_{\text{T1}}$ to $\mathcal{M}_{\text{T4}}$ are given by (4.19), (4.24), (4.31) and (4.41). As we include only the two dominant operators in the effective Lagrangian, we drop contributions stemming from kinematically suppressed operators like $\bar{\chi}\gamma_5\chi\bar{q}\gamma_5 q$ when evaluating the amplitudes in the full theory. Moreover, we have explicitly added the identification mark $^{\text{tree}}$ to stress that this is just the tree-level matching procedure. As demonstrated in section 4.3, this procedure leads to

$$C_1^{\text{tree}} = \alpha_{q,\text{T1}}^{\text{SI}} + \alpha_{q,\text{T3}}^{\text{SI}} + \alpha_{q,\text{T4}}^{\text{SI}} \quad \text{and} \quad C_2^{\text{tree}} = \alpha_{q,\text{T2}}^{\text{SD}} + \alpha_{q,\text{T3}}^{\text{SD}} + \alpha_{q,\text{T4}}^{\text{SD}}. \tag{4.159}$$

---

[16]The effective Lagrangian given in (4.157) describes the interactions between quarks and neutralinos. The usual kinematic terms and in particular the interactions between quarks and gluons remain unaltered.

The relevant contributions are given in (4.21), (4.39), (4.43), (4.28), (4.40) and (4.44).

4.5.2. Matching at next-to-leading order

We continue with the matching calculation at next-to-leading order. The matching condition remains basically unchanged, we have

$$\mathcal{M}_{\text{full}}^{\text{NLO}} \stackrel{!}{=} \mathcal{M}_{\text{eff}}^{\text{NLO}} \Leftrightarrow \mathcal{M}_{\text{full}}^{\text{tree}} + \mathcal{M}_{\text{full}}^{\text{1loop}} \stackrel{!}{=} C_1^{\text{NLO}} Q_1^{\text{NLO}} + C_2^{\text{NLO}} Q_2^{\text{NLO}}. \tag{4.160}$$

In this nomenclature, the full NLO result consists of the tree-level result and its $\mathcal{O}(\alpha_s)$ one-loop correction. The latter includes all the corrections calculated in section 4.4: The propagator corrections and their counterterm, the vertex corrections and their counterterms and the box contributions.

What about the right-hand side of (4.160)? The crucial point is that there is a one-loop correction to the Wilson coefficients *and* the effective operators. Hence, we write

$$\begin{aligned}
\mathcal{M}_{\text{full}}^{\text{tree}} + \mathcal{M}_{\text{full}}^{\text{1loop}} \quad \stackrel{!}{=} \quad & (C_1^{\text{tree}} + C_1^{\text{1loop}})(Q_1^{\text{tree}} + Q_1^{\text{1loop}}) + (C_2^{\text{tree}} + C_2^{\text{1loop}})(Q_2^{\text{tree}} + Q_2^{\text{1loop}}) \\
= \quad & C_1^{\text{tree}} Q_1^{\text{tree}} + C_2^{\text{tree}} Q_2^{\text{tree}} + C_1^{\text{1loop}} Q_1^{\text{tree}} + C_2^{\text{1loop}} Q_2^{\text{tree}} \\
+ \quad & C_1^{\text{tree}} Q_1^{\text{1loop}} + C_2^{\text{tree}} Q_2^{\text{1loop}} + \mathcal{O}(\alpha_s^2).
\end{aligned} \tag{4.161}$$

At $\mathcal{O}(\alpha_s^0)$ we have reproduced the tree-level matching condition (4.158) which is already fulfilled. Therefore, we obtain at $\mathcal{O}(\alpha_s)$

$$\mathcal{M}_{\text{full}}^{\text{1loop}} - C_1^{\text{tree}} Q_1^{\text{1loop}} - C_2^{\text{tree}} Q_2^{\text{1loop}} = C_1^{\text{1loop}} Q_1^{\text{tree}} + C_2^{\text{1loop}} Q_2^{\text{tree}}. \tag{4.162}$$

The aim of the matching procedure is to calculate the $\mathcal{O}(\alpha_s)$ corrections to the Wilson coefficients, i.e. to determine C_1^{1loop} and C_2^{1loop}. Before we can achieve this, we have to identify the one-loop corrections to the effective operators Q_1^{1loop} and Q_2^{1loop}. In the end of this section we demonstrate that they are given by

$$Q_1^{\text{1loop}} = (\mathcal{K}_{\text{EFTV1}} + \mathcal{K}_{\text{EFTVC1}}) Q_1^{\text{tree}} \quad \text{and} \quad Q_2^{\text{1loop}} = (\mathcal{K}_{\text{EFTV2}} + \mathcal{K}_{\text{EFTVC2}}) Q_2^{\text{tree}}, \tag{4.163}$$

i.e. that they can be expressed as the tree-level operators multiplied with correction factors describing vertex corrections and vertex counterterms in the effective field theory. This allows us to explicitly write down the one-loop Wilson coefficients as

$$\begin{aligned}
C_1^{\text{1loop}} \quad = \quad & \alpha_{q,\text{P1}}^{\text{SI}} + \alpha_{q,\text{P2}}^{\text{SI}} + \alpha_{q,\text{P4}}^{\text{SI}} + \alpha_{q,\text{PC}}^{\text{SI}} \\
+ \quad & \alpha_{q,\text{V1}}^{\text{SI}} + \alpha_{q,\text{V2}}^{\text{SI}} + \alpha_{q,\text{V5}}^{\text{SI}} + \alpha_{q,\text{V6}}^{\text{SI}} + \alpha_{q,\text{V7}}^{\text{SI}} + \alpha_{q,\text{V8}}^{\text{SI}} + \alpha_{q,\text{VC1}}^{\text{SI}} + \alpha_{q,\text{VC3}}^{\text{SI}} + \alpha_{q,\text{VC4}}^{\text{SI}} \\
+ \quad & \alpha_{q,\text{B1}}^{\text{SI}} + \alpha_{q,\text{B2}}^{\text{SI}} + \alpha_{q,\text{B3}}^{\text{SI}} + \alpha_{q,\text{B4}}^{\text{SI}} \\
- \quad & C_1^{\text{tree}} (\mathcal{K}_{\text{EFTV1}} + \mathcal{K}_{\text{EFTVC1}}).
\end{aligned} \tag{4.164}$$

$$\begin{aligned}
C_2^{\text{1loop}} \quad = \quad & \alpha_{q,\text{P1}}^{\text{SD}} + \alpha_{q,\text{P2}}^{\text{SD}} + \alpha_{q,\text{P4}}^{\text{SD}} + \alpha_{q,\text{PC}}^{\text{SD}} \\
+ \quad & \alpha_{q,\text{V3}}^{\text{SD}} + \alpha_{q,\text{V4}}^{\text{SD}} + \alpha_{q,\text{V5}}^{\text{SD}} + \alpha_{q,\text{V6}}^{\text{SD}} + \alpha_{q,\text{V7}}^{\text{SD}} + \alpha_{q,\text{V8}}^{\text{SD}} + \alpha_{q,\text{VC2}}^{\text{SD}} + \alpha_{q,\text{VC3}}^{\text{SD}} + \alpha_{q,\text{VC4}}^{\text{SD}} \\
+ \quad & \alpha_{q,\text{B1}}^{\text{SD}} + \alpha_{q,\text{B2}}^{\text{SD}} + \alpha_{q,\text{B3}}^{\text{SD}} + \alpha_{q,\text{B4}}^{\text{SD}} \\
- \quad & C_2^{\text{tree}} (\mathcal{K}_{\text{EFTV2}} + \mathcal{K}_{\text{EFTVC2}}).
\end{aligned} \tag{4.165}$$

These two formulae include all the virtual corrections calculated in section 4.4 plus the correction factors to be given. We stress that each of the lines above is separately

ultraviolet finite. However, there are also *infrared divergences* (cf. section F.1) involved, which have not been discussed yet. Although most of the individual terms given above are infrared divergent, C_1^{1loop} and C_2^{1loop} as a whole are infrared finite, which is an essential feature of the matching procedure (cf. subsection H.3.2). The appearance of infrared divergences is connected to massless particles such as gluons. These particles are likewise degrees of freedom in the full and the effective theory. In other words: The infrared regimes of both theories are the same. Whenever there occurs an infrared divergence in the full theory, the very same infrared divergence occurs in the effective theory as well and both cancel during the matching procedure. In our calculation, this cancellation is due to the correction factors $\mathcal{K}_{\text{EFTV1}}$, $\mathcal{K}_{\text{EFTVC1}}$, $\mathcal{K}_{\text{EFTV2}}$ and $\mathcal{K}_{\text{EFTVC2}}$ which we determine now.

We start with the vertex correction incorporated in $\mathcal{K}_{\text{EFTV1}}$. The underlying process is depicted in the middle of figure 4.12. Starting on the top, we label the couplings clockwise as

$$i\boxed{1} = iC_1^{\text{tree}}, \quad i\boxed{2}\gamma^\mu = -ig_s\gamma^\mu \quad \text{and} \quad i\boxed{3}\gamma^\nu = -ig_s\gamma^\nu \qquad (4.166)$$

and obtain the amplitude

$$
\begin{aligned}
i\mathcal{M}_{\text{EFTV1}} &= C_F\mu^{4-D}\int\frac{\mathrm{d}^Dq}{(2\pi)^D}\Big[\bar{u}(p_2)i\boxed{2}\gamma^\mu\frac{i(\slashed{q}+\slashed{p}_2+m_q)}{(q+p_2)^2-m_q^2}i\boxed{1} \\
&\quad \frac{i(\slashed{q}+\slashed{p}_b+m_q)}{(q+p_b)^2-m_q^2}i\boxed{3}\gamma^\nu u(p_b)\Big]\left(\frac{-ig_{\mu\nu}}{q^2}\right)[\bar{u}(p_1)u(p_a)].
\end{aligned}
\qquad (4.167)
$$

After some algebra and using (4.64) we get

$$
\begin{aligned}
\mathcal{M}_{\text{EFTV1}} &= \frac{\alpha_s C_F}{4\pi}\left(4B_0 - 2 + 4p_bp_2(C_0 + C_1 + C_2)\right) \\
&\quad C_1^{\text{tree}}[\bar{u}(p_2)u(p_b)][\bar{u}(p_1)u(p_a)].
\end{aligned}
\qquad (4.168)
$$

The two- and three-point functions possess the arguments $B = B(p_b - p_2, m_q^2, m_q^2)$ and $C = C(p_2, p_b, 0, m_q^2, m_q^2)$. We replace the spinors by their corresponding spinor fields and identify the operator Q_1^{tree} and its vertex correction factor $\mathcal{K}_{\text{EFTV1}}$.

$$
\begin{aligned}
\mathcal{M}_{\text{EFTV1}} &= \frac{\alpha_s C_F}{4\pi}\left(4B_0 - 2 + 4p_bp_2(C_0 + C_1 + C_2)\right)C_1^{\text{tree}}[\bar{q}q][\bar{\chi}\chi] \\
&= \mathcal{K}_{\text{EFTV1}}C_1^{\text{tree}}Q_1^{\text{tree}}.
\end{aligned}
\qquad (4.169)
$$

We stress that the algebraic form of this vertex correction is identical to V1, i.e. to (4.63). This has two important consequences. On the one hand, the vertex correction V1 completely cancels in the matching procedure. The gluon is likewise a degree of freedom in the full and the effective theory and therefore the vertex correction V1 occurs in both theories. It is included in the effective operator, not the Wilson coefficient. Moreover, the correction factor $\mathcal{K}_{\text{EFTV1}}$ is ultraviolet divergent as it includes the two-point function B_0. To allow for a consistent matching procedure, we have to renormalise the effective theory in the same way as the full theory. This means that we have to add a counterterm δC_1 to the four-fermion coupling, which is depicted on the right of figure 4.12. As this counterterm has to be of the very same form as $\delta g_{\phi qq}$ given in (4.104), it reads

$$\delta C_1^L = C_1^{\text{tree},L}\left(\frac{\delta Z_m}{m_q} + \frac{1}{2}\delta Z_q^L + \frac{1}{2}\delta Z_q^{R*}\right). \qquad (4.170)$$

The correction factor $\mathcal{K}_{\text{EFTVC1}}$ is then simply given by

$$\mathcal{K}_{\text{EFTVC1}} = \frac{\delta C_1^L / C_1^{\text{tree},L} + \delta C_1^R / C_1^{\text{tree},R}}{2}. \tag{4.171}$$

Remember that C_1^{tree} does not only incorporate Higgs contributions, squark processes contribute as well (cf. (4.159)). Whereas the Higgs vertex correction V1 and its associated counterterm completely vanish in the matching procedure, this is not true for the vertex corrections V5 and V7 and their counterterms. However, the infrared divergences of these corrections and the ones stemming from the boxes B1 and B3 are precisely cancelled by the correction factors. This is an important consistency check of the whole calculation.

We continue with the determination of $\mathcal{K}_{\text{EFTV2}}$, i.e. the vertex correction factor for the spin-dependent operator Q_2. The associated diagram is shown in the middle of figure 4.12 again, the only difference to the previous case is the included four-fermion coupling. More precisely, we label the couplings clockwise as

$$i\boxed{1}\gamma^\nu\gamma_5 = iC_2^{\text{tree}}\gamma^\nu\gamma_5, \quad i\boxed{2}\gamma^\mu = -ig_s\gamma^\mu \quad \text{and} \quad i\boxed{3}\gamma^\rho = -ig_s\gamma^\rho, \tag{4.172}$$

where we start on the top again. The corresponding amplitude reads

$$\begin{aligned}
i\mathcal{M}_{\text{EFTV2}} &= C_F\mu^{4-D}\int\frac{\mathrm{d}^D q}{(2\pi)^D}\left[\bar{u}(p_2)i\boxed{2}\gamma^\mu\frac{i(\slashed{q}+\slashed{p}_2+m_q)}{(q+p_2)^2-m_q^2}i\boxed{1}\gamma^\nu\gamma_5\right. \\
&\quad \left.\frac{i(\slashed{q}+\slashed{p}_b+m_q)}{(q+p_b)^2-m_q^2}i\boxed{3}\gamma^\rho u(p_b)\right]\left(\frac{-ig_{\mu\rho}}{q^2}\right)[\bar{u}(p_1)\gamma_\nu\gamma_5 u(p_a)]. \tag{4.173}
\end{aligned}$$

Thanks to the additional gamma matrices, the evaluation of this amplitude is a bit lengthier. Keeping only the relevant effective operators, we finally obtain

$$\begin{aligned}
\mathcal{M}_{\text{EFTV2}} &= \frac{\alpha_s C_F}{4\pi}\left(2B_0 + 4p_b p_2(C_0 + C_1 + C_2) - 4C_{00} - 1\right) \\
&\quad C_2^{\text{tree}}[\bar{u}(p_1)\gamma_\nu\gamma_5 u(p_a)][\bar{u}(p_2)\gamma^\nu\gamma_5 u(p_b)]. \tag{4.174}
\end{aligned}$$

The two- and three-point functions possess the same arguments as before, namely $B = B(p_b - p_2, m_q^2, m_q^2)$ and $C = C(p_2, p_b, 0, m_q^2, m_q^2)$. We replace the spinors by their corresponding spinor fields and identify the operator Q_2^{tree} and its associated vertex correction factor $\mathcal{K}_{\text{EFTV2}}$.

$$\begin{aligned}
\mathcal{M}_{\text{EFTV2}} &= \frac{\alpha_s C_F}{4\pi}\left(2B_0 + 4p_b p_2(C_0 + C_1 + C_2) - 4C_{00} - 1\right)C_2^{\text{tree}}[\bar{\chi}\gamma_\nu\gamma_5\chi][\bar{q}\gamma^\nu\gamma_5 q] \\
&= \mathcal{K}_{\text{EFTV2}}C_2^{\text{tree}}Q_2^{\text{tree}}. \tag{4.175}
\end{aligned}$$

The missing piece is the counterterm δC_2 which renders the vertex correction given above ultraviolet finite. This counterterm is constructed in analogy to $\delta g_{Z^0 qq}$ given in (4.105) and reads

$$\delta C_2^L = C_2^{\text{tree},L}\left(\frac{1}{2}\delta Z_q^{\text{SM},L} + \frac{1}{2}\delta Z_q^{\text{SM},L*} + \frac{\alpha_s C_F}{\pi}\right). \tag{4.176}$$

As before, the correction factor $\mathcal{K}_{\text{EFTVC2}}$ is obtained via

$$\mathcal{K}_{\text{EFTVC2}} = \frac{\delta C_2^L / C_2^{\text{tree},L} + \delta C_2^R / C_2^{\text{tree},R}}{2}. \tag{4.177}$$

Note that we have included the additional finite term $\frac{\alpha_s C_F}{\pi}$ to retain a conventional axial current divergence, which is in agreement with [179] and [171].[17] Moreover, we incorporate just Standard Model contributions to δZ_q in this case. The reason is as follows: In case of the Higgs vertex corrections, i.e. V1 and V2, only the former is ultraviolet divergent. The whole counterterm $\delta g_{\phi qq}$ as given in (4.104) is responsible for the cancellation of this divergence. As the vertex V1 occurs likewise in the effective theory, we have constructed its associated counterterm δC_1 in complete analogy to $\delta g_{\phi qq}$. In case of the Z^0 vertex corrections, i.e. V3 and V4, both are ultraviolet divergent. The divergences of the first diagram are removed by the Standard Model part of $\delta g_{Z^0 qq}$ and those of the latter by the SUSY part of $\delta g_{Z^0 qq}$. During the matching procedure, the vertex correction V3 and its corresponding counterterm has to cancel, whereas V4 and its counterterm contribute to the Wilson coefficient. Hence, we only include Standard Model contributions to the spinor field counterterms in δC_2. This completes our matching calculation at NLO. We briefly summarise it by the following four steps.

Determination of Wilson coefficients at NLO

1. Write down and simplify the one-loop amplitudes of the full and effective theory, respectively. Identify the spinors with their corresponding spinor fields.

2. Sort out irrelevant effective operators.

3. If necessary, perform a Fierz transformation.

4. Obtain the one-loop corrections to the Wilson coefficients by matching the full theory onto the effective theory. The final result has to be infrared safe.

4.6. Running of operators and Wilson coefficients

The matching calculation presented in the previous section has fixed the Wilson coefficients of the effective theory. This calculation has been performed at the high scale $\mu_{\text{high}} \sim 1$ TeV. In contrast, the nuclear matrix elements, i.e. the scalar coefficients f_{Tq}^N and the polarised quark densities $(\Delta q)_N$, are defined at the low scale $\mu_{\text{low}} \sim 5$ GeV. This is the energy regime we finally aim to describe with our effective field theory. To connect the two energy regimes, we have to evolve the effective operators and associated Wilson coefficients from the high scale down to the low scale by solving the corresponding renormalisation group equations (RGEs, cf. section G.4). This part of the calculation is briefly referred to as *running* and presented here.

The scale dependence, i.e. the running of the effective operators and associated Wilson coefficients is intimately linked. More precisely, it has to be inverse as the scale dependence of the product vanishes in every operator product expansion (OPE) and our effective

---

[17]The results given in [179] were obtained using the $\overline{\text{MS}}$ scheme and dimensional regularisation. Transferring results from this scheme to the $\overline{\text{DR}}$ scheme and dimensional reduction – which we are using – is non-trivial in general. Discrepancies may arise due to the treatment of γ_5 in D dimensions. However, these problems should occur at the three-loop order for the first time and do neither affect the finite contribution included in (4.176) nor the running of the axial-vector operator presented in the next section [180].

Lagrangian

$$\mathcal{L}_{\text{eff}} = C_1 Q_1 + C_2 Q_2 = C_1 \bar{\chi}\chi\bar{q}q + C_2 \bar{\chi}\gamma_5\gamma_\mu\chi\bar{q}\gamma_5\gamma^\mu q \tag{4.178}$$

is nothing but an operator product expansion, where higher dimensional operators have been neglected (cf. chapter H). Therefore, we can deduce the running of the Wilson coefficients from the running of the effective operators. As we are only interested in QCD effects, the running of the two operators given above is solely determined by their quark parts $\bar{q}q$ and $\bar{q}\gamma_5\gamma^\mu q$.

4.6.1. Running of $m_q \bar{q}q$

We start with the discussion of the running of the scalar operator $\bar{q}q$ and its Wilson coefficient C_1. In this case, the evolution down to the low scale is rather simple. The reason is that the operator $m_q\bar{q}q$ is scale-independent [171]. Hence, we have to simply factor out the quark mass $m_q(\mu_{\text{high}})$ from the coefficient C_1. This quark mass has to be evolved down to the low scale μ_{low} in the usual way, i.e. by solving its RGE (cf. subsection G.4.2). We then replace the combination $m_q(\mu_{\text{low}})\bar{q}q$ via (4.8).

4.6.2. Running of $\bar{q}\gamma_5\gamma^\mu q$

In contrast to the running of the scalar operator, the renormalisation and the resulting running of the axial-vector operator is not trivial. This calculation has first been performed in [179]. The relevant renormalisation constant reads

$$Z_A^{\text{Singlet}} = 1 + \frac{\alpha_s C_F}{\pi} - \frac{1}{\epsilon}\left(\frac{\alpha_s}{4\pi}\right)^2\left(\frac{20}{9}n_f + \frac{88}{3}\right) + \mathcal{O}(\alpha_s^3), \tag{4.179}$$

where n_f denotes the number of active flavours and an additional finite term has been added to cure the axial anomaly. It is precisely this term which has been included in (4.176) as well. Finite terms of order $\mathcal{O}(\alpha_s^2)$ have been neglected as they are irrelevant for the running up to the desired order. Given this renormalisation constant, we can calculate the corresponding anomalous dimension via

$$
\begin{aligned}
\gamma_A^{\text{Singlet}} &= (Z_A^{\text{Singlet}})^{-1}\frac{\mathrm{d}}{\mathrm{d}\ln\mu}Z_A^{\text{Singlet}} \\
&= \left(1 - \frac{\alpha_s C_F}{\pi} + \frac{1}{\epsilon}\left(\frac{\alpha_s}{4\pi}\right)^2\left(\frac{20}{9}n_f + \frac{88}{3}\right)\right)\frac{\mathrm{d}g_s}{\mathrm{d}\ln\mu} \\
&\quad \frac{\mathrm{d}}{\mathrm{d}g_s}\left(1 + \frac{\alpha_s C_F}{\pi} - \frac{1}{\epsilon}\left(\frac{\alpha_s}{4\pi}\right)^2\left(\frac{20}{9}n_f + \frac{88}{3}\right)\right) + \mathcal{O}(\alpha_s^3).
\end{aligned}
\tag{4.180}
$$

We substitute $\frac{\mathrm{d}g_s}{\mathrm{d}\ln\mu}$ by the RGE of the strong coupling constant including its divergent part as derived in subsection G.4.1 and obtain

$$
\begin{aligned}
\gamma_A^{\text{Singlet}} &= \left(1 - \frac{\alpha_s C_F}{\pi} + \frac{1}{\epsilon}\left(\frac{\alpha_s}{4\pi}\right)^2\left(\frac{20}{9}n_f + \frac{88}{3}\right)\right)(-\epsilon g_s + \beta(g_s)) \\
&\quad \frac{1}{g_s}\left(\frac{2\alpha_s C_F}{\pi} - \frac{4}{\epsilon}\left(\frac{\alpha_s}{4\pi}\right)^2\left(\frac{20}{9}n_f + \frac{88}{3}\right)\right) + \mathcal{O}(\alpha_s^3) \\
&= \left(\frac{2\alpha_s C_F}{\pi} - 2\left(\frac{\alpha_s C_F}{\pi}\right)^2 - \frac{4}{\epsilon}\left(\frac{\alpha_s}{4\pi}\right)^2\left(\frac{20}{9}n_f + \frac{88}{3}\right)\right) \\
&\quad \left(-\epsilon + \frac{\beta(g_s)}{g_s}\right) + \mathcal{O}(\alpha_s^3).
\end{aligned}
\tag{4.181}
$$

Next we perform the physical limit $D \to 4$ and insert $C_F = 4/3$ explicitly. Keeping only terms of $\mathcal{O}(\alpha_s^2)$ leads to

$$
\begin{aligned}
\gamma_A^{\text{Singlet}} &= -\frac{32}{3}\left(\frac{\alpha_s}{4\pi}\right)^2 \beta_0 + 4\left(\frac{\alpha_s}{4\pi}\right)^2\left(\frac{20}{9}n_f + \frac{88}{3}\right) + \mathcal{O}(\alpha_s^3) \\
&= \left(\frac{\alpha_s}{4\pi}\right)^2 16 n_f + \mathcal{O}(\alpha_s^3),
\end{aligned}
\tag{4.182}
$$

where we have used $\beta_0 = 11 - \frac{2}{3}n_f$ according to (G.31). The remaining step is to determine the running of the Wilson coefficient C_2 given by

$$
\frac{\mathrm{d}}{\mathrm{d}\ln\mu}C_2(\mu) = \gamma_A^{\text{Singlet}}C_2(\mu).
\tag{4.183}
$$

This differential equation can be solved via

$$
\begin{aligned}
\int_{C_2(\mu_{\text{low}})}^{C_2(\mu_{\text{high}})} \frac{\mathrm{d}C_2(\mu)}{C_2(\mu)} &= \int_{\ln\mu_{\text{low}}}^{\ln\mu_{\text{high}}} \mathrm{d}\ln\mu\, \gamma_A^{\text{Singlet}} = \int_{g_s(\mu_{\text{low}})}^{g_s(\mu_{\text{high}})} \mathrm{d}g_s'\, \frac{\mathrm{d}\ln\mu}{dg_s'}\gamma_A^{\text{Singlet}} \\
\Leftrightarrow \ln\left(\frac{C_2(\mu_{\text{high}})}{C_2(\mu_{\text{low}})}\right) &= \int_{g_s(\mu_{\text{low}})}^{g_s(\mu_{\text{high}})} \mathrm{d}g_s'\, \frac{\gamma_A^{\text{Singlet}}}{\beta(g_s',\epsilon)} \\
\Leftrightarrow C_2(\mu_{\text{low}}) &= C_2(\mu_{\text{high}})\exp\left(-\int_{g_s(\mu_{\text{low}})}^{g_s(\mu_{\text{high}})} \mathrm{d}g_s'\, \frac{\gamma_A^{\text{Singlet}}}{\beta(g_s',\epsilon)}\right).
\end{aligned}
\tag{4.184}
$$

We perform the physical limit $D \to 4$ and restrict ourselves to the leading contributions to $\beta(g_s')$ as given in (G.31) to finally obtain the result presented in [171].

$$
\begin{aligned}
C_2(\mu_{\text{low}}) &= C_2(\mu_{\text{high}})\exp\left(-\int_{g_s(\mu_{\text{low}})}^{g_s(\mu_{\text{high}})} \mathrm{d}g_s'\, \frac{\frac{g_s'^4}{256\pi^4}16 n_f}{-\beta_0\frac{g_s'^3}{16\pi^2}}\right) \\
&= C_2(\mu_{\text{high}})\exp\left(\int_{g_s(\mu_{\text{low}})}^{g_s(\mu_{\text{high}})} \mathrm{d}g_s'\, \frac{g_s' n_f}{\beta_0\pi^2}\right) \\
&= C_2(\mu_{\text{high}})\exp\left(\frac{2n_f}{\beta_0\pi}(\alpha_s(\mu_{\text{high}}) - \alpha_s(\mu_{\text{low}}))\right).
\end{aligned}
\tag{4.185}
$$

5. Calculation of neutralino relic density

In this chapter we introduce a second dark matter observable, namely the *neutralino relic density*. We illustrate how to calculate it by solving the *Boltzmann equation*, describe the constituents of the latter and comment on the associated uncertainties. One of these constituents is the (co)annihilation cross section including all processes under which SUSY particles transform into Standard Model particles. In many scenarios of the MSSM, gaugino (co)annihilation into quarks contributes dominantly to this cross section. To render the relic density calculation more precisely, a full $\mathcal{O}(\alpha_s)$ calculation of these processes has been carried out in collaboration with Björn Herrmann, Karol Kovařík and Moritz Meinecke. The author of this thesis contributed significantly to the final numerical implementation (cf. chapter 6) and generated almost all numerical results published in [147]. However, as the original analytical work has mainly been done by the aforementioned people, the corresponding section 5.4 is of rather brief and summarising character. Further technical details on this calculation can be found in [63, 181].

5.1. Basic idea of relic density calculations

The neutralino relic density can be understood as its recent quantity and is a parameter of great phenomenological relevance. A typical relic density calculation is based on the following line of arguments:

1. We assume that the evolution of the universe is correctly described by a certain cosmological model, e.g. the ΛCDM model. In addition, we postulate that dark matter consists of WIMPs with known mass and interactions, e.g. of the lightest neutralino in a concrete MSSM scenario.

2. Given these presuppositions, we perform a thermodynamical calculation to predict the relic density Ω_χ. In our case, this step corresponds to solving the Boltzmann equation described in the next section.

3. We compare this prediction with the cold dark matter density Ω_{CDM}, which can be experimentally extracted from the cosmic microwave background very precisely (cf. subsection 3.1.4). The comparison ends up in one of the following three possibilities:

   a) $\Omega_\chi > \Omega_{\mathrm{CDM}}$

   The relic density exceeds the experimental value. The underlying particle physics model is falsified with respect to the assumptions.

   b) $\Omega_\chi = \Omega_{\mathrm{CDM}}$

   The relic density agrees with the experimental value. The underlying particle physics model is experimentally favoured.

c) $\Omega_\chi < \Omega_{\mathrm{CDM}}$

The relic density falls below the experimental value. The underlying particle physics model can not solely explain dark matter.

In this way, the neutralino relic density permits to constrain the MSSM. Thanks to the remarkable precision of experimental data stemming from the Planck satellite, this constraint turns out to be very incisive and allows to exclude large parts of the MSSM space. This is of particular interest as the MSSM contains more than one hundred undetermined SUSY breaking parameters (cf. section 2.3). In order to fully benefit from the experimental precision and to reliably select the cosmological preferred region of the MSSM parameter space, the theoretical prediction should be of comparable precision. In section 5.3, we discuss several sources of theoretical uncertainties and finally minimise one of them by including radiative corrections to gaugino (co)annihilation into quarks in section 5.4.

5.2. Boltzmann equation

5.2.1. Boltzmann equation excluding coannihilations

To introduce the Boltzmann equation, we start with a simplified situation. We assume that there is only one additional particle χ which pairwisely interacts with Standard Model particles X. The latter resembles the conservation of R-parity in the MSSM. We denote the cross section of all possible pairwise annihilations of χ particles by σ. More precisely, we have

$$\sigma = \sum_X \sigma(\chi\chi \to X), \tag{5.1}$$

where we sum over all Standard Model particles X. Furthermore, we denote the relative velocity of two interacting χ particles by v. Given this setup, the number density n of particles χ is governed by the non-linear differential equation

$$\frac{\mathrm{d}n}{\mathrm{d}t} = -3Hn - \langle\sigma v\rangle \left(n^2 - (n^{\mathrm{eq}})^2\right). \tag{5.2}$$

The first term on the right-hand side is proportional to the Hubble expansion rate H and describes the dilution due to the expansion of the universe. The second term is proportional to the thermally averaged[18] annihilation cross section σ multiplied by the relative velocity v and responsible for the annihilation and creation of χ particles. If the number density n is larger than its corresponding number density in thermal equilibrium n^{eq}, annihilation dominates and the number density is reduced. On the other hand, creation increases the number density as long as it is smaller than the number density in thermal equilibrium. The latter depends on the mass of the new particle m_χ and the current temperature of the universe T. According to [39], the following approximations for large and small temperatures hold:

$$n^{\mathrm{eq}} \sim \begin{cases} T^3, & \text{if } T \gg m_\chi, \\ \left(\frac{m_\chi T}{2\pi}\right)^{\frac{3}{2}} \exp\left(-\frac{m_\chi}{T}\right), & \text{if } T \ll m_\chi. \end{cases} \tag{5.3}$$

---

[18]More details on the thermal averaging procedure can be found in [182, 183].
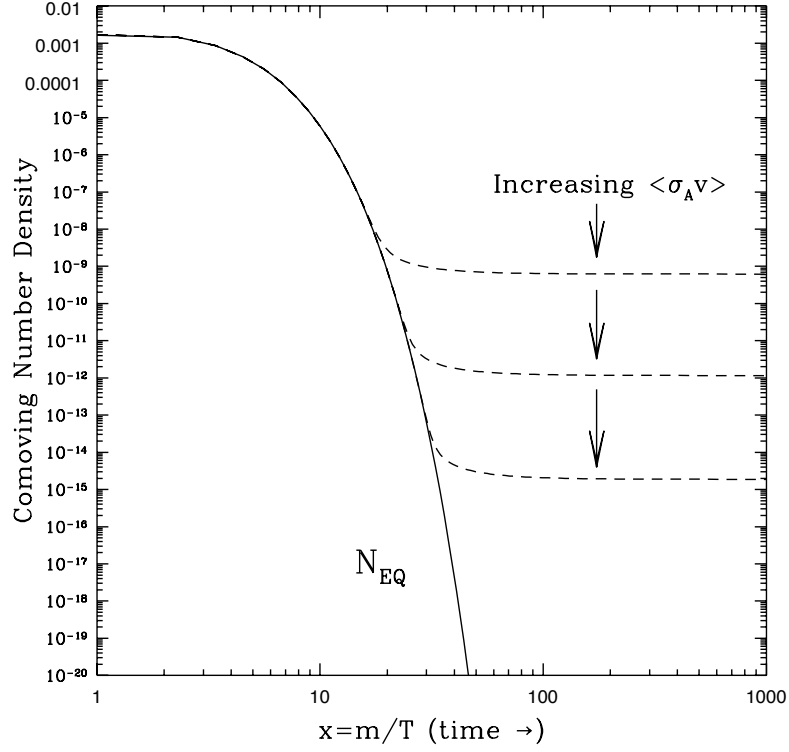
Figure 5.1.: Illustration of the freeze-out mechanism

This means that the hot early universe contains roughly as many χ particles as photons. In the course of time, the temperature decreases heavily and the number density in thermal equilibrium becomes exponentially suppppressed.

All in all, the Boltzmann equation describes the so-called *freeze-out mechanism* illustrated in figure 5.1 (taken from [39]). This plot shows the number of χ particles per comoving volume in dependence of time, the latter being parametrised as $x = m_\chi/T$. In the early universe, the χ particles are in thermal equilibrium, i.e. they are created and destroyed in equal rates. The expansion of the universe is negligible and the number density indicated by the solid line is initially almost constant. For smaller temperatures, annihilation dominates over creation and the number density decreases exponentially. However, at a certain point the Hubble expansion is not negligible anymore and the χ particles *freeze out*. The interaction rate falls below the expansion rate and the number of particles per comoving volume stays asymptotically constant. This remnant is called the relic density. The associated chemical decoupling is shown by the dashed lines in figure 5.1 and depends on the thermally averaged cross section. Larger cross sections delay the freeze-out and lead to a smaller resulting relic density.

To allow for comparison with the experimentally determined cold dark matter density Ω_{CDM} (cf. subsection 3.1.4), we have to multiply the number density by the mass of the χ particle and divide by the critical density. The result is roughly antiproportional to the thermally averaged cross section $\langle \sigma v \rangle$.

$$\Omega_\chi h^2 = \frac{n m_\chi}{\rho_{\mathrm{c}}} \sim \frac{1}{\langle \sigma v \rangle}. \tag{5.4}$$

5.2.2. Boltzmann equation including coannihilations

We continue by generalising the formalism of the previous section to a more realistic scenario involving coannihilating particles, wherein we basically follow [183]. We assume that N additional particles exist which are labelled $\chi_1, \chi_2, ..., \chi_N$ and ordered by mass, i.e. $m_1 < m_2 < ... < m_N$. In case of the MSSM, N equals the total number of supersymmetric partners and the lightest supersymmetric particle corresponds to χ_1. Postulating that the χ_i interact pairwise, we obtain a system of coupled Boltzmann equations. The number density n_i of particle χ_i is given by

$$
\begin{aligned}
\frac{\mathrm{d}n_i}{\mathrm{d}t} = {} & -3Hn_i - \sum_{j=1}^{N} \langle \sigma_{ij} v_{ij} \rangle \left(n_i n_j - n_i^{\mathrm{eq}} n_j^{\mathrm{eq}} \right) \\
& - \sum_{X} \sum_{j=1}^{N} \left[\langle \sigma_{Xij} v_{ij} \rangle \left(n_i n_X - n_i^{\mathrm{eq}} n_X^{\mathrm{eq}} \right) - \langle \sigma_{Xji} v_{ij} \rangle \left(n_j n_X - n_j^{\mathrm{eq}} n_X^{\mathrm{eq}} \right) \right] \\
& - \sum_{j=1}^{N} \left[\Gamma_{ij}(n_i - n_i^{\mathrm{eq}}) - \Gamma_{ji}(n_j - n_j^{\mathrm{eq}}) \right].
\end{aligned}
\tag{5.5}
$$

In comparison to (5.2), the term proportional to the Hubble expansion rate remains unchanged, whereas the second term is extended and does not only include annihilations ($i = j$) but also coannihilations ($i \neq j$). The generalised (co)annihilation cross section σ_{ij} reads

$$
\sigma_{ij} = \sum_{X} \sigma(\chi_i \chi_j \to X)
\tag{5.6}
$$

and the relative velocity between χ_i and χ_j is given by

$$
v_{ij} = \frac{\sqrt{(p_i p_j)^2 - m_i^2 m_j^2}}{E_i E_j}.
\tag{5.7}
$$

The second line of (5.5) includes scattering or conversion processes of the form

$$
\sigma_{Xij} = \sum_{Y} \sigma(\chi_i X \to \chi_j Y),
\tag{5.8}
$$

where we sum over all Standard Model particles Y. Note that we include all possible conversions of χ_i and all possible conversions leading to χ_i. The third line of (5.5) describes decay processes given by

$$
\Gamma_{ij} = \sum_{X} \Gamma(\chi_i \to \chi_j X).
\tag{5.9}
$$

Just like before, we sum over all Standard Model particles X and include all possible decays of χ_i and all possible decays into χ_i.

Solving this system of coupled Boltzmann equations in full generality seems to be cumbersome. However, due to the fact that the χ_i interact only pairwise, all of them decay or convert into the lightest new particle χ_1 in the course of time. This means that the final relic density of χ_1 particles corresponds to the sum $n = \sum_{i=1}^{N} n_i$. Performing this summation on both sides of (5.5) simplifies the Boltzmann equation and we are left with

$$
\frac{\mathrm{d}n}{\mathrm{d}t} = -3Hn - \sum_{i,j=1}^{N} \langle \sigma_{ij} v_{ij} \rangle \left(n_i n_j - n_i^{\mathrm{eq}} n_j^{\mathrm{eq}} \right).
\tag{5.10}
$$

Conversion and decay processes precisely cancel. This is as expected as the total number of χ particles is only changed by (co)annihilations but not by scattering or decay processes. Nevertheless, the scattering processes are important as they lead to a thermalisation of all individual χ_i, which implies

$$\frac{n_i}{n} \sim \frac{n_i^{\text{eq}}}{n^{\text{eq}}}. \tag{5.11}$$

This allows us to rewrite the Boltzmann equation as

$$\frac{\text{d}n}{\text{d}t} = -3Hn - \left\langle \sigma_{\text{(co)ann}} v \right\rangle \left(n^2 - (n^{\text{eq}})^2 \right) \tag{5.12}$$

and to reobtain the algebraic form of (5.2). Here we have introduced the (co)annihilation cross section $\sigma_{\text{(co)ann}}$ given by

$$\left\langle \sigma_{\text{(co)ann}} v \right\rangle = \sum_{i,j=1}^{N} \left\langle \sigma_{ij} v_{ij} \right\rangle \frac{n_i^{\text{eq}}}{n^{\text{eq}}} \frac{n_j^{\text{eq}}}{n^{\text{eq}}}. \tag{5.13}$$

This quantity includes all possible annihilation and coannihilation processes under which χ particles transform into Standard Model particles. However, coannihilations are accompanied by a Boltzmann suppression factor of the form

$$\frac{n_i^{\text{eq}}}{n^{\text{eq}}} \sim \exp\left(-\frac{(m_i - m_1)}{T} \right), \tag{5.14}$$

which means that coannihilations are negligible unless there is a second particle close in mass to χ_1. In our studies, the lightest particle χ_1 corresponds to the lightest neutralino and possible coannihilation partners include other gauginos. Another typical coannihilation partner within the MSSM is given by the lightest stop (cf. [148–150]). More details on the Boltzmann equation can be found in [182–185].

5.3. Uncertainties of relic density calculations

Having introduced the Boltzmann equation, we collect and briefly comment on the associated theoretical uncertainties. As discussed in section 5.1, these uncertainties have to be minimised to fully benefit from the precise experimental data.

- **Cosmological model**

  Any relic density calculation is based on some underlying cosmological model as e.g. the ΛCDM model. Modifications of the cosmological model affect the relic density calculation in two ways. On the one hand, the extraction of the cold dark matter density from the cosmic microwave background gets altered. In [186] the ΛCDM model was extended by five additional free parameters including non-zero neutrino masses. Given this setup, the cold dark matter density was found to be

$$\Omega_{\text{CDM}} h^2 = 0.115 \pm 0.021 \tag{5.15}$$

  at the 2σ level. In comparison to the WMAP analysis[19], no significant change of the central value was observed, but the associated uncertainty broadened by a factor

---

[19]Planck data were not present at that time. However, the main conclusion of [186] should still hold.

of two. On the other hand, the Boltzmann equation includes the Hubble expansion rate. Variations of this rate during the cosmic evolution directly affect the freeze out and thus the resulting relic density. Even modest variations of the Hubble expansion rate before big bang nucleosynthesis heavily alter the resulting relic density while having no consequences on other cosmological observables (cf. [187]).

- **Three-body final states**

  Relic density calculations are not only affected by cosmological but also by microscopic uncertainties stemming from particle physics. A first example for such an uncertainty is given by three-body final states. Standard relic density calculations implicitly assume that dark matter (co)annihilates or converts dominantly into real two-body final states, i.e. into two on-shell Standard Model particles. However, one might also end up with one real and a second massive virtual particle which subsequently decays into two real particles. Although these processes are of higher-order and usually propagator-suppressed, they can be relevant near production thresholds. Such a situation has been investigated in [188], where it has been shown that the inclusion of the process $\tilde{\chi}_1^0 \tilde{\chi}_1^0 \to t\bar{t}^* \to tW^+b$ may decrease the resulting neutralino relic density by up to 10%.

- **Higher-order corrections**

  Even if three-body final states can be safely neglected and real two-body final states dominate, there is a second microscopic uncertainty affecting the (co)annihilation cross section, namely higher-order corrections. The evaluation of the relevant (co)-annihilation processes is usually restricted to the tree-level and higher-order corrections are either completely neglected or only approximately included via effective masses and effective couplings (cf. [189]). In particular, public codes like `DarkSUSY` or `micrOMEGAs` are following this approach. However, it is well known that QCD corrections may shift cross sections by up to $30 - 40\%$. These shifts of cross sections result in a shift of the neutralino relic density in the MSSM parameter space which is found to be larger than the experimental uncertainty stemming from the Planck data (cf. e.g. [147–150]). Therefore, higher-order corrections have to be taken into account to precisely identify the cosmologically preferred region of the MSSM. The calculation of these kinds of radiative corrections and the analysis of their phenomenological impact is the original aim of the `DM@NLO` project (cf. chapter 6). We also stress that the inclusion of NLO corrections permits to estimate the remaining theoretical uncertainty in terms of a variation of the renormalisation scale, which is not possible in a consistent way at tree-level (cf. [190]).

- **Thermal corrections**

  Perturbative calculations in the framework of quantum field theory such as the calculation of higher-order corrections within the `DM@NLO` project are based on the evaluation of the scattering matrix S. This unitary matrix connects asymptotically free particles and can be expanded into the Dyson series [172]. However, in case of non-zero temperatures such as the temperature at and before freeze-out, quantum mechanics can not solely be described by the S matrix anymore and one has to revert to methods of finite temperature field theory [191].

  This machinery has been applied to relic density calculations in e.g. [192, 193] and in

particular to neutralino dark matter in [194]. Even though specific and parameter-sensitive scenarios (including e.g. stau coannihilation) were investigated in [194], the final modification of the relic density was found to be of $\mathcal{O}(10^{-4})$, which is well below recent experimental sensitivity.

An extensive study of finite temperature effects on relic density calculations at NLO was performed in [195]. The main results of this paper are threefold. Firstly, it was shown that the algebraic structure of the Boltzmann equation as given in (5.12) is reobtained even when derived from general principles of non-equilibrium quantum field theory at NLO accuracy. Secondly, thermal corrections to the (co)annihilation cross section were determined and found to be of $\mathcal{O}(\alpha T^2/m_\chi^2)$. Here α denotes the fine structure constant and m_χ the WIMP mass. As usually $T \ll m_\chi$ at freeze-out, thermal corrections are smaller than the previously mentioned zero temperature higher-order corrections. Finally, the cancellation of infrared divergences (cf. section F.1) was investigated in detail and it was confirmed that the thermally averaged annihilation cross section is a well-defined quantity also at non-zero temperatures.

We finally mention [196, 197], where the QCD equation of state has been investigated in the context of relic density calculations. The derivation of the Boltzmann equation bases on the assumption that quarks and gluons can be treated as an ideal gas for temperatures above $T_{\mathrm{QCD}} \sim 200$ MeV. However, significant deviations from ideal behaviour were found for temperatures up to a few GeV. Incorporating these deviations into an improved QCD equation of state increases the resulting relic density by up to 3.5%.

- **Determination of physical spectrum**

  Another possible uncertainty stems from the determination of the physical spectrum of the considered WIMP model. In case of the MSSM, practical calculations are usually performed within a phenomenological model such as the pMSSM (cf. section 2.5) and the required physical spectrum, i.e. all the particle masses and mixing angles, is calculated numerically by a spectrum generator such as `SPheno` (cf. [198, 199]). This calculation is based on solving renormalisation group equations (cf. section G.4) up to a certain loop order for a given set of input parameters. However, depending on the precision of the numerical routines, different generators may lead to different spectra for the same input (cf. [200]). Although these differences were found to be small in general, it was shown that in some scenarios even small mass deviations of 1% may modify the resulting relic density by 10% (cf. [201]).

5.4. Gaugino (co)annihilation into quarks at $\mathcal{O}(\alpha_s)$

In this section we briefly present the calculation of SUSY QCD corrections to gaugino (co)annihilation into quarks, i.e. to processes of the form

$$\tilde{\chi}_i^0 \tilde{\chi}_j^0 \to q\bar{q}, \quad \tilde{\chi}_k^\pm \tilde{\chi}_i^0 \to q\bar{q}' \quad \text{and} \quad \tilde{\chi}_k^+ \tilde{\chi}_l^- \to q\bar{q}, \tag{5.16}$$

where $i, j = 1, 2, 3, 4$, $k, l = 1, 2$ and $q = u, d, c, s, t, b$ can be chosen independently. The quark type q' is fixed by charge conservation. These processes are referred to as neutralino annihilation, neutralino-chargino coannihilation and chargino annihilation in the following
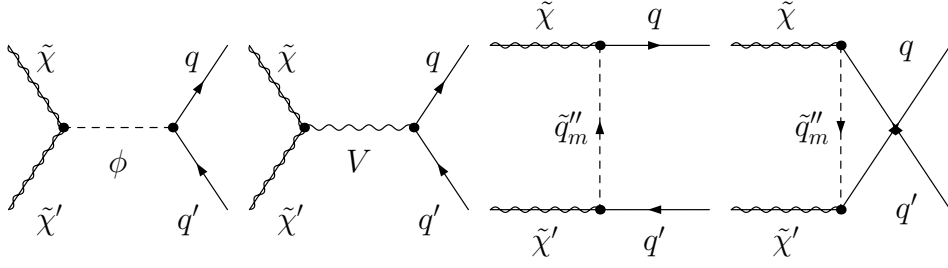
Figure 5.2.: Tree-level contributions to gaugino (co)annihilation

Table 5.1.: Possible gaugino (co)annihilation channels

Initial state	s-channel		t-channel	u-channel	Final state
	ϕ	V	$\tilde{q}''_m$	$\tilde{q}''_m$	
$\tilde{\chi}\tilde{\chi}' = \tilde{\chi}^0_i \tilde{\chi}^0_j$	h^0, H^0, A^0, G^0	Z^0	$q'' = q$	$q'' = q$	$q' = q$
$\tilde{\chi}\tilde{\chi}' = \tilde{\chi}^+_k \tilde{\chi}^0_i$	H^+, G^+	W^+	$q'' \overset{!}{\neq} q$	$q'' = q$	$q' \overset{!}{\neq} q$
$\tilde{\chi}\tilde{\chi}' = \tilde{\chi}^+_k \tilde{\chi}^-_l$	h^0, H^0, A^0, G^0	Z^0, γ	$q'' \overset{!}{\neq} q$, absent if $q = d, s, b$	$q'' \overset{!}{\neq} q$, absent if $q = u, c, t$	$q' = q$

and contribute dominantly to the (co)annihilation cross section $\sigma_{(\mathrm{co})\mathrm{ann}}$ entering the Boltzmann equation in many scenarios of the MSSM.[20] As discussed before, the inclusion of the corresponding radiative corrections reduces the theoretical uncertainty of the resulting neutralino relic density.

5.4.1. Tree-level processes

The Feynman diagrams of the relevant tree-level diagrams are shown in generalised notation in figure 5.2. This notation is understood as follows: The initial state consists of two gauginos $\tilde{\chi}$ and $\tilde{\chi}'$ which are either given by two neutralinos, one chargino and one neutralino or two charginos as explicated in (5.16). If there is only one chargino involved, it is chosen to be the upper gaugino $\tilde{\chi}$ and to be positively charged by convention. The respective processes including one negatively charged chargino are related by charge conjugation. In case of chargino annihilation, we choose the upper gaugino $\tilde{\chi}$ to be positively charged and the lower gaugino $\tilde{\chi}'$ to be negatively charged. The final state consists of a quark-antiquark pair. If the initial state is electrically neutral, i.e. in case of neutralino or chargino annihilation, this pair consists of two quarks of the same type $q = q'$.[21] In case of neutralino-chargino coannihilation, the final state consists of an up-type quark q and the corresponding down-type quark q'. A prominent example for such a process is given by $\tilde{\chi}^+_1 \tilde{\chi}^0_1 \to t\bar{b}$. These initial and final states can be connected in four topologically

---

[20] Note that coannihilation processes as e.g. $\tilde{\chi}^0_1 \tilde{\chi}^0_2 \to q\bar{q}$ are subsumed under neutralino annihilation in this nomenclature. In the same way, coannihilation processes of the form $\tilde{\chi}^+_1 \tilde{\chi}^-_2 \to q\bar{q}$ are simply referred to as chargino annihilation.

[21] We neglect flavour mixing effects in the following, i.e. we choose the Cabibbo-Kobayashi-Maskawa matrix to be the unit matrix.
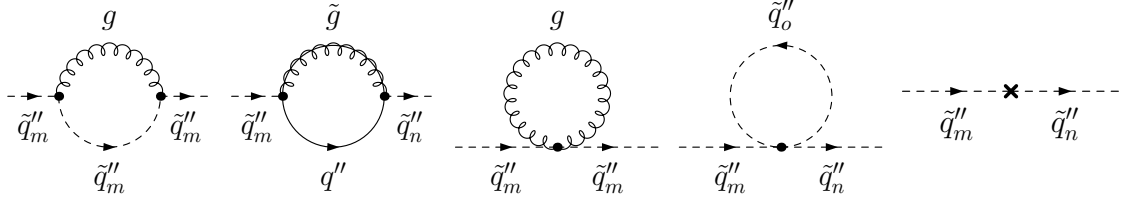
Figure 5.3.: Propagator corrections (first four diagrams) and associated counterterm (rightmost diagram) for gaugino (co)annihilation

different ways: s-channel exchange of a scalar boson ϕ[22], s-channel exchange of a vector boson V, t-channel exchange of a squark $\tilde{q}_m''$ and u-channel exchange of a squark $\tilde{q}_m''$, where $m = 1, 2$. To be more precise, the mediated particles can be chosen as listed in table 5.1. Note that we include the Goldstone bosons G^0 and G^+ explicitly as we are working in the Feynman gauge.[23] The squark type of $\tilde{q}_m''$ occuring in the t- and u-channels is fixed by charge conservation. We stress that in case of chargino annihilation, depending on the final quark type q, either the t- or the u-channel exists.

The tree-level cross section is obtained by standard methods of perturbation theory (c.f. e.g. [172]). The first step is to write down the amplitudes of all tree-level processes $\mathcal{M}_{\text{tree}}$ and square this sum afterwards. Having the squared tree-level amplitude at hand, we have to average over initial and sum over final state spins. Moreover, we include a colour factor of $N_C = 3$ to account for the coloured quarks in the final state. The last step is to carry out the integration over the $2 \to 2$ phase space and divide by the associated flux factor. A detailed tree-level calculation of this kind can be found in e.g. section 3.2 of [57], where the process $\tilde{\chi}_1^0 \tilde{\chi}_1^0 \to A^0 \to \bar{b}b$ is considered. We finally stress that all tree-level cross sections have been numerically compared with `CalcHEP` [202, 203], where we deactivated all effective masses and effective couplings in `CalcHEP` to allow for a meaningful check. Excellent agreement has been found throughout with relative deviations of $\mathcal{O}(10^{-3} - 10^{-5})$.

5.4.2. Virtual corrections

The tree-level processes presented in the previous subsection can be extended by additional internal interactions. These processes correspond to higher orders in perturbation theory and are called virtual corrections. In the following we are focussing on strong virtual corrections of next-to-leading order which involve additional gluons, gluinos, quarks or squarks. As in section 4.4, we distinguish between propagator corrections, vertex corrections and box diagrams. The propagator and vertex corrections give rise to ultraviolet divergences which are regularised via dimensional reduction (cf. chapter F) and removed via renormalisation (cf. chapter G), i.e. by adding suitable counterterms. More precisely, we use the renormalisation scheme presented in section G.5.

The simplest virtual corrections are the propagator corrections depicted in figure 5.3.

---

[22]We stress that the corresponding Yukawa couplings between Higgs bosons and quarks have to be treated with special care. This is described in more detail in subsection G.5.1.

[23]In the last chapter we have omitted all contributions stemming from the pseudoscalar particles A^0 and G^0 as they lead to the effective operator $[\bar{\chi}\gamma_5\chi][\bar{q}\gamma_5 q]$ which is kinematically suppressed. In contrast, we perform a full calculation for non-zero relative velocities here and these contributions are no longer negligible.
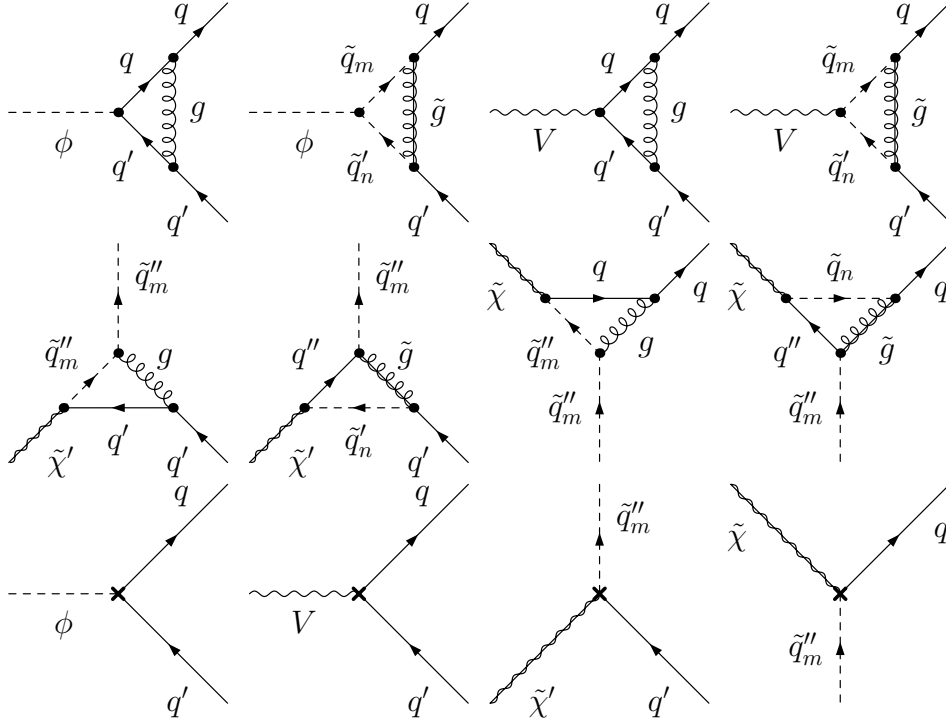
Figure 5.4.: Vertex corrections (upper two rows) and associated counterterms (lower row) for gaugino (co)annihilation

We have encountered these corrections already in subsection 4.4.1 and the evaluation presented there remains completely unchanged. This demonstrates the strength of calculating radiative corrections in generic form: A single result can be reused several times in different contexts. The propagator corrections have to be inserted in the t- and u- channel tree-level diagrams. To finally obtain a correction of $\mathcal{O}(\alpha_s)$ of the cross section, we multiply the corresponding amplitudes $\mathcal{M}_{\mathrm{prop}}$ with the tree-level amplitudes $\mathcal{M}_{\mathrm{tree}}$ as $|\mathcal{M}_{\mathrm{prop}}|^2$ leads to a correction of $\mathcal{O}(\alpha_s^2)$. The same holds true for the associated propagator counterterm which has been discussed in subsection 4.4.2 and is shown on the right of figure 5.3.

The vertex corrections are shown in the upper two rows of figure 5.4. In comparison to the vertex corrections presented in subsection 4.4.3, these corrections are rotated and generalised but otherwise topologically equivalent. Therefore, the evaluation is performed in the same manner as before. The vertex corrections are calculated in generic form and rewritten as loop couplings which are then inserted into the corresponding tree-level diagrams. However, in contrast to the calculation presented in the previous chapter, we keep all parts of the resulting loop couplings and not just those contributing to the dominant effective operators. Apart from that, the involved couplings have to be treated with special care as different particles may occur internally, depending on the concrete initial and final state as listed in table 5.1. We stress that in particular internal squark types can differ from external quark types. The associated vertex counterterms are shown in the lower row of figure 5.4. They correspond to generalisations of those discussed in subsection 4.4.4 and have to be inserted in the tree-level diagrams in the same way as the vertex corrections. Remember that the sums of propagator corrections plus associated
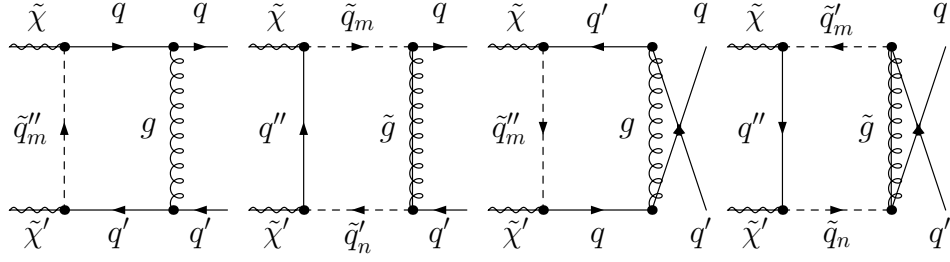
Figure 5.5.: Box contributions to gaugino (co)annihilation

counterterm and vertex corrections plus associated counterterms have to be ultraviolet finite. This has been checked explicitly for every possible initial and final state by Moritz Meinecke and the author of this thesis.

We are left with the box diagrams shown in figure 5.5. In contrast to the propagator and vertex corrections, a modular approach is not possible here as the boxes are not inserted into tree-level diagrams but form complete $2 \to 2$ processes themselves. In subsection 4.4.5 we have calculated these box topologies in rotated form and kept only those parts leading to the dominant effective operators. These results can not be directly transferred to the present situation and an independent calculation has to be performed. This calculation has been carried out by Karol Kovařík with the help of `Mathematica` and `FeynCalc` [178] and the numerical implementation into `DM@NLO` (cf. chapter 6) has been done by the author of this thesis.

5.4.3. Real corrections

The virtual corrections discussed in the previous subsection lead to ultraviolet divergences which have been removed by adding suitable counterterms. However, these loop diagrams also give rise to a second class of divergences, namely infrared divergences (cf. section F.1). Infrared divergences are connected to the low energy regime of the respective theory. In the last chapter these divergences cancelled precisely during the matching procedure as the low energy behaviour of full and effective theory has to be the same (cf. section 4.5). In the present case, we are not performing an effective but a full calculation of the gaugino (co)annihilation cross section.

The cancellation of infrared divergences in the present situation is guaranteed by the *Bloch-Nordsieck* and *Kinoshita-Lee-Nauenberg theorems* (cf. [204–206]). As described in section F.1, infrared divergences cancel automatically if so-called inclusive quantities are considered. The gaugino (co)annihilation cross section we are interested in becomes an inclusive quantity if not only virtual but also real corrections are included. Real corrections are given by processes in which an additional gluon is emitted, i.e. by $2 \to 3$ processes of the form $\tilde{\chi}\tilde{\chi}' \to q\bar{q}'g$. The associated Feynman diagrams are shown in figure 5.6. The additional gluon can either be emitted from one of the final state quarks or – in case of a t- or u-channel process – the exchanged squark.

The calculation of the real corrections follows the usual path: One has to write down all fundamental amplidutes $\mathcal{M}_{\mathrm{real}}$ and square them to obtain a correction of the cross section of $\mathcal{O}(\alpha_s)$. In contrast to the virtual corrections, we do not multiply with the tree-level amplitudes. On the one hand, we have to multiply by another real amplitude to end up with a correction of $\mathcal{O}(\alpha_s)$ as a single real amplitude is only of $\mathcal{O}(g_s)$. On the other hand,
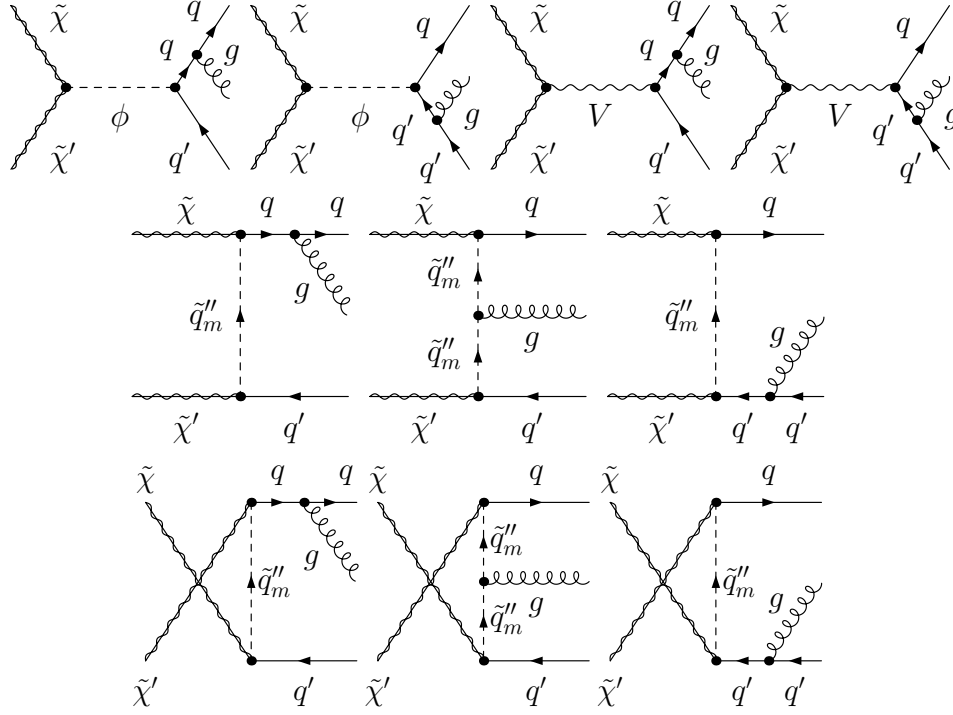
Figure 5.6.: Real corrections to gaugino (co)annihilation

we can not combine the $2 \to 3$ real corrections with the $2 \to 2$ tree-level processes as the underlying phase spaces differ.

These amplitudes have been calculated by Moritz Meinecke with the help of `Mathematica` and `FeynCalc`. However, another technical difficulty arises at this point. The cross section at NLO as a whole is infrared safe and consists of the tree-level contribution and its virtual and real corrections.

$$\sigma^{\text{NLO}} = \int_{2 \to 2} d\sigma^{\text{tree}} + \int_{2 \to 2} d\sigma^{\text{virtual}} + \int_{2 \to 3} d\sigma^{\text{real}}. \tag{5.17}$$

Even though the sum as a whole is infrared safe, the last two terms themselves are not. This is problematic as they are integrated over different phase spaces and these integrations are usually performed numerically. The numerical integrations result in two ill-defined expressions which lead to an ill-defined NLO cross section. To obtain a physically meaningful result and to check the cancellation of infrared divergences explicitly while still performing the phase space integration numerically, one has to render both of the integrands infrared safe. This modification has to be such that the final cross section remains unchanged. There exist basically two popular but sophisticated methods to do so, the so-called *phase space slicing* [207] and the *dipole subtraction method* [208–211]. Both of these methods have been applied by Moritz Meinecke to obtain an infrared safe gaugino (co)annihilation cross section. Numerical checks of the implemented results and the associated infrared safety have been performed by Moritz Meinecke and the author of this thesis. The final result was found to be infrared safe and independent of the chosen method. For more details on the calculation of real corrections to gaugino (co)annihilation into quarks we refer to [63].

6. The `DM@NLO` project

The neutralino-nucleon cross section and relic density calculations presented in the last two chapters have been implemented in the Fortran package `DM@NLO` (cf. [9]). In the following we briefly introduce this project and describe its interface to `micrOMEGAs`. Moreover, we comment on the chronological development of `DM@NLO` and its subprojects.

6.1. Basic idea of the `DM@NLO` project

As described in the previous chapter, the recent neutralino relic density can be obtained by solving the Boltzmann equation. Assuming that cold dark matter solely consists of neutralinos, the predicted value may then be compared with the Planck limit. We stress again that this measurement is very precise, the relative error amounts to roughly $\pm 2\%$. To allow for an adequate comparison, the theoretical calculation should be of similar precision. However, the resulting neutralino relic density depends on the (co)annihilation cross section $\sigma_{(\mathrm{co})\mathrm{ann}}$ which includes all processes, where two SUSY particles (co)annihilate into Standard Model particles. These processes are subject to radiative corrections. It is well known that in particular QCD corrections may shift cross sections by up to 30-40%. The idea of the `DM@NLO` project is to perform a full $\mathcal{O}(\alpha_s)$ calculation of the (co)annihilation cross section $\sigma_{(\mathrm{co})\mathrm{ann}}$ in order to reduce the theoretical uncertainty of the predicted neutralino relic density and to allow for an adequate comparison with the precise experimental data. This is of special importance when the relic density is used to constrain the MSSM parameter space. Note that these radiative corrections are either neglected or only approximatively included in publicly available codes like `micrOMEGAs` or `DarkSUSY`.

The typical steps of a relic density calculation with `DM@NLO` are illustrated in figure 6.1. The starting point is the definition of a concrete SUSY scenario. In this thesis we work within the so-called phenomenological MSSM (pMSSM) with eleven free parameters as described in section 2.5. The chosen pMSSM parameters are handed over to a spectrum generator which determines the physical SUSY spectrum, i.e. all the particle masses and mixing angles, by solving the corresponding renormalisation group equations (cf. section G.4) numerically. We choose to work with `SPheno` [198, 199]. Other possible generators include `SuSpect` [212], `ISAJET` [213] and `SOFTSUSY` [214].

The obtained physical spectrum is imported by `micrOMEGAs`, which solves the Boltzmann equation numerically and determines the desired neutralino relic density. Before doing this, the relevant (co)annihilation cross sections of the model have to be given. This part of the calculation is usually performed by `CalcHEP` [202, 203]. Afterwards the resulting tree-level cross sections are imported by `micrOMEGAs`. To approximate certain one-loop effects, effective couplings and masses are introduced. However, there are no full one-loop corrections implemented in `micrOMEGAs`.[24]

---

[24] Albeit there are processes implemented which are inherently of one-loop order, as e.g. $\tilde{\chi}_1^0 \tilde{\chi}_1^0 \to \gamma\gamma$.
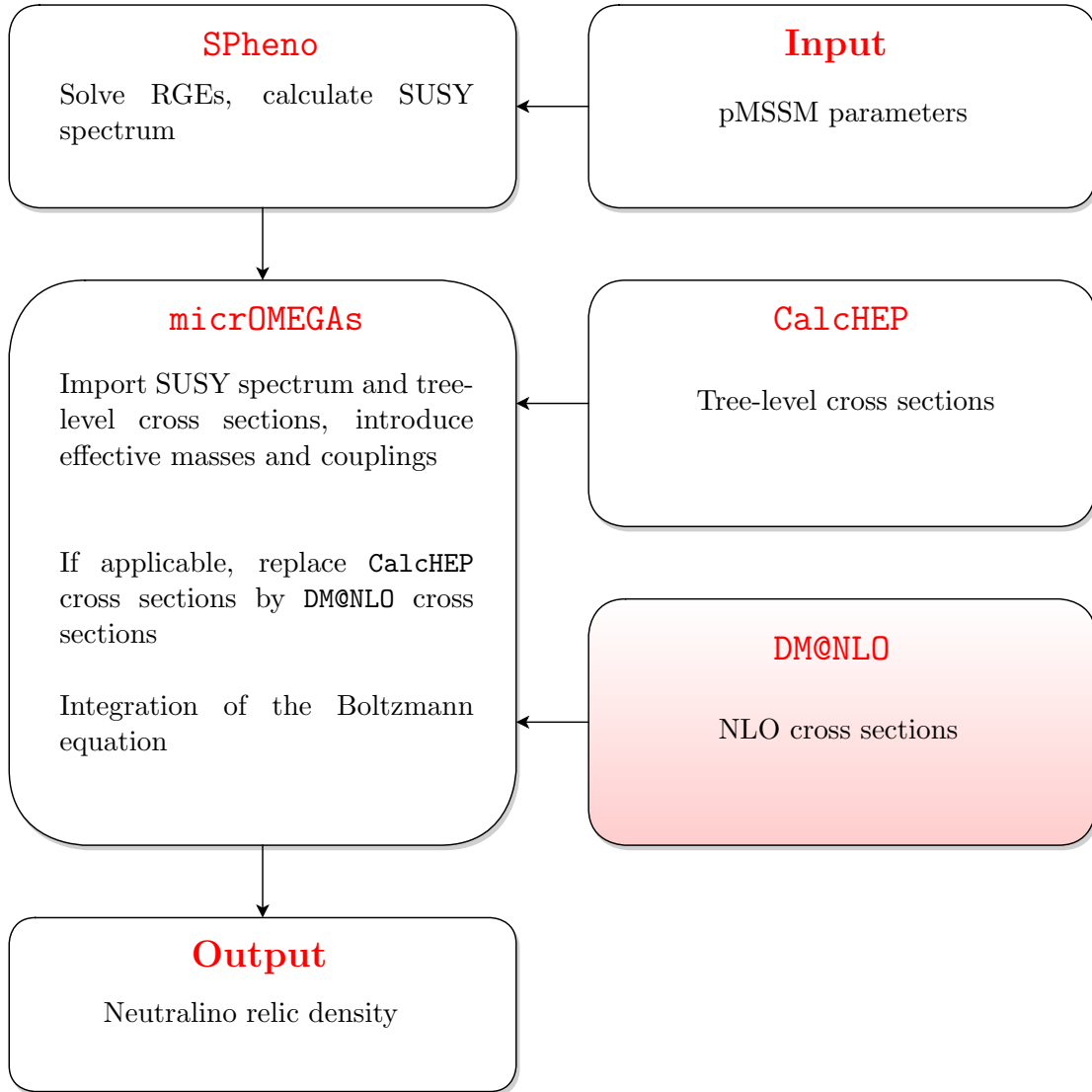
Figure 6.1.: Flowchart of a relic density calculation with `DM@NLO`

At this point our project `DM@NLO` enters the stage. If a certain (co)annihilation process is relevant for the determination of the relic density and this process is available at $\mathcal{O}(\alpha_s)$ in `DM@NLO`, we replace the corresponding `CalcHEP` cross section by ours. In this way we modify the resulting neutralino relic density and reduce its theoretical uncertainty. The impact of the NLO corrections on the relic density is investigated numerically in the next chapter.

We also mention the `SloopS` project, which can be seen as complementary to `DM@NLO`. The idea of the project is very similar, the difference being that electroweak corrections to σ_{ann} are calculated. Some selected results can be found in [215, 216]. However, due to the large number of involved diagrams, the evaluation has to be performed automatically, which leads to additional problems.

6.2. Subprojects within `DM@NLO`

At this time, there are five completed `DM@NLO` subprojects which we present in this section.

- `ntnt2qq`

  The `DM@NLO` project was initiated by Björn Herrmann, Michael Klasen and Karol Kovařík around 2006. The starting point was a SUSY QCD one-loop calculation of the process $\tilde{\chi}_1^0 \tilde{\chi}_1^0 \to A^0 \to b\bar{b}$. This process is dominant in the so-called Higgs-funnel region of the constrained MSSM. Therefore, the resulting relic density in the Higgs-funnel region heavily depends on this process and its radiative corrections. The results of this calculation contributed to the diploma thesis of Björn Herrmann [217] and have been published in [218]. In 2013 the calculation has been performed again by the author of this thesis, where additional two-loop contributions to the Yukawa coupling of A^0 and bottom quarks have been taken into account [57].

  The chronological next step was the complete calculation of the processes

  $$\tilde{\chi}_1^0 \tilde{\chi}_1^0 \to b\bar{b} \quad \text{and} \quad \tilde{\chi}_1^0 \tilde{\chi}_1^0 \to t\bar{t} \tag{6.1}$$

  at $\mathcal{O}(\alpha_s)$. This project is called `ntnt2qq` (sometimes also `ntnt2bb`) and the results have been published in [219, 220]. A more detailed description can be found in the PhD thesis of Björn Herrmann [181].

- `ChiChi2qq`

  The `ChiChi2qq` project was started by Björn Herrmann, Michael Klasen and Karol Kovařík directly after the `ntnt2qq` project and is meant as a generalisation of the latter. More precisely, all gaugino[25] annihilation and coannihilation processes of the form

  $$\tilde{\chi}_i^0 \tilde{\chi}_j^0 \to q\bar{q}, \quad \tilde{\chi}_k^\pm \tilde{\chi}_i^0 \to q\bar{q}' \quad \text{and} \quad \tilde{\chi}_k^+ \tilde{\chi}_l^- \to q\bar{q} \tag{6.2}$$

  have been implemented at $\mathcal{O}(\alpha_s)$. Note that all kinds of combinations are included, i.e. $i, j = 1, 2, 3, 4$, $k, l = 1, 2$ and $q = u, d, c, s, t, b$. The quark q' is fixed by charge conservation. We stress that this generalisation is quite extensive. Whereas the `ntnt2qq` project includes exactly two processes, the `ChiChi2qq` project covers 108 different processes in total.[26]

  However, for several reasons the project was not finished before 2014. The real corrections were calculated by Moritz Meinecke [63]. Box contributions and missing photon processes were implemented by Karol Kovařík and the author of this thesis. The whole code was checked and debugged by Moritz Meinecke and the author of this thesis. The results of this project have been published in [147] and the underlying calculation is briefly presented in section 5.4.

- `NeuQ2qx`

  Apart from coannihilating with another gaugino, the neutralino might also coannihilate with a squark if the mass difference between them is small enough. The prime

---

[25]We stick to the nomenclature introduced in chapter 2: Charginos and neutralinos are called gauginos, whereas gluinos are not.

[26]There are $(4 + 3 + 2 + 1) \cdot 6 = 60$ different possible realisations for neutralino annihilation, $2 \cdot 4 \cdot 3 = 24$ different neutralino-chargino coannihilation processes and $2 \cdot 2 \cdot 6 = 24$ different combinations for chargino annihilation.

candidate for a light squark in the MSSM is the lightest stop $\tilde{t}_1$. The idea of the `NeuQ2qx` project is to calculate the most important stop coannihilation processes at $\mathcal{O}(\alpha_s)$ to allow for a precise prediction of the relic density in case of sizeable coannihilations between neutralinos and stops. More precisely, the processes

$$\tilde{\chi}_1^0 \tilde{t}_1 \to qV, \quad \tilde{\chi}_1^0 \tilde{t}_1 \to qH \quad \text{and} \quad \tilde{\chi}_1^0 \tilde{t}_1 \to tg \tag{6.3}$$

have been implemented by Julia Harz and Quentin Le Boulc'h. Here $V = \gamma, Z^0, W^+$, $H = h^0, H^0, A^0, H^+$ and $q = t$ or b so that charge is conserved. The results of this project can be found in [148, 149] and the PhD theses [62, 64].

- `QQ2xx`

  For even smaller mass differences between the lightest neutralino and the lightest stop, stop annihilation becomes relevant as well. This is the basis of the `QQ2xx` project executed by Moritz Meinecke, where the processes

  $$\tilde{t}_1 \tilde{t}_1^* \to VV, \quad \tilde{t}_1 \tilde{t}_1^* \to VH \quad \text{and} \quad \tilde{t}_1 \tilde{t}_1^* \to HH \tag{6.4}$$

  have been calculated at $\mathcal{O}(\alpha_s)$. As before, $V = \gamma, Z^0, W^\pm$ and $H = h^0, H^0, A^0, H^\pm$ can be arbitrarily combined as long as charge is conserved. In contrast to the `ChiChi2qq` project, the SUSY QCD corrections occur in the initial rather than the final state. In particular, n gluons can be exchanged between the incoming stop-antistop pair in ladder diagrams. These so-called Coulomb corrections lead to contributions proportional to $(\alpha_s/v)^n$. In the region of low relative velocity v between the incoming stop-antistop pair, this factor can become large and spoil the convergence of the perturbative series in α_s. Hence, these multiple gluon exchanges have to be resummed to all orders in perturbation theory in order to get a reliable result, which is a special feature of the `QQ2xx` project. More details on this project can be found in [63, 150].

  It is planned to extend the `QQ2xx` project to strong interacting final states, i.e. to calculate the full $\mathcal{O}(\alpha_s)$ corrections to the processes

  $$\tilde{t}_1 \tilde{t}_1^* \to gg, \quad \tilde{t}_1 \tilde{t}_1^* \to t\bar{t} \quad \text{and} \quad \tilde{t}_1 \tilde{t}_1 \to tt. \tag{6.5}$$

- `DD`

  The direct detection project (`DD`) substantially differs from all other previous sub-projects. As mentioned before, the original idea of the `DM@NLO` project is to include $\mathcal{O}(\alpha_s)$ corrections to the (co)annihilation cross section entering the Boltzmann equation to allow for a precise prediction of the neutralino relic density. In contrast to that, the aim of the `DD` project is to calculate a second, loop-improved dark matter observable, namely the neutralino-nucleon cross sections which enter the direct detection rate. The underlying fundamental process reads

  $$\tilde{\chi}_1^0 q \to \tilde{\chi}_1^0 q \tag{6.6}$$

  and the corresponding calculations are presented in chapter 4 in great detail.

  The `DD` project is motivated by the fact that the sensitivity of direct detection experiments has increased impressively during the last decade (cf. [7, 8]) and that this

trend is planned to be continued (cf. [221, 222]). Although no indisputable positive signal has been found yet, it is desirable to increase the precision on the theory side as well for mainly two reasons: On the one hand, in case of continous non-detection of WIMPs, improved theoretical precision allows to set more robust bounds on the MSSM parameter space. On the other hand, in case of WIMP detection, precise theoretical calculations permit to reliably identify the WIMP and its properties. In our situation, the theoretical precision is improved by including SUSY QCD corrections to the neutralino-nucleon cross sections. A complete and consistent calculation of this kind has not been done before.

We also stress that the direct detection rate and the relic density are linked at the microscopic level. The fundamental process given in (6.6) corresponds to neutralino annihilation into quarks (as included in the `ChiChi2qq` project) rotated by ninety degrees. Remember that the latter is only one out of many processes incorporated in the (co)annihilation cross section $\sigma_{(\mathrm{co)ann}}$ entering the Boltzmann equation. Other processes include electroweak final states which are not directly subject to QCD corrections. In contrast, the neutralino-nucleon cross sections always involve strong interacting particles and are therefore always affected by QCD corrections.

When including the relic density and the direct detection rate simultaneously to e.g. constrain the MSSM parameter space, both observables have to be calculated in a consistent way. This is of special importance at NLO to avoid mismatches between different renormalisation schemes and to ensure that all parameters are uniquely defined (cf. section G.3). A consistent numerical investigation incorporating both observables is given in the next chapter.

The implementation of the `DD` project has solely been performed by the author of this thesis and can be seen as its core part. Thanks to our modular approach of calculating vertex and propagator corrections, parts of the needed loop amplitudes were already present and could be transferred from the `ChiChi2qq` to the `DD` project.

7. Numerical results

In this chapter we perform a numerical investigation with the help of `DM@NLO` and analyse the phenomenological impact of the radiative corrections calculated in chapters 4 and 5. We examine five pMSSM scenarios which are introduced and described in the next section. A common feature of these scenarios is that they are dominated by gaugino (co)annihilation into quarks. Hence, the resulting neutralino relic density depends sensitively on these kinds of processes and is influenced by the associated NLO corrections. This influence is analysed in great detail and compared with the experimental uncertainty given by the Planck data in section 7.2. Afterwards we combine our relic density and neutralino-nucleon cross section calculations at NLO to heavily constrain the pMSSM parameter space and to precisely predict the neutralino-nucleon cross sections. The resulting shifts of the neutralino-nucleon cross sections due to the inclusion of SUSY QCD corrections are compared with typical nuclear uncertainties. Most of the results presented in this chapter have been published in [103, 147, 190].

7.1. Introduction of reference scenarios

Throughout this thesis we work within the pMSSM with eleven free parameters as presented in section 2.5. The input parameters of our five reference scenarios are listed in table 7.1, where dimensionful quantities are given in GeV and all parameters are defined at a scale $\tilde{M} = 1$ TeV according to the SPA convention [223]. This scale is identified with our renormalisation scale μ, which corresponds to the high scale μ_{high} of our EFT calculation simultaneously. We stress that the chosen pMSSM setup is designed for relic density calculations including light stops (cf. [148–150]). As it has proven sufficient for finding interesting direct detection scenarios, we stick to it for consistency and keep in mind that a more specific pMSSM setup may lead to considerably larger loop contributions to the neutralino-nucleon cross sections. In particular, such a setup should allow for (at least) three independent mass parameters of the first two squark generations, namely $M_{\tilde{q}_{1,2}}$, $M_{\tilde{u}_{1,2}}$ and $M_{\tilde{d}_{1,2}}$. However, we leave this analysis for future work.

Following the procedure described in chapter 6, the pMSSM input parameters are handed over to a spectrum generator to obtain the physical spectrum, i.e. all the particle masses and mixing angles. We choose to work with `SPheno 3.2.3`. The spectrum gained this way is imported by `micrOMEGAs 2.4.1`, which is used to solve the Boltzmann equation. Moreover, the neutralino relic density and neutralino-nucleon cross sections calculated by `micrOMEGAs` are used for comparison. However, we have modified the default configuration of `micrOMEGAs` in three ways. Firstly, we neglect the quark masses of the first two generations in the kinematics. This simplification increases the numerical stability of the implemented dipole subtraction method (cf. subsection 5.4.3) and the numerical stability of loop integrals (cf. chapter F). To allow for Higgs exchange processes, we keep those masses in the Yukawa couplings. This is of particular importance when calculating the spin-independent neutralino-nucleon cross sections, where the Yukawa masses are

Table 7.1.: pMSSM input parameters for five selected reference scenarios

Parameter	Scenario				
	I	II	III	IV	V
$\tan\beta$	13.4	6.6	10.0	13.7	7.0
μ	1286.3	842.3	1100.0	493.0	815.0
m_{A^0}	1592.9	1566.9	1951.4	500.8	1452.8
M_1	731.0	705.4	1848.0	270.0	675.3
M_2	766.0	1928.4	1800.0	1123.4	1423.4
M_3	1906.3	1427.0	1102.3	1020.3	1020.3
$M_{\tilde{q}_{1,2}}$	3252.6	1238.5	3988.5	479.9	809.9
$M_{\tilde{q}_3}$	1634.3	2352.1	2302.0	1535.5	1835.5
$M_{\tilde{u}_3}$	1054.4	774.1	1636.6	836.7	1436.7
$M_{\tilde{l}}$	3589.6	2933.2	1982.1	3469.4	3469.4
A_t	-2792.3	-3174.6	-2495.3	-2070.9	-2670.9

basically factored out of the amplitudes and replaced by the nuclear matrix elements via (4.8). It has been checked explicitly that the effect of this simplification on the final results is negligible. The second modification concerns the scalar coefficients f_{Tq}^N. We are working with `micrOMEGAs 2.4.1` to benefit from our established interface for relic density calculations at NLO. As the scalar coefficients implemented in `micrOMEGAs 2.4.1` are outdated, we have updated them manually to those implemented in the most recent version `micrOMEGAs 4.2.5` as listed in table 4.1. Thirdly, we have modified the treatment of particle widths in `micrOMEGAs` such that they are always activated. By default particle widths are switched on only in a narrow interval around resonances. This last change allows for better comparison of our calculation with `micrOMEGAs` in figures 7.1 and 7.5, but does not affect the resulting neutralino relic density in any scenario.

The physical spectrum generated by `SPheno` is imported by `DM@NLO` as well. However, as we are interested in a consistent calculation of full $\mathcal{O}(\alpha_s)$ corrections, we have to carefully choose a suitable renormalisation scheme and redefine some of the physical parameters. In the following we are working with the hybrid on-shell/$\overline{\text{DR}}$-scheme presented in detail in section G.5. Within this scheme, the top and lighter stop mass are defined on-shell. In contrast, the bottom mass and the strong coupling constant are defined in the $\overline{\text{DR}}$ scheme and calculated by us.

Note that effective field theory calculations such as the calculation of the neutralino-nucleon cross section presented in chapter 4 are usually performed in a minimal scheme like $\overline{\text{MS}}$ or $\overline{\text{DR}}$ (cf. section G.3). Nevertheless, we stick to the hybrid scheme mentioned above for basically three reasons. Firstly, we want to combine our relic density and neutralino-nucleon cross section calculations consistently. This can only be achieved if all parameters are uniquely defined, i.e. if the same renormalisation scheme is used throughout. The hybrid scheme has proven very reliable for relic density calculations at NLO, in particular for scenarios including light stops (cf. [148–150]). Moreover, it has been shown that the on-shell treatment of the top and lighter stop mass leads to improved perturbative stability

Table 7.2.: Gaugino, squark, gluino and Higgs boson masses in GeV, the composition of the lightest neutralino and other selected observables corresponding to the reference scenarios of table 7.1

Observable	Scenario				
	I	**II**	**III**	**IV**	**V**
$m_{\tilde{\chi}_1^0}$	738.2	698.9	1106.7	265.7	669.2
$m_{\tilde{\chi}_2^0}$	802.4	850.5	1114.9	498.4	826.6
$m_{\tilde{\chi}_3^0}$	1288.4	854.0	1855.0	502.6	826.7
$m_{\tilde{\chi}_4^0}$	1294.5	1940.2	1865.6	1135.1	1438.6
$m_{\tilde{\chi}_1^\pm}$	802.3	845.6	1109.6	495.7	819.6
$m_{\tilde{\chi}_2^\pm}$	1295.1	1940.4	1856.3	1135.3	1438.9
$m_{\tilde{u}_1}$	3270.9	1284.0	4024.9	549.5	865.0
$m_{\tilde{d}_1}$	3271.6	1286.1	4025.5	555.7	868.4
$m_{\tilde{t}_1}$	1009.0	874.8	1664.1	834.2	1407.9
$m_{\tilde{b}_1}$	1631.0	2361.9	2311.8	1541.4	1837.3
$m_{\tilde{g}}$	2049.9	1496.8	1303.0	1061.2	1090.7
m_{h^0}	126.3	125.2	126.0	124.8	125.2
m_{H^0}	1592.7	1567.1	1951.5	500.9	1453.0
$m_{H^\pm}$	1595.1	1569.0	1953.2	507.2	1455.1
N_{11}	-0.996	-0.969	0.046	-0.988	-0.972
N_{12}	0.049	0.012	-0.082	0.008	0.018
N_{13}	-0.059	-0.187	0.706	-0.131	-0.178
N_{14}	0.037	0.162	-0.702	0.077	0.152
$\Omega_{\tilde{\chi}_1^0} h^2$	0.1243	0.1034	0.1190	0.1199	0.1179
$\text{BR}(b \to s\gamma)$	$3.0 \cdot 10^{-4}$	$3.2 \cdot 10^{-4}$	$3.2 \cdot 10^{-4}$	$3.6 \cdot 10^{-4}$	$3.3 \cdot 10^{-4}$

in comparison to a definition in the $\overline{\text{DR}}$ scheme (cf. [190]). Thus, it seems plausible to use this scheme in the context of direct detection as well. A second reason is given by the end of subsection 7.3.3, where the aforementioned improved perturbative stability becomes evident once more. The last reason is a more pragmatic one. When using the hybrid scheme, `DM@NLO` and `micrOMEGAs` are using the same on-shell squark masses calculated by `SPheno`, which allows for simpler comparison of the leading order result with `micrOMEGAs`.

Having described the numerical setup, we continue with the phenomenological discussion. Table 7.2 lists gaugino, squark, gluino and Higgs boson masses in GeV, the composition of the lightest neutralino, the neutralino relic density $\Omega_{\tilde{\chi}_1^0} h^2$ in units of the critical density ρ_c and the branching ratio of the decay process $b \to s\gamma$ for the five reference scenarios. The squark masses $m_{\tilde{u}_2}$, $m_{\tilde{d}_2}$, $m_{\tilde{c}_1}$, $m_{\tilde{c}_2}$, $m_{\tilde{s}_1}$ and $m_{\tilde{s}_2}$ are not explicitly shown. However, as we are working with a common soft mass parameter $M_{\tilde{q}_{1,2}}$ for the first two generations, all of these squark masses are very similar. The mass of the pseudoscalar Higgs boson A^0

is an input parameter and shown in table 7.1. Note that m_{H^0} and $m_{H^\pm}$ are roughly the same as the corresponding m_{A^0}, which is in agreement with (2.27) and (2.28). The 4×4 neutralino mixing matrix N is defined in subsection 2.4.2. The elements N_{11}, N_{12}, N_{13} and N_{14} denote the bino, wino and higgsino admixture of the lightest neutralino, respectively. These relative fractions add up to one, i.e. $|N_{11}|^2 + |N_{12}|^2 + |N_{13}|^2 + |N_{14}|^2 = 1$. The neutralino composition is of fundamental importance for the resulting neutralino-nucleon cross sections and discussed in more detail in section 7.3.

All of the reference scenarios fulfill certain experimental bounds. The first bound is given by the mass of the Higgs boson m_{h^0}. Remember that m_{h^0} is not a free parameter of the pMSSM (cf. subsection 2.4.1) but has to be correctly reproduced. More precisely, we demand the mass of the light scalar Higgs boson to lie in the range

$$m_{h^0} = 125 \pm 1.5 \text{ GeV}. \tag{7.1}$$

This range is larger than the recent experimental uncertainty (cf. [224]) and motivated by the limited precision of the spectrum generator `SPheno`. Higher order corrections to the Higgs mass are not implemented yet and may slightly change the resulting Higgs mass for a given set of pMSSM input parameters (cf. [225]).

The second bound is of cosmological origin. We assume that the lightest neutralino solely accounts for the amount of cold dark matter as inferred from the Planck data. However, the values given in table 7.2 are obtained by an (effective) tree-level calculation with `micrOMEGAs`. As we are expecting that this result is modified by our radiative corrections, we apply the Planck limit in rather loose form. We demand the scenarios to lie near the cosmologically preferred region and to fulfill

$$\Omega_{\tilde{\chi}_1^0} h^2 = 0.12 \pm 0.02. \tag{7.2}$$

The branching ratio of the rare process $b \to s\gamma$ is included as the last bound. This electroweak decay has been measured very precisely and no significant deviation from Standard Model predictions has been found. Therefore, any non-SM contribution to this process has to be highly suppressed and the associated branching ratio permits to constrain the MSSM parameter space (cf. e.g. [226–228]). We impose the limit

$$\text{BR}(b \to s\gamma) = (3.42 \pm 0.65) \cdot 10^{-4}, \tag{7.3}$$

which corresponds to the 3σ range given in [229].

Table 7.3 shows the most relevant gaugino (co)annihilation processes into quarks and their relative contributions to the thermally averaged (co)annihilation cross section rounded to full percent for the five reference scenarios. These fractions are based on the (effective) tree-level calculation implemented in `micrOMEGAs`. Processes which contribute less than 1% or which are not implemented in `DM@NLO` are not shown. When performing a relic density calculation, the `CalcHEP` tree-level cross sections of the listed channels are replaced by ours. To be more precise, this replacement works as follows:

- All processes with a relative contribution larger than x_1 to the thermally averaged (co)annihilation cross section are taken into account when calculating the neutralino relic density with `micrOMEGAs`.[27] The corresponding cross sections are imported

---

[27]The parameter x_1 is called `Beps` in `micrOMEGAs`.

Table 7.3.: Most relevant gaugino (co-)annihilation processes into quarks in the reference scenarios of table 7.1

Process	Scenario				
	I	**II**	**III**	**IV**	**V**
$\tilde{\chi}_1^0\tilde{\chi}_1^0 \to t\bar{t}$	1%	15%		10%	52%
$\tilde{\chi}_1^0\tilde{\chi}_1^0 \to b\bar{b}$	9%	6%		78%	40%
$\tilde{\chi}_1^0\tilde{\chi}_2^0 \to t\bar{t}$	3%	12%	3%		
$\tilde{\chi}_1^0\tilde{\chi}_2^0 \to b\bar{b}$	23%	7%	2%		
$\tilde{\chi}_1^0\tilde{\chi}_2^0 \to c\bar{c}$			1%		
$\tilde{\chi}_1^0\tilde{\chi}_2^0 \to s\bar{s}$			2%		
$\tilde{\chi}_1^0\tilde{\chi}_2^0 \to u\bar{u}$			1%		
$\tilde{\chi}_1^0\tilde{\chi}_2^0 \to d\bar{d}$			2%		
$\tilde{\chi}_1^0\tilde{\chi}_3^0 \to t\bar{t}$		9%			
$\tilde{\chi}_1^0\tilde{\chi}_3^0 \to b\bar{b}$		5%			
$\tilde{\chi}_1^+\tilde{\chi}_1^0 \to t\bar{b}$	43%	40%	1%		
$\tilde{\chi}_1^+\tilde{\chi}_1^0 \to c\bar{s}$			9%		
$\tilde{\chi}_1^+\tilde{\chi}_1^0 \to u\bar{d}$			9%		
$\tilde{\chi}_1^+\tilde{\chi}_2^0 \to c\bar{s}$	1%		5%		
$\tilde{\chi}_1^+\tilde{\chi}_2^0 \to u\bar{d}$	1%		5%		
$\tilde{\chi}_1^+\tilde{\chi}_1^- \to t\bar{t}$			3%		
$\tilde{\chi}_1^+\tilde{\chi}_1^- \to b\bar{b}$	1%		3%		
$\tilde{\chi}_1^+\tilde{\chi}_1^- \to c\bar{c}$			2%		
$\tilde{\chi}_1^+\tilde{\chi}_1^- \to s\bar{s}$			1%		
$\tilde{\chi}_1^+\tilde{\chi}_1^- \to u\bar{u}$			2%		
$\tilde{\chi}_1^+\tilde{\chi}_1^- \to d\bar{d}$			1%		
Total	82%	94%	52%	88%	92%

from `CalcHEP`. We are working with $x_1 = 0.001\%$, i.e. we also include processes that contribute only marginally and are not shown in table 7.3.

- If a process possesses a relative contribution larger than x_1 but smaller than or equal to x_2 to the thermally averaged (co)annihilation cross section and is implemented in `DM@NLO`, the corresponding `CalcHEP` cross section gets replaced by our tree-level cross section.[28] The parameter x_2 can be chosen freely, but we recommend and use $x_2 = 2\%$.

- If a process possesses a relative contribution larger than x_2 to the thermally averaged (co)annihilation cross section and is implemented in `DM@NLO`, the corresponding `CalcHEP` cross section gets replaced by our NLO cross section.

---

[28]The parameter x_2 is called `ChannelFilter` in `DM@NLO`.

The second criterion based on x_2 is introduced for practical reasons. As full NLO calculations are far more time conusuming than tree-level calculations, we want to activate the former only when really relevant. If a certain process is less relevant but implemented in `DM@NLO`, we replace the corresponding `CalcHEP` cross section by ours at tree-level for consistency, i.e. to ensure that all parameters appearing in gaugino (co)annihilation processes into quarks are uniquely defined. The given value of $x_2 = 2\%$ has proven reliable in practice and can be seen as a reasonable compromise between accuracy and computation time. If we assume that SUSY QCD corrections modify cross sections by maximally 50%, the error due to the non-activation of NLO corrections for a single process contributing maximally 2% can be naively estimated to be $50\% \cdot 2\% \leq 1\%$. This relative error is smaller than the recent experimental uncertainty given by the Planck data. On the other hand, typical computation times for relic density scans at NLO as presented in the next section amount to a few days if the second criterion is considered. If this discrimination is dropped and all gaugino (co)annihilation processes into quarks are calculated at NLO regardless of their respective relevance, computation times may increase to more than a week without any significant change of the final result.[29]

In the next section, the phenomenology of the first three scenarios is discussed in detail. More precisely, we investigate how the individual channels listed in table 7.3 affect the resulting neutralino relic density and how this result is modified when including NLO corrections. However, let us emphasise a common feature of the first three scenarios at this point: The thermally averaged (co)annihilation cross section can be dominated by processes including not only the lightest neutralino but other gauginos such as $\tilde{\chi}_2^0$, $\tilde{\chi}_3^0$ or $\tilde{\chi}_1^+$ as well. Moreover, the final state may include not only heavy but also light quarks of the first two generations as in scenario III. This fact is the original motivation for the generalisation of the `ntnt2qq` to the `ChiChi2qq` project (cf. chapter 6).

7.2. Neutralino relic density

7.2.1. Analysis of scenario I

Having introduced the reference scenarios, we continue our phenomenological analysis by taking a closer look at the most relevant (co)annihilation processes of scenario I (cf. table 7.3). The dominant channel is given by $\tilde{\chi}_1^+ \tilde{\chi}_1^0 \to t\bar{b}$, followed by coannihilation of the lightest and second lightest neutralino into bottom quarks. Annihilation between lightest neutralinos into bottom quarks ranks third. Top quark final states are disfavoured as $\tan \beta = 13.4$ is rather large, which decreases the Yukawa couplings of up-type quarks and increases the Yukawa couplings of down-type quarks.

The observed hierarchy of (co)annihilation processes is mainly due to Higgs resonances. The first process $\tilde{\chi}_1^+ \tilde{\chi}_1^0 \to t\bar{b}$ occurs preferably via s-channel exchange of a charged Higgs boson H^+. As the total mass in the initial state given by $m_{\tilde{\chi}_1^\pm} + m_{\tilde{\chi}_1^0} = 1540.5$ GeV is close to $m_{H^\pm} = 1595.1$ GeV, this process is resonantly enhanced. The same holds true for the second process $\tilde{\chi}_1^0 \tilde{\chi}_2^0 \to b\bar{b}$, which is preferably realised via s-channel exchange of a pseu-

---

[29]In contrast, the computation time of a relic density scan at leading order usually amounts to less than two or even less than one hour. The given computation times refer to the usage of a single, recent processor. Note that relic density scans can be parallelised easily by dividing the considered parameter space into smaller subspaces and starting an independent scan for each of these subspaces on different machines simultaneously.
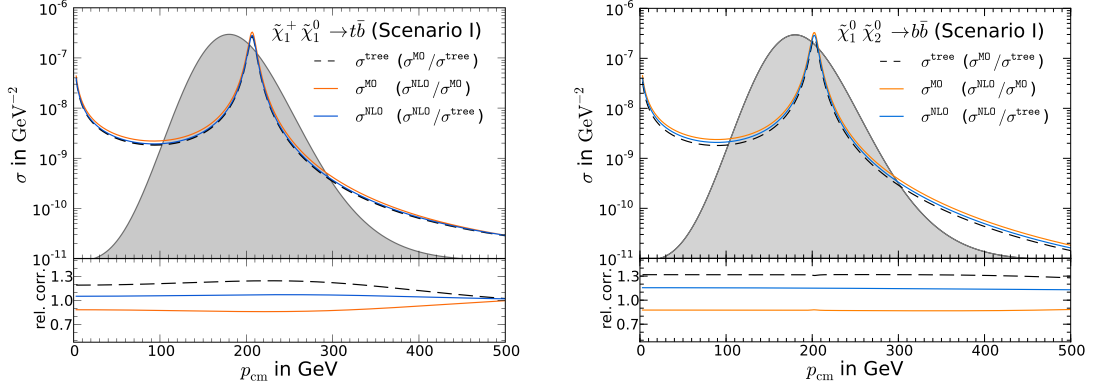
Figure 7.1.: Tree-level (black dashed line), full one-loop (blue solid line) and `micrOMEGAs` (orange solid line) cross sections for selected channels in scenario I

doscalar Higgs boson A^0. Here we have $m_{\tilde{\chi}_1^0} + m_{\tilde{\chi}_2^0} = 1540.6$ GeV and $m_{A^0} = 1592.9$ GeV leading to a resonance as well. Although both of these processes are Boltzmann-suppressed according to (5.14), they turn out to be more relevant than the unsuppressed annihilation process $\tilde{\chi}_1^0 \tilde{\chi}_1^0 \to b\bar{b}$ as $m_{\tilde{\chi}_1^0} + m_{\tilde{\chi}_1^0} = 1476.4$ GeV is further away from the A^0 resonance. Note that the initial states $m_{\tilde{\chi}_2^0} + m_{\tilde{\chi}_2^0} \sim m_{\tilde{\chi}_1^\pm} + m_{\tilde{\chi}_1^\pm} \sim 1600$ GeV are even closer to the A^0 resonance. However, due to their strong Boltzmann suppression, annihilation processes of second lightest neutralinos or charginos are numerically irrelevant in this scenario.

The cross sections of the two most relevant processes are depicted in figure 7.1. More precisely, we show the absolute value of σ in GeV^{-2} in dependence of the momentum in the center-of-mass frame p_{cm} for the processes $\tilde{\chi}_1^+ \tilde{\chi}_1^0 \to t\bar{b}$ and $\tilde{\chi}_1^0 \tilde{\chi}_2^0 \to b\bar{b}$ calculated with `DM@NLO` at tree-level (black dashed line), at NLO (blue solid line) and the corresponding value obtained with `micrOMEGAs` (orange solid line). The grey areas indicate the Boltzmann velocity distributions of the considered gauginos in arbitrary units. The lower parts of the plots show the corresponding ratios of the cross sections (second item in the legends).

The most striking feature of the left plot of figure 7.1 is the previously discussed H^+ resonance at roughly 200 GeV. This resonance is located near the maximum of the thermal distribution, which renders this process highly relevant for the relic density calculation. The black dashed and blue solid lines are lying closely together, the relative shift due to the NLO corrections amounts to less than 10% as shown by the solid blue line in the lower part of the plot. Note that this shift is towards the direction of the orange solid line, i.e. towards the effective tree-level calculation of `micrOMEGAs` which is meant to approximate NLO effects. The deviation between `micrOMEGAs` and our tree-level calculation is rather large and amounts to more than 20% as indicated by the black dashed line in the lower part of the plot. This difference is due to a different treatment of bottom and top masses and the inclusion of effective couplings in `micrOMEGAs`.

The right plot of figure 7.1 looks similar to the left one. Once again, we encounter a pronounced resonance around 200 GeV, which is due to the exchange of pseudoscalar A^0 Higgs bosons in the s-channel this time. The black dashed and blue solid lines are more separated than previously, the NLO corrections lead to a shift of almost 20% in this case. As before, the shift is towards the effective tree-level calculation of `micrOMEGAs`,
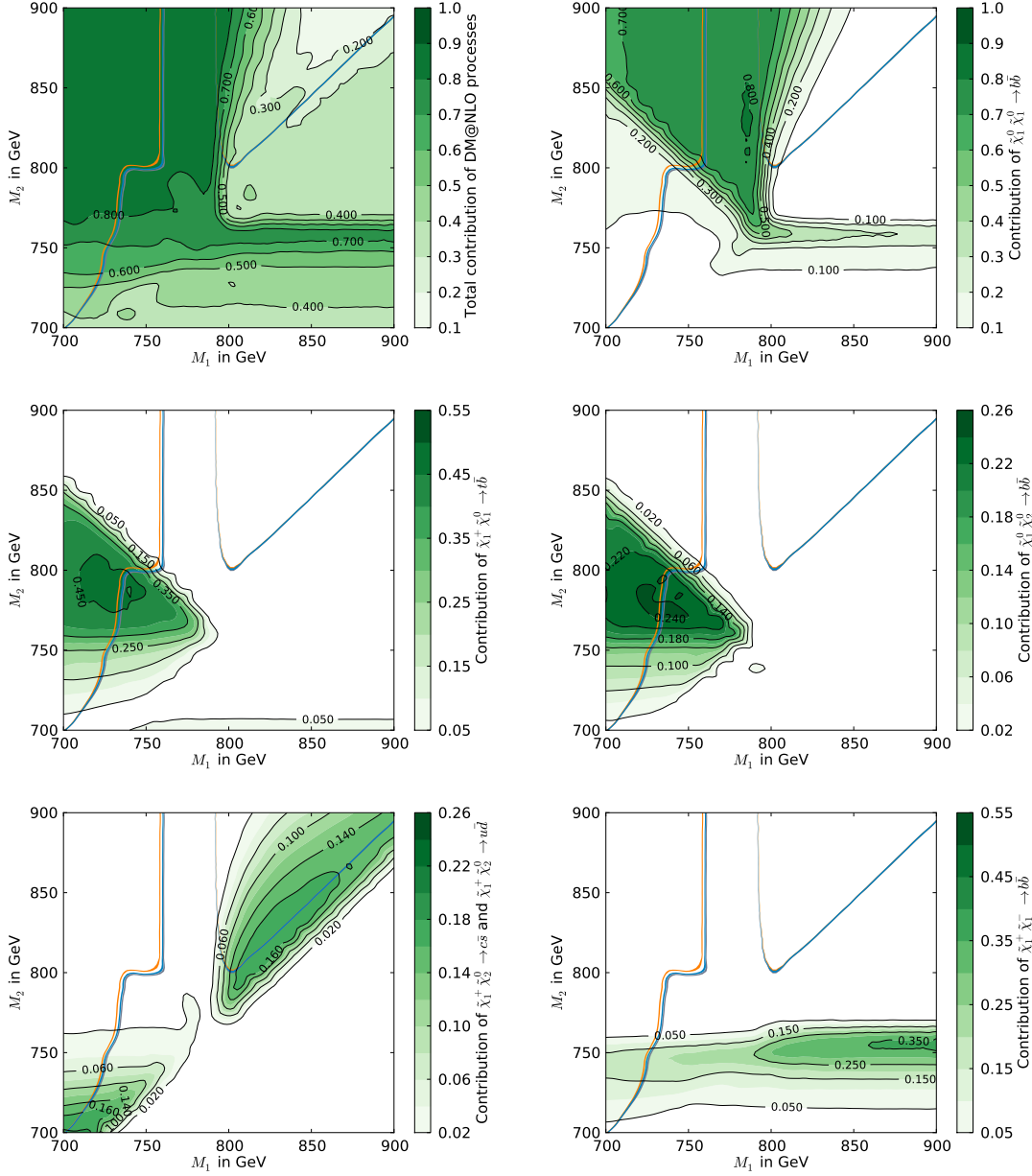
Figure 7.2.: Relative importance of the processes that contribute to the neutralino relic density in the M_1-M_2 plane surrounding scenario I

i.e. towards the orange solid line. The deviation between `micrOMEGAs` and our tree-level correction is even larger and amounts to roughly 30%. This shift is caused by different treatments of the bottom mass and the associated couplings.

We continue by investigating the impact of the individual processes listed in table 7.3 on the resulting neutralino relic density in more detail. The green background contours in the upper left plot of figure 7.2 show the total contribution of gaugino (co)annihilation processes into quarks, i.e. the relative fraction of processes implemented in `DM@NLO`, to the

thermally averaged cross section in the M_1-M_2 plane surrounding scenario I. As a quick reminder: Scenario I is located at $M_1 = 731.0$ GeV and $M_2 = 766.0$ GeV. The contribution of gaugino (co)annihilation into quarks reaches more than 80% in the upper left corner of the plot and drops below 20% in the upper right corner, where electroweak final states become dominant.

The three coloured lines represent the cosmologically preferred part of the parameter space, i.e. the region leading to a neutralino relic density compatible with the Planck limit given in (3.5) when using the standard `micrOMEGAs` calculation (orange), our tree-level calculation (grey) and our full one-loop calculation (blue). Note that these lines are very thin and select only a tiny fraction of the pMSSM parameter space. This demonstrates how constraining the Planck limit actually is, if one assumes lightest neutralinos to fully account for cold dark matter. We continue with the analysis of the individual (co)annihilation processes first and return to the relic density afterwards.

The remaining five plots of figure 7.2 depict the individual contributions from selected processes. The most relevant process in the considered pMSSM parameter plane is given by $\tilde{\chi}_1^0 \tilde{\chi}_1^0 \rightarrow b\bar{b}$ and the corresponding contribution is shown in the upper right plot of figure 7.2. This process makes up more than 70% in large parts of the parameter plane but only about 20% in the center left region near scenario I, where gaugino (co)annihilation still amounts to more than 80% in total. In this part of the parameter space the processes $\tilde{\chi}_1^+ \tilde{\chi}_1^0 \rightarrow t\bar{b}$ and $\tilde{\chi}_1^0 \tilde{\chi}_2^0 \rightarrow b\bar{b}$ contribute up to 45% and 24%, respectively, as shown in the middle plots of figure 7.2. The shape of both contours is very similar as the underlying mechanisms are the same. Both processes are enhanced by Higgs resonances and the involved masses are roughly equal ($m_{\tilde{\chi}_1^+} \sim m_{\tilde{\chi}_2^0}$ and $m_{H^\pm} \sim m_{A^0}$).

The lower left plot of figure 7.2 shows the contributions of the rather exotic processes $\tilde{\chi}_1^+ \tilde{\chi}_2^0 \rightarrow c\bar{s}$ and $\tilde{\chi}_1^+ \tilde{\chi}_2^0 \rightarrow u\bar{d}$ which have been summed as the individual contributions are basically identical. We see that this sum amounts to 16-18% in the cosmologically preferred region, which demonstrates that light quark final states are non-negligible. The contribution of the process $\tilde{\chi}_1^+ \tilde{\chi}_1^- \rightarrow b\bar{b}$ is shown in the lower right plot of figure 7.2 and accounts for 15% inside and up to 35% outside the cosmologically preferred region. Not shown are the less important contributions stemming from the channels $\tilde{\chi}_1^+ \tilde{\chi}_1^0 \rightarrow c\bar{s}$ and $\tilde{\chi}_1^+ \tilde{\chi}_1^0 \rightarrow u\bar{d}$ (up to 10% each) and $\tilde{\chi}_2^+ \tilde{\chi}_2^- \rightarrow b\bar{b}$ (up to 5%).

These findings are quite remarkable. We have analysed the surrounding parameter space of a single scenario and encountered a plethora of different gaugino (co)annihilation processes. Using the filter mechanism described in the previous section, we correct up to twelve processes in parallel in the individual scenarios of figure 7.2. This evidences the necessity to treat gaugino (co)annihilation in full generality when calculating the neutralino relic density in the pMSSM.

Let us now return to the analysis of the relic density. Figure 7.3 shows a more detailed version of the upper left plot of figure 7.2. As before, the coloured lines represent the cosmologically preferred region of the parameter space when calculating the neutralino relic density with `micrOMEGAs` (orange line), `DM@NLO` at tree-level (grey line) or including full $\mathcal{O}(\alpha_s)$ corrections (blue line). These three lines separate, i.e. the impact of the radiative corrections is larger than the experimental uncertainty given by the Planck data. This observation agrees with our previous findings on the cross sections. The dominant processes $\tilde{\chi}_1^+ \tilde{\chi}_1^0 \rightarrow t\bar{b}$ and $\tilde{\chi}_1^0 \tilde{\chi}_2^0 \rightarrow b\bar{b}$ are subject to large radiative corrections of roughly 10% and 20%, respectively. These shifts of cross sections are translated into a shift of the relic density via the Boltzmann equation. The black contour lines denote the relative shift
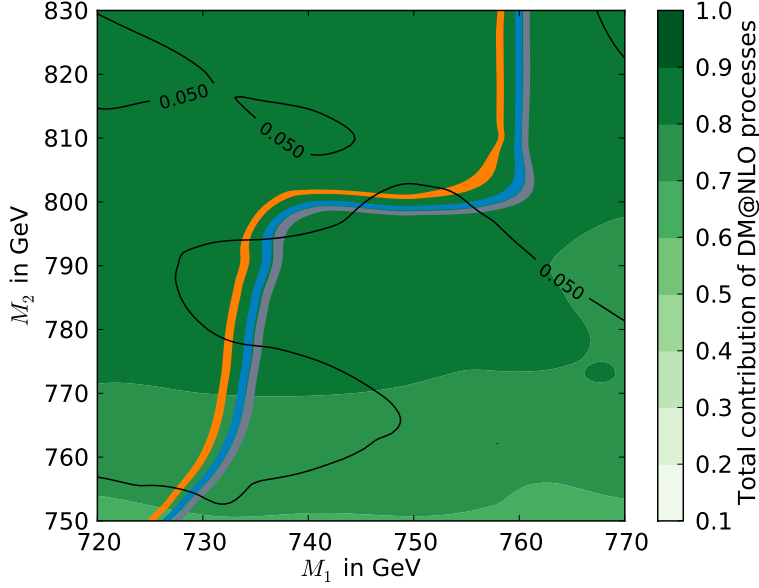
Figure 7.3.: Neutralino relic density in the M_1-M_2 plane surrounding scenario I

between the tree-level and one-loop relic density, i.e. $\left|1-\Omega_\chi^{\mathrm{NLO}}/\Omega_\chi^{\mathrm{tree}}\right|$. In the present case, the latter amounts to roughly 5%, whereas the relic density obtained with `micrOMEGAs` differs by 14% from our tree-level result.

One might wonder if this result is changed again when including not only one- but also two- or three-loop corrections. Although the calculation of these corrections is very laborious and clearly beyond the scope of the `DM@NLO` project, we are able to estimate their impact in terms of a variation of the renormalisation scale. Remember that any regularisation method introduces an artificial scale μ (cf. chapter F). The final result is independent of μ when all orders in perturbation theory are included. If the calculation is restricted up to a certain order, e.g. up to NLO, an unphysical dependence on μ remains. To minimise potentially large logarithms, μ is usually chosen to be of similar size as typical process energies or involved particle masses. In our case, we are following the aforementioned SPA convention and set $\mu = 1$ TeV. However, this choice is basically arbitrary. Hence, we can vary μ by a factor of two and investigate its effect on the corresponding cross sections and the associated neutralino relic density. The resulting shifts can be seen as an indicator for the relevance of the neglected higher-order corrections. We stress that this analysis is not possible at tree-level, meaningful results can only be obtained if a full NLO calculation is performed.

The scale dependence of processes implemented in `DM@NLO` has been investigated in detail in [190]. In this publication scenario I was considered as well and we briefly highlight the respective findings at this point. As already mentioned, the most relevant processes in scenario I are given by $\tilde\chi_1^+\tilde\chi_1^0 \to t\bar b$ and $\tilde\chi_1^0\tilde\chi_2^0 \to b\bar b$, which are preferably realised via resonant Higgs exchanges and of purely electroweak origin at leading order. Thus, one could be led to the naive conclusion that the scale dependence is increased when adding SUSY QCD corrections involving the scale-dependent strong coupling constant. In fact, the opposite is the case here, which is explained as follows. The effect of varying the strong
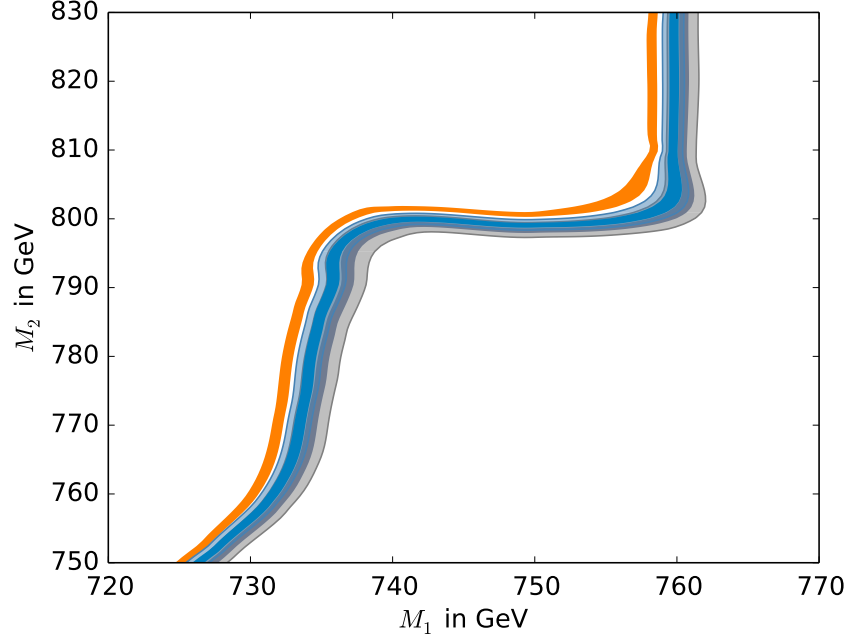
Figure 7.4.: Neutralino relic density in the M_1-M_2 plane surrounding scenario I when varying the renormalisation scale

coupling constant between 500 and 2000 GeV is of minor importance as we are working deeply in the perturbative regime, where α_s is small anyway. In contrast, other scale-dependent parameters such as the bottom quark mass m_b enter the calculation already at tree-level. Remember that m_b is defined within the $\overline{\text{DR}}$ scheme and therefore scale-dependent. This mass appears in the Yukawa couplings between Higgs bosons and bottom quarks, which are crucial in the present case. As a consequence, the scale dependence of m_b dominates the overall scale dependence.

Let us investigate this connection more quantitavely. The tree-level cross section of the process $\tilde{\chi}_1^0 \tilde{\chi}_2^0 \to b\bar{b}$ is decreased by 7% if μ is chosen to be 2000 GeV instead of 1000 GeV and increased by 9% if μ is chosen to be 500 GeV. These shifts are in agreement with the ratios $m_b^2(\mu = 2 \text{ TeV})/m_b^2(\mu = 1 \text{ TeV}) = 0.93$ and $m_b^2(\mu = 0.5 \text{ TeV})/m_b^2(\mu = 1 \text{ TeV}) = 1.09$. When NLO corrections are added and the vertex corrections to the Higgs-quark Yukawa couplings are explicitly included, the scale dependence reduces to less than $\pm 5\%$.

The additional uncertainty in the cross sections translates into an additional uncertainty of the resulting relic density and leads to enlarged cosmologically preferred regions in the pMSSM parameter space. This is shown in figure 7.4, where we have left aside the green contours for better visibility and added grey and blue bands to the original grey and blue lines which indicate the cosmologically preferred regions at tree-level and NLO, respectively. The tree-level and NLO bands clearly overlap. However, note that the blue band is smaller than the grey one, which corresponds to the aforementioned reduction of the scale dependence at NLO. We also stress that the `micrOMEGAs` line lies outside of both bands, which can be traced back to the usage of effective couplings and different treatments of top and bottom masses.
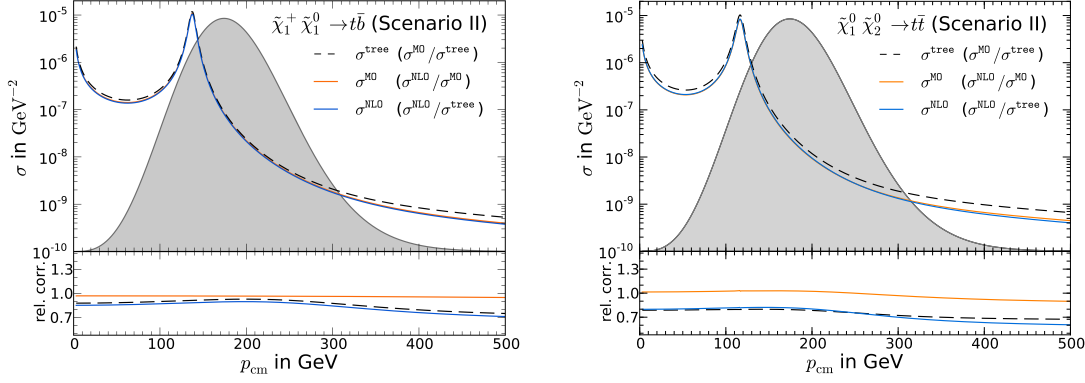
Figure 7.5.: Tree-level (black dashed line), full one-loop (blue solid line) and `micrOMEGAs` (orange solid line) cross sections for selected channels in scenario II

More distinct scale-dependent features have been found in the two other scenarios investigated in [190], which include not only gaugino (co)annihilation but also neutralino-stop coannihilation and stop-antistop annihilation. A peculiarity of the process $\tilde{t}_1\tilde{\chi}_1^0 \to tg$ is the presence of the strong coupling constant at tree-level. The scale-dependence of the latter turns out to be relevant here and is reduced by the inclusion of NLO corrections. In case of stop-antistop annihilation, so-called Coulomb corrections become relevant at low relative velocities. Coulomb corrections are caused by multiple gluon exchanges between the initial squarks in ladder diagrams and have to be resummed to all orders to obtain a reliable result. In the course of this resummation, the so-called Coulomb scale μ_C is introduced, which can be varied independently of the renormalisation scale and constitutes a second source of theoretical uncertainty. For more details on the scale dependence of these processes we refer to [190].

7.2.2. Analysis of scenario II

We continue with the discussion of the most relevant gaugino (co)annihilation processes in scenario II (cf. table 7.3). As before, the dominant channel is given by $\tilde{\chi}_1^+\tilde{\chi}_1^0 \to t\bar{b}$, which contributes 40% to the thermally averaged (co)annihilation cross section. This process is resonantly enhanced again, since we have $m_{\tilde{\chi}_1^+} + m_{\tilde{\chi}_1^0} = 1544.5$ GeV and $m_{H^+} = 1569.0$ GeV. In comparison to the previous scenario, not only $m_{\tilde{\chi}_1^+}$ and $m_{\tilde{\chi}_2^0}$ but also $m_{\tilde{\chi}_3^0}$ are close in mass. Thus, we encounter sizeable contributions from coannihilations between lightest and second or third lightest neutralinos into top quarks, which are preferred over bottom quarks as $\tan\beta = 6.6$ is smaller than previously. Both of these processes are realised via resonant s-channel exchanges of H^0 bosons ($m_{\tilde{\chi}_1^0} + m_{\tilde{\chi}_2^0} = 1549.4$ GeV, $m_{\tilde{\chi}_1^0} + m_{\tilde{\chi}_3^0} = 1552.9$ GeV and $m_{H^0} = 1567.1$ GeV). Pair annihilation of lightest neutralinos into top quarks accounts for 15%. Note that $m_{\tilde{\chi}_1^0} + m_{\tilde{\chi}_1^0} = 1397.8$ GeV is rather far away from the H^0 resonance. In fact, this annihilation process is preferably realised via $\tilde{t}_1$ exchange in the t- or u-channel, which are kinematically favoured as $m_{\tilde{t}_1} = 874.8$ GeV happens to be relatively light in this scenario.

Figure 7.5 shows the cross sections of the processes $\tilde{\chi}_1^+\tilde{\chi}_1^0 \to t\bar{b}$ and $\tilde{\chi}_1^0\tilde{\chi}_2^0 \to t\bar{t}$ in GeV^{-2} in scenario II calculated by `micrOMEGAs` (orange solid line), `DM@NLO` at tree-level
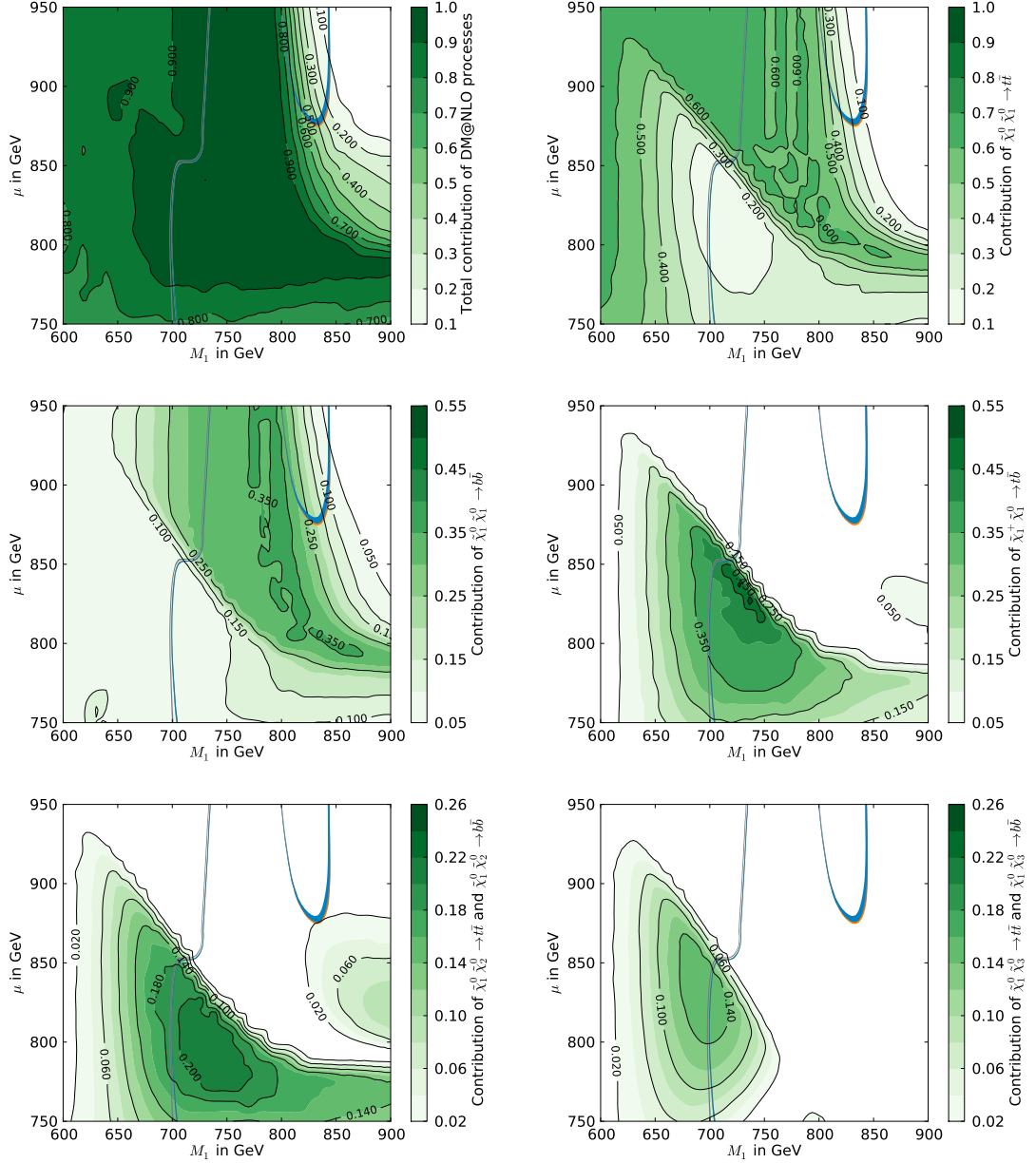
Figure 7.6.: Relative importance of the processes that contribute to the neutralino relic density in the M_1-μ plane surrounding scenario II

(black dashed line) and NLO (blue solid line) in dependence of p_{cm}. As discussed before, both processes are resonantly enhanced and we observe large peaks at 140 GeV and 120 GeV, respectively. The positions of the peaks differ more than in scenario I as $m_{\tilde{\chi}_1^+}$ and $m_{\tilde{\chi}_2^0}$ are less degenerated (cf. table 7.2). As a consequence, the H^0 resonance enhancing the process $\tilde{\chi}_1^0 \tilde{\chi}_2^0 \to t\bar{t}$ is located at lower p_{cm} and further away from the maximum of the thermal distribution shown in grey, which is why this process contributes only 12% to the final relic density, whereas $\tilde{\chi}_1^+ \tilde{\chi}_1^0 \to t\bar{b}$ accounts for 40%. Since both of the processes are
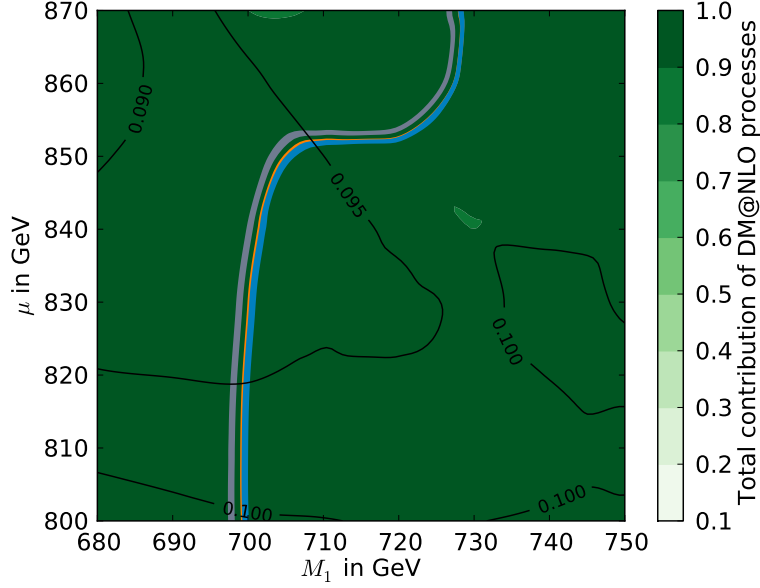
Figure 7.7.: Neutralino relic density in the M_1-μ plane surrounding scenario II

subject to large radiative corrections, the black dashed and blue solid lines cleary separate in the upper parts of the plots. The relative shift amounts to 10-30% in case of neutralino-chargino annihilation and remarkably 20-40% for the process $\tilde{\chi}_1^0 \tilde{\chi}_2^0 \to t\bar{t}$ as depicted by the solid blue lines in the respective lower parts of the plots. However, note that the radiative corrections are well approximated by effective couplings included in `micrOMEGAs` in this case, the orange and blue lines basically coincide in the upper parts of the plots.

The impact of the individual gaugino (co)annihilation processes on the resulting neutralino relic density is shown by the green contours in figure 7.6, where we have investigated the M_1-μ plane surrounding scenario II. Remember that scenario II is located at $M_1 = 705.4$ GeV and $\mu = 842.3$ GeV. The coloured lines represent the cosmologically preferred regions when using `micrOMEGAs` (orange line), `DM@NLO` at tree-level (grey line) and NLO (blue line).

As shown in the upper left plot of figure 7.6, gaugino (co)annihilation makes up more than 90% in a large part of the considered parameter plane but drops to less than 10% in its upper right corner. Here the lightest neutralino becomes degenerated in mass with the lightest stop, rendering neutralino-stop coannihilation and stop-antistop annihilation processes highly relevant for relic density calculations (cf. [148–150]). The overall dominant processes are given by the annihilation processes $\tilde{\chi}_1^0 \tilde{\chi}_1^0 \to t\bar{t}$ and $\tilde{\chi}_1^0 \tilde{\chi}_1^0 \to b\bar{b}$, which contribute about 60% and 35% in the cosmologically preferred region, respectively. However, both of these channels are of minor importance in the center left region near scenario II. In this part of the parameter space, we encounter sizeable contributions from the processes $\tilde{\chi}_1^+ \tilde{\chi}_1^0 \to t\bar{b}$ ($\sim 45\%$), $\tilde{\chi}_1^0 \tilde{\chi}_2^0 \to t\bar{t}$ ($\sim 13\%$), $\tilde{\chi}_1^0 \tilde{\chi}_2^0 \to b\bar{b}$ ($\sim 7\%$), $\tilde{\chi}_1^0 \tilde{\chi}_3^0 \to t\bar{t}$ ($\sim 9\%$) and $\tilde{\chi}_1^0 \tilde{\chi}_3^0 \to b\bar{b}$ ($\sim 5\%$), which are shown in the remaining plots of figure 7.6. Thus, the neutralino relic density is determined by a multitude of processes in parallel again.

To analyse the impact of the radiative corrections on the resulting neutralino relic density, we show a more detailed version of the upper left plot of figure 7.6 in figure 7.7.

Note that the blue and orange lines basically coincide. These lines correspond to the cosmologically preferred region when calculating the neutralino relic density with `DM@NLO` at $\mathcal{O}(\alpha_s)$ and `micrOMEGAs`, respectively. In contrast, the grey line indicating our tree-level calculation is clearly separated. The relative shift between our tree-level and NLO result is very large in this scenario and accounts for almost 10% as shown by the black contour lines. Both of these observations agree with our previous findings on the cross sections. In this scenario, the effective couplings included in `micrOMEGAs` approximate the NLO corrections of the leading processes quite well. Hence, our relic density calculation at $\mathcal{O}(\alpha_s)$ is in good agreement with `micrOMEGAs`. We stress that this may happen but has not to be the case necessarily as illustrated in e.g. scenario I. Moreover, the tree-level cross sections of the considered processes $\tilde{\chi}_1^+ \tilde{\chi}_1^0 \to t\bar{b}$ and $\tilde{\chi}_1^0 \tilde{\chi}_2^0 \to t\bar{t}$ are shifted by 10-30% and 20-40% when including SUSY QCD corrections, respectively. These large shifts lead to the significant deviation between the relic density obtained at tree-level and NLO.

7.2.3. Analysis of scenario III

The phenomenology of the third scenario Is quite different and more complex. Central features are relatively large mass parameters which result in large SUSY particle masses (cf. tables 7.1 and 7.2). Moreover, $m_{\tilde{\chi}_1^0}$, $m_{\tilde{\chi}_2^0}$ and $m_{\tilde{\chi}_1^+}$ are almost degenerated and in contrast to the previous scenarios, the lightest neutralino is mostly higgsino.

The given neutralino admixture increases the coupling to vector bosons, i.e. to Z^0 bosons in case of neutralino annihilation and to W^+ bosons in case of neutralino-chargino coannihilation. Higgs resonances are absent as the gauginos are too heavy, we have e.g. $m_{\tilde{\chi}_1^0} + m_{\tilde{\chi}_1^0} = 2213.4$ GeV and $m_{A^0} = 1951.4$ GeV. Consequently, s-channel processes involving vector bosons contribute significantly. In contrast to Higgs processes, the latter do not include Yukawa couplings and thus do not favour heavy fermions, which is why light quark final states are relevant in this scenario (cf. table 7.3). In fact, the most relevant processes not shown in table 7.3 include light fermions as well and are given by $\tilde{\chi}_1^+ \tilde{\chi}_1^0 \to e^+ \nu_e$, $\tilde{\chi}_1^+ \tilde{\chi}_1^0 \to \mu^+ \nu_\mu$ and $\tilde{\chi}_1^+ \tilde{\chi}_1^0 \to \tau^+ \nu_\tau$, which account for 3% each.

t- and u-channel processes involving squarks of the first two generations are strongly suppressed as those squarks are very heavy (cf. table 7.2). Therefore, all processes leading to light quarks listed in table 7.3 are almost exclusively realised via vector boson exchange in the s-channel. Third generation squarks are lighter and the corresponding t- and u-channel processes are relevant. This is especially true for the lightest stop with a mass of $m_{\tilde{t}_1} = 1664.1$ GeV. As a consequence, the process $\tilde{\chi}_1^0 \tilde{\chi}_2^0 \to t\bar{t}$ contributes slightly more than the processes $\tilde{\chi}_1^0 \tilde{\chi}_2^0 \to c\bar{c}$ or $\tilde{\chi}_1^0 \tilde{\chi}_2^0 \to u\bar{u}$ (cf. table 7.3). On the other hand, the t- and u-channel processes may destructively interfere with the vector boson processes. This happens in case of the process $\tilde{\chi}_1^+ \tilde{\chi}_1^0 \to t\bar{b}$ which makes up only 1%, whereas $\tilde{\chi}_1^+ \tilde{\chi}_1^0 \to c\bar{s}$ and $\tilde{\chi}_1^+ \tilde{\chi}_1^0 \to u\bar{d}$ contribute 9% each.

The cross sections of the processes $\tilde{\chi}_1^+ \tilde{\chi}_1^0 \to c\bar{s}$ and $\tilde{\chi}_1^+ \tilde{\chi}_2^0 \to c\bar{s}$ are illustrated in figure 7.8. Both plots are very similar. Resonances are absent and the curves drop monotonously with increasing energy in the center-of-mass frame. Note that our tree-level calculations are in perfect agreement with `micrOMEGAs`. The respective ratios have a constant value of one as indicated by the black dashed lines in the lower parts of the plots. In contrast to the processes investigated previously, effective couplings are absent within `micrOMEGAs` and light quark masses are not modified by our renormalisation scheme.

The impact of the radiative corrections is rather small in both processes, leading to relative shifts of 5% and 3%, respectively. Remember that SUSY QCD corrections involve
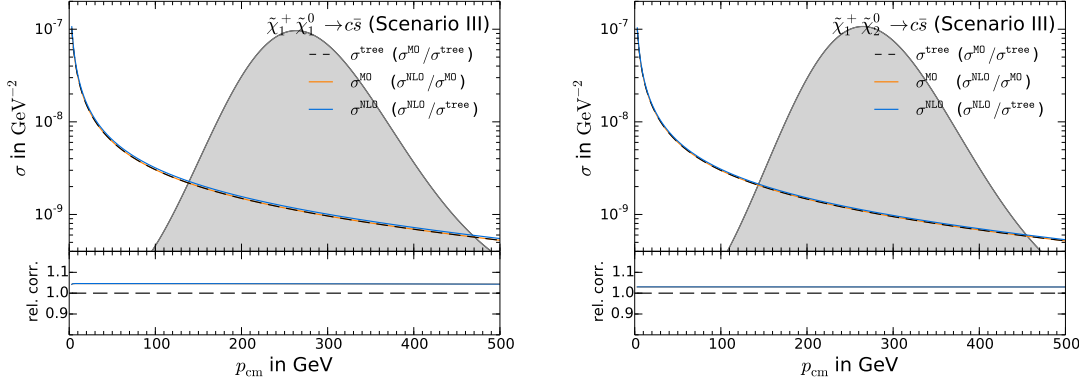
Figure 7.8.: Tree-level (black dashed line), full one-loop (blue solid line) and `micrOMEGAs` (orange solid line) cross sections for selected channels in scenario III

squarks and gluinos as virtual particles. As these particles are very heavy in scenario III (cf. table 7.2), the corresponding loops are strongly suppressed. Given the additional fact that gaugino (co)annihilation processes make up only 52% in this scenario (cf. table 7.3), the corresponding radiative corrections affect the resulting relic density only slightly. Therefore, we refrain from analysing the relic density at NLO in more detail at this point.

However, let us stress once again that light quark final states are indeed relevant for relic density calculations within the pMSSM. Although the associated radiative corrections turn out to be of minor importance in the considered scenario, this may change in a more general setup allowing for more free parameters. In particular, such a setup should generate relatively light masses for the first two generations of squarks while simultaneously fulfilling the experimental bounds discussed in section 7.1. All loop corrections in `DM@NLO` are implemented in the most general form and suitable for any MSSM setup.

7.3. Neutralino-nucleon cross sections

The phenomenological analysis performed so far has focussed on the neutralino relic density and its modification due to the radiative corrections discussed in chapter 5. We continue by investigating the impact of the $\mathcal{O}(\alpha_s)$ corrections presented in chapter 4 on the resulting neutralino-nucleon cross sections. In addition, we combine both NLO calculations to precisely predict the latter in a given scenario.

7.3.1. Analysis of scenario I

We start with an investigation of scenario I once again. This scenario is interesting in terms of relic density calculations as many gaugino (co)annihilation processes contribute in parallel (cf. table 7.3). However, in the context of direct detection, this scenario is by no means special and should thus be considered as a rather arbitrary and conservative case in the following.

Although most of the phenomenological features of this scenario have been discussed in subsection 7.2.1, we begin by studying the composition of the lightest neutralino in more
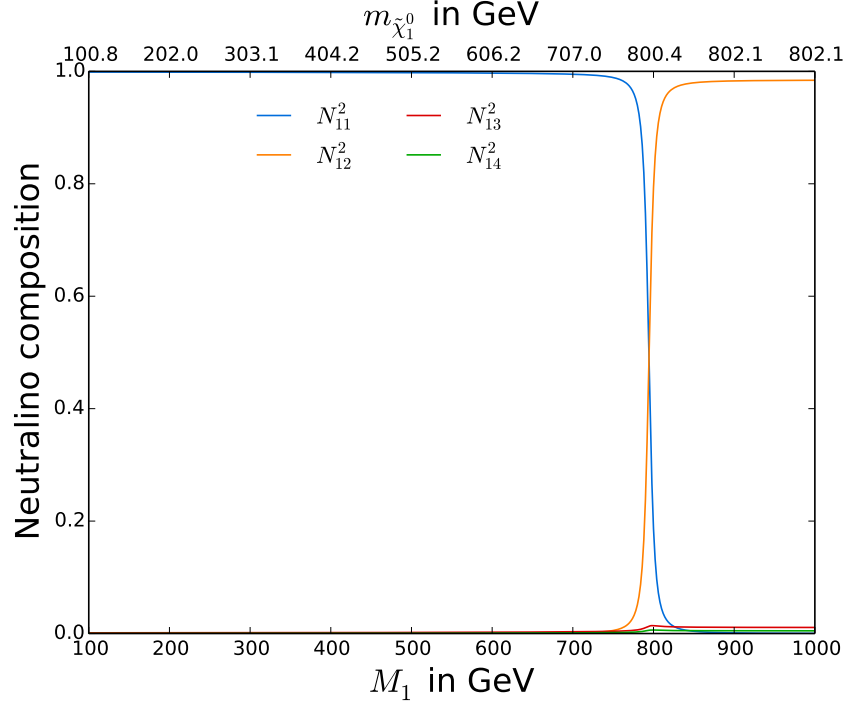
Figure 7.9.: Neutralino composition in scenario I

detail as this parameter turns out to be essential for the resulting neutralino-nucleon cross sections. Figure 7.9 shows the aforementioned composition in dependence of the mass parameter M_1. The lightest neutralino is mostly bino as long as $M_1 < M_2 = 766.0$ GeV and turns into mostly wino for larger values of M_1. The higgsino content stays always small as $M_1, M_2 < \mu = 1286.3$ GeV (cf. table 7.1). The upper horizontal axis shows the corresponding mass of the lightest neutralino in GeV as a derived parameter. This shall connect our theoretical predictions to experimental exclusion limits, which are usually given in dependence of the WIMP mass. Note that the correspondence between M_1 and $m_{\tilde{\chi}_1^0}$ is basically 1:1 for M_1 up to 800 GeV. For larger values of M_1, the lightest neutralino becomes mostly wino and its mass almost independent of M_1. We finally stress that scenario I itself, i.e. the cosmologically preferred region, sits near the turn-over ($M_1 = 731.0$ GeV). Such a situation is encountered in many pMSSM scenarios and clearly calls for a general treatment of the neutralino admixture in the context of direct detection.

We turn to the neutralino-nucleon cross sections which are displayed in figure 7.10. The upper left plot of figure 7.10 depicts the spin-independent neutralino-proton cross section in cm^2 in dependence of M_1 calculated by `micrOMEGAs` (orange solid line), `DM@NLO` at tree-level (black solid line) and including the radiative corrections presented in chapter 4 (blue solid line). The shift between our tree-level calculation and `micrOMEGAs` stems mainly from different nuclear input values for the scalar coefficients f_{Nq}^T (cf. section 4.2 and table 4.1). If we use the same nuclear input as `micrOMEGAs`, the deviation vanishes as indicated by the black dotted line. The tree-level cross sections are rather small (10^{-47}-10^{-46} cm^2) as long as the lightest neutralino is mostly bino. The bino nature suppresses couplings to Higgs bosons, whereas squark processes are kinematically disfavoured because the squarks are relatively heavy in this scenario (cf. table 7.2).
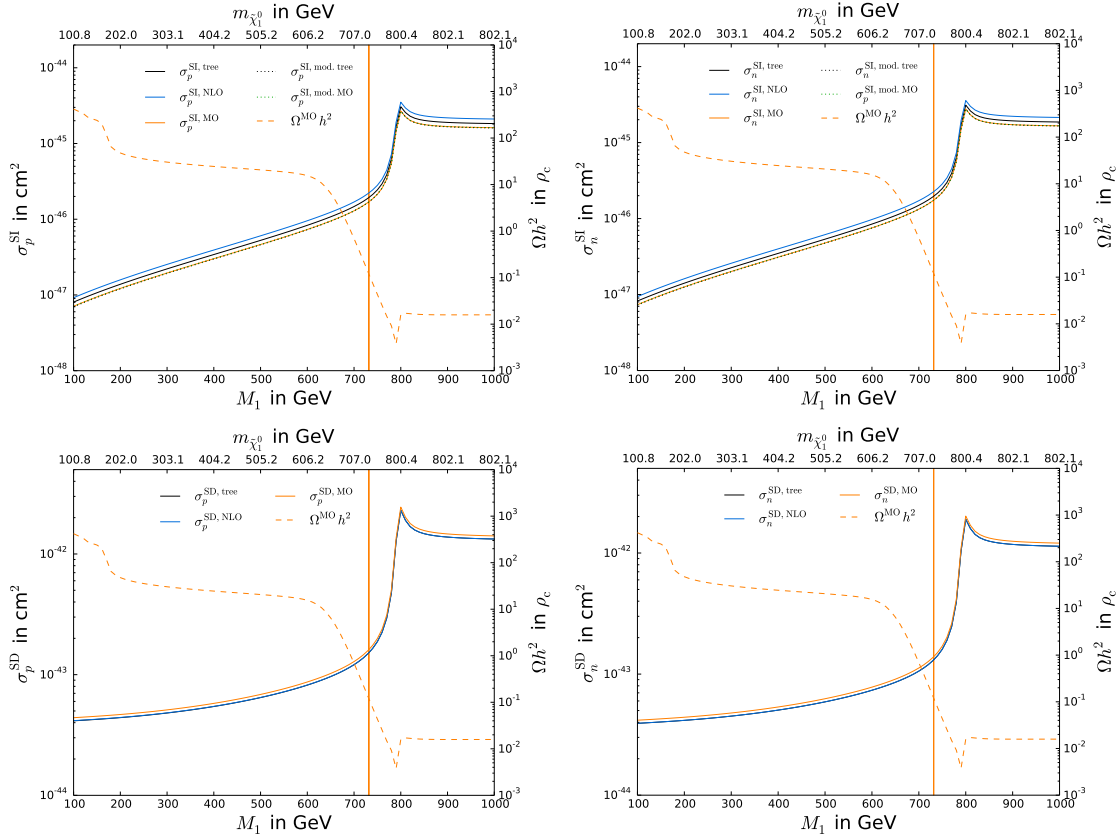
Figure 7.10.: Spin-independent (top) and spin-dependent (bottom) neutralino-nucleon cross sections in scenario I for protons (left) and neutrons (right)

We also observe a shift between our tree-level and NLO result. This shift is comparable to the shift between our tree-level and `microMEGAs`, i.e. of the order of typical recent nuclear uncertainties. In the present situation, SUSY QCD corrections to the Higgs-quark coupling including third generation squarks turn out to be the major NLO contributions as the other squarks are much heavier (cf. table 7.2).

The improved calculation of `microMEGAs` is shown as the green dotted line.[30] Amongst some minor improvements, this calculation is supposed to replace heavy quark contributions by gluonic one-loop processes as given in [151, 152]. However, we could not find a significant difference in the final result in any scenario. Consequently, the green dotted line coincides with the orange solid line.

The neutralino relic density obtained with `microMEGAs` in units of the critical density is shown as the orange dashed line (right ordinate). Note that the relic density is roughly inverse to the neutralino-proton cross section. This correlation is not completely unexpected as larger neutralino-proton cross sections are linked to larger cross sections for gaugino (co)annihilation into quarks which in turn lead to a smaller relic density. The crucial condition for this interlinking is that the relic density calculation is dominantly governed by quark final states. In the present case, this is true for $M_1 > 200$ GeV. For smaller M_1,

---

[30]More precisely, the improved calculation corresponds to the choice `MSSMDDTest(loop=1, ...)`, whereas we use `MSSMDDTest(loop=0, ...)` for the orange solid line.
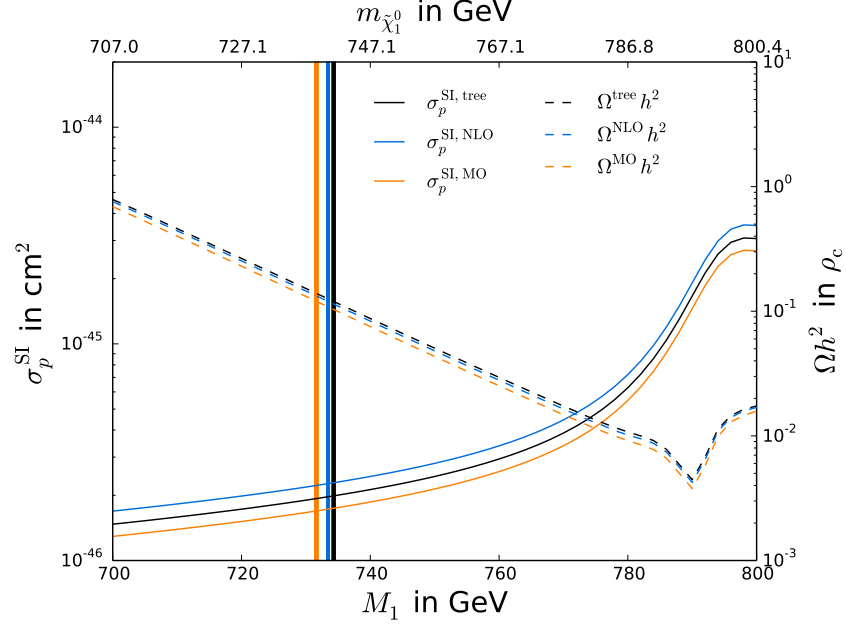
Figure 7.11.: Combined relic density and direct detection calculation in scenario I

electroweak final states become relevant and the observed bump in the relic density has no counterpart in the neutralino-proton cross section. The cosmologically preferred region is indicated by the orange vertical band. We return to this region later and continue with the discussion of the remaining neutralino-nucleon cross sections.

The upper left plot of figure 7.10 shows the spin-independent neutralino-neutron cross section. No major difference is found in comparison to the proton case. Within the chosen setup, this usually happens to be true for mainly two reasons. On the one hand, isospin-dependent effects can arise only if the cross sections of the fundamental processes including up or down quarks differ in magnitude. This could be achieved by e.g. vastly different first generation squark masses. However, as we are working with a common mass parameter $M_{\tilde{q}_{1,2}}$ for the first two squark generations, such a situation can not be realised within the given pMSSM setup (cf. section 2.5). Secondly, isospin-dependent effects are not significantly pronounced as the scalar coefficients listed in table 4.1 are rather similar for protons and neutrons.

The spin-dependent neutralino-proton cross section is shown in the lower left plot of figure 7.10. The blue and black lines completely overlap, indicating that the radiative corrections are negligible. This is indeed the case. Remember that only light quarks, i.e. only u, d and s contribute to the spin-dependent cross section. The associated squarks are very heavy in scenario I (cf. table 7.2), which is why the corresponding SUSY QCD corrections are strongly suppressed.

In contrast, the orange line is clearly separated and we observe a relative shift between `micrOMEGAs` and our tree-level calculation of roughly $+7\%$. This shift is not caused by different nuclear input values as we are using the same polarised quark densities $(\Delta q)_N$ as `micrOMEGAs` (cf. section 4.2). It is rather due to the running of the axial-vector operator as described in subsection 4.6.2 which is neglected in `micrOMEGAs`. If we manually deactivate this running in `DM@NLO`, we find perfect agreement with `micrOMEGAs`. The lower left plot

Table 7.4.: Resulting M_1 and spin-independent neutralino-proton cross section when combining direct detection and relic density routines in scenario I

	M_1 in GeV	σ_p^{SI} in $10^{-46}\mathrm{cm}^2$	Shift of σ_p^{SI}
microOMEGAs	731	1.68	-15%
Tree-level	734	1.98	
NLO	733	2.26	$+14\%$

of figure 7.10 illustrates the spin-dependent neutralino-neutron cross section. As before, no significant difference is found in comparison to the proton case.

Let us investigate the cosmologically preferred region around $700\,\mathrm{GeV} < M_1 < 800\,\mathrm{GeV}$ of the upper left plot of figure 7.10 in more detail. The situation is depicted in figure 7.11. Apart from the previously discussed spin-independent neutralino-proton cross section calculated by microOMEGAs (orange solid line), DM@NLO at tree-level (black solid line) and including $\mathcal{O}(\alpha_s)$ corrections (blue solid line), we show the neutralino relic density obtained by microOMEGAs (orange dashed line), DM@NLO at tree-level (black dashed line) and at NLO (blue dashed line). The three dashed lines separate and result in different cosmologically preferred regions which are indicated by the vertical bands of the respective colour.

We can use these bands to predict the spin-independent neutralino-proton cross section in the given scenario by identifying the intersections of the vertical bands and the solid lines of the same colour. Depending on the chosen routine, different results are obtained for M_1 and the neutralino-proton cross section as listed in table 7.4. The relative shifts of the latter between microOMEGAs, our NLO and our tree-level calculation amount to -15% and $+14\%$, respectively.

7.3.2. Analysis of scenario IV

We continue with a brief discussion of the phenomenology of scenario IV. The most salient feature is given by the relatively small mass parameter $M_{\tilde{q}_{1,2}}$ which results in light squark masses for the first two generations (cf. table 7.2). The composition of the lightest neutralino in dependence of M_1 is shown in figure 7.12. As long as $M_1 < \mu = 493.0\,\mathrm{GeV}$, the lightest neutralino is mostly bino. For larger values of M_1 it turns into mostly higgsino while its wino content is always small due to $M_1, \mu < M_2 = 1123.4\,\mathrm{GeV}$ (cf. table 7.1). In comparison to figure 7.9, the transition is smoother, which results in a larger remaining dependence of $m_{\tilde{\chi}_1^0}$ on M_1.

The corresponding neutralino-nucleon cross sections are depicted in figure 7.13. As before, the orange, black and blue solid lines show these cross sections calculated by microOMEGAs, DM@NLO at tree-level and including the $\mathcal{O}(\alpha_s)$ corrections presented in chapter 4, respectively. Moreover, the orange dashed line denotes the neutralino relic density resulting from a pure microOMEGAs calculation.

We observe three orange vertical bands which indicate three cosmologically preferred regions in agreement with (3.5). Apart from scenario IV itself at $M_1 = 270.0\,\mathrm{GeV}$, we have a second vertical band on the other side of the peak of the orange dashed line and a third one around $M_1 \sim 475\,\mathrm{GeV}$. The latter is directly located at the turn-over of the neutralino composition (cf. figure 7.12), which stresses the necessity to treat the
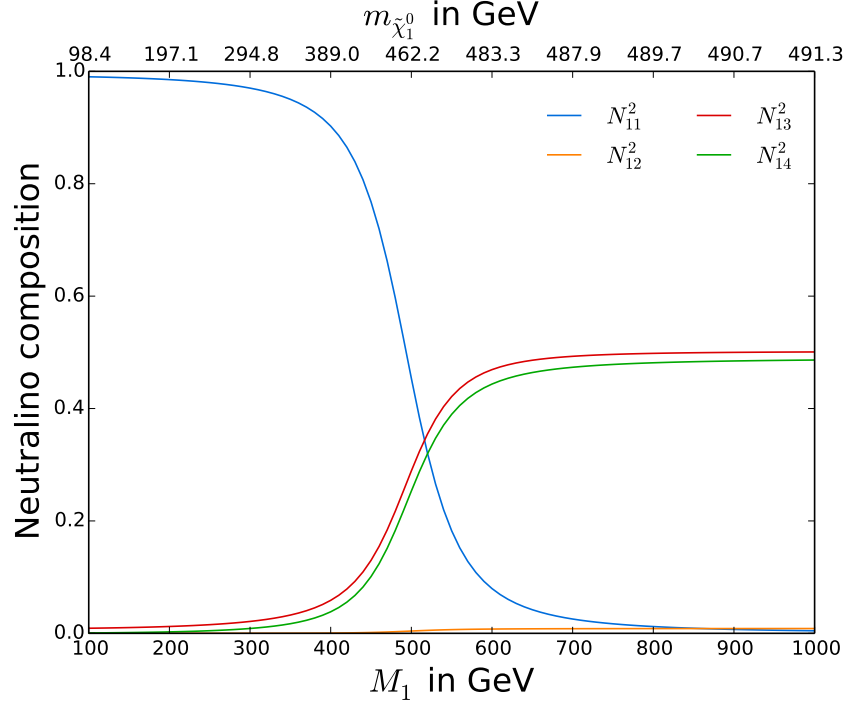
Figure 7.12.: Neutralino composition in scenario IV

neutralino admixture in full generality once again. The steep drop of the neutralino relic density at $M_1 \sim m_{\tilde{\chi}_1^0} \sim 250$ GeV is mainly caused by a peak of the s-channel process $\tilde{\chi}_1^0 \tilde{\chi}_1^0 \to A^0 \to b\bar{b}$, which is resonantly enhanced as we have $2m_{\tilde{\chi}_1^0} \sim m_{A^0} = 500.8$ GeV at this point. Moreover, the coupling between bottom quarks and the pseudoscalar Higgs boson is increased as $\tan \beta = 13.7$ is rather large in scenario IV. In case of the neutralino-nucleon cross section, this resonant s-channel process turns into a non-resonant t-channel process. The associated effective operator is kinematically suppressed and its contributions are negligible. Thus, there is no analogous peak in the neutralino-nucleon cross sections.

The spin-independent neutralino-proton and -neutron cross sections are shown in the upper plots of figure 7.13. As before, no major difference is found between the proton and the neutron case. The relative shifts between our tree-level and `micrOMEGAs` or our NLO calculation are roughly as before. No significant change is found when activating the improved calculation of `micrOMEGAs`, the orange solid and green dotted lines coincide again. In contrast to scenario I, a minor deviation between our tree-level calculation and `micrOMEGAs` remains even after adopting the nuclear input, i.e. the black dotted line separates slightly from the orange solid line. This is due to different treatments of the top mass and the associated stop sector. Moreover, `micrOMEGAs` does not kinematically differ between the squark s- and u-channels (cf. figure 4.4). These differences are present in general and may lead to mild deviations, as e.g. in the present situation, or may be completely negligible, as e.g. in scenario I.

Completely new features show up in the spin-dependent cross-sections depicted in the lower plots of figure 7.13. The neutralino-proton and -neutron cross sections differ by almost an order of magnitude in the small M_1 regime. Moreover, we observe a large splitting

Figure 7.13.: Spin-independent (top) and spin-dependent (bottom) neutralino-nucleon cross sections in scenario IV for protons (left) and neutrons (right)

of our tree-level and NLO result in the proton case in this region. Both phenomena have a related origin. For small M_1, the lightest neutralino is mostly bino (cf. figure 7.12). The bino nature suppresses the coupling to the Z^0 boson and decreases the associated, usually dominant contribution. In addition, squarks of the first two generations are rather light in scenario IV (cf. table 7.2). Due to these facts, squark processes contribute significantly in the region of small M_1. In contrast to contributions stemming from the Z^0 boson, the latter depend on the involved quark flavour and are thus sensitive to different choices of the polarised quark densities $(\Delta q)_N$ as given in (4.14). Note that these densities can have positive or negative signs. In the proton case, this results in a cancellation of the individually large squark contributions and a strong decrease of the cross section in the small M_1 regime. Due to the cancellation of the leading terms, the cross section becomes more sensitive to the radiative corrections, which are sizeable in the present situation as the squarks are very light. This explains the observed splitting between the black and blue solid line for small M_1. For larger values of M_1, the lightest neutralino becomes mostly higgsino, the Z^0 processes dominate and the corresponding NLO corrections are less important. As before, we observe a small deviation between `micrOMEGAs` and our tree-level result, which is due to the missing running of the axial-vector operator in `micrOMEGAs`.

We continue by taking a closer look at the region around the A^0 resonance in figure 7.14. As before, the relic density calculated by `micrOMEGAs`, `DM@NLO` at tree-level and including

Figure 7.14.: Combined relic density and direct detection calculation in scenario IV

Table 7.5.: Resulting M_1 and spin-dependent neutralino-proton cross section when combining direct detection and relic density routines in scenario IV

	M_1 in GeV	σ_p^{SD} in 10^{-43}cm^2	Shift of σ_p^{SD}
`micrOMEGAs`	226	2.78	+3%
Tree-level	228	2.70	
Full NLO	227	1.65	−39%
`micrOMEGAs`	270	4.14	+8%
Tree-level	267	3.84	
NLO	269	2.47	−36%

the $\mathcal{O}(\alpha_s)$ corrections discussed in chapter 5 is indicated by the orange, black and blue dashed line, respectively. The associated cosmologically preferred regions are shown by the vertical bands of the respective colour. Thanks to the precision of the Planck limit given in (3.5) and due to the fact that the relic density changes rapidly near the resonance, these bands are very thin in the present situation and allow for a precise selection of the preferred parameter space. We can read off the corresponding neutralino-proton cross section by identifying the intersections of the dashed lines and vertical bands of the same colour. The results are presented in table 7.5.

The deviations between `micrOMEGAs` and our tree-level result amount to +3% and +8% and are smaller than in scenario I (cf. table 7.4) as we are using the same nuclear input in
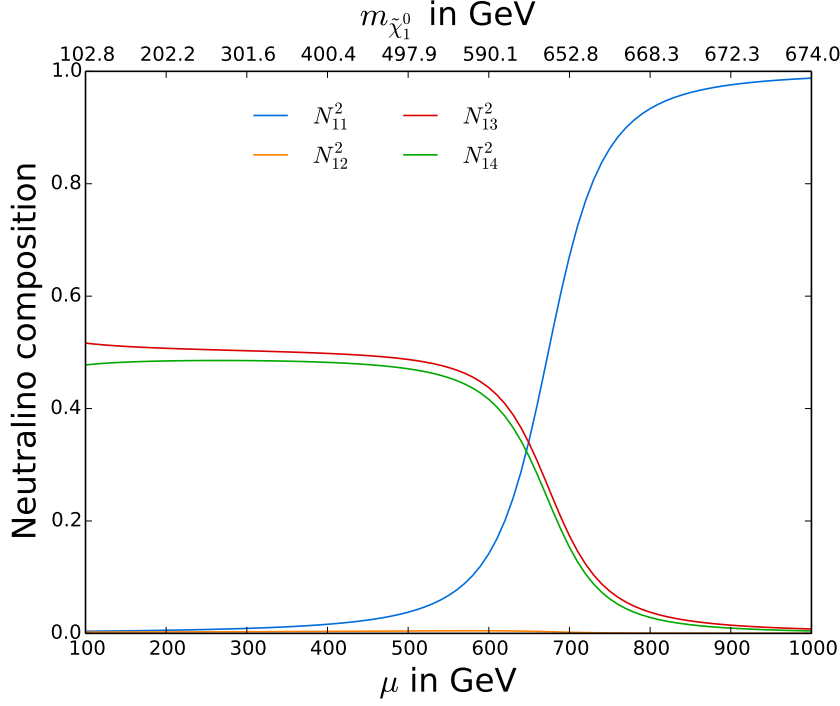
Figure 7.15.: Neutralino composition in scenario V

the spin-dependent case. Note that the relative position of the vertical bands decreases the resulting shift at $M_1 \sim 230$ GeV and increases it at $M_1 \sim 270$ GeV. The exact opposite occurs when comparing our tree-level and NLO results. The relative shifts are very large here, accounting for almost -40%.

7.3.3. Analysis of scenario V

In the last considered scenario, squarks and gauginos are heavier than in scenario IV, but $m_{\tilde{\chi}_1^0}$ and the masses of first two generation squarks are still below 1 TeV (cf. table 7.2). When varying the higgsino mass parameter μ, the lightest neutralino changes its composition from mostly higgsino into mostly bino as illustrated in figure 7.15. The transition occurs at $\mu \sim M_1 = 675.3$ GeV. Considering the neutralino admixture, this scenario can be seen as a mirrored version of scenario IV (cf. figure 7.12).

The neutralino-nucleon cross sections are depicted in figure 7.16, where the labelling is as before. Note that the slope of the relic density shown by the orange dashed line is relatively small, which results in a broader cosmologically preferred region indicated by a broader orange vertical band. The spin-independent cross sections are shown in the upper plots of figure 7.16, where no essentially new features are found. The relative shift between `micrOMEGAs` and our tree-level calculation is of similar size as the relative shift between our NLO result and the tree-level calculation. For reasons already discussed in subsection 7.3.1, no significant difference is found between the proton and neutron case.

In contrast, the spin-dependent cross sections depend on the considered nucleon as evidenced in the lower plots of figure 7.16. This dependence and the rather strong deviation between our tree-level and NLO result have a similar origin as in the previous subsection.
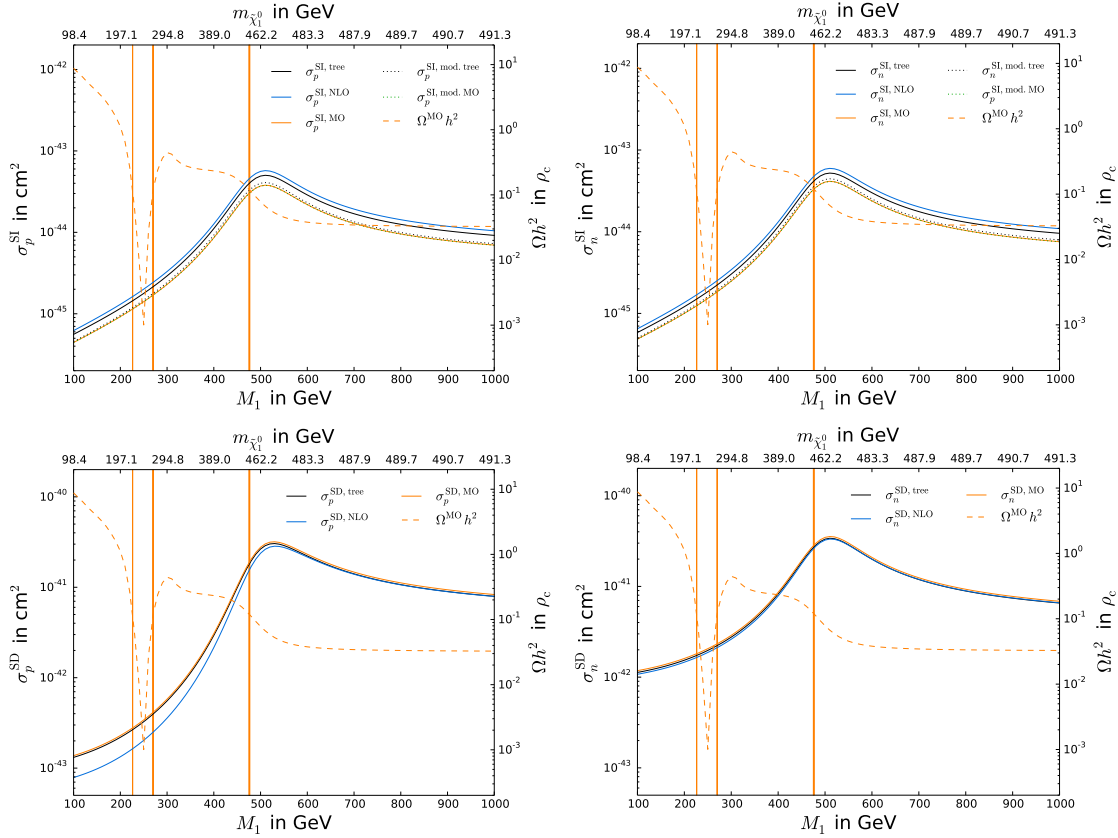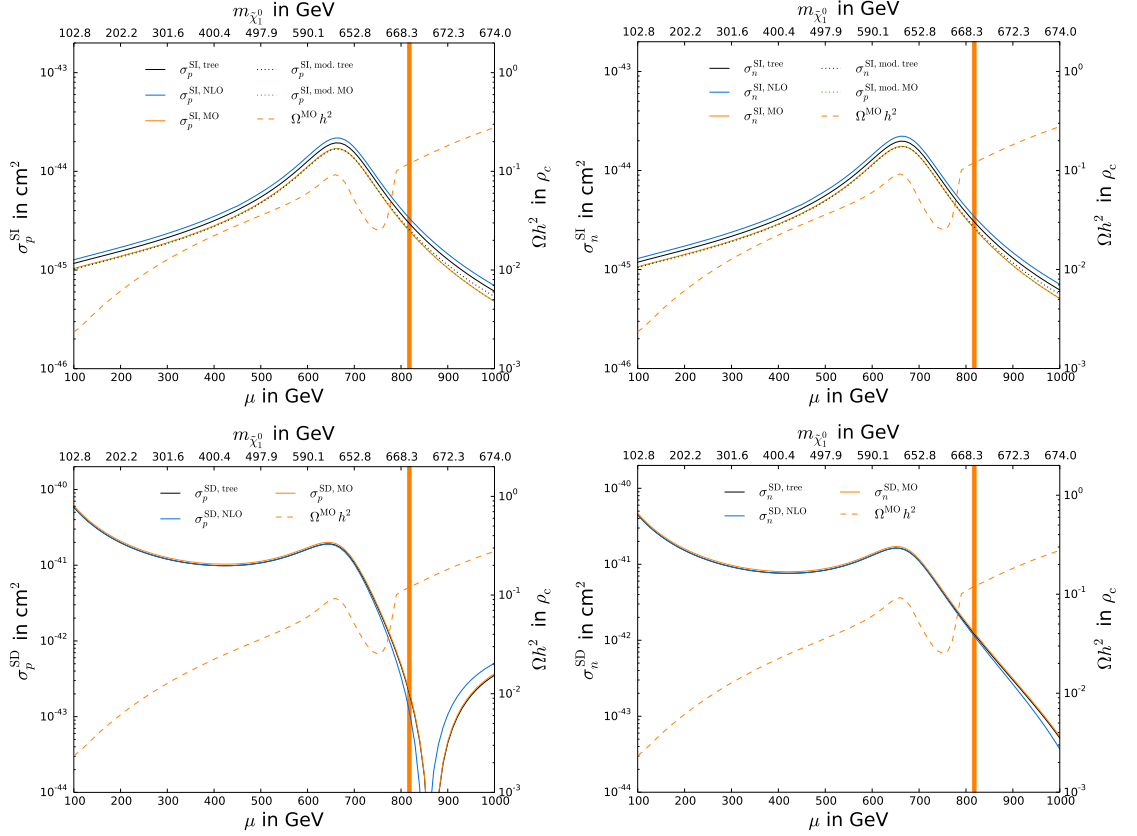
Figure 7.16.: Spin-independent (top) and spin-dependent (bottom) neutralino-nucleon cross sections in scenario V for protons (left) and neutrons (right).

For large values of μ, the lightest neutralino is mostly bino (cf. figure 7.15) and its coupling to Z^0 bosons is suppressed. In addition, squark processes are kinematically favoured again. Remember that the denominators of these processes read $s - m_{\tilde{q}_i}^2$ and $u - m_{\tilde{q}_i}^2$ at tree-level, which simplifies to $(m_{\tilde{\chi}_1^0} \pm m_q)^2 - m_{\tilde{q}_i}^2$ in the considered non-relativistic limit according to (4.45). Hence, it is the neutralino-squark mass difference that actually matters and not the squark mass itself. This difference decreases with increasing μ, which is why squark processes contribute significantly in the large μ regime. As disussed in the last subsection, squark processes depend on the involved quark flavour and are thus sensitive to the choice of the polarised quark densities. In the proton case, we encounter a destructive interference of the individual squark contributions. The four-fermion coupling changes its sign at $\mu \sim 850$ GeV and the associated neutralino-proton cross section vanishes. A similar situation would be encountered in the neutron case for larger values of μ. However, we do not investigate this region in more detail as the corresponding neutralino relic density is way too large.

Instead, we investigate the spin-dependent neutralino-proton cross section near the cosmologically preferred region around 700 GeV $< \mu <$ 900 GeV in more detail. The situation is depicted in figure 7.17. As mentioned before, the vertical bands are rather broad because the neutralino relic density increases less rapidly. The orange and blue vertical bands clearly overlap, which signalises that the effective couplings implemented in `micrOMEGAs`
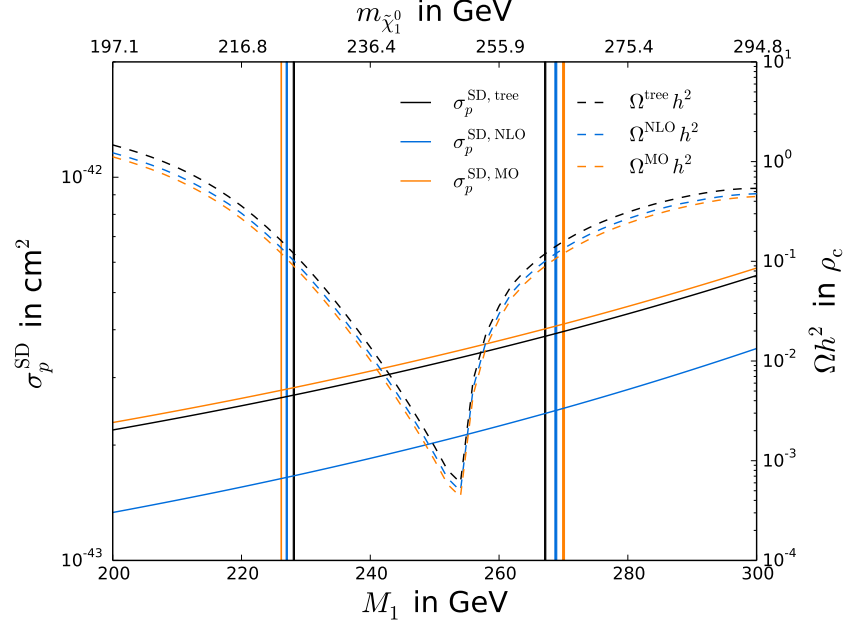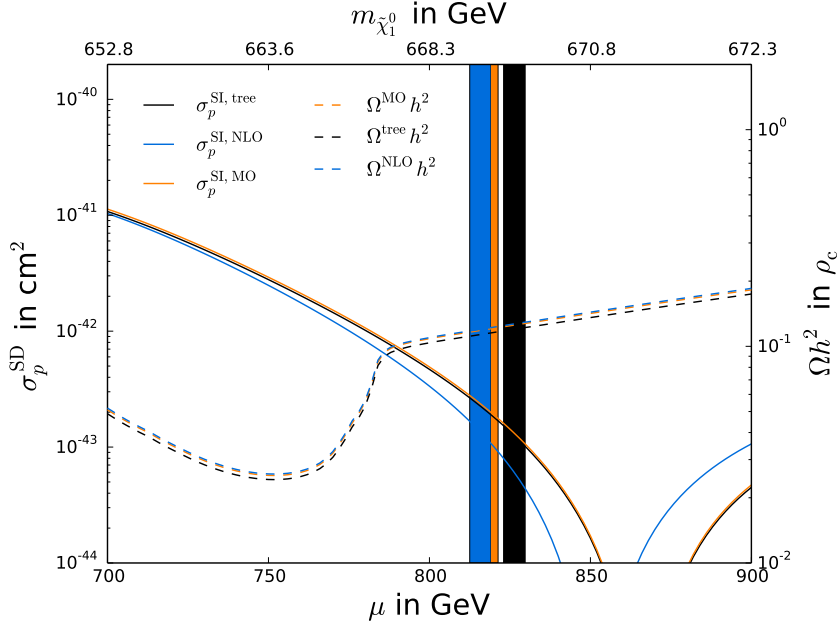
Figure 7.17.: Combined relic density and direct detection calculation in scenario V

Table 7.6.: Resulting μ and spin-dependent neutralino-proton cross section when combining direct detection and relic density routines in scenario V

	μ in GeV	σ_p^{SD} in $10^{-43}\mathrm{cm}^2$	Shift of σ_p^{SD}
`micrOMEGAs`	815 - 821	1.80 - 2.43	+63%
Tree-level	823 - 829	1.06 - 1.53	
NLO	813 - 819	1.08 - 1.62	+4%

approximate the leading SUSY QCD corrections to the relic density quite well in this scenario. On the other hand, the spin-dependent neutralino-proton cross section calculated by `micrOMEGAs` neither includes effective couplings nor full one-loop corrections. Consequently, the orange solid line closely follows our tree-level result shown as the black solid line. The remaining difference is due to the running of the axial-vector operator which is missing in `micrOMEGAs`.

We can combine both calculations again to determine the cosmologically preferred value of μ and to predict the neutralino-proton cross section. The resulting intervals are shown in table 7.6.[31] Note that our NLO and tree-level calculations favour distinct regions of

---

[31]These intervals are present in general but very small in scenario I and IV, where the vertical bands are much thinner. Therefore, we have omitted them for reasons of simplicity so far but include them explicitly in scenario V, which features rather broad vertical bands. The relative shifts presented in table 7.6 are exemplary and have simply been obtained by comparing the mean values of the cross sections.
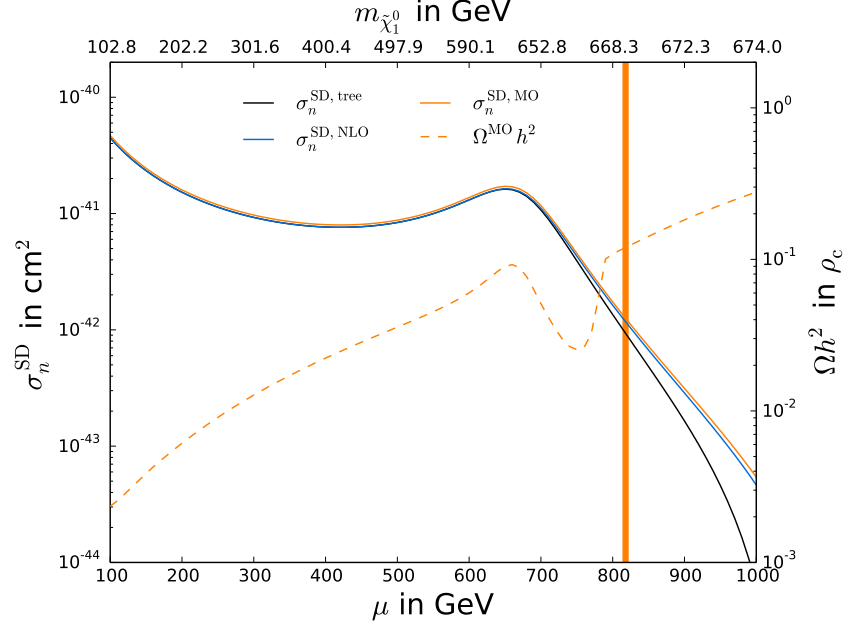
Figure 7.18.: Spin-dependent neutralino-neutron cross section in scenario V using a pure $\overline{\text{DR}}$ scheme

μ. Moreover, the impact of the radiative corrections is very large. The relative deviation between the NLO and tree-level cross section amounts to more than -50% near the drop. However, when identifying the neutralino-proton cross section at the respective cosmologically preferred region, both effects cancel and the result is basically the same. In contrast, we observe a deviation of more than $+60\%$ between `micrOMEGAs` and our tree-level calculation.

Before we conclude, we take a small detour and comment on the chosen renormalisation scheme. As discussed in the beginning of this chapter, we are working with the hybrid on-shell/$\overline{\text{DR}}$-scheme presented in detail in section G.5, even though EFT calculations are usually carried out in a minimal scheme like $\overline{\text{MS}}$ or $\overline{\text{DR}}$ (cf. section G.3). In particular, the hybrid scheme uses on-shell masses $m_{\tilde{q}}^{\text{OS}}$ for the squarks of the first two generations, just like `micrOMEGAs`. Our code also supports a pure $\overline{\text{DR}}$ scheme, where these on-shell masses are replaced by their smaller and scale-dependent $\overline{\text{DR}}$ equivalents $m_{\tilde{q}}^{\overline{\text{DR}}}(\mu)$. The spin-dependent neutralino-neutron cross section in scenario V has proven useful to compare both approaches and to illustrate scheme-dependent effects.

Therefore, we show this cross section in figure 7.18 once again, this time using a pure $\overline{\text{DR}}$ scheme. In comparison to the lower right plot of figure 7.16, no significant difference is found for small values of μ. In this region virtual corrections are of minor importance, which is not modified by choosing another renormalisation scheme. For larger values of μ, our tree-level calculation clearly separates from `micrOMEGAs`, which has previously not been the case (cf. figure 7.16). Remember that the cross section in this regime is largely driven by squark processes which are sensitive to the neutralino-squark mass difference and thus the definition of the squark mass. To investigate this in more detail, we write

the scale-independent on-shell mass as

$$m_{\tilde{q}}^{\mathrm{OS}} = m_{\tilde{q}}^{\overline{\mathrm{DR}}}(\mu) + \Delta m_{\tilde{q}}^{\overline{\mathrm{DR}}}(\mu), \tag{7.4}$$

where the second term resums virtual corrections. Choosing a pure $\overline{\mathrm{DR}}$ scheme corresponds to neglecting this term and working with a smaller squark mass at tree-level. As a consequence, the neutralino-squark mass difference appearing in the squark propagators is reduced, which leads to the observed drop of the black solid line in figure 7.18.

However, this effect diminishes at NLO and the blue solid lines in the lower right plot of figure 7.16 and in figure 7.18 basically agree. The reason is that the leading corrections included in $\Delta m_{\tilde{q}}^{\overline{\mathrm{DR}}}(\mu)$ reappear as virtual corrections to the squark propagators (cf. subsection 4.4.1). Consequently, the NLO result is more stable than the tree-level result. The main difference between both approaches is that parts of the virtual corrections are already absorbed in the squark masses within the on-shell scheme, whereas these corrections become manifest as large propagator corrections within the $\overline{\mathrm{DR}}$ scheme. We prefer the former to avoid large virtual corrections and to improve perturbative stability.

We finally stress that the considered situation should be regarded as rather extreme. In many other scenarios, the choice of the renormalisation scheme was found to be of minor importance. More details on scheme-dependent effects in the context of relic density calculations can be found in [190].

8. Conclusion

In this thesis we have calculated radiative corrections to elastic neutralino-nucleon scattering within the framework of effective field theory. More precisely, we have performed a full $\mathcal{O}(\alpha_s)$ matching calculation of the MSSM and an effective theory including the four-fermion operators $\bar{\chi}\chi\bar{q}q$ and $\bar{\chi}\gamma_5\gamma_\mu\chi\bar{q}\gamma_5\gamma^\mu q$. These effective operators govern the dominant spin-independent and spin-dependent contributions to the direct detection rate of neutralinos, respectively. The calculation of the corresponding virtual corrections has been presented in great detail. The regularisation of the divergent loop integrals has been carried out by using dimensional reduction, where we distinguished between infrared and ultraviolet poles. In order to apply the associated and well-established method of tensor reduction, it has proven necessary to stabilise this method for vanishing Gram determinants, which occur naturally for vanishing relative velocities. An alternative solution for all needed tensor coefficients has been worked out. We have compared our results with the standard approach for small but non-vanishing Gram determinants and found excellent agreement throughout. Given this improved regularisation procedure, we were able to check explicitly that all ultraviolet poles vanish when adding the corresponding counterterms to the virtual corrections. Moreover, we have verified that all infrared divergences cancel in the course of the matching procedure. We have finally described the running of the effective operators and their corresponding Wilson coefficients, i.e. their evolution from the high scale $\mu_{\text{high}} \sim 1000$ GeV, where the matching calculation is performed, down to the low scale $\mu_{\text{low}} \sim 5$ GeV, where the nuclear matrix elements are defined. It turned out that the running of the axial-vector operator is not taken into account properly in publicly available codes such as `micrOMEGAs`.

Furthermore, we have illustrated the calculation of SUSY QCD corrections to general gaugino (co)annihilation into quarks. These processes contribute dominantly to the (co)annihilation cross section entering the Boltzmann density in many scenarios of the MSSM and are thus relevant for the prediction of the neutralino relic density. The corresponding cross sections are inclusive quantities, i.e. the infrared divergences stemming from the virtual corrections cancel when adding the corresponding real corrections which include the emission of an additional gluon. The cancellation of infrared and ultraviolet poles has been checked explicitly.

Both of the calculations have been implemented in the numerical package `DM@NLO`. With the help of this program, we performed a phenomenological analysis and studied the impact of the radiative corrections. We started with an investigation of the cross sections of gaugino (co)annihilation processes, where we found relative shifts of 10-40% caused by the NLO corrections. The NLO results were found to be in tension with the effective tree-level approach implemented in `micrOMEGAs` in scenario I, whereas reasonable accordance was found in scenario II. Afterwards we analysed the influence of these processes on the resulting relic density. It was found that the latter may depend on a multitude of gaugino (co)annihilation processes in parallel. In particular, processes including gauginos other than the lightest neutralino or light quarks in the final state may contribute as well, which

confirms the necessity to treat gaugino (co)annihilation processes in full generality. The radiative corrections lead to a relative shift of the relic density of about 5% in scenario I and of roughly 10% in scenario II. Both of the shifts exceed the recent experimental uncertainty given by the Planck data, which demonstrates that these radiative corrections should be taken into account when identifying the cosmologically preferred region of the MSSM parameter space.

Thereafter we turned to the neutralino-nucleon cross sections. It was shown that these quantities depend sensitively on the neutralino admixture. Moreover, it was demonstrated that the neutralino-nucleon cross sections may be roughly inverse to the corresponding relic density if the latter is driven by (co)annihilation processes including quarks in the final state dominantly. We have combined our relic density and direct detection routines to identify the cosmologically preferred region of the MSSM parameter space and to predict the neutralino-nucleon cross sections precisely. This prediction is modified by about +14% in the spin-independent case when radiative corrections are included consistently. The observed modification is of similar size as recent nuclear uncertainties, which affect the neutralino-nucleon cross sections as well. The spin-dependent neutralino-nucleon cross sections were found to be subject to even larger corrections, accounting for almost -40% in scenario IV and more than -50% in scenario V. The reasons for these large shifts are given by destructive interferences of the leading squark processes which render the resulting cross sections more sensitive to the otherwise more subleading radiative corrections. Squark processes were favoured over Z^0 processes due to the bino nature of the lightest neutralino and relatively small neutralino-squark mass differences. Moreover, the running of the axial-vector operator was found to modify the result by -7%.

The implementation of the presented neutralino-nucleon cross section calculations adds a second loop-improved observable to our numerical package `DM@NLO` and permits to consistently analyse correlations between the direct detection of neutralino dark matter and its relic density including $\mathcal{O}(\alpha_s)$ corrections for the first time. However, we stress again that both calculations are affected by several other uncertainties as well.

The work presented in this thesis can be extended in several ways. First of all, one may calculate radiative corrections to processes not yet implemented in `DM@NLO` to allow for a precise prediction of the relic density in additional parts of the MSSM parameter space, where these processes contribute. Here SUSY QCD corrections to stop-antistop annihilation processes including strongly interacting particles in the final state are of particular relevance. In the context of direct detection, one may include additional effective operators. The spin-independent contributions from heavy quarks can either be included as presented in this thesis or be traced back to one-loop processes including gluonic operators. It is an interesting option to implement both approaches and to contrast them. Moreover, one may include the tree-level contributions from kinematically suppressed operators such as e.g. $\bar{\chi}\gamma_5\chi\bar{q}\gamma_5 q$ and compare them with e.g. the NLO corrections to unsuppressed operators. Apart from that, it might be interesting to perform a phenomenological analysis based on a more general pMSSM setup which allows for independent squark mass parameters of the first two generations.

A. Choice of conventions

The conventions used throughout this thesis agree with those in [57] and the following sections are basically a translation of the corresponding appendices.

A.1. System of units

In theoretical particle physics one usually works with *natural units*, wherein the given thesis is no exception. In natural units, the reduced Planck constant $\hbar$, the speed of light in vacuum c and the Boltzmann constant k_B have value 1 and are omitted in calculations. To transform a result from natural units into e.g. the SI system ("Le Système international d'unités") one has to multiply or divide by a combination of these constants until the desired unit is obtained. This transformation is unique. Some examples are given in table A.1. The numerical values of the fundamental constants can be found in e.g. [230] and read

$$c \quad = \quad 2.99792458 \cdot 10^8 \text{ m/s.} \tag{A.1}$$

$$\hbar \quad = \quad 1.054571726 \cdot 10^{-34} \text{ Js.} \tag{A.2}$$

$$k_B \quad = \quad 1.3806488 \cdot 10^{-23} \text{ J/K.} \tag{A.3}$$

A.2. Concerning the notation

We use the *summation convention* due to Albert Einstein. According to this convention, summing over doubly appearing indices is automatically understood. As an example, we write down the product of two $n \times n$ matrices A and B.

$$(A \cdot B)_{ij} = \sum_{k=1}^{n} A_{ik} B_{kj} = A_{ik} B_{kj}. \tag{A.4}$$

Furthermore, the *slash notation* of Richard Feynman is used. In this notation, the contraction of a four-vector with a vector of Dirac matrices can be written down compactly. We have

$$\not{p} = \gamma^\mu p_\mu. \tag{A.5}$$

A.3. Kinematical variables

The Feynman diagrams appearing in this thesis are all labelled in a common manner, which is explicated here. The diagrams have to be read from left to right. Particles in the initial state (on the left) are named a, b, c etc. The corresponding four-momenta are given by p_a, p_b, p_c and so on. Analogously the particles in the final state (on the right) are

Table A.1.: On the transformation of natural units

Quantity	Natural unit	Real unit
Energy	eV	eV
Time	1/eV	$\hbar$/eV
Length	1/eV	$\hbar c$/eV
Mass	eV	eV/c^2
Temperature	eV	eV/k_B
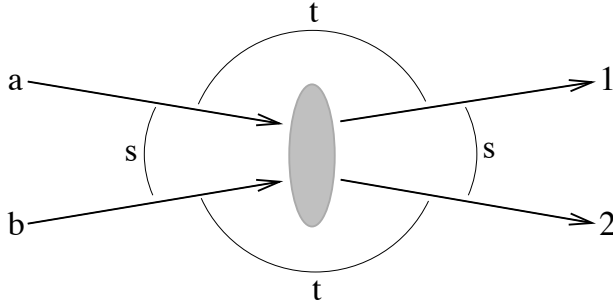
Figure A.1.: Kinematics of a $2 \to 2$ process

called 1, 2, 3 and so on and their four-momenta are labelled p_1, p_2, p_3 etc. Four-momenta are generally understood as

$$p_i = (E_i, \vec{p}_i), \tag{A.6}$$

where E_i is the energy of the considered particle i. Three-momenta $\vec{p}_i$ are explicitly marked by an arrow. Spin variables are usually omitted.

In case of a $2 \to 2$ process, as shown in figure A.1 (taken from [217]), one can additionally introduce the *Mandelstam variables* s, t and u.

$$s = (p_a + p_b)^2 = (p_1 + p_2)^2. \tag{A.7}$$
$$t = (p_a - p_1)^2 = (p_b - p_2)^2. \tag{A.8}$$
$$u = (p_a - p_2)^2 = (p_b - p_1)^2. \tag{A.9}$$

Due to energy and momentum conservation, namely

$$p_a + p_b = p_1 + p_2, \tag{A.10}$$

the Mandelstam variables are linked to the particle masses via

$$s + t + u = m_a^2 + m_b^2 + m_1^2 + m_2^2. \tag{A.11}$$

B. Special mathematical functions and useful mathematical relations

In this chapter we introduce some special mathematical functions, namely the *Gamma function*, the *Beta function*, the *Dilogarithm* and the *hypergeometric function*. We list some useful properties which are partially taken from [166] and [231]. One encounters these functions when evaluating loop diagrams (cf. chapter F). Furthermore, we present the concept of *Feynman parameters*.

B.1. Gamma function

The *Gamma function* can be understood as a shifted continuation of the factorial function to real and complex numbers. It is also known as Eulerian integral of second order and defined as

$$\Gamma(x) = \int_0^\infty \mathrm{d}t\, t^{x-1} e^{-t}. \tag{B.1}$$

It obeys the functional equation

$$\Gamma(x+1) = x\Gamma(x), \tag{B.2}$$

which can be proven by integration by parts. Combining this result with $\Gamma(1) = 1$, we obtain via complete induction

$$\Gamma(n+1) = n! \quad \text{for} \quad n \in \mathbb{N}. \tag{B.3}$$

Sometimes the *Pi function* is used instead of the Gamma function to stress the connection to the factorial function.

$$\Pi(x) = \Gamma(x+1) = \int_0^\infty \mathrm{d}t\, t^x e^{-t} \quad \Leftrightarrow \quad \Pi(n) = n! \quad \text{for} \quad n \in \mathbb{N}. \tag{B.4}$$

The Gamma function is also needed when calculating the volume V or surface A of a sphere with radius r in D dimensions. We have

$$V_D = \frac{\pi^{\frac{D}{2}}}{\Gamma\left(\frac{D}{2}+1\right)} r^D \quad \text{and} \quad A_D = \frac{2\pi^{\frac{D}{2}}}{\Gamma\left(\frac{D}{2}\right)} r^{D-1}. \tag{B.5}$$

The second formula above can be obtained from the first one by derivating with respect to the radius. The well known special cases for $D = 2$ or $D = 3$ can be found when using the functional equation given in (B.2) and

$$\Gamma\left(\frac{1}{2}\right) = \sqrt{\pi}. \tag{B.6}$$

This value can be directly obtained by transforming the Gamma function to a Gaussian integral.

$$\Gamma\left(\frac{1}{2}\right) = \int_0^\infty \mathrm{d}t \frac{e^{-t}}{\sqrt{t}} \underbrace{=}_{x=\sqrt{t}} 2\int_0^\infty \mathrm{d}x e^{-x^2} = \sqrt{\pi}. \tag{B.7}$$

In the context of loop calculations, the following expansion of the Gamma function proves useful.

$$
\begin{aligned}
\Gamma(1+\epsilon) &= \epsilon\Gamma(\epsilon) = \Gamma(1) + \epsilon \left.\frac{\partial\Gamma(x)}{\partial x}\right|_{x=1} + \frac{\epsilon^2}{2}\left.\frac{\partial^2\Gamma(x)}{\partial x^2}\right|_{x=1} + \mathcal{O}(\epsilon^3) \\
\Leftrightarrow \Gamma(\epsilon) &= \frac{1}{\epsilon} + \left.\frac{\partial\Gamma(x)}{\partial x}\right|_{x=1} + \frac{\epsilon}{2}\left.\frac{\partial^2\Gamma(x)}{\partial x^2}\right|_{x=1} + \mathcal{O}(\epsilon^2) \\
&= \frac{1}{\epsilon} - \gamma_E + \frac{\epsilon}{2}\left(\gamma_E^2 + \frac{\pi^2}{6}\right) + \mathcal{O}(\epsilon^2).
\end{aligned}
\tag{B.8}
$$

Therein we have introduced the *Euler-Mascheroni constant*

$$\gamma_E = -\left.\frac{\partial\Gamma(x)}{\partial x}\right|_{x=1} = \lim_{n\to\infty}\left(\sum_{k=1}^n \frac{1}{k} - \ln(n)\right) \approx 0,57721. \tag{B.9}$$

B.2. Beta function

The *Beta function* is also known as Eulerian integral of first order and defined as

$$B(x,y) = \int_0^1 \mathrm{d}t\, t^{x-1}(1-t)^{y-1}. \tag{B.10}$$

The Beta function is symmetric under $x \leftrightarrow y$, which can be seen explicitly by using the substitution $t = 1-u$. Another substitution, namely $t = \frac{u}{1+u}$, leads us to the alternative representation

$$B(x,y) = \int_0^\infty \mathrm{d}u \frac{u^{x-1}}{(1+u)^{x+y}}. \tag{B.11}$$

The most important property of the Beta function is its connection to the previously introduced Gamma function

$$B(x,y) = \frac{\Gamma(x)\Gamma(y)}{\Gamma(x+y)}. \tag{B.12}$$

This useful identity can be shown as follows. We start with the product of two Gamma functions

$$I(p,q) = \Gamma(p)\Gamma(q) = \int_0^\infty \mathrm{d}x \int_0^\infty \mathrm{d}y\, x^{p-1}y^{q-1}e^{-x}e^{-y} \tag{B.13}$$

and substitute $x = u(1-v)$ and $y = uv$. Taking into account the Jacobi determinant

$$\det(J) = \det\begin{pmatrix} 1-v & -u \\ v & u \end{pmatrix} = u, \tag{B.14}$$

we obtain

$$
\begin{aligned}
I(p,q) &= \int_0^\infty \mathrm{d}u \int_0^1 \mathrm{d}v \, \det(J) u^{p-1}(1-v)^{p-1} u^{q-1} v^{q-1} e^{-u} \\
&= \int_0^\infty \mathrm{d}u u^{p+q-1} e^{-u} \int_0^1 \mathrm{d}v v^{q-1}(1-v)^{p-1} = \Gamma(p+q)B(q,p) \\
\Leftrightarrow B(q,p) &= B(p,q) = \frac{\Gamma(p)\Gamma(q)}{\Gamma(p+q)}.
\end{aligned}
\tag{B.15}
$$

Furthermore, the Beta function obeys

$$
B(x+1,y) = B(x,y+1) = \frac{x}{x+y}B(x,y). \tag{B.16}
$$

B.3. Dilogarithm

The *Dilogarithm* or *Spence function* is defined as

$$
\mathrm{Li}_2(z) = \mathrm{Sp}(z) = -\int_0^1 \frac{\mathrm{d}t}{t}\ln(1-zt) = -\int_0^z \frac{\mathrm{d}t}{t}\ln(1-t). \tag{B.17}
$$

It is the special case $s = 2$ of the more general *Polylogarithm* $\mathrm{Li}_s(z)$ which can be written as a series of the form

$$
\mathrm{Li}_s(z) = \sum_{k=1}^\infty \frac{z^k}{k^s}. \tag{B.18}
$$

Some concrete values are

$$
\mathrm{Li}_2(0) = 0, \quad \mathrm{Li}_2(1) = \frac{\pi^2}{6}, \quad \mathrm{Li}_2(-1) = -\frac{\pi^2}{12} \quad \text{and} \quad \mathrm{Li}_2\left(\frac{1}{2}\right) = \frac{\pi^2}{12} - \frac{\ln^2(2)}{2}. \tag{B.19}
$$

Several useful identities including the Dilogarithm can be found in [166].

B.4. Hypergeometric function

The hypergeometric function $_2F_1(a,b,c,z)$ is the general solution to the second-order linear differential equation

$$
z(1-z)w''(z) + (c - (a+b+1)z)\,w'(z) - abw(z) = 0 \quad \text{with} \quad w(0) = 1. \tag{B.20}
$$

It can be written as an infinite series via

$$
_2F_1(a,b,c,z) = \frac{\Gamma(c)}{\Gamma(a)\Gamma(b)} \sum_{n=0}^\infty \frac{\Gamma(a+n)\Gamma(b+n)}{\Gamma(c+n)} \frac{z^n}{n!} \tag{B.21}
$$

or via its integral representation

$$
_2F_1(a,b,c,z) = \frac{\Gamma(c)}{\Gamma(b)\Gamma(c-b)} \int_0^1 \mathrm{d}t t^{b-1}(1-t)^{c-b-1}(1-zt)^{-a}. \tag{B.22}
$$

There are thousands of relations and identities including the hypergeometric function. Impressive collections can be found in [232, 233]. We use the hypergeometric function to evaluate special cases of scalar Passarino Veltman integrals (cf. subsections F.3.1 and F.3.2).

B.5. Feynman parameters

The basic idea of Feynman parameters is to rewrite a fraction as a multidimensional integral. The most simple relation of this kind is

$$\frac{1}{ab} = \int_0^1 dx \, (a(1-x) + bx)^{-2} , \tag{B.23}$$

which can simply be proven by direct calculation.

$$\int_0^1 dx \, (a(1-x) + bx)^{-2} = \left. \frac{-1}{(b-a)(a(1-x) + bx)} \right|_0^1 = \frac{1}{ab} . \tag{B.24}$$

The analogous equation for three denominators reads

$$\frac{1}{abc} = 2 \int_0^1 dx \int_0^{1-x} dy \, (a(1-x-y) + bx + cy)^{-3} . \tag{B.25}$$

Both of the previously presented formulae (B.23) and (B.25) are special cases of the more general relation

$$\frac{1}{A_1...A_n} = \int_0^1 dx_1... \int_0^1 dx_n \delta\left(\sum_{i=1}^n x_i - 1\right) \frac{(n-1)!}{(x_1 A_1 + ... + x_n A_n)^n} , \tag{B.26}$$

where we have used the *Dirac distribution* δ. This relation can be proven via complete induction. We also list the special case of k equal denominators.

$$\frac{1}{AB^k} = \int_0^1 dx \int_0^1 dy \delta(x + y - 1) \frac{k y^{k-1}}{(xA + yB)^{k+1}} . \tag{B.27}$$

C. Dirac algebra

When evaluating the invariant amplitude of a given Feynman diagram, one has to calculate products and traces of *Dirac matrices*. These terms originate from the vertices and fermion propagators of the process. In the following we list fundamental properties of the Dirac matrices and useful formulae for the aforementioned calculations. This appendix is partially a translation of the respective parts of [57].

C.1. Dirac algebra in four dimensions

The Dirac or gamma matrices are 4×4 matrices which are defined by the anticommutation relation

$$\{\gamma^\mu, \gamma^\nu\} = \gamma^\mu\gamma^\nu + \gamma^\nu\gamma^\mu = 2g^{\mu\nu}\mathbb{1}. \tag{C.1}$$

Herein $g^{\mu\nu}$ is the metric tensor in four dimensions and $\mathbb{1}$ is the four dimensional unity matrix. The Dirac matrices generate a Clifford algebra. We normalise them via

$$(\gamma^0)^\dagger = \gamma^0 \quad \text{and} \quad (\gamma^i)^\dagger = -\gamma^i \quad \text{with} \quad i = 1, 2, 3 \tag{C.2}$$

and define the fifth gamma matrix as

$$\gamma_5 = i\gamma^0\gamma^1\gamma^2\gamma^3. \tag{C.3}$$

With these definitions one can derive the equations given below (cf. e.g. [234]).

Properties of γ_5 and its connection to the Levi-Civita tensor

$$(\gamma_5)^\dagger = \gamma_5, \quad (\gamma_5)^2 = \mathbb{1} \quad \text{and} \quad \{\gamma_5, \gamma^\mu\} = 0. \tag{C.4}$$

We can also rewrite the fifth gamma matrix by using the four dimensional *Levi-Civita tensor*.

$$\gamma_5 = i\gamma^0\gamma^1\gamma^2\gamma^3 = -\frac{i}{4!}\epsilon_{\mu\nu\rho\sigma}\gamma^\mu\gamma^\nu\gamma^\rho\gamma^\sigma = -\frac{i}{4!}\epsilon^{\mu\nu\rho\sigma}\gamma_\mu\gamma_\nu\gamma_\rho\gamma_\sigma. \tag{C.5}$$

The Levi-Civita tensor is defined as

$$\epsilon^{\mu\nu\rho\sigma} = \begin{cases} 1 & \text{if } \mu\nu\rho\sigma \text{ is an even permutation of 0123,} \\ -1 & \text{if } \mu\nu\rho\sigma \text{ is an odd permutation of 0123,} \\ 0 & \text{otherwise.} \end{cases} \tag{C.6}$$

Sometimes one encounters products of two Levi-Civita tensors which can be expressed in terms of Kronecker deltas [235].

$$\epsilon_{\mu\nu\rho\sigma}\epsilon^{\mu\nu\rho\sigma} = -24. \tag{C.7}$$

$$\epsilon_{\mu\nu\rho\alpha}\epsilon^{\mu\nu\rho\beta} = -6\delta_\alpha^\beta. \tag{C.8}$$

$$\epsilon_{\mu\nu\alpha\beta}\epsilon^{\mu\nu\gamma\delta} = -2(\delta_\alpha^\gamma\delta_\beta^\delta - \delta_\alpha^\delta\delta_\beta^\gamma). \tag{C.9}$$

Trace theorems

$$\text{Tr}(\gamma^\mu\gamma^\nu) = 4g^{\mu\nu}. \tag{C.10}$$

$$\text{Tr}(\gamma^\mu\gamma^\nu\gamma^\rho\gamma^\sigma) = 4(g^{\mu\nu}g^{\rho\sigma} - g^{\mu\rho}g^{\nu\sigma} + g^{\mu\sigma}g^{\nu\rho}). \tag{C.11}$$

$$\text{Tr}(\underbrace{\gamma^\mu\gamma^\nu\gamma^\rho...}_{2n+1}) = 0 \quad \text{with} \quad n \in \mathbb{N}. \tag{C.12}$$

$$\text{Tr}(\gamma_5) = 0. \tag{C.13}$$

$$\text{Tr}(\gamma^\mu\gamma^\nu\gamma_5) = 0. \tag{C.14}$$

$$\text{Tr}(\gamma^\mu\gamma^\nu\gamma^\rho\gamma^\sigma\gamma_5) = 4i\epsilon^{\mu\nu\rho\sigma}. \tag{C.15}$$

$$\text{Tr}(\underbrace{\gamma^\mu\gamma^\nu\gamma^\rho...}_{2n+1}\gamma_5) = 0 \quad \text{with} \quad n \in \mathbb{N}. \tag{C.16}$$

Contraction identities

$$\gamma^\mu\gamma_\mu = 4\mathbb{1}. \tag{C.17}$$

$$\gamma^\mu\gamma^\nu\gamma_\mu = -2\gamma^\nu. \tag{C.18}$$

$$\gamma^\mu\gamma^\nu\gamma^\rho\gamma_\mu = 4g^{\nu\rho}\mathbb{1}. \tag{C.19}$$

$$\gamma^\mu\gamma^\nu\gamma^\rho\gamma^\sigma\gamma_\mu = -2\gamma^\sigma\gamma^\rho\gamma^\nu. \tag{C.20}$$

Chisholm identity

$$\gamma^\mu\gamma^\nu\gamma^\rho = g^{\mu\nu}\gamma^\rho - g^{\mu\rho}\gamma^\nu + g^{\nu\rho}\gamma^\mu + i\epsilon^{\mu\nu\rho\sigma}\gamma_\sigma\gamma_5. \tag{C.21}$$

The Chisholm identity can be used to shift factors of gamma matrices between two contracted spinor chains, see e.g. [236]. By doing this, it can be shown that for arbitrary spinors $\bar{a}$, b, $\bar{c}$ and d the following relations are fulfilled.

$$[\bar{a}\gamma_\mu\gamma_\sigma\gamma_\nu(\mathbb{1} - \gamma_5)b][\bar{c}\gamma^\mu\gamma^\sigma\gamma^\nu(\mathbb{1} - \gamma_5)d] = 16[\bar{a}\gamma_\mu(\mathbb{1} - \gamma_5)b][\bar{c}\gamma^\mu(\mathbb{1} - \gamma_5)d]. \tag{C.22}$$

$$[\bar{a}\gamma_\mu\gamma_\sigma\gamma_\nu(\mathbb{1} - \gamma_5)b][\bar{c}\gamma^\nu\gamma^\sigma\gamma^\mu(\mathbb{1} - \gamma_5)d] = 4[\bar{a}\gamma_\mu(\mathbb{1} - \gamma_5)b][\bar{c}\gamma^\mu(\mathbb{1} - \gamma_5)d]. \tag{C.23}$$

C.2. Dirac algebra in D dimensions

In the framework of dimensional reduction (see chapter F), the phase space becomes D-dimensional. Lorentz indices now run from 0 to $D-1$. The defining Dirac algebra remains unchanged, we have $\{\gamma^\mu, \gamma^\nu\} = 2g^{\mu\nu}\mathbb{1}$, where the Dirac matrices are still 4×4 objects and $\text{Tr}\,\mathbb{1} = 4$.

Unfortunately, it is not possible to generalise the fifth gamma matrix with the properties of (C.4) in a trivial way to D dimensions (cf. [237–242]). We follow the so-called *naive dimensional reduction* prescription which is based on the identities

$$\{\gamma^\mu, \gamma^\nu\} = 2g^{\mu\nu}\mathbb{1}, \quad g_\mu^\mu = D \quad \text{and} \quad \{\gamma_\mu, \gamma_5\} = 0. \tag{C.24}$$

This set of rules is inconsistent with $\text{Tr}(\gamma^\mu\gamma^\nu\gamma^\rho\gamma^\sigma\gamma_5) = 4i\epsilon^{\mu\nu\rho\sigma}$ in four dimensions but works quite well in practice [243]. The trace theorems of the previous section remain unchanged. In contrast, the contraction identities generalise as follows.

Contraction identities

$$\gamma^\mu \gamma_\mu = D \mathbb{1}. \tag{C.25}$$

$$\gamma^\mu \gamma^\nu \gamma_\mu = (2 - D)\gamma^\nu. \tag{C.26}$$

$$\gamma^\mu \gamma^\nu \gamma^\rho \gamma_\mu = 4g^{\nu\rho} \mathbb{1} + (D - 4)\gamma^\nu \gamma^\rho. \tag{C.27}$$

$$\gamma^\mu \gamma^\nu \gamma^\rho \gamma^\sigma \gamma_\mu = -2\gamma^\sigma \gamma^\rho \gamma^\nu - (D - 4)\gamma^\nu \gamma^\rho \gamma^\sigma. \tag{C.28}$$

D. Fierz identities

The *Fierz identities* have first been found by Swiss physicist Markus Fierz in 1932 (cf. [244]) and are briefly mentioned in most textbooks on quantum field theory (cf. e.g. [231, 235, 245]). However, a detailed discussion including the derivation of the coefficients is rarely found. As the Fierz identities play a crucial role for our calculation of neutralino-nucleon cross sections, we give this detailed discussion in the following. The most useful references are [246–248]. One of the few articles commenting briefly on the Fierz transformation in the context of dark matter is [249]. We agree with the final transformation given there and in particular with the discussion about the sign which we present in section D.3.

D.1. Basic idea of Fierz identities

Let $\bar{a}$ and b denote two spinors which may correspond to two different particles. It is possible to construct five different and independent Lorentz-covariant quantities out of these spinors which are classified in table D.1. Here we introduced

$$\gamma^{\mu\nu} = \frac{i}{2}[\gamma^\mu, \gamma^\nu] = \frac{i}{2}(\gamma^\mu\gamma^\nu - \gamma^\nu\gamma^\mu). \tag{D.1}$$

As obviously $\gamma^{\mu\mu} = 0$ and $\gamma^{\mu\nu} = -\gamma^{\nu\mu}$ the number of independent components of $\gamma^{\mu\nu}$ is six. Note that the classification scheme in table D.1 is not unique. Other authors include additional factors of i or a factor of $\frac{1}{\sqrt{2}}$ in front of $\gamma^{\mu\nu}$, which affects of course the final results, i.e. the coefficients as they are given in table D.3. Thus, when reading off the coefficients of such a table it is important to ensure that the conventions concerning the operators agree.

Let $\bar{c}$ and d denote two more spinors which may correspond to two more independent particles. Given these additional spinors, we can use the covariant quantities listed in table D.1 to construct the Lorentz scalar in five different ways which are presented in table D.2. By introducing the operators O_i as given in table D.2, we can write the Lorentz scalar compactly as

$$[\bar{a}O_i b][\bar{c}O^i d], \quad \text{where} \quad i = S, V, T, A, P. \tag{D.2}$$

In this case, there is no summation over i. The central idea of the Fierz identities is to rewrite this expression as a linear combination of similar terms with changed spinor order.

$$[\bar{a}O_i b][\bar{c}O^i d] = \sum_k c_{ik}[\bar{a}O_k d][\bar{c}O^k b]. \tag{D.3}$$

This is possible as the 16 matrices included in the operators O_i form a complete basis. All that remains is to determine the coefficients c_{ik}. They are given in table D.3 and derived in the next section. Note the symmetry of table D.3 with respect to its central

Table D.1.: Lorentz-covariant quantities constructed out of two spinors

Covariant quantity	Name	Number of components
$\bar{a}b$	Scalar	1
$\bar{a}\gamma^\mu b$	Vector	4
$\bar{a}\gamma^{\mu\nu}b$	Tensor	6
$\bar{a}\gamma_5\gamma^\mu b$	Axial-vector	4
$\bar{a}\gamma_5 b$	Pseudoscalar	1

Table D.2.: Lorentz scalar obtained in five different ways

Lorentz scalar	Name	Operator O_i
$[\bar{a}b][\bar{c}d]$	S-variant	$O_S = \mathbb{1}$
$[\bar{a}\gamma_\mu b][\bar{c}\gamma^\mu d]$	V-variant	$O_V = \gamma_\mu$
$[\bar{a}\gamma_{\mu\nu} b][\bar{c}\gamma^{\mu\nu} d]$	T-variant	$O_T = \gamma_{\mu\nu}$
$[\bar{a}\gamma_5\gamma_\mu b][\bar{c}\gamma_5\gamma^\mu d]$	A-variant	$O_A = \gamma_5\gamma_\mu$
$[\bar{a}\gamma_5 b][\bar{c}\gamma_5 d]$	P-variant	$O_P = \gamma_5$

Table D.3.: Fierz coefficients for spinors

	S	V	T	A	P
S	$\frac{1}{4}$	$\frac{1}{4}$	$\frac{1}{8}$	$-\frac{1}{4}$	$\frac{1}{4}$
V	1	$-\frac{1}{2}$	0	$-\frac{1}{2}$	-1
T	3	0	$-\frac{1}{2}$	0	3
A	-1	$-\frac{1}{2}$	0	$-\frac{1}{2}$	1
P	$\frac{1}{4}$	$-\frac{1}{4}$	$\frac{1}{8}$	$\frac{1}{4}$	$\frac{1}{4}$

element. As an example for using this table, we give the Fierz identity for the S-variant.

$$
\begin{aligned}
[\bar{a}O_S b][\bar{c}O^S d] &= \frac{1}{4}[\bar{a}O_S d][\bar{c}O^S b] + \frac{1}{4}[\bar{a}O_V d][\bar{c}O^V b] + \frac{1}{8}[\bar{a}O_T d][\bar{c}O^T b] \\
&\quad - \frac{1}{4}[\bar{a}O_A d][\bar{c}O^A b] + \frac{1}{4}[\bar{a}O_P d][\bar{c}O^P b] \\
\Leftrightarrow [\bar{a}b][\bar{c}d] &= \frac{1}{4}[\bar{a}d][\bar{c}b] + \frac{1}{4}[\bar{a}\gamma_\mu d][\bar{c}\gamma^\mu b] + \frac{1}{8}[\bar{a}\gamma_{\mu\nu} d][\bar{c}\gamma^{\mu\nu} b] \\
&\quad - \frac{1}{4}[\bar{a}\gamma_5\gamma_\mu d][\bar{c}\gamma_5\gamma^\mu b] + \frac{1}{4}[\bar{a}\gamma_5 d][\bar{c}\gamma_5 b].
\end{aligned}
\tag{D.4}
$$

D.2. Derivation of the Fierz coefficients

To derive the Fierz coefficients c_{ik} we start with (D.3) and write it in components.

$$\bar{a}_\alpha b_\beta \bar{c}_\gamma d_\delta (O_i)_{\alpha\beta}(O^i)_{\gamma\delta} = \sum_k c_{ik}\bar{a}_\alpha d_\delta \bar{c}_\gamma b_\beta (O_k)_{\alpha\delta}(O^k)_{\gamma\beta}$$

$$= \sum_k c_{ik}\bar{a}_\alpha b_\beta \bar{c}_\gamma d_\delta (O_k)_{\alpha\delta}(O^k)_{\gamma\beta}. \tag{D.5}$$

In the last step we have assumed that the individual components of the spinors are complex numbers, i.e. that the spinor components commute. We return to this issue in section D.3. Remember that the four spinors $\bar{a}, b, \bar{c}$ and d are completely arbitrary. Hence, the equation above can only hold if all of the tensor components agree, i.e. if

$$(O_i)_{\alpha\beta}(O^i)_{\gamma\delta} = \sum_k c_{ik}(O_k)_{\alpha\delta}(O^k)_{\gamma\beta}. \tag{D.6}$$

In the next step, we multiply this expression with an operator $(O^j)_{\beta\gamma}$ and sum over β and γ.

$$(O_i)_{\alpha\beta}(O^j)_{\beta\gamma}(O^i)_{\gamma\delta} = \sum_k c_{ik}(O_k)_{\alpha\delta}(O^j)_{\beta\gamma}(O^k)_{\gamma\beta}$$

$$\Leftrightarrow O_i O^j O^i = \sum_k c_{ik}O_k \operatorname{Tr}(O^j O^k). \tag{D.7}$$

To determine the c_{ik} one has to insert all 25 possible combinations of O_i and O^j in (D.7). We start with the right-hand side as it is always the same for a given i. In the following calculations we use the formulae given in appendix C extensively.

Right-hand side

- $j = S$

$$c_{iS}\mathbb{1}\operatorname{Tr}(\mathbb{1}\mathbb{1}) + c_{iV}\gamma_\mu \operatorname{Tr}(\mathbb{1}\gamma^\mu) + c_{iT}\gamma_{\mu\nu}\operatorname{Tr}(\mathbb{1}\gamma^{\mu\nu})$$
$$+\ c_{iA}\gamma_5\gamma_\mu \operatorname{Tr}(\mathbb{1}\gamma_5\gamma^\mu) + c_{iP}\gamma_5 \operatorname{Tr}(\mathbb{1}\gamma_5)$$
$$=\ 4c_{iS}\mathbb{1}. \tag{D.8}$$

- $j = V$

$$c_{iS}\mathbb{1}\operatorname{Tr}(\gamma^\rho \mathbb{1}) + c_{iV}\gamma_\mu \operatorname{Tr}(\gamma^\rho\gamma^\mu) + c_{iT}\gamma_{\mu\nu}\operatorname{Tr}(\gamma^\rho\gamma^{\mu\nu})$$
$$+\ c_{iA}\gamma_5\gamma_\mu \operatorname{Tr}(\gamma^\rho\gamma_5\gamma^\mu) + c_{iP}\gamma_5 \operatorname{Tr}(\gamma^\rho\gamma_5)$$
$$=\ 4c_{iV}\gamma^\rho. \tag{D.9}$$

- $j = T$

$$c_{iS}\mathbb{1}\operatorname{Tr}(\gamma^{\rho\eta} \mathbb{1}) + c_{iV}\gamma_\mu \operatorname{Tr}(\gamma^{\rho\eta}\gamma^\mu) + c_{iT}\gamma_{\mu\nu}\operatorname{Tr}(\gamma^{\rho\eta}\gamma^{\mu\nu})$$
$$+\ c_{iA}\gamma_5\gamma_\mu \operatorname{Tr}(\gamma^{\rho\eta}\gamma_5\gamma^\mu) + c_{iP}\gamma_5 \operatorname{Tr}(\gamma^{\rho\eta}\gamma_5)$$
$$=\ 2ic_{iS}\mathbb{1}(g^{\rho\eta} - g^{\eta\rho}) + c_{iT}\gamma_{\mu\nu}\operatorname{Tr}(\gamma^{\rho\eta}\gamma^{\mu\nu})$$
$$=\ -\frac{i}{8}c_{iT}(\gamma_\mu\gamma_\nu - \gamma_\nu\gamma_\mu)\operatorname{Tr}((\gamma^\rho\gamma^\eta - \gamma^\eta\gamma^\rho)(\gamma^\mu\gamma^\nu - \gamma^\nu\gamma^\mu))$$
$$=\ -ic_{iT}\gamma_\mu\gamma_\nu \operatorname{Tr}(\gamma^\rho\gamma^\eta\gamma^\mu\gamma^\nu) \quad \text{with} \quad \mu \neq \nu, \rho \neq \eta$$
$$=\ 8c_{iT}\gamma^{\rho\eta}. \tag{D.10}$$

- $j = A$

$$c_{iS} \mathbb{1} \operatorname{Tr}(\gamma_5 \gamma^\rho \mathbb{1}) + c_{iV} \gamma_\mu \operatorname{Tr}(\gamma_5 \gamma^\rho \gamma^\mu) + c_{iT} \gamma_{\mu\nu} \operatorname{Tr}(\gamma_5 \gamma^\rho \gamma^{\mu\nu})$$
$$+ \quad c_{iA} \gamma_5 \gamma_\mu \operatorname{Tr}(\gamma_5 \gamma^\rho \gamma_5 \gamma^\mu) + c_{iP} \gamma_5 \operatorname{Tr}(\gamma_5 \gamma^\rho \gamma_5)$$
$$= \quad -4 c_{iA} \gamma_5 \gamma^\rho. \tag{D.11}$$

- $j = P$

$$c_{iS} \mathbb{1} \operatorname{Tr}(\gamma_5 \mathbb{1}) + c_{iV} \gamma_\mu \operatorname{Tr}(\gamma_5 \gamma^\mu) + c_{iT} \gamma_{\mu\nu} \operatorname{Tr}(\gamma_5 \gamma^{\mu\nu})$$
$$+ \quad c_{iA} \gamma_5 \gamma_\mu \operatorname{Tr}(\gamma_5 \gamma_5 \gamma^\mu) + c_{iP} \gamma_5 \operatorname{Tr}(\gamma_5 \gamma_5)$$
$$= \quad 4 c_{iP} \gamma_5. \tag{D.12}$$

The results obtained so far are very interesting. By explicit calculation, we have shown that for a given j the term proportional to c_{ij} is the only one contributing from the right-hand side. This simplifies the calculation enormously. Besides the practical aspect, the result implies that

$$\operatorname{Tr}(O^j O^k) \sim \delta_{jk}. \tag{D.13}$$

This means that $\operatorname{Tr}(O^j O^k)$ defines a suitable scalar product on the set of operators O_i. In the sense of this scalar product, the operators form an orthogonal basis. We can even construct an orthonormal basis, i.e.

$$\operatorname{Tr}(O^j O^k) = \delta_{jk}, \tag{D.14}$$

by redefining

$$O_S \to \frac{1}{2} O_S, \quad O_V \to \frac{1}{2} O_V, \quad O_T \to \frac{1}{2\sqrt{2}} O_T, \quad O_A \to \frac{i}{2} O_A \quad \text{and} \quad O_P \to \frac{1}{2} O_P. \tag{D.15}$$

However, in the following we stick to the original definitions given in the beginning of this appendix and continue with the evaluation of the left-hand side for all possible i and j.

Left-hand side, $i = S$

- $j = S$

$$\mathbb{1} \mathbb{1} \mathbb{1} = \mathbb{1} \quad \Rightarrow \quad c_{SS} = \frac{1}{4}. \tag{D.16}$$

- $j = V$

$$\mathbb{1} \gamma^\rho \mathbb{1} = \gamma^\rho \quad \Rightarrow \quad c_{SV} = \frac{1}{4}. \tag{D.17}$$

- $j = T$

$$\mathbb{1} \gamma^{\rho\eta} \mathbb{1} = \gamma^{\rho\eta} \quad \Rightarrow \quad c_{ST} = \frac{1}{8}. \tag{D.18}$$

- $j = A$

$$\mathbb{1} \gamma_5 \gamma^\rho \mathbb{1} = \gamma_5 \gamma^\rho \quad \Rightarrow \quad c_{SA} = -\frac{1}{4}. \tag{D.19}$$

- $j = P$

$$\mathbb{1} \gamma_5 \mathbb{1} = \gamma_5 \quad \Rightarrow \quad c_{SP} = \frac{1}{4}. \tag{D.20}$$

Left-hand side, $i = V$

- $j = S$

$$\gamma_\mu \mathbb{1} \gamma^\mu = \gamma_\mu \gamma^\mu \mathbb{1} = 4\mathbb{1} \quad \Rightarrow \quad c_{VS} = 1. \tag{D.21}$$

- $j = V$

$$\gamma_\mu \gamma^\rho \gamma^\mu = -2\gamma^\rho \quad \Rightarrow \quad c_{VV} = -\frac{1}{2}. \tag{D.22}$$

- $j = T$

$$\gamma_\mu \gamma^{\rho\eta} \gamma^\mu = 0 \quad \Rightarrow \quad c_{VT} = 0. \tag{D.23}$$

- $j = A$

$$\gamma_\mu \gamma_5 \gamma^\rho \gamma^\mu = 2\gamma_5 \gamma^\rho \quad \Rightarrow \quad c_{VA} = -\frac{1}{2}. \tag{D.24}$$

- $j = P$

$$\gamma_\mu \gamma_5 \gamma^\mu = -4\gamma_5 \quad \Rightarrow \quad c_{VP} = -1. \tag{D.25}$$

Left-hand side, $i = T$

- $j = S$

$$
\begin{aligned}
\gamma_{\mu\nu} \mathbb{1} \gamma^{\mu\nu} &= -\frac{1}{2}(\gamma_\mu \gamma_\nu - \gamma_\nu \gamma_\mu)\gamma^\mu \gamma^\nu \\
&= -\frac{1}{2}(-2\gamma_\nu - 4\gamma_\nu)\gamma^\nu = 12\mathbb{1} \quad \Rightarrow \quad c_{TS} = 3.
\end{aligned} \tag{D.26}
$$

- $j = V$

$$
\begin{aligned}
\gamma_{\mu\nu} \gamma^\rho \gamma^{\mu\nu} &= -\frac{1}{4}(\gamma_\mu \gamma_\nu - \gamma_\nu \gamma_\mu)\gamma^\rho (\gamma^\mu \gamma^\nu - \gamma^\nu \gamma^\mu) \\
&= -\frac{1}{4}(\gamma_\mu \gamma_\nu \gamma^\rho \gamma^\mu \gamma^\nu - \gamma_\mu \gamma_\nu \gamma^\rho \gamma^\nu \gamma^\mu \\
&\quad + \gamma_\nu \gamma_\mu \gamma^\rho \gamma^\nu \gamma^\mu - \gamma_\nu \gamma_\mu \gamma^\rho \gamma^\mu \gamma^\nu) \\
&= -\frac{1}{2}(\gamma_\mu \gamma_\nu \gamma^\rho \gamma^\mu \gamma^\nu - \gamma_\mu \gamma_\nu \gamma^\rho \gamma^\nu \gamma^\mu) \\
&= -\frac{1}{2}(4\gamma^\rho - 4\gamma^\rho) = 0 \quad \Rightarrow \quad c_{TV} = 0.
\end{aligned} \tag{D.27}
$$

- $j = T$

$$
\begin{aligned}
\gamma_{\mu\nu} \gamma^{\rho\eta} \gamma^{\mu\nu} &= -\frac{i}{8}(\gamma_\mu \gamma_\nu - \gamma_\nu \gamma_\mu)(\gamma^\rho \gamma^\eta - \gamma^\eta \gamma^\rho)(\gamma^\mu \gamma^\nu - \gamma^\nu \gamma^\mu) \\
&= -\frac{i}{4}\gamma_\mu \gamma_\nu (\gamma^\rho \gamma^\eta - \gamma^\eta \gamma^\rho)(\gamma^\mu \gamma^\nu - \gamma^\nu \gamma^\mu) \\
&= \frac{i}{2}(\gamma^\eta \gamma^\rho \gamma_\nu - \gamma^\rho \gamma^\eta \gamma_\nu)\gamma^\nu \\
&= 2i(\gamma^\eta \gamma^\rho - \gamma^\rho \gamma^\eta) = -4\gamma^{\rho\eta} \quad \Rightarrow \quad c_{TT} = -\frac{1}{2}.
\end{aligned} \tag{D.28}
$$

- $j = A$

$$\gamma_{\mu\nu} \gamma_5 \gamma^\rho \gamma^{\mu\nu} = \gamma_5 \gamma_{\mu\nu} \gamma^\rho \gamma^{\mu\nu} = 0 \quad \Rightarrow \quad c_{TA} = 0. \tag{D.29}$$

- $j = P$

$$\gamma_{\mu\nu}\gamma_5\gamma^{\mu\nu} = \gamma_5\gamma_{\mu\nu}\gamma^{\mu\nu} = 12\gamma_5 \quad \Rightarrow \quad c_{TP} = 3. \tag{D.30}$$

Left-hand side, $i = A$

- $j = S$

$$\gamma_5\gamma_\mu \mathbb{1}\gamma_5\gamma^\mu = -4\mathbb{1} \quad \Rightarrow \quad c_{AS} = -1. \tag{D.31}$$

- $j = V$

$$\gamma_5\gamma_\mu\gamma^\rho\gamma_5\gamma^\mu = -2\gamma^\rho \quad \Rightarrow \quad c_{AV} = -\frac{1}{2}. \tag{D.32}$$

- $j = T$

$$\gamma_5\gamma_\mu\gamma^{\rho\eta}\gamma_5\gamma^\mu = 0 \quad \Rightarrow \quad c_{AT} = 0. \tag{D.33}$$

- $j = A$

$$\gamma_5\gamma_\mu\gamma_5\gamma^\rho\gamma_5\gamma^\mu = 2\gamma_5\gamma^\rho \quad \Rightarrow \quad c_{AA} = -\frac{1}{2}. \tag{D.34}$$

- $j = P$

$$\gamma_5\gamma_\mu\gamma_5\gamma_5\gamma^\mu = 4\gamma_5 \quad \Rightarrow \quad c_{AP} = 1. \tag{D.35}$$

Left-hand side, $i = P$

- $j = S$

$$\gamma_5\mathbb{1}\gamma_5 = \mathbb{1} \quad \Rightarrow \quad c_{PS} = \frac{1}{4}. \tag{D.36}$$

- $j = V$

$$\gamma_5\gamma^\rho\gamma_5 = -\gamma^\rho \quad \Rightarrow \quad c_{PV} = -\frac{1}{4}. \tag{D.37}$$

- $j = T$

$$\gamma_5\gamma^{\rho\eta}\gamma_5 = \gamma^{\rho\eta} \quad \Rightarrow \quad c_{PT} = \frac{1}{8}. \tag{D.38}$$

- $j = A$

$$\gamma_5\gamma_5\gamma^\rho\gamma_5 = -\gamma_5\gamma^\rho \quad \Rightarrow \quad c_{PA} = \frac{1}{4}. \tag{D.39}$$

- $j = P$

$$\gamma_5\gamma_5\gamma_5 = \gamma_5 \quad \Rightarrow \quad c_{PP} = \frac{1}{4}. \tag{D.40}$$

We close this section with a remark. The derivation above bases on the fact that the operators $\mathcal{O}_i$ listed in table D.2 form a complete basis for 4×4 matrices. This works out nicely in four dimensions. However, in the context of dimensional reduction (cf. chapter F) the Lorentz indices run from 0 to $D-1$ and performing a Fierz transformation becomes highly non-trivial [250, 251]. Fortunately, we do not have to worry about all the extra formalism involved as the corresponding problems become manifest only in higher order corrections, e.g. at three-loop order [252–254].

Table D.4.: Fierz coefficients for spinor fields

	S	**V**	**T**	**A**	**P**
S	$-\frac{1}{4}$	$-\frac{1}{4}$	$-\frac{1}{8}$	$\frac{1}{4}$	$-\frac{1}{4}$
V	-1	$\frac{1}{2}$	0	$\frac{1}{2}$	1
T	-3	0	$\frac{1}{2}$	0	-3
A	1	$\frac{1}{2}$	0	$\frac{1}{2}$	-1
P	$-\frac{1}{4}$	$\frac{1}{4}$	$-\frac{1}{8}$	$-\frac{1}{4}$	$-\frac{1}{4}$

D.3. On the sign of the Fierz coefficients

In this section we clarify what is meant by a *spinor* in the context of Fierz identities as this turned out to be a possible source of sign errors. The field equation for a free spin $1/2$ particle with mass m is the Dirac equation

$$(i\slashed{\partial} - m)\Psi = 0. \tag{D.41}$$

In classical field theory Ψ can be understood as the wave function of the particle. In quantum field theory Ψ is quantised, i.e. Ψ contains annihilation and creation operators. A general quantised plane-wave solution of the Dirac equation in position space can be written as (cf. [172])

$$\Psi = \Psi(x) = \int \frac{d^3\vec{p}}{(2\pi)^3\sqrt{2E}} \sum_{s=1,2} \left(c_s(p)u(p,s)e^{-ipx} + d_s^\dagger(p)v(p,s)e^{ipx} \right), \tag{D.42}$$

where $E = \sqrt{m^2 + \vec{p}^2}$ is the energy of the particle and s denotes its spin. $c_s(p)$ is the annihilation operator for the considered particle and $d_s^\dagger(p)$ is the creation operator for the corresponding antiparticle. We call $u(p,s)$ and $v(p,s)$ the *spinors* for the particle and antiparticle, respectively. As stated in the Feynman rules, they occur in scattering amplitudes including external fermions. The components of the spinors are complex numbers, which is why the derivation of the Fierz coefficients as given in section D.2 is valid.

However, in other situations one might use Fierz identities for *spinor fields* like $\Psi(x)$. In this (arbitrarily chosen) nomenclature, the components of a spinor are complex numbers, whereas the components of a spinor field include fermionic creation and annihilation operators. Fermionic operators anticommute and so do spinor fields and their components. This enters the calculation in (D.5). For spinor fields we obtain

$$\begin{aligned}
\bar{a}_\alpha b_\beta \bar{c}_\gamma d_\delta (O_i)_{\alpha\beta}(O^i)_{\gamma\delta} &= \sum_k c_{ik} \bar{a}_\alpha d_\delta \bar{c}_\gamma b_\beta (O_k)_{\alpha\delta}(O^k)_{\gamma\beta} \\
&= (-1)^3 \sum_k c_{ik} \bar{a}_\alpha b_\beta \bar{c}_\gamma d_\delta (O_k)_{\alpha\delta}(O^k)_{\gamma\beta} \\
&= -\sum_k c_{ik} \bar{a}_\alpha b_\beta \bar{c}_\gamma d_\delta (O_k)_{\alpha\delta}(O^k)_{\gamma\beta}, \tag{D.43}
\end{aligned}$$

as we need three permutations to achieve the desired order of spinor field components. Hence, in the case of spinor fields all Fierz coefficients as given in table D.3 change sign.

Whenever we use Fierz identities in the context of direct detection, we use them for spinor fields in this sense, i.e. we use table D.4.

D.4. Fierz transformations of tensorial quantities

Here we collect and prove some useful relations for the Fierz transformation of tensorial objects. They are needed for the `Mathematica` program mentioned in subsection 4.4.5 to evaluate the box contributions to the neutralino-quark cross section.

Proposition 1. $\bar{a}\gamma_\mu\gamma_\nu b\bar{c}\gamma^\nu\gamma^\mu d = \bar{a}\gamma_{\mu\nu}b\bar{c}\gamma^{\mu\nu}d + 4\bar{a}b\bar{c}d.$

Proof. Let $\bar{a}, b, \bar{c}$ and d denote four independent spinors. We have

$$
\begin{aligned}
\bar{a}\gamma_\mu\gamma_\nu b\bar{c}\gamma^\nu\gamma^\mu d &= \frac{1}{4}\bar{a}(\gamma_\mu\gamma_\nu + \gamma_\mu\gamma_\nu)b\bar{c}(\gamma^\nu\gamma^\mu + \gamma^\nu\gamma^\mu)d \\
&= \frac{1}{4}\bar{a}(\gamma_\mu\gamma_\nu - \gamma_\nu\gamma_\mu + 2g_{\mu\nu})b\bar{c}(\gamma^\nu\gamma^\mu - \gamma^\mu\gamma^\nu + 2g^{\nu\mu})d \\
&= -\frac{1}{4}\bar{a}(\gamma_\mu\gamma_\nu - \gamma_\nu\gamma_\mu)b\bar{c}(\gamma^\mu\gamma^\nu - \gamma^\nu\gamma^\mu)d + g^\mu_\mu\bar{a}b\bar{c}d \\
&= \bar{a}\gamma_{\mu\nu}b\bar{c}\gamma^{\mu\nu}d + 4\bar{a}b\bar{c}d.
\end{aligned}
\tag{D.44}
$$

$\square$

Proposition 2. $\gamma^{\mu\nu}\gamma_5 = \frac{i}{2}\epsilon^{\mu\nu\alpha\beta}\gamma_{\alpha\beta}.$

Proof. This identity deals with the pseudotensor $\gamma^{\mu\nu}\gamma_5$. As the operators given in table D.1 form a complete basis, this operator can be reexpressed as a linear combination of them. We start by inserting the definition of the tensor operator given in (D.1) and the definition of the fifth gamma matrix according to (C.5).

$$
\begin{aligned}
\gamma^{\mu\nu}\gamma_5 &= -\frac{i}{2}(\gamma^\mu\gamma^\nu - \gamma^\nu\gamma^\mu)\frac{i}{4!}\epsilon^{\alpha\beta\gamma\delta}\gamma_\alpha\gamma_\beta\gamma_\gamma\gamma_\delta \\
&= \frac{1}{48}(\gamma^\mu\gamma^\nu - \gamma^\nu\gamma^\mu)\epsilon^{\alpha\beta\gamma\delta}\gamma_\alpha\gamma_\beta\gamma_\gamma\gamma_\delta \\
&= \frac{1}{24}\gamma^\mu\gamma^\nu\epsilon^{\alpha\beta\gamma\delta}\gamma_\alpha\gamma_\beta\gamma_\gamma\gamma_\delta \quad \text{with} \quad \mu \neq \nu.
\end{aligned}
\tag{D.45}
$$

In the last step we have assumed $\mu \neq \nu$. However, for $\mu = \nu$ we obtain directly $\gamma^{\mu\nu}\gamma_5 = \frac{i}{2}\epsilon^{\mu\nu\alpha\beta}\gamma_{\alpha\beta} = 0$. The next step is to observe that ν has to equal either α, β, γ or δ. Hence, we write

$$
\begin{aligned}
\frac{1}{24}\gamma^\mu\gamma^\nu\epsilon^{\alpha\beta\gamma\delta}\gamma_\alpha\gamma_\beta\gamma_\gamma\gamma_\delta &= \frac{1}{24}\gamma^\mu\gamma^\nu\epsilon^{\nu\beta\gamma\delta}\gamma_\nu\gamma_\beta\gamma_\gamma\gamma_\delta + \frac{1}{24}\gamma^\mu\gamma^\nu\epsilon^{\alpha\nu\gamma\delta}\gamma_\alpha\gamma_\nu\gamma_\gamma\gamma_\delta \\
&\quad + \frac{1}{24}\gamma^\mu\gamma^\nu\epsilon^{\alpha\beta\nu\delta}\gamma_\alpha\gamma_\beta\gamma_\nu\gamma_\delta + \frac{1}{24}\gamma^\mu\gamma^\nu\epsilon^{\alpha\beta\gamma\nu}\gamma_\alpha\gamma_\beta\gamma_\gamma\gamma_\nu \\
&= \frac{1}{24}\gamma^\mu\epsilon^{\nu\beta\gamma\delta}\gamma_\beta\gamma_\gamma\gamma_\delta - \frac{1}{24}\gamma^\mu\epsilon^{\alpha\nu\gamma\delta}\gamma_\alpha\gamma_\gamma\gamma_\delta \\
&\quad + \frac{1}{24}\gamma^\mu\epsilon^{\alpha\beta\nu\delta}\gamma_\alpha\gamma_\beta\gamma_\delta - \frac{1}{24}\gamma^\mu\epsilon^{\alpha\beta\gamma\nu}\gamma_\alpha\gamma_\beta\gamma_\gamma \\
&= \frac{1}{6}\gamma^\mu\epsilon^{\nu\beta\gamma\delta}\gamma_\beta\gamma_\gamma\gamma_\delta,
\end{aligned}
\tag{D.46}
$$

where we do not sum over the triple index ν. In the last step we have renamed and reordered the indices, obtaining the same expression four times. Now we proceed with the index μ in complete analogy. As $\mu \neq \nu$, μ has to equal either β, γ or δ. We get

$$
\begin{aligned}
\frac{1}{6}\gamma^\mu \epsilon^{\nu\beta\gamma\delta}\gamma_\beta\gamma_\gamma\gamma_\delta &= \frac{1}{6}\gamma^\mu\epsilon^{\nu\mu\gamma\delta}\gamma_\mu\gamma_\gamma\gamma_\delta + \frac{1}{6}\gamma^\mu\epsilon^{\nu\beta\mu\delta}\gamma_\beta\gamma_\mu\gamma_\delta + \frac{1}{6}\gamma^\mu\epsilon^{\nu\beta\gamma\mu}\gamma_\beta\gamma_\gamma\gamma_\mu \\
&= \frac{1}{2}\epsilon^{\nu\mu\gamma\delta}\gamma_\gamma\gamma_\delta = \frac{i^2}{4}\epsilon^{\mu\nu\gamma\delta}(\gamma_\gamma\gamma_\delta + \gamma_\gamma\gamma_\delta) = \frac{i}{2}\epsilon^{\mu\nu\gamma\delta}\gamma_{\gamma\delta}.
\end{aligned}
\tag{D.47}
$$

$\square$

Proposition 3. $\bar{a}\gamma_\mu\gamma_\nu\gamma_5 b\bar{c}\gamma^\nu\gamma^\mu\gamma_5 d = \bar{a}\gamma_{\mu\nu}b\bar{c}\gamma^{\mu\nu}d + 4\bar{a}\gamma_5 b\bar{c}\gamma_5 d.$

Proof. This identity is similar to proposition 1 but contains additional factors of γ_5. As before, a, b, c and d denote arbitrary independent spinors. By complete analagous steps as in proposition 1 we obtain

$$
\bar{a}\gamma_\mu\gamma_\nu\gamma_5 b\bar{c}\gamma^\nu\gamma^\mu\gamma_5 d = \bar{a}\gamma_{\mu\nu}\gamma_5 b\bar{c}\gamma^{\mu\nu}\gamma_5 d + 4\bar{a}\gamma_5 b\bar{c}\gamma_5 d.
\tag{D.48}
$$

We use proposition 2 and (C.9) to modify the first term.

$$
\begin{aligned}
\bar{a}\gamma_{\mu\nu}\gamma_5 b\bar{c}\gamma^{\mu\nu}\gamma_5 d &= -\frac{1}{4}\epsilon_{\mu\nu\alpha\beta}\epsilon^{\mu\nu\gamma\delta}\bar{a}\gamma^{\alpha\beta}b\bar{c}\gamma_{\gamma\delta}d = -\frac{1}{4}\left(-2(\delta^\gamma_\alpha\delta^\delta_\beta - \delta^\gamma_\beta\delta^\delta_\alpha)\right)\bar{a}\gamma^{\alpha\beta}b\bar{c}\gamma_{\gamma\delta}d \\
&= \frac{1}{2}(\bar{a}\gamma^{\alpha\beta}b\bar{c}\gamma_{\alpha\beta}d - \bar{a}\gamma^{\alpha\beta}b\bar{c}\gamma_{\beta\alpha}d) = \bar{a}\gamma^{\alpha\beta}b\bar{c}\gamma_{\alpha\beta}d.
\end{aligned}
\tag{D.49}
$$

$\square$

E. Weyl spinor formalism and Majorana fermions

This chapter deals with the *Weyl spinor formalism*, named after German physicist Hermann Weyl. We use it to derive two identities for Majorana fermions in section E.3. Weyl spinor fields are solutions to the *Weyl equation* which is just the massless case of the Dirac equation (cf. [255] and [256]). The Weyl equation reads

$$i\slashed{\partial}\Psi = 0. \tag{E.1}$$

Remember that the Dirac spinor field[32] Ψ is a four-component object in spinor space. In the following we decompose Ψ into two Weyl spinor fields which are two-component objects.

E.1. Weyl representation

Before we can discuss the connection between Weyl and Dirac spinor fields, we have to develop the Weyl formalism, wherein we basically follow [257]. The starting point is the *Weyl or chiral representation* of the Dirac matrices. In this representation the Dirac matrices take the form

$$\gamma^0 = \begin{pmatrix} 0 & 0 & 1 & 0 \\ 0 & 0 & 0 & 1 \\ 1 & 0 & 0 & 0 \\ 0 & 1 & 0 & 0 \end{pmatrix}, \quad \gamma^1 = \begin{pmatrix} 0 & 0 & 0 & 1 \\ 0 & 0 & 1 & 0 \\ 0 & -1 & 0 & 0 \\ -1 & 0 & 0 & 0 \end{pmatrix}, \quad \gamma^2 = \begin{pmatrix} 0 & 0 & 0 & -i \\ 0 & 0 & i & 0 \\ 0 & i & 0 & 0 \\ -i & 0 & 0 & 0 \end{pmatrix},$$

$$\gamma^3 = \begin{pmatrix} 0 & 0 & 1 & 0 \\ 0 & 0 & 0 & -1 \\ -1 & 0 & 0 & 0 \\ 0 & 1 & 0 & 0 \end{pmatrix} \quad \text{and} \quad \gamma_5 = \begin{pmatrix} -1 & 0 & 0 & 0 \\ 0 & -1 & 0 & 0 \\ 0 & 0 & 1 & 0 \\ 0 & 0 & 0 & 1 \end{pmatrix}. \tag{E.2}$$

Let us introduce the shorthand notation

$$\gamma^\mu = \begin{pmatrix} & \sigma^\mu \\ \bar{\sigma}^\mu & \end{pmatrix} \quad \text{and} \quad \gamma_5 = \begin{pmatrix} -\mathbb{1} & \\ & \mathbb{1} \end{pmatrix}, \tag{E.3}$$

where $\mathbb{1}$ corresponds to the 2×2 identity matrix and the empty spaces correspond to 2×2 zero matrices. Moreover, we encounter the generalised Pauli matrices σ^μ and $\bar{\sigma}^\mu$ again,

---

[32]We stick to the nomenclature of section D.3. The components of a spinor are complex numbers and commute, whereas the components of a spinor field include fermionic creation and annihilation operators and anticommute.

which have been introduced in chapter 2. They are defined as

$$\sigma^\mu = (\mathbb{1}, \sigma^i) \quad \text{and} \quad \bar{\sigma}^\mu = (\mathbb{1}, -\sigma^i), \tag{E.4}$$

where σ^i denotes the usual Pauli matrices. In addition, we define

$$\sigma^{\mu\nu} = \frac{i}{2}(\sigma^\mu \bar{\sigma}^\nu - \sigma^\nu \bar{\sigma}^\mu) \quad \text{and} \quad \bar{\sigma}^{\mu\nu} = \frac{i}{2}(\bar{\sigma}^\mu \sigma^\nu - \bar{\sigma}^\nu \sigma^\mu). \tag{E.5}$$

Now we decompose the Dirac spinor field Ψ in its left- and right-handed part via

$$\Psi = \begin{pmatrix} \psi_L \\ \xi_R \end{pmatrix} \quad \text{and} \quad \bar{\Psi} = \Psi^\dagger \gamma^0 = \begin{pmatrix} \xi_L, & \psi_R \end{pmatrix}. \tag{E.6}$$

We call ψ_L the left-handed Weyl spinor field and ξ_R the right-handed Weyl spinor field. They obey

$$\psi_L^* = \psi_R \quad \text{and} \quad \xi_R^* = \xi_L \tag{E.7}$$

and can be picked out of Ψ by the projection operators

$$P_L = \frac{\mathbb{1} - \gamma_5}{2} \quad \text{and} \quad P_R = \frac{\mathbb{1} + \gamma_5}{2}. \tag{E.8}$$

In the Weyl representation the Weyl equation decouples into a left- and right-handed part. We obtain

$$p_\mu \bar{\sigma}^\mu \psi_L = 0 \quad \text{and} \quad p_\mu \sigma^\mu \xi_R = 0. \tag{E.9}$$

E.2. Weyl spinor formalism

In this section we define scalar products for left- and right-handed Weyl spinor fields, respectively. Let A_L and B_L denote two left-handed Weyl spinor fields. The associated scalar product is defined via

$$A_L B_L = (A_L)^a (B_L)_a = (A_L)^1 (B_L)_1 + (A_L)^2 (B_L)_2. \tag{E.10}$$

For the scalar product of right-handed Weyl spinor fields A_R and B_R we use dotted indices and define

$$A_R B_R = (A_R)_{\dot{a}} (B_R)^{\dot{a}} = (A_R)_{\dot{1}} (B_R)^{\dot{1}} + (A_R)_{\dot{2}} (B_R)^{\dot{2}}. \tag{E.11}$$

The metric tensor $g_{\mu\nu}$ raises and lowers the Lorentz indices of four-vectors. In case of Weyl spinor fields we can define the similar quantities

$$\epsilon^{ab} = \epsilon^{\dot{a}\dot{b}} = i\sigma^2 = \begin{pmatrix} 0 & 1 \\ -1 & 0 \end{pmatrix} \quad \text{and} \quad \epsilon_{ab} = \epsilon_{\dot{a}\dot{b}} = -i\sigma^2 = \begin{pmatrix} 0 & -1 \\ 1 & 0 \end{pmatrix}, \tag{E.12}$$

which can be used to raise and lower the indices of Weyl spinor fields.

$$(A_L)^a = \epsilon^{ab}(A_L)_b. \quad (A_L)_a = \epsilon_{ab}(A_L)^b. \quad (A_R)^{\dot{a}} = \epsilon^{\dot{a}\dot{b}}(A_R)_{\dot{b}}. \quad (A_R)_{\dot{a}} = \epsilon_{\dot{a}\dot{b}}(A_R)^{\dot{b}}. \tag{E.13}$$

As a first exercise, we calculate

$$
\begin{aligned}
(A_L)_a(B_L)^a &= \epsilon_{ab}\epsilon^{ac}(A_L)^b(B_L)_c = -\delta_b{}^c(A_L)^b(B_L)_c \\
&= -(A_L)^b(B_L)_b = -A_L B_L. \quad\quad (E.14) \\
(A_R)^{\dot{a}}(B_R)_{\dot{a}} &= \epsilon^{\dot{a}\dot{b}}\epsilon_{\dot{a}\dot{c}}(A_R)_{\dot{b}}(B_R)^{\dot{c}} = -\delta^{\dot{b}}{}_{\dot{c}}(A_R)_{\dot{b}}(B_R)^{\dot{c}} \\
&= -(A_R)_{\dot{b}}(B_R)^{\dot{b}} = -A_R B_R. \quad\quad (E.15)
\end{aligned}
$$

Prior to calculating the desired identities for Majorana fermions, we return to the generalised Pauli matrices. The corresponding Weyl structure can be found by investigating the Lorentz transformation properties of those matrices (cf. [257]). We find

$$
(\sigma^\mu)_{a\dot{b}} \quad \text{and} \quad (\bar{\sigma}^\mu)^{\dot{a}b} \quad \text{and accordingly} \quad (\sigma^{\mu\nu})_a{}^b \quad \text{and} \quad (\bar{\sigma}^{\mu\nu})^{\dot{a}}{}_{\dot{b}}. \quad\quad (E.16)
$$

Furthermore, the generalised Pauli matrices fulfill

$$
(\sigma^\mu)^T = \sigma^2 \bar{\sigma}^\mu \sigma^2, \quad\quad (E.17)
$$

which can be checked easily by explicit calculation. Let us write this expression with Weyl indices and use (E.12).

$$
(\sigma^\mu)_{a\dot{b}} = (\sigma^\mu)^T_{\dot{b}a} = -\epsilon_{\dot{b}\dot{c}}(\bar{\sigma}^\mu)^{\dot{c}d}\epsilon_{da} = \epsilon_{\dot{b}\dot{c}}\epsilon_{ad}(\bar{\sigma}^\mu)^{\dot{c}d} = (\bar{\sigma}^\mu)_{\dot{b}a}. \quad\quad (E.18)
$$

E.3. Identities for Majorana fermions

Majorana fermions, named after Italian physicist Ettore Majorana, are their own antiparticles (cf. [258]). This is only possible for electrically neutral particles. There are no Majorana fermions in the Standard Model of particle physics. Examples in the context of SUSY are the neutralinos and gluinos. The Dirac spinor field Ψ of a Majorana fermion can be written as

$$
\Psi = \begin{pmatrix} \psi_L \\ \psi_R \end{pmatrix} \quad \text{and} \quad \bar{\Psi} = \Psi^\dagger \gamma^0 = \begin{pmatrix} \psi_L, & \psi_R \end{pmatrix}. \quad\quad (E.19)
$$

In the following we use the formalism developed in the last sections to prove two identities for Majorana fermions, namely

$$
\bar{\Psi}\gamma^\mu\Psi = 0 \quad \text{and} \quad \bar{\Psi}\gamma^{\mu\nu}\Psi = 0. \quad\quad (E.20)
$$

The definition of $\gamma^{\mu\nu}$ is given in (D.1).

Proposition 4. $\bar{\Psi}\gamma^\mu\Psi = 0.$

Proof. In the Weyl representation we have

$$
\bar{\Psi}\gamma^\mu\Psi = \psi_R\bar{\sigma}^\mu\psi_L + \psi_L\sigma^\mu\psi_R. \quad\quad (E.21)
$$

The second term can be written as

$$
(\psi_L)^a(\sigma^\mu)_{a\dot{b}}(\psi_R)^{\dot{b}} = -(\psi_R)^{\dot{b}}(\sigma^\mu)_{a\dot{b}}(\psi_L)^a \underbrace{=}_{(E.18)} -(\psi_R)^{\dot{b}}(\bar{\sigma}^\mu)_{\dot{b}a}(\psi_L)^a
$$

$$
\underbrace{=}_{(E.14),\ (E.15)} -(-1)^2(\psi_R)_{\dot{b}}(\bar{\sigma}^\mu)^{\dot{b}a}(\psi_L)_a = -\psi_R\bar{\sigma}^\mu\psi_L. \quad\quad (E.22)
$$

The first minus sign occured because Weyl spinor fields anticommute. Hence, we have $\bar{\Psi}\gamma^\mu\Psi = \psi_R\bar{\sigma}^\mu\psi_L - \psi_R\bar{\sigma}^\mu\psi_L = 0.$ $\qquad\square$

Proposition 5. $\bar{\Psi}\gamma^{\mu\nu}\Psi = 0$.

Proof. In the Weyl representation we have

$$\bar{\Psi}\gamma^{\mu\nu}\Psi = \frac{i}{2}\bar{\Psi}(\gamma^\mu\gamma^\nu - \gamma^\nu\gamma^\mu)\Psi = \psi_L\sigma^{\mu\nu}\psi_L + \psi_R\bar{\sigma}^{\mu\nu}\psi_R. \tag{E.23}$$

The first term can be written as

$$
\begin{aligned}
\psi_L\sigma^{\mu\nu}\psi_L \quad &= \quad (\psi_L)^a(\sigma^{\mu\nu})_a{}^b(\psi_L)_b \\
&= \quad \frac{i}{2}\left((\psi_L)^a(\sigma^\mu)_{a\dot{c}}(\bar{\sigma}^\nu)^{\dot{c}b}(\psi_L)_b - (\psi_L)^a(\sigma^\nu)_{a\dot{c}}(\bar{\sigma}^\mu)^{\dot{c}b}(\psi_L)_b\right) \\
&= \quad -\frac{i}{2}\left((\psi_L)_b(\sigma^\mu)_{a\dot{c}}(\bar{\sigma}^\nu)^{\dot{c}b}(\psi_L)^a - (\psi_L)_b(\sigma^\nu)_{a\dot{c}}(\bar{\sigma}^\mu)^{\dot{c}b}(\psi_L)^a\right) \\
&\underbrace{=}_{(E.18)} \quad -\frac{i}{2}\left((\psi_L)_b(\bar{\sigma}^\mu)_{\dot{c}a}(\sigma^\nu)^{b\dot{c}}(\psi_L)^a - (\psi_L)_b(\bar{\sigma}^\nu)_{\dot{c}a}(\sigma^\mu)^{b\dot{c}}(\psi_L)^a\right) \\
&= \quad \frac{i}{2}\left((\psi_L)_b(\sigma^\mu)^{b\dot{c}}(\bar{\sigma}^\nu)_{\dot{c}a}(\psi_L)^a - (\psi_L)_b(\sigma^\nu)^{b\dot{c}}(\bar{\sigma}^\mu)_{\dot{c}a}(\psi_L)^a\right) \\
&\underbrace{=}_{(E.14),\ (E.15)} \quad (-1)^3\frac{i}{2}\left((\psi_L)^b(\sigma^\mu)_{b\dot{c}}(\bar{\sigma}^\nu)^{\dot{c}a}(\psi_L)_a - (\psi_L)^b(\sigma^\nu)_{b\dot{c}}(\bar{\sigma}^\mu)^{\dot{c}a}(\psi_L)_a\right) \\
&= \quad -\psi_L\sigma^{\mu\nu}\psi_L. \tag{E.24}
\end{aligned}
$$

Hence, we have $\psi_L\sigma^{\mu\nu}\psi_L = 0$. A completely analogous calculation shows $\psi_R\bar{\sigma}^{\mu\nu}\psi_R = 0$ and thus $\bar{\Psi}\gamma^{\mu\nu}\Psi = 0$. $\qquad\square$

F. Regularisation

When evaluating Feynman diagrams including loops, one encounters a symptomatic problem. To discuss it, we depict the simplest loop diagram of QCD in figure F.1. It shows the one-loop correction to the quark propagator, the so-called *self-energy*. Due to energy and momentum conservation, the ingoing four-momentum p_a equals the outgoing four-momentum p_1. However, this does not fully determine the four-momenta of the inner, *virtual* particles. If we label the four-momenta of the virtual quark with q, the gluon has four-momentum $q - p_1$, where q is still unrestricted. To include all possible kinematics, we have to integrate over all values of q.

Unfortunately, the resulting integral is divergent. This is a problem for an empirical science like physics. The theory – in this case QCD – should make predictions about observables in nature which are obviously finite. On the first glimpse, it seems that theory has failed. Interestingly, this is not the case. Instead it turned out that the finite observables are kind of "hidden beneath the infinities" and are actually calculable within the theory. During the second half of the last century, a sophisticated machinery was developed to do this. The procedure is based on two steps:

1. **Regularisation**

   The divergent integrals are evaluated, the divergences are identified and isolated.

2. **Renormalisation**

   The divergences are removed via redefining the original parameters of the theory.

There exist several ways for both steps. In this chapter we discuss the method of *dimensional regularisation*, which was mainly developed by Giampiero Passarino, Gerardus 't Hooft and Martinus Veltman [259–261] and is one variant of performing the first step. Although this technique is well known, we also repeat the basics. This is necessary to discuss the tensor reduction in the case of a vanishing Gram determinant, which is important for our calculations. We follow the conventions of [166] and [262], which are also the most relevant references for this chapter. The second step of this procedure is discussed in the next chapter G.

F.1. Different kinds of divergences

Before introducing the concept of dimensional regularisation and the Passarino Veltman integrals in the following sections, we move a step backwards and take a closer look at the divergences themselves. The divergences we have sketched above are called *ultraviolet divergences*. They occur for large internal momenta, which naturally arise as the integration over internal momenta is unrestricted. Provided that the singularities are properly regularised, ultraviolet divergences can be removed via renormalisation.
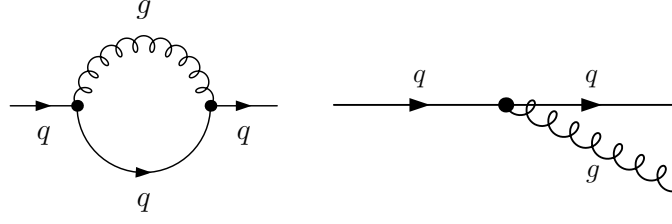
Figure F.1.: Quark self-energy in QCD (left) and a quark emitting a gluon (right)

However, there exists a second class of divergences which has a different origin. These are called *infrared divergences* and they are connected to specific configurations of the internal loop masses and the external momenta. A systematic study of the occurrence of infrared divergences was performed by Lew Dawidowitsch Landau in 1959 [263]. He derived the so-called *Landau equations*, which are necessary conditions for the appearance of such singularities. Fulfilling the Landau equations in practice is usually related to the exchange of at least one internal massless particle like a gluon or photon. Classical examples for infrared divergent processes are given by V1, V3, B1 and B3 (cf. subsections 4.4.3 and 4.4.5 and figures 4.7 and 4.11). We also explicitly evaluate two infrared divergent loop integrals in the following (cf. subsections F.3.1 and F.3.2).

In order to obtain a meaningful result, these divergences have to disappear somehow. Interestingly, infrared divergences cancel out automatically if one calculates a physical observable. In this context, such observables are called *inclusive quantities* and the famous *Bloch-Nordsieck* and *Kinoshita-Lee-Nauenberg theorems* state that inclusive quantities are infrared safe [204–206].

What is meant by an inclusive quantity and how do the divergences vanish? Consider the electroweak process $e^+e^- \to \bar{q}q$ as an example. One may calculate strong corrections to this process, where amongst others the vertex V3 shows up in rotated form (cf. subsection 4.4.3 and figure 4.7). The exchange of the internal massless gluon leads to an infrared divergence. However, when actually realising this process at a lepton collider and detecting the final state, one can not exclude that an additional gluon has escaped detection. This is especially true if the gluon either possesses vanishing energy or is emitted along the direction of an emitting massless particle. These two situations give rise to so-called *soft* and *collinear divergences*, respectively. Let us investigate this in greater detail.

We assume that one of the final state quarks emits an additional gluon. This emission process is called a *real correction* and is depicted in figure F.1. We label the ingoing quark momentum p_a, the outgoing quark momentum p_1 and the gluon momentum p_2, where $p_a = p_1 + p_2$ due to energy and momentum conservation. Note that the ingoing quark is a virtual particle in the process $e^+e^- \to \bar{q}qg$. Hence, we encounter its propagator when writing down the amplitude of the process. The relevant part of this propagator reads

$$\frac{1}{p_a^2 - m_q^2} = \frac{1}{(p_1 + p_2)^2 - m_q^2} = \frac{1}{2p_1 p_2}, \tag{F.1}$$

where we have used the on-shell conditions $p_1^2 = m_q^2$ and $p_2^2 = m_g^2 = 0$. We insert the four-vectors $p_1 = (E_1, \vec{p_1})$ and $p_2 = (E_2, \vec{p_2})$, introduce the angle θ between the two outgoing particles and obtain

$$\frac{1}{2p_1 p_2} = \frac{1}{2(E_1 E_2 - \vec{p_1}\vec{p_2})} = \frac{1}{2E_2(E_1 - |\vec{p_1}|\cos\theta)}. \tag{F.2}$$

We can identify two cases causing this expression to diverge. The first possibility is that the gluon possesses vanishing energy, i.e.

$$E_2 \to 0. \tag{F.3}$$

We refer to this as a soft divergence. The second option is that the emitting quark is massless and the gluon is emitted in the direction of the quark.

$$E_1 - |\vec{p_1}| \cos\theta \to 0, \quad \text{i.e.} \quad E_1 \to |\vec{p_1}| \quad \text{and} \quad \theta \to 0. \tag{F.4}$$

We call this a collinear divergence and both the soft and collinear divergence are subsumed under infrared divergences.[33]

To construct an inclusive quantity, we have to sum the cross sections of the processes $e^+e^- \to \bar{q}q$ and $e^+e^- \to \bar{q}qg$ as this is the actual observable. The Kinoshita-Lee-Nauenberg theorem states that this sum is infrared safe. The infrared divergences stemming from the virtual corrections cancel with those from the real corrections.

This cancellation only works if the divergences are properly regularised. One possibility to regularise infrared divergences is to introduce a fictitious gluon (or photon) mass λ. If the final result is an inclusive quanitity, it should be independent of λ and the limit $\lambda \to 0$ can be performed safely. However, in practice this method is usually avoided in case of QCD calculations as it breaks gauge symmetry. Fortunately, there is no need for a specific regularisation method for infrared divergences as both ultraviolet and infrared divergences can be regularised via dimensional regularisation. This approach[34] is chosen within the DM@NLO project, where we differ between infrared poles and ultraviolet poles. The infrared behaviour of many loop integrals is taken over from [264] and [265].

There is yet another complication in this context we have not mentioned yet. The cancellation of infrared singularities works on the level of cross sections. The inclusive cross section at NLO is infrared safe and given by the sum of the tree-level and its virtual and real corrections.

$$\sigma^{\text{NLO}} = \int_{2\to2} d\sigma^{\text{tree}} + \int_{2\to2} d\sigma^{\text{virtual}} + \int_{2\to3} d\sigma^{\text{real}}. \tag{F.5}$$

Note that the virtual and real corrections possess different phase spaces and hence have to be integrated separately. Although the sum is infrared finite, the individual terms are not. This is a problem as the integration is usually performed numerically, which leads to two ill-defined terms. There are two popular but involved methods to cure this problem, the so-called *phase space slicing* [207] and the *dipole subtraction method* [208–211]. Both of these methods have been implemented in the DM@NLO project but not by the author of this thesis. Therefore, we do not go into details here and refer to the PhD theses of Julia Harz and Moritz Meinecke for detailed descriptions of these methods and their numerical implementation instead [62, 63].

We can skip these details because we do not face this problem in the context of direct detection. Here the cancellation of infrared divergences happens on the level of amplitudes when matching the full and the effective theory (cf. section H). An explicit calculation of real corrections is not needed.

---

[33]Note that this nomenclature is not always chosen. Sometimes people speak of infrared and collinear divergences, i.e. only soft singularities are called infrared singularities.

[34]To be more precise, we are working with dimensional reduction, which is explained in the next section.

F.2. Basic idea of dimensional regularisation

The main idea of dimensional regularisation is to modify the dimensionality of the momenta. To illustrate this, note that e.g.

$$\int_a^\infty \mathrm{d}^D x \frac{1}{x^2} \quad \text{with} \quad a > 0 \tag{F.6}$$

diverges linearly for $D = 3$, logarithmically for $D = 2$ and converges for $D = 1$. The dimensional regularisation method makes use of this fact. The integration over the unrestricted loop momentum q is replaced by

$$\int \frac{\mathrm{d}^4 q}{(2\pi)^4} \to \mu^{4-D} \int \frac{\mathrm{d}^D q}{(2\pi)^D}. \tag{F.7}$$

The integration is then carried out for an arbitrary D. The mathematical basis of this continuation is presented in chapter four of [237]. Afterwards one can identify and isolate the terms diverging in the limit $D \to 4$.

μ is an arbitrary mass scale, the so-called *renormalisation scale*. It has no direct physical meaning and is introduced to fix the dimensionality of the integral. The final result, e.g. the cross section, should be independent of the choice of μ. However, in practice observables like cross sections are typically calculated only up to a fixed order in perturbation theory, which leads to an artificial remaining dependence on the renormalisation scale. This dependence decreases in general with increasing order of perturbation theory and should (in principle) vanish completely, if the calculation is performed to all orders.

Dimensional regularisation is more technical than e.g. a simple momentum cut-off method. Nevertheless, dimensional regularisation is usually preferred as it preserves Lorentz covariance. Another symmetry, namely SUSY, can be preserved if one uses *dimensional reduction* [266, 267]. Dimensional reduction is a modification of the dimensional regularisation scheme. The main difference between these two schemes is that vector bosons in the dimensional reduction scheme stay four-dimensional, whereas in the dimensional regularisation scheme vector bosons are D-dimensional objects. The mathematical details of this regularisation scheme are still under discussion [252, 254, 268]. However, in practical calculations dimensional reduction has proven reliable so far. A common advantage of both schemes is the possibility to classify all possible loop diagrams and reduce them in an algorithmic manner to a set consisting of only four fundamental scalar integrals at one-loop order. This very efficient technique is presented in the next sections.

F.3. Scalar Passarino Veltman integrals

The aforementioned four fundamental scalar integrals are given by:

$$A_0(m_0^2) = \frac{(2\pi\mu)^{4-D}}{i\pi^2} \int \mathrm{d}^D q \frac{1}{\mathcal{D}_0}. \tag{F.8}$$

$$B_0(p_1, m_0^2, m_1^2) = \frac{(2\pi\mu)^{4-D}}{i\pi^2} \int \mathrm{d}^D q \frac{1}{\mathcal{D}_0 \mathcal{D}_1}. \tag{F.9}$$

$$C_0(p_1, p_2, m_0^2, m_1^2, m_2^2) = \frac{(2\pi\mu)^{4-D}}{i\pi^2} \int \mathrm{d}^D q \frac{1}{\mathcal{D}_0 \mathcal{D}_1 \mathcal{D}_2}. \tag{F.10}$$

$$D_0(p_1, p_2, p_3, m_0^2, m_1^2, m_2^2, m_3^2) = \frac{(2\pi\mu)^{4-D}}{i\pi^2} \int \mathrm{d}^D q \frac{1}{\mathcal{D}_0 \mathcal{D}_1 \mathcal{D}_2 \mathcal{D}_3}. \tag{F.11}$$

The denominators are defined by

$$\mathcal{D}_i = (q + p_i)^2 - m_i^2 + i\varepsilon \quad \text{with} \quad p_0 = 0, \tag{F.12}$$

where the infinitesimal terms $i\varepsilon$ are added to shift possible poles from the real axis into the complex plane. We omit them whenever they are not needed explicitly. A_0, B_0, C_0 and D_0 are also referred to as one-, two-, three- and four-point functions. They can be further evaluated by substitutions, the use of Feynman parameters, the Gamma function and the Dilogarithm (cf. chapter B). Furthermore, we need the auxiliary integral

$$I_n(A) = \int \mathrm{d}^D q \frac{1}{(q^2 - A + i\varepsilon)^n} = i(-1)^n \pi^{D/2} \frac{\Gamma(n - D/2)}{\Gamma(n)} (A - i\varepsilon)^{D/2-n}. \tag{F.13}$$

We finally find

$$A_0(m_0^2) = m_0^2 \left(\Delta - \ln\left(\frac{m_0^2}{\mu^2}\right) + 1 \right) + \mathcal{O}(D - 4) \tag{F.14}$$

and

$$B_0(p_1, m_0^2, m_1^2) = \Delta - \int_0^1 \mathrm{d}x \ln\left(\frac{x^2 p_1^2 - x(p_1^2 - m_1^2 + m_0^2) + m_0^2 - i\varepsilon}{\mu^2} \right) + \mathcal{O}(D-4), \tag{F.15}$$

where we have introduced the divergent factor

$$\Delta = \frac{2}{4 - D} - \gamma_E + \ln(4\pi) = \frac{1}{\epsilon} - \gamma_E + \ln(4\pi). \tag{F.16}$$

The corresponding analytical expressions for C_0 and D_0 in the most general case have an impressive length and can be looked up elsewhere (cf. [166, 265, 269]). In the following two subsections we evaluate the scalar integrals C_0 and D_0 for rather unusual sets of arguments which we encounter in chapter 4 when calculating the neutralino-nucleon cross sections. The standard methods and results given in the literature fail under these circumstances and these special cases have to be treated separately.

F.3.1. Evaluation of $C_0(p, 0, 0, m^2, 0)$

The first special case we consider is $C_0(p, 0, 0, m^2, 0)$, which is needed for the vertex corrections V5 and V7 in the case of massless quarks (cf. subsection 4.4.3 and figure 4.7). As the integral leads to an infrared divergence (cf. section F.1), we evaluate it in $D = 4 - 2\epsilon$ dimensions. This three-point function reads

$$C_0 = \frac{(2\pi\mu)^{4-D}}{i\pi^2} \int \mathrm{d}^D q \frac{1}{(q^2 + i\varepsilon)^2((q + p)^2 - m^2 + i\varepsilon)}. \tag{F.17}$$

We rewrite it by using the identity (B.27) for $k = 2$.

$$
\begin{aligned}
C_0 &= \frac{(2\pi\mu)^{4-D}}{i\pi^2} \int \mathrm{d}^D q \int_0^1 \mathrm{d}x_1 \int_0^1 \mathrm{d}x_2 \frac{\delta(x_1 + x_2 - 1)2x_2}{(x_1((q+p)^2 - m^2 + i\varepsilon) + x_2(q^2 + i\varepsilon))^3} \\
&= 2\frac{(2\pi\mu)^{4-D}}{i\pi^2} \int \mathrm{d}^D q \int_0^1 \mathrm{d}x_2 x_2 \big((q + (1 - x_2)p)^2 - (1 - x_2)^2 p^2 \\
&+ (1 - x_2)p^2 - (1 - x_2)m^2 + i\varepsilon \big)^{-3}.
\end{aligned}
\tag{F.18}
$$

The next step is to substitute $q' = q + (1 - x_2)p$ and to use the auxiliary integral (F.13) with $n = 3$ and $A = (1 - x_2)m^2 - x_2(1 - x_2)p^2$. We obtain

$$
\begin{aligned}
C_0 &= -(4\pi)^\epsilon \Gamma(1 + \epsilon)(\mu^2)^\epsilon \int_0^1 \mathrm{d}x_2 x_2 \big((1 - x_2)m^2 - x_2(1 - x_2)p^2 - i\varepsilon\big)^{-1-\epsilon} \\
&= -c_\epsilon(\mu^2)^\epsilon \int_0^1 \mathrm{d}x_2 x_2 (1 - x_2)^{-1-\epsilon} \left(m^2 - x_2 p^2 - \frac{i\varepsilon}{1 - x_2} \right)^{-1-\epsilon} \\
&= -c_\epsilon(\mu^2)^\epsilon \int_0^1 \mathrm{d}x_2 x_2 (1 - x_2)^{-1-\epsilon} \big(\bar{m}^2 - x_2 p^2\big)^{-1-\epsilon} \\
&= -c_\epsilon \frac{1}{\bar{m}^2} \left(\frac{\mu^2}{\bar{m}^2} \right)^\epsilon \int_0^1 \mathrm{d}x_2 x_2 (1 - x_2)^{-1-\epsilon} \left(1 - \frac{p^2}{\bar{m}^2} x_2 \right)^{-1-\epsilon}. \qquad\text{(F.19)}
\end{aligned}
$$

In the previous steps we have introduced the shorthand notation $c_\epsilon = (4\pi)^\epsilon \Gamma(1 + \epsilon)$ and absorbed the infinitesimal complex part into a redefinition of the mass $\bar{m}^2 = m^2 - i\varepsilon' = m^2 - \frac{i\varepsilon}{1-x_2}$. As the fraction $\frac{1}{1-x_2}$ does not change its sign in the domain of integration, it makes no difference in avoiding poles. Hence, we can treat $\bar{m}^2$ as independent of x_2. Given these substitutions, the integral above is nothing but a hypergeometric function (cf. section B.4) with parameters $a = 1 + \epsilon$, $b = 2$, $c = 2 - \epsilon$ and $z = \frac{p^2}{\bar{m}^2}$.

$$
\begin{aligned}
C_0 &= -c_\epsilon \frac{1}{\bar{m}^2} \left(\frac{\mu^2}{\bar{m}^2} \right)^\epsilon \frac{\Gamma(2)\Gamma(-\epsilon)}{\Gamma(2 - \epsilon)}\, {}_2F_1\left(1 + \epsilon, 2, 2 - \epsilon, \frac{p^2}{\bar{m}^2} \right) \\
&= c_\epsilon \frac{1}{\bar{m}^2} \left(\frac{\mu^2}{\bar{m}^2} \right)^\epsilon \frac{1}{\epsilon(1 - \epsilon)}\, {}_2F_1\left(1 + \epsilon, 2, 2 - \epsilon, \frac{p^2}{\bar{m}^2} \right). \qquad\text{(F.20)}
\end{aligned}
$$

In the last step the $1/\epsilon$ divergence shows up explicitly. All that remains is to expand this expression in a series in ϵ.[35] This leads to an infrared divergent part proportional to $1/\epsilon$ which cancels out in the matching procedure (cf. chapter H), a finite contribution and negligible terms of $\mathcal{O}(\epsilon)$. To expand the hypergeometric function, we start with its defining differential equation (B.20), insert the given parameters and choose the ansatz

$$
w(z) = r(z) + \epsilon s(z) + \mathcal{O}(\epsilon^2) \quad \text{with} \quad r(0) = 1 \quad \text{and} \quad s(0) = 0. \qquad\text{(F.21)}
$$

We obtain the differential equations

$$
\begin{aligned}
\mathcal{O}(\epsilon^0) : 0 &= z(1 - z)r''(z) + (2 - 4z)r'z - 2r(z) \quad \text{and} \qquad\text{(F.22)} \\
\mathcal{O}(\epsilon^1) : 0 &= z(1 - z)s''(z) + (2 - 4z)s'z - 2s(z) - (1 + z)r'(z) - 2r(z), \qquad\text{(F.23)}
\end{aligned}
$$

which can be solved with e.g. `Mathematica`. The result reads

$$
r(z) = \frac{1}{1 - z} \quad \text{and} \quad s(z) = \frac{z(1 - i\pi) + (z + 1)\ln(z - 1) - i\pi}{z(z - 1)}. \qquad\text{(F.24)}
$$

We insert this back into the three-point function and finally get

$$
\begin{aligned}
C_0 &= c_\epsilon \frac{1}{\bar{m}^2} \left(\frac{\mu^2}{\bar{m}^2} \right)^\epsilon \frac{1}{\epsilon(1 - \epsilon)} (r(z) + \epsilon s(z) + \mathcal{O}(\epsilon^2)) \\
&= c_\epsilon \frac{1}{\bar{m}^2} \left(\frac{1}{\epsilon} r(z) + \left(1 + \ln\left(\frac{\mu^2}{\bar{m}^2} \right) \right) r(z) + s(z) \right) + \mathcal{O}(\epsilon). \qquad\text{(F.25)}
\end{aligned}
$$

---

[35] For conventional reasons we leave the factor c_ϵ unexpanded.

F.3.2. Evaluation of $D_0(p, 0, 0, 0, m^2, 0, 0)$

The second special case we investigate is $D_0(p, 0, 0, 0, m^2, 0, 0)$. This four-point function is needed for the boxes B1 and B3 in the case of massless quarks (cf. subsection 4.4.5 and figure 4.11) and reads

$$D_0 = \frac{(2\pi\mu)^{4-D}}{i\pi^2} \int \mathrm{d}^D q \frac{1}{(q^2 + i\varepsilon)^3((q+p)^2 - m^2 + i\varepsilon)}. \tag{F.26}$$

As one might guess when comparing the expression above with (F.17), the evaluation of this integral completely follows the steps of the last subsection. We start by introducing Feynman parameters as in (B.27) for $k = 3$ and get

$$
\begin{aligned}
D_0 &= \frac{(2\pi\mu)^{4-D}}{i\pi^2} \int \mathrm{d}^D q \int_0^1 \mathrm{d}x_1 \int_0^1 \mathrm{d}x_2 \frac{\delta(x_1 + x_2 - 1)3x_2^2}{(x_1((q+p)^2 - m^2 + i\varepsilon) + x_2(q^2 + i\varepsilon))^4} \\
&= 3\frac{(2\pi\mu)^{4-D}}{i\pi^2} \int \mathrm{d}^D q \int_0^1 \mathrm{d}x_2 x_2^2 \big((q + (1 - x_2)p)^2 - (1 - x_2)^2 p^2 \\
&\quad + (1 - x_2)p^2 - (1 - x_2)m^2 + i\varepsilon\big)^{-4}. \tag{F.27}
\end{aligned}
$$

We substitute $q' = q + (1 - x_2)p$ and use the auxiliary integral (F.13) with $n = 4$ and $A = (1 - x_2)m^2 - x_2(1 - x_2)p^2$ to obtain

$$
\begin{aligned}
D_0 &= \frac{1}{2}c_\epsilon(\mu^2)^\epsilon(1 + \epsilon) \int_0^1 \mathrm{d}x_2 x_2^2 \big((1 - x_2)m^2 - x_2(1 - x_2)p^2 - i\varepsilon\big)^{-2-\epsilon} \\
&= \frac{1}{2}c_\epsilon \frac{1}{\bar{m}^4} \left(\frac{\mu^2}{\bar{m}^2}\right)^\epsilon (1 + \epsilon) \int_0^1 \mathrm{d}x_2 x_2^2 (1 - x_2)^{-2-\epsilon} \left(1 - \frac{p^2}{\bar{m}^2}x_2\right)^{-2-\epsilon}. \tag{F.28}
\end{aligned}
$$

Once again we encounter a hypergeometric function, this time with arguments $a = 2 + \epsilon$, $b = 3$, $c = 2 - \epsilon$ and $z = \frac{p^2}{\bar{m}^2}$.

$$
\begin{aligned}
D_0 &= \frac{1}{2}c_\epsilon \frac{1}{\bar{m}^4} \left(\frac{\mu^2}{\bar{m}^2}\right)^\epsilon (1 + \epsilon)\frac{\Gamma(3)\Gamma(-1 - \epsilon)}{\Gamma(2 - \epsilon)} \, {}_2F_1\left(2 + \epsilon, 3, 2 - \epsilon, \frac{p^2}{\bar{m}^2}\right) \\
&= c_\epsilon \frac{1}{\bar{m}^4} \left(\frac{\mu^2}{\bar{m}^2}\right)^\epsilon \frac{1}{\epsilon(1 - \epsilon)} \, {}_2F_1\left(2 + \epsilon, 3, 2 - \epsilon, \frac{p^2}{\bar{m}^2}\right). \tag{F.29}
\end{aligned}
$$

To expand the hypergeometric function, we proceed as in the last section and choose the ansatz (F.21). For the given parameters we obtain the differential equations

$$
\begin{aligned}
\mathcal{O}(\epsilon^0) : 0 &= z(1 - z)r''(z) + (2 - 6z)r'z - 6r(z) \quad \text{and} \tag{F.30} \\
\mathcal{O}(\epsilon^1) : 0 &= z(1 - z)s''(z) + (2 - 6z)s'z - 6s(z) - (1 + z)r'(z) - 3r(z), \tag{F.31}
\end{aligned}
$$

which are solved by

$$r(z) = -\frac{1}{(z - 1)^3} \quad \text{and} \quad s(z) = \frac{2\ln(1 - z) - z}{(z - 1)^3}. \tag{F.32}$$

Inserting this back into the four-point function, we obtain the final result

$$D_0 = c_\epsilon \frac{1}{\bar{m}^4} \left(\frac{1}{\epsilon}r(z) + \left(1 + \ln\left(\frac{\mu^2}{\bar{m}^2}\right)\right)r(z) + s(z)\right) + \mathcal{O}(\epsilon). \tag{F.33}$$

F.4. Tensor Passarino Veltman integrals

In case of the scalar integrals introduced before, only the denominators $\mathcal{D}_i$ depend on q. This is not the most general case, especially fermion propagators lead to factors of q in the nominator. Integrals of this form are called tensor integrals. We classify them as follows:

$$A_\mu(m_0^2) = \frac{(2\pi\mu)^{4-D}}{i\pi^2} \int \mathrm{d}^D q \frac{q_\mu}{\mathcal{D}_0}. \tag{F.34}$$

$$A_{\mu\nu}(m_0^2) = \frac{(2\pi\mu)^{4-D}}{i\pi^2} \int \mathrm{d}^D q \frac{q_\mu q_\nu}{\mathcal{D}_0}. \tag{F.35}$$

$$\vdots$$

$$B_\mu(p_1, m_0^2, m_1^2) = \frac{(2\pi\mu)^{4-D}}{i\pi^2} \int \mathrm{d}^D q \frac{q_\mu}{\mathcal{D}_0 \mathcal{D}_1}. \tag{F.36}$$

$$B_{\mu\nu}(p_1, m_0^2, m_1^2) = \frac{(2\pi\mu)^{4-D}}{i\pi^2} \int \mathrm{d}^D q \frac{q_\mu q_\nu}{\mathcal{D}_0 \mathcal{D}_1}. \tag{F.37}$$

$$\vdots$$

$$C_\mu(p_1, p_2, m_0^2, m_1^2, m_2^2) = \frac{(2\pi\mu)^{4-D}}{i\pi^2} \int \mathrm{d}^D q \frac{q_\mu}{\mathcal{D}_0 \mathcal{D}_1 \mathcal{D}_2}. \tag{F.38}$$

$$C_{\mu\nu}(p_1, p_2, m_0^2, m_1^2, m_2^2) = \frac{(2\pi\mu)^{4-D}}{i\pi^2} \int \mathrm{d}^D q \frac{q_\mu q_\nu}{\mathcal{D}_0 \mathcal{D}_1 \mathcal{D}_2}. \tag{F.39}$$

$$\vdots$$

$$D_\mu(p_1, p_2, p_3, m_0^2, m_1^2, m_2^2, m_3^2) = \frac{(2\pi\mu)^{4-D}}{i\pi^2} \int \mathrm{d}^D q \frac{q_\mu}{\mathcal{D}_0 \mathcal{D}_1 \mathcal{D}_2 \mathcal{D}_3}. \tag{F.40}$$

$$D_{\mu\nu}(p_1, p_2, p_3, m_0^2, m_1^2, m_2^2, m_3^2) = \frac{(2\pi\mu)^{4-D}}{i\pi^2} \int \mathrm{d}^D q \frac{q_\mu q_\nu}{\mathcal{D}_0 \mathcal{D}_1 \mathcal{D}_2 \mathcal{D}_3}. \tag{F.41}$$

$$\vdots$$

Note that $A_\mu = 0$ as the integrand is an odd function of q. The idea of the *tensor reduction* method is not to calculate all of these integrals directly but rather rewrite them in terms of the fundamental scalar integrals given in (F.8)-(F.11). In the following we focus on the evaluation of B_μ, $B_{\mu\nu}$, C_μ and $C_{\mu\nu}$ as these integrals turn out to be the most important ones. The procedure works the same for all other tensor integrals.

Before we start with the tensor reduction, we set up a shorthand notation for the arguments of the scalar two-point function. We introduce

$$B_0(i, j) = B_0(p_j - p_i, m_i^2, m_j^2), \tag{F.42}$$

so that i and j correspond to the contributing denominators $\mathcal{D}_i$ and $\mathcal{D}_j$. As an example, we give

$$B_0(1, 2) = \frac{(2\pi\mu)^{4-D}}{i\pi^2} \int \mathrm{d}^D q \frac{1}{\mathcal{D}_1 \mathcal{D}_2} = B_0(p_2 - p_1, m_1^2, m_2^2). \tag{F.43}$$

Later on, we use the same notation for the two-point tensor coefficients, i.e. for B_1, B_{00} and B_{11}.

F.4.1. Evaluation of B_μ

The tensor reduction method makes use of the fact that dimensional regularisation (as well as dimensional reduction) preserves Lorentz covariance. This implies that the final results can be written as linear combinations of covariant four-vectors. The only available four-vector in the case of B_μ is the external momentum p_1, so we choose the ansatz

$$B_\mu(p_1, m_0^2, m_1^2) = p_{1,\mu} B_1(p_1, m_0^2, m_1^2). \tag{F.44}$$

The goal is to determine the unknown tensor coefficient B_1. To do so, we contract both sides with p_1^μ. We obtain

$$
\begin{aligned}
p_1^\mu B_\mu(p_1, m_0^2, m_1^2) &= p_1^2 B_1(p_1, m_0^2, m_1^2) = \frac{(2\pi\mu)^{4-D}}{i\pi^2} \int \mathrm{d}^D q \frac{p_1 q}{\mathcal{D}_0 \mathcal{D}_1} \\
&= \frac{(2\pi\mu)^{4-D}}{i\pi^2} \int \mathrm{d}^D q \frac{((q+p_1)^2 - m_1^2) - (q^2 - m_0^2) - (p_1^2 - m_1^2 + m_0^2)}{2\mathcal{D}_0 \mathcal{D}_1} \\
&= \frac{(2\pi\mu)^{4-D}}{i\pi^2} \int \mathrm{d}^D q \frac{\mathcal{D}_1 - \mathcal{D}_0 - (p_1^2 - m_1^2 + m_0^2)}{2\mathcal{D}_0 \mathcal{D}_1} \\
&= \frac{1}{2} \left(A_0(m_0^2) - A_0(m_1^2) - (p_1^2 - m_1^2 + m_0^2) B_0(p_1, m_0^2, m_1^2) \right) \\
\Leftrightarrow B_1(p_1, m_0^2, m_1^2) &= \frac{1}{2p_1^2} \left(A_0(m_0^2) - A_0(m_1^2) - (p_1^2 - m_1^2 + m_0^2) B_0(p_1, m_0^2, m_1^2) \right). \tag{F.45}
\end{aligned}
$$

Hereby we have reduced the tensor integral B_μ to the scalar integrals A_0 and B_0. In the next three subsections we apply the same procedure to the tensor expressions $B_{\mu\nu}$, C_μ and $C_{\mu\nu}$. Therein we regularly use

$$p_i q = \frac{1}{2} \left(((q+p_i)^2 - m_i^2) - (q^2 - m_0^2) - (p_i^2 - m_i^2 + m_0^2) \right) = \frac{1}{2} \left(\mathcal{D}_i - \mathcal{D}_0 - f_i \right), \tag{F.46}$$

where

$$f_i = p_i^2 - m_i^2 + m_0^2. \tag{F.47}$$

F.4.2. Evaluation of $B_{\mu\nu}$

Our ansatz for $B_{\mu\nu}$ is

$$B_{\mu\nu}(p_1, m_0^2, m_1^2) = g_{\mu\nu} B_{00}(p_1, m_0^2, m_1^2) + p_{1,\mu} p_{1,\nu} B_{11}(p_1, m_0^2, m_1^2). \tag{F.48}$$

We contract the expression with $g^{\mu\nu}$ and obtain

$$
\begin{aligned}
g^{\mu\nu} B_{\mu\nu}(0,1) &= D B_{00}(0,1) + p_1^2 B_{11}(0,1) = \frac{(2\pi\mu)^{4-D}}{i\pi^2} \int \mathrm{d}^D q \frac{(q^2 - m_0^2) + m_0^2}{\mathcal{D}_0 \mathcal{D}_1} \\
&= A_0(m_1^2) + m_0^2 B_0(0,1), \tag{F.49}
\end{aligned}
$$

where we have used the shorthand notation introduced in (F.42). Contraction with p_1^μ gives

$$
\begin{aligned}
p_1^\mu B_{\mu\nu}(0,1) &= p_{1,\nu}(B_{00}(0,1) + p_1^2 B_{11}(0,1)) \\
&= \frac{(2\pi\mu)^{4-D}}{i\pi^2} \int \mathrm{d}^D q \frac{q_\nu}{2} \frac{\mathcal{D}_1 - \mathcal{D}_0 - f_1}{\mathcal{D}_0 \mathcal{D}_1} \\
&= \frac{p_{1,\nu}}{2} \left(A_0(m_1^2) - f_1 B_1(0,1) \right) \\
\Leftrightarrow B_{00}(0,1) + p_1^2 B_{11}(0,1) &= \frac{1}{2} \left(A_0(m_1^2) - f_1 B_1(0,1) \right). \tag{F.50}
\end{aligned}
$$

In the second step above we have used $A_\nu(m_i^2) = 0$ and substituted $q' = q + p_1$ in the second term of the integrand. Combining (F.49) and (F.50) leads to

$$B_{00}(0,1) = \frac{1}{2(D-1)}\left(A_0(m_1^2) + 2m_0^2 B_0(0,1) + f_1 B_1(0,1)\right). \tag{F.51}$$

$$B_{11}(0,1) = \frac{1}{2(D-1)p_1^2}\left((D-2)A_0(m_1^2) - 2m_0^2 B_0(0,1) - Df_1 B_1(0,1)\right). \tag{F.52}$$

One has to be careful when taking the limit $D \to 4$ of the expressions above. As the integrals A_0, B_0 and B_1 are divergent (cf. section F.6), the fraction in front has to be expanded in terms of $D - 4$. We perform this for $B_{11}(0,1)$ and begin with the Taylor expansion of the fraction.

$$\frac{1}{D-1} = \frac{1}{D-4+3} := \frac{1}{x+3} = \frac{1}{3} - \frac{1}{9}x + \mathcal{O}(x^2). \tag{F.53}$$

There are no ultraviolet double poles, so terms of order $(D-4)^2$ can be neglected. Therefore, we get in the limit $D \to 4$

$$\begin{aligned}
B_{11}(0,1) &= \frac{1}{6p_1^2}\left(1 - \frac{1}{3}(D-4)\right)\left((D-2)A_0(m_1^2) - 2m_0^2 B_0(0,1) - Df_1 B_1(0,1)\right) \\
&= \frac{1}{6p_1^2}\left(1 - \frac{1}{3}(D-4)\right)\left((D-4)A_0(m_1^2) + 2A_0(m_1^2) - 2m_0^2 B_0(0,1)\right. \\
&\quad - (D-4)f_1 B_1(0,1) - 4f_1 B_1(0,1)\Big) \\
&= \frac{1}{6p_1^2}\left(2A_0(m_1^2) - 2m_0^2 B_0(0,1) - 4f_1 B_1(0,1) + (1 - \frac{2}{3})(D-4)A_0(m_1^2)\right. \\
&\quad + \frac{2}{3}m_0^2(D-4)B_0(0,1) + (-1 + \frac{4}{3})f_1(D-4)B_1(0,1)\Big) \\
&= \frac{1}{6p_1^2}\left(2A_0(m_1^2) - 2m_0^2 B_0(0,1) - 4f_1 B_1(0,1) - \frac{2}{3}m_1^2 - \frac{4}{3}m_0^2 + \frac{1}{3}f_1\right) \\
&= \frac{1}{6p_1^2}\left(2A_0(m_1^2) - 2m_0^2 B_0(0,1) - 4f_1 B_1(0,1) - m_1^2 - m_0^2 + \frac{1}{3}p_1^2\right). \tag{F.54}
\end{aligned}$$

Applying the same procedure for B_{00} as given in (F.51) leads to

$$B_{00}(0,1) = \frac{1}{6}\left(A_0(m_1^2) + 2m_0^2 B_0(0,1) + f_1 B_1(0,1) + m_0^2 + m_1^2 - \frac{1}{3}p_1^2\right). \tag{F.55}$$

F.4.3. Evaluation of C_μ

In the case of the three-point function, we have in general two independent external momenta, so our ansatz is

$$C_\mu = p_{1,\mu}C_1 + p_{2,\mu}C_2, \tag{F.56}$$

where we have omitted the arguments for the sake of readability. Contracting this expression with p_1^μ gives

$$\begin{aligned}
p_1^\mu C_\mu &= p_1^2 C_1 + p_1 p_2 C_2 = \frac{(2\pi\mu)^{4-D}}{i\pi^2}\int d^D q \frac{\mathcal{D}_1 - \mathcal{D}_0 - f_1}{2\mathcal{D}_0 \mathcal{D}_1 \mathcal{D}_2} \\
&= \frac{1}{2}\left(B_0(0,2) - B_0(1,2) - f_1 C_0\right) := R_1. \tag{F.57}
\end{aligned}$$

In complete analogy a contraction with p_2^μ leads to

$$
\begin{aligned}
p_2^\mu C_\mu &= p_1 p_2 C_1 + p_2^2 C_2 = \frac{(2\pi\mu)^{4-D}}{i\pi^2} \int \mathrm{d}^D q \frac{\mathcal{D}_2 - \mathcal{D}_0 - f_2}{2\mathcal{D}_0 \mathcal{D}_1 \mathcal{D}_2} \\
&= \frac{1}{2} \left(B_0(0,1) - B_0(1,2) - f_2 C_0 \right) := R_2.
\end{aligned}
\tag{F.58}
$$

This can be written in matrix form as

$$
\begin{pmatrix} p_1^2 & p_1 p_2 \\ p_1 p_2 & p_2^2 \end{pmatrix} \begin{pmatrix} C_1 \\ C_2 \end{pmatrix} := A \begin{pmatrix} C_1 \\ C_2 \end{pmatrix} = \begin{pmatrix} R_1 \\ R_2 \end{pmatrix},
\tag{F.59}
$$

hence C_1 and C_2 are given by

$$
\begin{pmatrix} C_1 \\ C_2 \end{pmatrix} = A^{-1} \begin{pmatrix} R_1 \\ R_2 \end{pmatrix} = \frac{1}{\det A} \begin{pmatrix} p_2^2 & -p_1 p_2 \\ -p_1 p_2 & p_1^2 \end{pmatrix} \begin{pmatrix} R_1 \\ R_2 \end{pmatrix}.
\tag{F.60}
$$

F.4.4. Evaluation of $C_{\mu\nu}$

The ansatz for $C_{\mu\nu}$ is given by

$$
C_{\mu\nu} = g_{\mu\nu} C_{00} + p_{1,\mu} p_{1,\nu} C_{11} + (p_{1,\mu} p_{2,\nu} + p_{2,\mu} p_{1,\nu}) C_{12} + p_{2,\mu} p_{2,\nu} C_{22}.
\tag{F.61}
$$

Note that $C_{\mu\nu}$ is symmetric under $1 \leftrightarrow 2$, so only the sum $p_{1,\mu} p_{2,\nu} + p_{2,\mu} p_{1,\nu}$ has an independent coefficient and not the single terms $p_{1,\mu} p_{2,\nu}$ and $p_{2,\mu} p_{1,\nu}$. Contracting with the metric tensor $g^{\mu\nu}$ gives

$$
\begin{aligned}
g^{\mu\nu} C_{\mu\nu} &= D C_{00} + p_1^2 C_{11} + 2 p_1 p_2 C_{12} + p_2^2 C_{22} \\
&= \frac{(2\pi\mu)^{4-D}}{i\pi^2} \int \mathrm{d}^D q \frac{(q^2 - m_0^2) + m_0^2}{\mathcal{D}_0 \mathcal{D}_1 \mathcal{D}_2} = B_0(1,2) + m_0^2 C_0.
\end{aligned}
\tag{F.62}
$$

Next we contract with p_1^μ.

$$
\begin{aligned}
p_1^\mu C_{\mu\nu} &= p_{1,\nu} C_{00} + p_1^2 p_{1,\nu} C_{11} + p_1^2 p_{2,\nu} C_{12} + p_1 p_2 p_{1,\nu} C_{12} + p_1 p_2 p_{2,\nu} C_{22} \\
&= \frac{(2\pi\mu)^{4-D}}{i\pi^2} \int \mathrm{d}^D q \frac{q_\nu}{2} \frac{\mathcal{D}_1 - \mathcal{D}_0 - f_1}{\mathcal{D}_0 \mathcal{D}_1 \mathcal{D}_2} \\
&= \frac{1}{2} (p_{2,\nu} B_1(0,2) + (p_{1,\nu} - p_{2,\nu}) B_1(1,2) + p_{1,\nu} B_0(1,2) \\
&\quad - f_1 p_{1,\nu} C_1 - f_1 p_{2,\nu} C_2)).
\end{aligned}
\tag{F.63}
$$

As $p_{1,\nu}$ and $p_{2,\nu}$ are completely arbitrary, we actually obtain two equations out of (F.63).

$$
\frac{1}{2} \left(B_1(1,2) + B_0(1,2) - f_1 C_1 \right) = p_1^2 C_{11} + p_1 p_2 C_{12} + C_{00}.
\tag{F.64}
$$

$$
\frac{1}{2} \left(B_1(0,2) - B_1(1,2) - f_1 C_2 \right) = p_1^2 C_{12} + p_1 p_2 C_{22}.
\tag{F.65}
$$

A contraction with p_2^μ gives analogously

$$
\begin{aligned}
p_2^\mu C_{\mu\nu} &= p_{2,\nu} C_{00} + p_1 p_2 p_{1,\nu} C_{11} + p_1 p_2 p_{2,\nu} C_{12} + p_2^2 p_{1,\nu} C_{12} + p_2^2 p_{2,\nu} C_{22} \\
&= \frac{(2\pi\mu)^{4-D}}{i\pi^2} \int \mathrm{d}^D q \frac{q_\nu}{2} \frac{\mathcal{D}_2 - \mathcal{D}_0 - f_2}{\mathcal{D}_0 \mathcal{D}_1 \mathcal{D}_2} \\
&= \frac{1}{2} (p_{1,\nu} B_1(0,1) + (p_{1,\nu} - p_{2,\nu}) B_1(1,2) + p_{1,\nu} B_0(1,2) \\
&\quad - f_2 p_{1,\nu} C_1 - f_2 p_{2,\nu} C_2)),
\end{aligned}
\tag{F.66}
$$

so we find

$$\frac{1}{2}\left(B_1(0,1) + B_1(1,2) + B_0(1,2) - f_2C_1\right) \;=\; p_1p_2C_{11} + p_2^2C_{12}. \tag{F.67}$$

$$\frac{1}{2}\left(-B_1(1,2) - f_2C_2\right) \;=\; p_1p_2C_{12} + p_2^2C_{22} + C_{00}. \tag{F.68}$$

Now we can determine C_{00} by subtracting (F.64) and (F.68) from (F.62).

$$(D-2)C_{00} = m_0^2C_0 + \frac{1}{2}\left(B_0(1,2) + f_1C_1 + f_2C_2\right). \tag{F.69}$$

Due to the B_0 on the right-hand side, this expression diverges in the limit $D \to 4$. When performing this limit, one has to proceed as described in the end of subsection F.4.2, which leads to

$$C_{00} = \frac{1}{2}m_0^2C_0 + \frac{1}{4}\left(B_0(1,2) + f_1C_1 + f_2C_2 + 1\right). \tag{F.70}$$

Finally, we can cast (F.64) and (F.67) in matrix form to determine C_{11} and C_{12}.

$$A\begin{pmatrix} C_{11} \\ C_{12} \end{pmatrix} = \begin{pmatrix} R_3 \\ R_4 \end{pmatrix} \Leftrightarrow \begin{pmatrix} C_{11} \\ C_{12} \end{pmatrix} = A^{-1}\begin{pmatrix} R_3 \\ R_4 \end{pmatrix} = \frac{1}{\det A}\begin{pmatrix} p_2^2 & -p_1p_2 \\ -p_1p_2 & p_1^2 \end{pmatrix}\begin{pmatrix} R_3 \\ R_4 \end{pmatrix}, \tag{F.71}$$

where

$$R_3 \;=\; \frac{1}{2}\left(B_1(1,2) + B_0(1,2) - f_1C_1 - 2C_{00}\right) \quad \text{and} \tag{F.72}$$

$$R_4 \;=\; \frac{1}{2}\left(B_1(0,1) + B_1(1,2) + B_0(1,2) - f_2C_1\right). \tag{F.73}$$

Note that the matrix A in (F.71) is exactly the same as in (F.60). Next we also write (F.65) and (F.68) in matrix form. This gives a second but analytically identical expression for C_{12} and one for C_{22}.

$$A\begin{pmatrix} C_{12} \\ C_{22} \end{pmatrix} = \begin{pmatrix} R_5 \\ R_6 \end{pmatrix} \Leftrightarrow \begin{pmatrix} C_{12} \\ C_{22} \end{pmatrix} = A^{-1}\begin{pmatrix} R_5 \\ R_6 \end{pmatrix} = \frac{1}{\det A}\begin{pmatrix} p_2^2 & -p_1p_2 \\ -p_1p_2 & p_1^2 \end{pmatrix}\begin{pmatrix} R_5 \\ R_6 \end{pmatrix}. \tag{F.74}$$

Hereby we have set

$$R_5 = \frac{1}{2}\left(B_1(0,2) - B_1(1,2) - f_1C_2\right) \quad \text{and} \quad R_6 = \frac{1}{2}\left(-B_1(1,2) - f_2C_2 - 2C_{00}\right). \tag{F.75}$$

Once more, we encounter the matrix A in front of the three-point functions C_{12} and C_{22}.

The next tensor integrals are D_μ and $D_{\mu\nu}$ which are defined by the decompositions

$$\begin{aligned} D_\mu \;=\;& p_{1,\mu}D_1 + p_{2,\mu}D_2 + p_{3,\mu}D_3 \qquad \text{and} & \text{(F.76)} \\ D_{\mu\nu} \;=\;& g_{\mu\nu}D_{00} + p_{1,\mu}p_{1,\nu}D_{11} + p_{2,\mu}p_{2,\nu}D_{22} + p_{3,\mu}p_{3,\nu}D_{33} \\ +\;& (p_{1,\mu}p_{2,\nu} + p_{2,\mu}p_{1,\nu})D_{12} + (p_{1,\mu}p_{3,\nu} + p_{3,\mu}p_{1,\nu})D_{13} \\ +\;& (p_{2,\mu}p_{3,\nu} + p_{3,\mu}p_{2,\nu})D_{23}. & \text{(F.77)} \end{aligned}$$

The associated tensor coefficients can be determined analogously to the presented procedure.

F.5. Tensor reduction for vanishing Gram determinant

In the last section we have presented the standard technique for evaluating the tensor Passarino-Veltman integrals. This technique works in an algorithmic manner. The more complicated tensor coefficients (e.g. C_{11} and C_{12}) are expressed as linear combinations of simpler ones (e.g. C_1 and B_1) which finally can be reduced to the fundamental scalar integrals. Unfortunately, this elegant method does not always work. To see this, recall the expressions determining C_1, C_2, C_{11}, C_{12} and C_{22}, namely

$$\begin{pmatrix} C_1 \\ C_2 \end{pmatrix} = A^{-1} \begin{pmatrix} R_1 \\ R_2 \end{pmatrix}, \quad \begin{pmatrix} C_{11} \\ C_{12} \end{pmatrix} = A^{-1} \begin{pmatrix} R_3 \\ R_4 \end{pmatrix} \quad \text{and} \quad \begin{pmatrix} C_{12} \\ C_{22} \end{pmatrix} = A^{-1} \begin{pmatrix} R_5 \\ R_6 \end{pmatrix}, \quad \text{(F.78)}$$

as given in (F.60), (F.71) and (F.74). All of these expressions implicitly assume that the matrix A is invertible. The quadratic matrix A is invertible if its determinant

$$\det(A) = p_1^2 p_2^2 - (p_1 p_2)^2 \tag{F.79}$$

does not equal zero. In general, the columns of a $m \times n$ matrix B are linearly independent if and only if the *Gram determinant*

$$\mathrm{Gram}(B) = \det(B^T B) \tag{F.80}$$

does not vanish. For quadratic matrices both criteria are equivalent. In the following we investigate how to perform tensor reduction if the Gram determinant vanishes, wherein we basically follow [270]. Concerning numerical procedures, this method is not only relevant for exactly vanishing Gram determinants – as in the context of direct detection in chapter 4 – but also for very small ones, where the standard procedure might give unstable and therefore unreliable results. Further references in this direction are [271–278].

We start with the reevaluation of (F.60). We have

$$\begin{pmatrix} C_1 \\ C_2 \end{pmatrix} = \frac{1}{\det A} \begin{pmatrix} p_2^2 & -p_1 p_2 \\ -p_1 p_2 & p_1^2 \end{pmatrix} \begin{pmatrix} R_1 \\ R_2 \end{pmatrix}. \tag{F.81}$$

If $\det(A) = 0$ and if we assume that C_1 and C_2 still exist, we get

$$p_2^2 R_1 - p_1 p_2 R_2 = 0 \quad \text{and} \quad -p_1 p_2 R_1 + p_1^2 R_2 = 0. \tag{F.82}$$

As R_1 and R_2 depend only on the fundamental two- and three-point functions B_0 and C_0 (cf. (F.57) and (F.58)), both of the equations above allow to express C_0 solely in terms of B_0. This means that in the case of a vanishing Gram determinant it is not necessary to calculate C_0 directly. Instead it is given by

$$C_0 = \frac{p_2^2 B_0(0,2) + (p_1 p_2 - p_2^2) B_0(1,2) - p_1 p_2 B_0(0,1)}{p_2^2 f_1 - p_1 p_2 f_2}. \tag{F.83}$$

$$C_0 = \frac{p_1^2 B_0(0,1) + (p_1 p_2 - p_1^2) B_0(1,2) - p_1 p_2 B_0(0,2)}{p_1^2 f_2 - p_1 p_2 f_1}. \tag{F.84}$$

These two equations clearly show the symmetry $1 \leftrightarrow 2$ of C_0. Although they are analytically equivalent, it is useful to keep both for numerical purposes.

149

Now we reconsider (F.71) and (F.74). We assume that C_{11}, C_{12} and C_{22} exist. The case of $\det(A) = 0$ then leads to

$$x_{11}R_3 + x_{12}R_4 = 0 \qquad \text{and} \qquad x_{21}R_3 + x_{22}R_4 = 0. \tag{F.85}$$
$$x_{11}R_5 + x_{12}R_6 = 0 \qquad \text{and} \qquad x_{21}R_5 + x_{22}R_6 = 0. \tag{F.86}$$

Therein we have defined

$$A^{-1} = \frac{1}{\det(A)}X \Leftrightarrow X = \begin{pmatrix} p_2^2 & -p_1p_2 \\ -p_1p_2 & p_1^2 \end{pmatrix} = \begin{pmatrix} x_{11} & x_{12} \\ x_{21} & x_{22} \end{pmatrix}. \tag{F.87}$$

Even in the case of a vanishing Gram determinant, (F.70) allows to determine C_{00}. Inserting this equation in the four expressions of (F.85) and (F.86) connects the unknown tensor coefficients C_1 and C_2 to the already determined quantities C_0, B_0 and B_1. After some calculation this can be casted in compact matrix form

$$Z_i \begin{pmatrix} C_1 \\ C_2 \end{pmatrix} = \begin{pmatrix} R_{7,i} \\ R_{8,i} \end{pmatrix} \Leftrightarrow \begin{pmatrix} C_1 \\ C_2 \end{pmatrix} = Z_i^{-1} \begin{pmatrix} R_{7,i} \\ R_{8,i} \end{pmatrix} \quad \text{with} \quad i = 1, 2. \tag{F.88}$$

The abbreviations used here are

$$\begin{aligned} R_{7,i} &= x_{i1}\left(B_1(1,2) + B_0(1,2) - \frac{2m_0^2}{D-2}C_0 - \frac{1}{D-2}B_0(1,2)\right) \\ &+ x_{i2}\left(B_1(0,1) + B_1(1,2) + B_0(1,2)\right). \end{aligned} \tag{F.89}$$

$$\begin{aligned} R_{8,i} &= x_{i1}\left(B_1(0,2) - B_1(1,2)\right) \\ &+ x_{i2}\left(-B_1(1,2) - \frac{2m_0^2}{D-2}C_0 - \frac{1}{D-2}B_0(1,2)\right). \end{aligned} \tag{F.90}$$

$$Z_i = \begin{pmatrix} Y_i + \frac{x_{i1}}{D-2}f_1 & \frac{x_{i1}}{D-2}f_2 \\ \frac{x_{i2}}{D-2}f_1 & Y_i + \frac{x_{i2}}{D-2}f_2 \end{pmatrix} \quad \text{with} \quad Y_i = x_{i1}f_1 + x_{i2}f_2. \tag{F.91}$$

This is a possible way to perform tensor reduction in case of a vanishing Gram determinant. The coefficients of tensor order n are determined by those equations which determine the tensor coefficients of order $n+1$ in the standard approach. As an example we have shown how to calculate the tensor coefficients C_1 and C_2 ($n = 1$). To do this, we needed the equations defining C_{00}, C_{11}, C_{12} and C_{22} ($n = 2$). The method is slower and more complex in comparison to the standard approach. Nevertheless, one can continue the procedure up to the desired tensor order in an algorithmic manner. However, the expressions soon get rather lengthy. Further results can be found in [270]. When looking closely at this alternative approach, two questions may show up.

On the one hand, one might ask oneself if all this extrawork in the case of a vanishing Gram determinant is actually needed. Why not taking the limit of the rational functions given on the right-hand sides of (F.78) and use l'Hôpital's rule to get the desired tensor coefficients? This does not work as the Gram determinant reappears in the denominator when taking the limit [270]. Therefore, the procedure described above is necessary.

The original motivation for the extended tensor reduction method presented in this section is the failure of the standard method in the case of a vanishing Gram determinant. In this case, the matrix A is not invertible and the tensor coefficients can not be obtained via (F.78). However, the final result for determining C_1 and C_2 in the extended approach

has the same algebraic form as before (cf. (F.88)) but the expressions hiding behind Z_i, $R_{7,i}$ and R_{8_i} are longer. There is no a priori reason why Z_i should be invertible in every case. Hence, one might think that the problem is shifted but not solved.

Indeed this is not the case. First note that we actually have two equations for obtaining e.g. C_1: We can either use Z_1 or Z_2. If one formula fails, the other one might still work. For precisely this reason we kept both equations leading to C_0 in (F.83) and (F.84). If one denominator vanishes, the other one might still be finite. Of course there are situations in which both formulae determining e.g. C_1 fail. Even in this case we improve because we can take the limit and apply l'Hôpital's rule without encountering $\det(Z_i)$ again.

Unfortunately, our calculation of the neutralino-nucleon cross sections leads exactly to this situation. In the remaining part of this section, we investigate in detail why the aforementioned approach fails and find yet another alternative analytic way to perform the tensor reduction. In this way we avoid applying l'Hôpital's rule in every individual case to allow for a more systematic approach. To the knowledge of the author, this method has not been worked out in detail before.

As we would like to keep things transparent and stress the main idea, we restrict ourselves to the evaluation of the tensor coefficients needed for the vertex corrections presented in subsection 4.4.3, namely C_1, C_2 and C_{00}. We identified four symptomatic sets of arguments and treat them in individual subsections. For all other cases with vanishing Gram determinant encountered here, the tensor reduction according to [270] has proven to be applicable. The brief notation $C(p_1, p_2, m_0^2, m_1^2, m_2^2)$ is meant to collect all kinds of three-point functions of the given argument set. The tensor reduction of the four-point functions needed for the box contributions can be performed in an analogous manner. As the resulting expressions are rather lengthy and unhandy, a self-written `Mathematica` script has been used in this case.

F.5.1. Tensor reduction for $C(p, p, m_0^2, m_1^2, m_2^2)$

In this situation the external momenta are equal, we have $p_1 = p_2 = p$. Note that this condition is stronger than just $p_1^2 = p_2^2$ which occurs regularly if two external particles are of the same type. This set of arguments leads directly to a vanishing Gram determinant as $\det(A) = p_1^2 p_2^2 - (p_1 p_2)^2 = p^4 - p^4 = 0$ and occurs for the t-channel vertex corrections V1, V2, V3 and V4 (cf. subsection 4.4.3 and figure 4.7) with massive quarks.

We begin by reinvestigating the expressions (F.83) and (F.84) for the scalar integral C_0. If $p_1^2 = p_2^2 = p_1 p_2 = p^2$ we simply get

$$C_0 = \frac{B_0(0,2) - B_0(0,1)}{f_1 - f_2} \underbrace{=}_{(F.47)} \frac{B_0(0,2) - B_0(0,1)}{m_2^2 - m_1^2}. \tag{F.92}$$

This expression diverges for $m_1^2 = m_2^2$. However, in this special case we encounter nothing but the derivative with respect to m_1^2.

$$C_0 = \lim_{m_1^2 \to m_2^2} \frac{B_0(0,2) - B_0(0,1)}{m_2^2 - m_1^2} = \frac{\partial}{\partial m_1^2} B_0(0,1). \tag{F.93}$$

We continue with the tensor reduction for C_μ. The crucial observation is that in this case the Lorentz decomposition for C_1 and C_2 breaks down to

$$C_\mu = p_{1,\mu} C_1 + p_{2,\mu} C_2 \to p_\mu C_a. \tag{F.94}$$

As there is just one independent external momentum, C_1 and C_2 are no longer uniquely defined. Instead of that we have just one alternative tensor coefficient denoted by C_a which can be identified with the sum $C_1 + C_2$ in the limit $p_1 \to p_2$. It is precisely this sum $C_1 + C_2$ that remains in all the corresponding amplitudes in the limit $p_1 \to p_2$. Terms containing C_1 or C_2 individually vanish. This has been checked explicitly. For simplicity we set $C_1 = C_2 = C_a/2$, but as already stated, it is the sum that matters.

The remaining task is to determine C_a. This is done in the usual way. We contract (F.94) with p^μ and obtain

$$
\begin{aligned}
p^2 C_a &= \frac{(2\pi\mu)^{4-D}}{i\pi^2} \int \mathrm{d}^D q \frac{pq}{(q^2 - m_0^2)((q+p)^2 - m_1^2)((q+p) - m_2^2)} \\
&\underbrace{=}_{(F.46)} \frac{(2\pi\mu)^{4-D}}{i\pi^2} \int \mathrm{d}^D q \frac{\mathcal{D}_1 - \mathcal{D}_0 - f_1}{2\mathcal{D}_0 \mathcal{D}_1 \mathcal{D}_2} \\
\Leftrightarrow C_a &= \frac{1}{2p^2} \left(B_0(0,2) - B_0(1,2) - f_1 C_0 \right).
\end{aligned}
\tag{F.95}
$$

Alternatively, we can use the substitution $pq = \mathcal{D}_2 - \mathcal{D}_0 - f_2$ for the nominator and get as a second, equivalent expression

$$
C_a = \frac{1}{2p^2} \left(B_0(0,1) - B_0(1,2) - f_2 C_0 \right).
\tag{F.96}
$$

The next step is to reinvestigate the tensor reduction for $C_{\mu\nu}$. The Lorentz decomposition breaks down to

$$
\begin{aligned}
C_{\mu\nu} &= g_{\mu\nu} C_{00} + p_{1,\mu} p_{1,\nu} C_{11} + (p_{1,\mu} p_{2,\nu} + p_{2,\mu} p_{1,\nu}) C_{12} + p_{2,\mu} p_{2,\nu} C_{22} \\
&\to g_{\mu\nu} C_{00} + p_\mu p_\nu C_{aa}.
\end{aligned}
\tag{F.97}
$$

The alternative tensor coefficient C_{aa} replaces the sum $C_{11} + 2C_{12} + C_{22}$ in the limit $p_1 \to p_2$ but does not occur in our calculations for the vertex corrections. We contract this equation with $g^{\mu\nu}$ and get

$$
p^2 C_{aa} + D C_{00} = \frac{(2\pi\mu)^{4-D}}{i\pi^2} \int \mathrm{d}^D q \frac{q^2 - m_0^2 + m_0^2}{\mathcal{D}_0 \mathcal{D}_1 \mathcal{D}_2} = B_0(1,2) + m_0^2 C_0.
\tag{F.98}
$$

A second equation is obtained by contracting with p^μ.

$$
\begin{aligned}
p^2 p_\nu C_{aa} + p_\nu C_{00} &= \frac{(2\pi\mu)^{4-D}}{i\pi^2} \int \mathrm{d}^D q \frac{pq\, q_\nu}{\mathcal{D}_0 \mathcal{D}_1 \mathcal{D}_2} = \frac{(2\pi\mu)^{4-D}}{i\pi^2} \int \mathrm{d}^D q \frac{q_\nu}{2} \frac{\mathcal{D}_1 - \mathcal{D}_0 - f_1}{\mathcal{D}_0 \mathcal{D}_1 \mathcal{D}_2} \\
&= \frac{1}{2}(B_\nu(0,2) - B_\nu(1,2) - f_1 C_\nu) = \frac{p_\nu}{2}(B_1(0,2) + B_0(1,2) - f_1 C_a) \\
\Leftrightarrow p^2 C_{aa} + C_{00} &= \frac{1}{2}(B_1(0,2) + B_0(1,2) - f_1 C_a).
\end{aligned}
\tag{F.99}
$$

Note that we have used our previous result $C_\nu = p_\nu C_a$ here. Subtracting (F.99) from (F.98) leads to

$$
\begin{aligned}
(D-1) C_{00} &= m_0^2 C_0 + \frac{1}{2}(B_0(1,2) - B_1(0,2) + f_1 C_a) \\
\Leftrightarrow C_{00} &= \frac{1}{D-1} \left(m_0^2 C_0 + \frac{1}{2}(B_0(1,2) - B_1(0,2) + f_1 C_a) \right) \\
&= \frac{1}{3} m_0^2 C_0 + \frac{1}{6}\left(B_0(1,2) - B_1(0,2) + f_1 C_a + 1 \right).
\end{aligned}
\tag{F.100}
$$

The substitution $pq = \mathcal{D}_2 - \mathcal{D}_0 - f_2$ for the nominator leads to the equivalent expression

$$C_{00} = \frac{1}{3}m_0^2 C_0 + \frac{1}{6}\left(B_0(1,2) - B_1(0,1) + f_2 C_a + 1\right). \tag{F.101}$$

F.5.2. Tensor reduction for $C(p, 0, m_0^2, m_1^2, m_2^2)$

The situation, that one external momentum equals zero while the other one does not, occurs for the s- and u-channel vertex corrections V5, V6, V7 and V8 (cf. subsection 4.4.3 and figure 4.7) with massless quarks. As before, the Gram determinant vanishes and there is only one external momentum available for the Lorentz decompostion of C_μ. Once again we have

$$C_\mu = p_{1,\mu}C_1 + p_{2,\mu}C_2 \rightarrow p_\mu C_a. \tag{F.102}$$

The difference to the previous subsection is that we have $p_1 = p$ and $p_2 = 0$. Hence, we set $C_1 = C_a$ and $C_2 = 0$ in the limit $p_2 \rightarrow 0$. The determination of C_a is carried out as previously. We contract with p^μ and obtain

$$\begin{aligned}
p^2 C_a &= \frac{(2\pi\mu)^{4-D}}{i\pi^2} \int d^D q \frac{pq}{(q^2 - m_0^2)((q+p)^2 - m_1^2)(q - m_2^2)} \\
&\underbrace{=}_{(F.46)} \frac{(2\pi\mu)^{4-D}}{i\pi^2} \int d^D q \frac{\mathcal{D}_1 - \mathcal{D}_0 - f_1}{2\mathcal{D}_0 \mathcal{D}_1 \mathcal{D}_2} \\
\Leftrightarrow C_a &= \frac{1}{2p^2}\left(B_0(0,2) - B_0(1,2) - f_1 C_0\right). \tag{F.103}
\end{aligned}$$

Note that there is no second choice for C_a in this case, i.e. we can not use (F.96) here.

F.5.3. Tensor reduction for $C(0, p, m_0^2, m_1^2, m_2^2)$

This case is just the permutation $1 \leftrightarrow 2$ of the previous case. Here we have $p_1 = 0$ and $p_2 = p$. Hence, we set $C_1 = 0$ and $C_2 = C_a$ in the limit $p_1 \rightarrow 0$. C_a is given by

$$C_a = \frac{1}{2p^2}\left(B_0(0,1) - B_0(1,2) - f_2 C_0\right), \tag{F.104}$$

i.e. here we use the second variant (F.96) and not the first one (F.95) as in the previous subsection.

F.5.4. Tensor reduction for $C(0, 0, m_0^2, m_1^2, m_2^2)$

If both external momenta are zero, the Gram determinant $\det(A) = p_1^2 p_2^2 - (p_1 p_2)^2$ obviously vanishes. This situation occurs for the t-channel vertex corrections V1, V2, V3 and V4 (cf. subsection 4.4.3 and figure 4.7) with massless quarks. The Lorentz decomposition for C_μ simplifies to

$$C_\mu = p_{1,\mu}C_1 + p_{2,\mu}C_2 \rightarrow 0, \tag{F.105}$$

as there is no Lorentz covariant quantity available. This can also be seen directly. For the given set of arguments we have

$$C_\mu = \frac{(2\pi\mu)^{4-D}}{i\pi^2} \int d^D q \frac{q_\mu}{(q^2 - m_0^2)(q^2 - m_1^2)(q^2 - m_2^2)} = 0. \tag{F.106}$$

This integral vanishes as the integrand is an antisymmetric function of q, whereas the integration interval is symmetric in q. Hence, we set $C_1 = C_2 = 0$. However, in practice this choice is irrelevant as all terms in the amplitudes proportional to C_1 and C_2 vanish in the limit $p_1, p_2 \to 0$. This has been checked explicitly.

In contrast to that, the tensor coefficient C_{00} is still relevant and non-zero. The tensor reduction for $C_{\mu\nu}$ reduces to

$$C_{\mu\nu} = g_{\mu\nu}C_{00} + p_{1,\mu}p_{1,\nu}C_{11} + (p_{1,\mu}p_{2,\nu} + p_{2,\mu}p_{1,\nu})C_{12} + p_{2,\mu}p_{2,\nu}C_{22} \to g_{\mu\nu}C_{00}. \quad \text{(F.107)}$$

We contract with $g^{\mu\nu}$ and obtain

$$
\begin{aligned}
DC_{00} &= \frac{(2\pi\mu)^{4-D}}{i\pi^2} \int \mathrm{d}^D q \frac{q^2 - m_0^2 + m_0^2}{\mathcal{D}_0 \mathcal{D}_1 \mathcal{D}_2} = B_0(1,2) + m_0^2 C_0 \\
\Leftrightarrow C_{00} &= \frac{1}{D}(B_0(1,2) + m_0^2 C_0) = \frac{1}{4}(B_0(1,2) + m_0^2 C_0 + \frac{1}{2}). \quad \text{(F.108)}
\end{aligned}
$$

As we can freely choose how to add the zero in the nominator above, we get two more analytically equivalent expressions.

$$C_{00} = \frac{1}{4}(B_0(0,2) + m_1^2 C_0 + \frac{1}{2}) = \frac{1}{4}(B_0(0,1) + m_2^2 C_0 + \frac{1}{2}). \quad \text{(F.109)}$$

F.5.5. Numerical investigation

We close this section with a numerical investigation of the tensor reduction in the limit of vanishing relative velocity and hence vanishing Gram determinant. For this purpose we have chosen a kinematical situation corresponding to vertex diagram V2 (cf. subsection 4.4.3 and figure 4.7). The three-point functions needed for this process possess the arguments $C_{(p_b, p_2, m_{\tilde{g}}^2, m_{\tilde{q}_i}^2, m_{\tilde{q}_j}^2)}$. The limit $v \to 0$ leads to $p_b = p_2$ and hence to $t = (p_b - p_2)^2 \to 0$.

The upper left plot of figure F.2 shows the numerical stability of the tensor coefficients C_1 and C_2 in the aforementioned limit. More precisely, we show the real parts of C_1 (in red) and C_2 (in blue) obtained by the regular tensor reduction method divided by $C_a/2$ obtained via (F.95) and subtracted by one. In this representation, the black null line corresponds directly to $C_a/2$. We observe that both C_1 and C_2 are relatively stable for $t \leq -0.5$ GeV^2 and marginally differ from $C_a/2$. This is as expected. The regular tensor reduction is still working here and the small but finite velocity leads to a small shift relative to the black null line. However, when we approach the limit $t \to 0$ the regular tensor method fails and both of the coefficients become numerically unstable.

As explained in subsection F.5.1 the individual tensor coefficients C_1 and C_2 are no longer uniquely defined in this limit, only their sum is. The real part of this sum divided by C_a and subtracted by one is shown in the upper right plot of figure F.2. It is more stable than the individual coefficients but still becomes noisy at very small relative velocities. For larger (but still small) relative velocities the agreement between $C_1 + C_2$ and C_a is excellent, which justifies our approach.

Although these coefficents are not directly needed for the vertex correction V2, we show analogous plots for the tensor coefficient C_{00} and the sum $C_{11} + 2C_{12} + C_{22}$ in the lower part of figure F.2. The main features are as before. Using the original tensor reduction method, the tensor coefficients become numerically unstable at very small relative velocities. When using the alternative approach described in this section, we obtain a stable result for $v = 0$
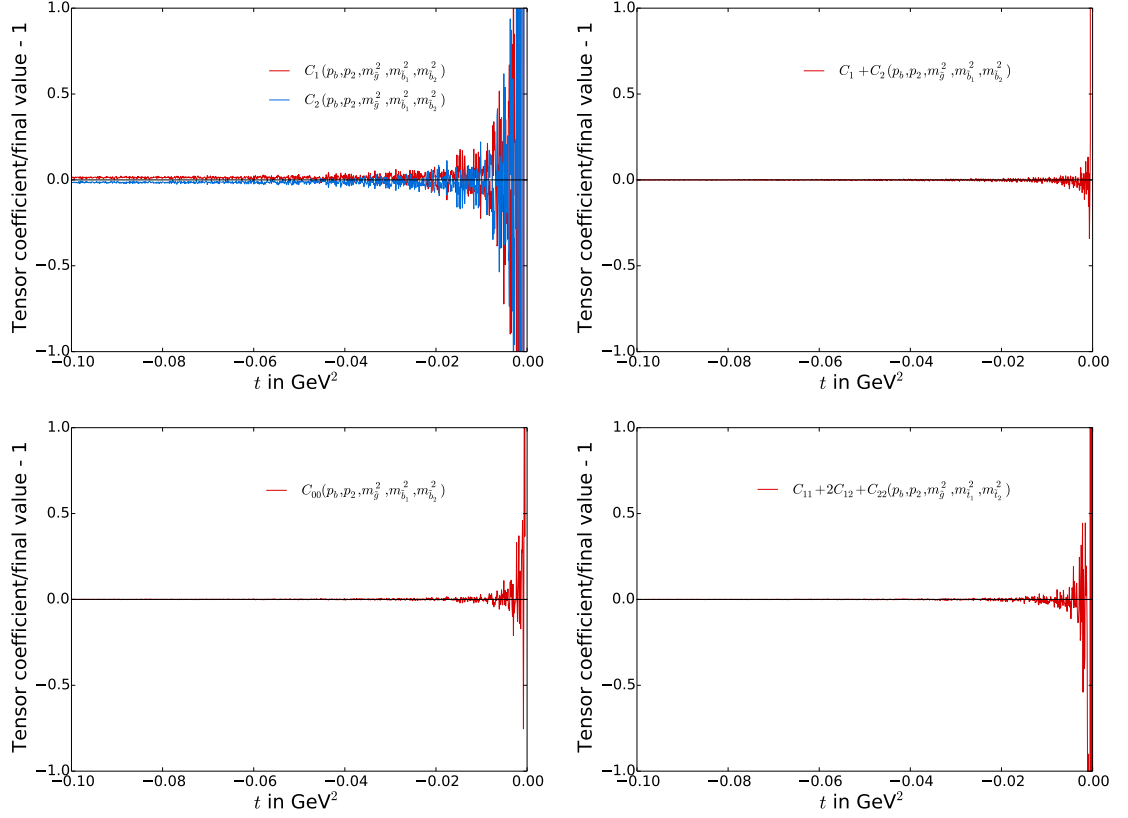
Figure F.2.: Numerical stability of the three-point tensor coefficients in the limit $v \to 0$ or equivalently $t \to 0$

which is in perfect agreement with the standard method for small but non-zero relative velocities.

We stress again that the alternative tensor reduction method has been implemented in `DM@NLO` not only for the three-point functions stemming from the vertex corrections but also for the box corrections. These corrections involve four-point tensor coefficents of second order i.e. D_{00}, D_{11}, D_{12} etc. The general idea behind the alternative reduction remains completely unchanged but the expressions blow up enormously.[36] Hence, a `Mathematica` script was written to perform these calculations. All of the resulting tensor coefficents have been tested extensively and excellent agreement with the standard method for small but non-zero relative velocities has been found throughout.

Although of minor importance for the tensor reduction itself, we list all the masses used in the plots above for reasons of completeness. They are given by $m_b = 2.3$ GeV, $m_t = 148.0$ GeV, $m_{\tilde{g}} = 1170.7$ GeV, $m_{\tilde{b}_1} = 1007.3$ GeV, $m_{\tilde{b}_2} = 1071.9$ GeV, $m_{\tilde{t}_1} = 827.9$ GeV and finally $m_{\tilde{t}_2} = 1042.6$ GeV. Note that we have $p_2^2 = p_b^2 = m_b^2$ in the first three plots, whereas $p_2^2 = p_b^2 = m_t^2$ in the lower right plot.

---

[36]Remember that the method of [270] requires the equations for tensor coefficients of third rank to determine those of second rank.

Table F.1.: UV behaviour of some scalar integrals and tensor coefficients

Scalar integral or tensor coefficient	UV Behaviour	$(D-4) \times$ integral
A_0	divergent	$-2m_0^2$
B_0	divergent	-2
B_1	divergent	1
B_{00}	divergent	$\frac{1}{6}\left(p_1^2 - 3(m_0^2 + m_1^2)\right)$
B_{11}	divergent	$-\frac{2}{3}$
C_{00}	divergent	$-\frac{1}{2}$
$C_0, C_1, C_2, C_{11}, C_{12}, C_{22}$	convergent	
D_0, D_1, D_2, D_3	convergent	
$D_{00}, D_{11}, D_{12}, D_{13}, D_{22}, D_{23}, D_{33}$	convergent	

F.6. Ultraviolet behaviour of Passarino Veltman integrals

In this section we investigate and collect the ultraviolet (UV) behaviour of some scalar Passarino Veltman integrals and tensor coefficients. We start with the most simple one, the scalar integral A_0 as given in (F.14). This integral contains the factor Δ as given in (F.16) which diverges in the limit $D \to 4$. We quantify the divergence by multiplying with $(D-4)$ and obtain

$$(D-4)A_0 = -2m_0^2 + \mathcal{O}(D-4). \tag{F.110}$$

In complete analogy we analyse B_0 as given in (F.15) and find

$$(D-4)B_0 = -2 + \mathcal{O}(D-4). \tag{F.111}$$

As expected, the mass dimension of this expression is two orders lower than the one before. The scalar integrals C_0 and D_0 are ultraviolet convergent, i.e.

$$(D-4)C_0 = \mathcal{O}(D-4) \quad \text{and} \quad (D-4)D_0 = \mathcal{O}(D-4). \tag{F.112}$$

Thanks to the tensor reduction method, the tensor coefficients can be expressed as linear combinations of the scalar integrals. Therefore, the ultraviolet behaviour of the tensor coefficients is determined by the ultraviolet behaviour of the scalar integrals and can be computed easily (cf. e.g. [262]). As an example, we investigate the tensor coefficient B_1 as given in (F.45).

$$
\begin{aligned}
(D-4)B_1 &= \frac{1}{2p_1^2}\left((D-4)A_0(m_0^2) - (D-4)A_0(m_1^2)\right) \\
&\quad - (p_1^2 - m_1^2 + m_0^2)(D-4)B_0(p_1, m_0^2, m_1^2)) \\
&= \frac{1}{2p_1^2}\left(-2m_0^2 + 2m_1^2 + 2(p_1^2 - m_1^2 + m_0^2)\right) + \mathcal{O}(D-4) \\
&= 1 + \mathcal{O}(D-4). \tag{F.113}
\end{aligned}
$$

In table F.1, we list the ultraviolet behaviour of all scalar integrals and tensor coefficients studied so far.

G. Renormalisation

In the last chapter we have introduced the concept of dimensional regularisation, a method to identify and isolate poles from divergent loop integrals. As already mentioned, there are two kind of poles, infrared and ultraviolet ones (cf. section F.1). Whereas the former cancel when adding up the corresponding real corrections, the latter have to be removed via *renormalisation.*

In the next sections, we sketch the basic idea of renormalisation, exemplarily apply renormalisation in the context of QCD and present the most common *renormalisation schemes.* Afterwards we discuss the so-called *renormalisation group equations* for the strong coupling constant and the quark mass. These formulae are needed for the running of the operators $m_q \bar{q} q$ and $\bar{q} \gamma_5 \gamma^\mu q$ (cf. section 4.6). The discussion is meant to be general and rather introductory. For further details on renormalisation we refer to [166, 237, 262, 279].

Moreover, we discuss the renormalisation scheme implemented in DM@NLO. Although the work on this thesis has significantly improved the numerical capability of the implemented regularisation routines, the renormalisation scheme itself remained basically unchanged. Hence, we do not reproduce all of its details and just list the counterterms needed for the calculation of the neutralino-nucleon cross sections. More details on this scheme can be found in [62, 148, 149].

G.1. Basic idea of renormalisation

So far we have demonstrated how to calculate and regularise divergent loop integrals. The final result still contains ultraviolet poles which diverge in the physical limit $D \to 4$ or equivalently $\epsilon \to 0$. To enable meaningful scientific predictions, these poles somehow have to disappear, which is precisely what happens after renormalisation. The reason for this disappearance is deeply connected with a profound question: What exactly is meant by a physical parameter like a coupling constant or a particle mass?

To illustrate this, we start with the Lagrangian of QCD which can be briefly written as

$$\mathcal{L}_{\text{QCD}} = \bar{q} \left(i \slashed{D} - m_q \right) q - \frac{1}{4} F^a_{\mu\nu} F^{\mu\nu}_a. \tag{G.1}$$

The first term describes the kinematics of the quarks and the interaction between quarks and gluons. It includes the quark spinor field q and its adjoint counterpart $\bar{q} = q^\dagger \gamma^0$, the quark mass m_q and the covariant derivative $D_\mu = \partial_\mu - i g_s T_a A^a_\mu$ which in turn consists out of the strong coupling constant g_s, the generators of the $SU(3)$ colour group T_a and the gluon fields A^a_μ. The last two carry a colour index a. The second term is responsible for the kinematics of the gluons and their self-interactions. The gluon field strength tensor reads $F^a_{\mu\nu} = \partial_\mu A^a_\nu - \partial_\nu A^a_\mu + g_s f^{abc} A^b_\mu A^c_\nu$. The essential feature of QCD as a non-abelian gauge theory is the appearance of the structure constant f^{abc}. This term vanishes in case of abelian theories like quantum electrodynamics, where the generators of the $U(1)$ gauge group permute and self-interactions between photons are absent.
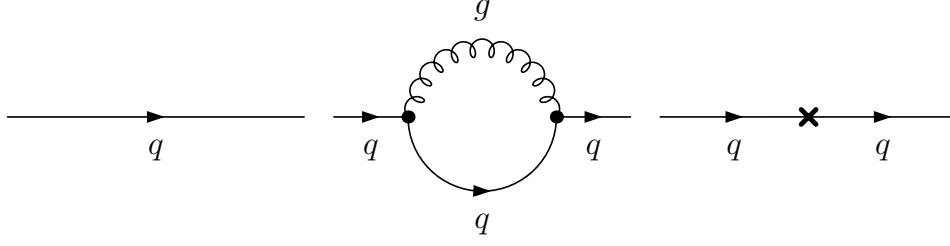
Figure G.1.: Quark propagator at tree-level, including the gluonic NLO correction and including the counterterm

What do we mean by e.g. the quark mass? Within classical mechanics, the mass of a particle corresponds to its resistance against acceleration and its susceptibility to gravitational attraction. The mass can be measured with a suitable scale and expressed as a fixed number. This might lead to the conclusion that the mass m_q entering the Lagrangian (G.1) is nothing but a fixed, directly measurable quantity as well. Unfortunately, things are more involved in quantum field theory (QFT) and its perturbative treatment.

We can define a *bare mass* m_{q_0} which appears in the one-particle irreducible two-point function $\Gamma^{\bar{q}q}_{\mathrm{tree}}(p)$ of quarks at tree-level.

$$\Gamma^{\bar{q}q}_{\mathrm{tree}}(p) = i(\not{p} - m_{q_0}). \tag{G.2}$$

The corresponding diagram is depicted on the left in figure G.1. The two-point function is linked with the quark propagator via

$$G^{\bar{q}q}_{\mathrm{tree}}(p) = -\Gamma^{\bar{q}q}_{\mathrm{tree}}(p)^{-1} = \frac{i}{\not{p} - m_{q_0}}. \tag{G.3}$$

At tree-level, the bare mass is nothing but the pole of the propagator.

Now we consider the relevant NLO correction, namely the quark self-energy shown in the middle of figure G.1. We write the amplitude of the self-energy as $i\mathcal{M}(p) = i\bar{u}(p)\Pi^{\bar{q}q}(p)u(p)$ and keep only its truncated part $\Pi^{\bar{q}q}(p)$. After a short calculation we obtain

$$\Pi^{\bar{q}q}(p) = -\frac{\alpha_S}{4\pi}C_F\left(Dm_qB_0(-p, m_q, 0) + (D-2)\not{p}B_1(-p, m_q, 0)\right), \tag{G.4}$$

where we have worked with an unspecified quark mass m_q provisionally. This modifies the two point-function to

$$\Gamma^{\bar{q}q}(p) = i(\not{p} - m_{q_0}) + i\Pi^{\bar{q}q}(p) \tag{G.5}$$

and leads to the propagator

$$G^{\bar{q}q}(p) = -\Gamma^{\bar{q}q}(p)^{-1} = \frac{i}{\not{p} - m_{q_0} + \Pi^{\bar{q}q}(p)}. \tag{G.6}$$

Remember that B_0 and B_1 and hence $\Pi^{\bar{q}q}(p)$ diverge in the limit $D \to 4$ (cf. chapter F). More precisely, the divergent part reads

$$\Pi^{\bar{q}q}_{\mathrm{div}}(p) = \frac{\alpha_S}{4\pi}C_F\frac{1}{\epsilon}\left(\not{p} - 4m_q\right). \tag{G.7}$$

If we assume that the bare quark mass is a directly measurable, fixed quantity, (G.5) leads to a divergent two-point function and hence ill-defined quark propagator. This demonstrates that the concept of mass in QFT is far from intuitive.

The problem is that there is no such observable like a bare mass in nature. We have introduced the bare mass as the pole mass of the tree-level propagator in the context of perturbation theory. But nature does not care about perturbation theory and its succeeding orders. In reality particles just interact and we can neither force nor beg them to restrict themselves to tree-level interactions. If we try to measure the mass of a particle by e.g. observing a resonance, all orders in perturbation theory contribute. Nevertheless, quarks seem to possess a finite mass as e.g. new decay channels open up at certain finite energies.

What does this tell us about the bare mass? To obtain a finite and observable mass in the end, the ultraviolet divergences stemming from the virtual corrections have to vanish order by order. Hence, the bare mass has to incorporate poles as well so that the sum in (G.5) becomes ultraviolet finite.[37] Therefore, we rewrite it as a sum of a finite renormalised mass m_q and an ultraviolet divergent *counterterm* δm_q.

$$m_{q_0} \to m_q + \delta m_q. \tag{G.8}$$

The counterterm is meant to cancel ultraviolet divergences. A theory is called renormalisable if all appearing ultraviolet divergences can be absorbed by a finite and constant number of counterterms order by order in perturbation theory. Fortunately, the Standard Model of particles turns out to be a renormalisable theory.

However, note that there is some freedom left in shifting finite terms between the renormalised mass and the counterterm. Using this freedom in different ways corresponds to choosing different *renormalisation schemes*. The most common renormalisation schemes are presented in section G.3. Furthermore, we stress that the self-energy given in (G.4) includes finite but scale-dependent terms. Depending on the chosen scheme, these contributions may be shifted into the renormalised mass or the counterterm. We return to the scale dependence of the mass in section G.4.

G.2. Renormalisation of QCD in a nutshell

Now that we have sketched the basic idea of renormalisation, we exemplarily apply it to QCD. Parts of the results presented here are taken from [280] and [238]. We start with the *bare Lagrangian* of QCD $\mathcal{L}_{\text{QCD},0}$, consisting only of bare quantities, i.e. the bare quark mass m_{q_0}, the bare coupling g_{s_0} and the bare fields q_0 and $A_{\mu,0}^a$. This Lagrangian reads

$$\mathcal{L}_{\text{QCD},0} = \bar{q}_0 \left(i\slashed{D}_0 - m_{q_0} \right) q_0 - \frac{1}{4} F_{\mu\nu,0}^a F_{a,0}^{\mu\nu}, \tag{G.9}$$

where $D_{\mu,0} = \partial_\mu - ig_{s_0} T_a A_{\mu,0}^a$ and $F_{\mu\nu,0}^a = \partial_\mu A_{\nu,0}^a - \partial_\nu A_{\mu,0}^a + g_{s_0} f^{abc} A_{\mu,0}^b A_{\nu,0}^c$. All the bare quantities are rewritten in terms of renormalised quantities and associated counterterms.

---

[37]To be more precise, the ultraviolet divergences stemming from the virtual corrections have to be absorbed by the combination of all bare parameters and not just the bare mass as we demonstrate in the next section.

This is done via *multiplicative renormalisation.* More precisely, we have

$$m_{q_0} \rightarrow Z_m m_q = m_q + \delta m_q. \tag{G.10}$$

$$q_0 \rightarrow \sqrt{Z_q} q = (1 + \frac{1}{2}\delta Z_q)q. \tag{G.11}$$

$$A_{\mu,0} \rightarrow \sqrt{Z_A} A_\mu = (1 + \frac{1}{2}\delta Z_A)A_\mu. \tag{G.12}$$

$$g_{s_0} \rightarrow Z_g \mu^\epsilon g_s = g_s \mu^\epsilon + \delta g_s \mu^\epsilon. \tag{G.13}$$

We have added the term μ^ϵ in case of the coupling constant renormalisation to retain g_s dimensionless when working in $D = 4-2\epsilon$ dimensions, where μ denotes the renormalisation scale introduced in section F.2.

Let us exemplarily perform this substitution for the kinematics of the quarks. Note that all counterterms are proportional to α_s. To obtain a consistent NLO result, we neglect all terms of order α_s^2.

$$
\begin{aligned}
\mathcal{L}_{q,0} &= i\bar{q}_0\slashed{\partial}q_0 - \bar{q}_0 m_{q_0} q_0 \rightarrow i\sqrt{Z_q}\bar{q}\slashed{\partial}\sqrt{Z_q}q - \sqrt{Z_q}\bar{q}Z_m m_q \sqrt{Z_q}q \\
&= i(1 + \delta Z_q)\bar{q}\slashed{\partial}q - (1 + \delta Z_q)\bar{q}(m_q + \delta m_q)q \\
&= i\bar{q}\slashed{\partial}q - \bar{q}m_q q + \delta Z_q \bar{q}\slashed{\partial}q - \delta Z_q \bar{q}m_q q - \bar{q}\delta m_q q = \mathcal{L}_q + \mathcal{L}_C. \tag{G.14}
\end{aligned}
$$

Multiplying out everything, we arrive at a sum of two Lagrangians. The first term $\mathcal{L}_q$ equals the initial bare Lagrangian but includes renormalised instead of bare quantities. The second term includes the counterterms and leads to new Feynman diagrams appearing at NLO for the first time.

We can now recalculate the one-particle irreducible two-point function $\Gamma^{\bar{q}q}(p)$ of quarks at NLO and get

$$\Gamma^{\bar{q}q}(p) = i(\slashed{p} - m_q) + i\Pi^{\bar{q}q}(p) + i\left(\delta Z_q \slashed{p} - (\delta Z_q + \frac{\delta m_q}{m_q})m_q\right). \tag{G.15}$$

These three terms correspond to the diagrams shown in figure G.1: The tree-level propagator, its gluonic correction and the propagator counterterm which is marked by a cross. Demanding that the sum of these three terms is ultraviolet finite fixes the divergent part of the counterterms δZ_q and δm_q, respectively. Comparing with (G.7) leads to

$$\delta Z_{q,\text{div}} = -\frac{\alpha_s}{4\pi}C_F\frac{1}{\epsilon} \quad \text{and} \quad \delta m_{q,\text{div}} = -\frac{\alpha_s}{4\pi}C_F\frac{3}{\epsilon}m_q. \tag{G.16}$$

The divergent parts of the counterterms δZ_A and δZ_g can be determined in a similar fashion. In this case one has to calculate one-loop corrections to the gluon propagator and the quark gluon vertex, respectively. The relevant diagrams are depicted in figure G.2. The third diagram in the upper row represents the contribution from Faddeev-Popov ghosts η. These unphysical particles have to be included in non-abelian gauge theories to compensate for the overcounting of degrees of freedom. The calculation is a bit lengthier and leads to

$$\delta Z_{A,\text{div}} = -\frac{\alpha_s}{4\pi}\left(\frac{2}{3}n_f - \frac{5}{3}N_C\right)\frac{1}{\epsilon} \quad \text{and} \quad \delta Z_{g,\text{div}} = -\frac{\alpha_s}{4\pi}\left(\frac{11}{6}N_C - \frac{2}{6}n_f\right)\frac{1}{\epsilon}, \tag{G.17}$$

where n_f denotes the number of quark flavours and $N_C = 3$ denotes the number of colours.
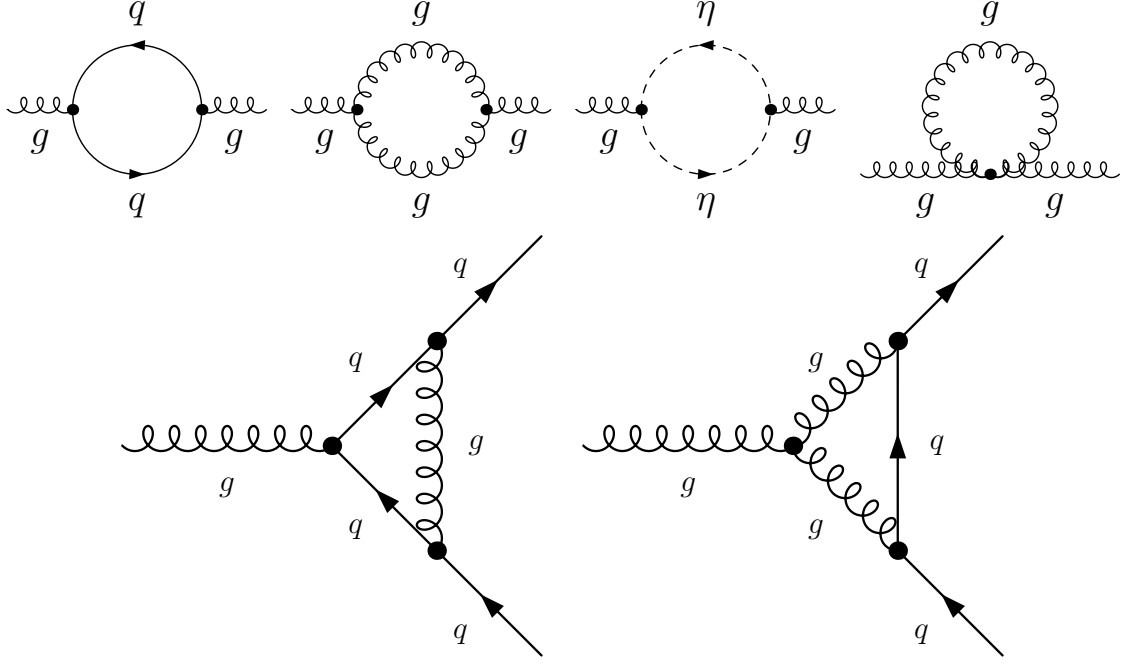
Figure G.2.: One-loop QCD corrections to the gluon propagator (upper row) and to the quark gluon vertex (lower row)

G.3. Different renormalisation schemes

G.3.1. MS and $\overline{\text{MS}}$ scheme

The so-called *minimal subtraction* (MS) scheme corresponds to the approach we have presented in the previous section. Within this scheme, the divergences are regulated via dimensional regularisation and the counterterms are meant to absorb nothing but the ultraviolet poles. This leads to the fact that the renormalisation constants Z_i and associated counterterms δZ_i are mass-independent and depend solely on the coupling constant. In the MS scheme, each renormalisation constant Z_i can be written as

$$Z_i = 1 + \sum_{n=1}^{\infty} \frac{Z_{i,n}(g_s)}{\epsilon^n}. \tag{G.18}$$

Another important feature is that additional finite but scale-dependent contributions are absorbed in physical parameters like quark masses or coupling constants rendering them scale-dependent. We return to this issue in the next section.

The *modified minimal subtraction* ($\overline{\text{MS}}$) scheme basically coincides with the MS scheme, the only difference is that universal constant terms are absorbed in the counterterms as well. More precisely, the whole divergent factor

$$\Delta = \frac{2}{4-D} - \gamma_E + \ln(4\pi) = \frac{1}{\epsilon} - \gamma_E + \ln(4\pi) \tag{G.19}$$

and not just the pole $1/\epsilon$ gets absorbed into the counterterms in the $\overline{\text{MS}}$ scheme.

G.3.2. DR and $\overline{\text{DR}}$ scheme

The *dimensional reduction* (DR) and the *modified dimensional reduction* ($\overline{\text{DR}}$) schemes can be seen as the SUSY equivalents of the MS and $\overline{\text{MS}}$ scheme, respectively. The sole difference consists in the chosen regularisation method, which is dimensional reduction in this case. In contrast to dimensional regularisation, dimensional reduction preserves SUSY (cf. section F.2).

G.3.3. OS scheme

The previously introduced renormalisation schemes are commonly referred to as minimal schemes. A popular example for a non-minimal, physical scheme is the so-called *on-shell* (OS) scheme, which is motivated differently and often used for directly measurable, heavy particles like the top quark. The main idea is that the renormalised mass should correspond to the observed, physical mass of the particle. In particular, this mass has to be scale-independent.

If we want to renormalise a quark on-shell, we have to impose two renormalisation conditions to fix its mass and spinor field counterterm. These conditions read

$$\Gamma^{\bar{q}q}(p)u(p)\Big|_{p^2=m_q^2} \overset{!}{=} 0 \quad \text{and} \quad \lim_{p^2 \to m_q^2} \frac{1}{\slashed{p}-m_q}\Gamma^{\bar{q}q}(p)u(p) \overset{!}{=} iu(p), \tag{G.20}$$

where we have used the two-point function $\Gamma^{\bar{q}q}(p)$ as given in (G.15). To investigate these renormalisation conditions, we decompose $\Pi^{\bar{q}q}(p)$ into a vector and a scalar part via

$$\Pi^{\bar{q}q}(p) = \slashed{p}\Pi_V^{\bar{q}q}(p) + m_q\Pi_S^{\bar{q}q}(p). \tag{G.21}$$

The first condition sets the renormalised mass to the physical mass, i.e. the pole mass. Using the Dirac equation $\slashed{p}u(p) = m_q u(p)$ leads to

$$0 \quad \overset{!}{=} \quad \Gamma^{\bar{q}q}(p)u(p)\Big|_{p^2=m_q^2} = \left(\Pi^{\bar{q}q}(p) - \delta m_q\right)u(p)\Big|_{p^2=m_q^2}$$

$$\Leftrightarrow \frac{\delta m_q}{m_q} \quad = \quad \Pi_V^{\bar{q}q}(p)\Big|_{p^2=m_q^2} + \Pi_S^{\bar{q}q}(p)\Big|_{p^2=m_q^2}. \tag{G.22}$$

The second condition fixes δZ_q. We obtain

$$iu(p) \quad \overset{!}{=} \quad \lim_{p^2 \to m_q^2} \frac{1}{\slashed{p}-m_q}\Gamma^{\bar{q}q}(p)u(p)$$

$$= \quad \lim_{p^2 \to m_q^2} \frac{i}{\slashed{p}-m_q}\left((\slashed{p}-m_q) + \Pi^{\bar{q}q}(p) + \delta Z_q(\slashed{p}-m_q) - \delta m_q\right)u(p)$$

$$\Leftrightarrow 0 \quad = \quad \lim_{p^2 \to m_q^2} \frac{1}{\slashed{p}-m_q}\left(\slashed{p}\Pi_V^{\bar{q}q}(p) + m_q\Pi_S^{\bar{q}q}(p) + \delta Z_q(\slashed{p}-m_q) - \delta m_q\right)u(p)$$

$$= \quad \lim_{p^2 \to m_q^2}\left(\Pi_V^{\bar{q}q}(p) + \delta Z_q + \frac{m_q}{\slashed{p}-m_q}\left(\Pi_V^{\bar{q}q}(p) + \Pi_S^{\bar{q}q}(p) - \frac{\delta m_q}{m_q}\right)u(p)\right)$$

$$= \quad \lim_{p^2 \to m_q^2}\left(\Pi_V^{\bar{q}q}(p) + \delta Z_q + \frac{m_q(\slashed{p}+m_q)}{p^2-m_q^2}\right.$$

$$\left.\left(\Pi_V^{\bar{q}q}(p) + \Pi_S^{\bar{q}q}(p) - \Pi_V^{\bar{q}q}(p)\Big|_{p^2=m_q^2} - \Pi_S^{\bar{q}q}(p)\Big|_{p^2=m_q^2}\right)u(p)\right)$$

$$\Leftrightarrow \delta Z_q \quad = \quad -\Pi_V^{\bar{q}q}(p)\Big|_{p^2=m_q^2} - 2m_q^2\left(\frac{\partial\Pi_V^{\bar{q}q}(p)}{\partial p^2}\Big|_{p^2=m_q^2} + \frac{\partial\Pi_S^{\bar{q}q}(p)}{\partial p^2}\Big|_{p^2=m_q^2}\right). \tag{G.23}$$

G.4. Renormalisation group equations

In the course of the regularisation procedure, we have introduced an artificial renormalisation scale μ. This scale drops out when calculating a physical observable like a cross section up to all orders in perturbation theory. However, human lifetime is limited and therefore practical perturbative calculations are performed only up to a certain order.[38] This results in a remaining dependence of the final result on the renormalisation scale. In minimal renormalisation schemes, even parameters like quark masses or coupling constants are scale-dependent. This dependence is described by so-called *renormalisation group equations* (RGEs). In this section we derive and discuss the RGEs of the strong coupling constant and the quark mass in the MS scheme.

G.4.1. Renormalisation group equation for $\alpha_s(\mu)$

The first step is to solve (G.13) for $g_s = g_s(\mu)$. We obtain

$$g_s = \frac{g_{s_0}}{Z_g \mu^\epsilon}. \tag{G.24}$$

Note that the bare coupling g_{s_0} does not depend on the renormalisation scale. Now we can define the *QCD beta function* via

$$\mu \frac{\mathrm{d}g_s}{\mathrm{d}\mu} = \frac{\mathrm{d}g_s}{\mathrm{d}\ln\mu} = \beta(g_s, \epsilon), \tag{G.25}$$

where

$$\beta(g_s, \epsilon) = -\epsilon g_s + \beta(g_s) = -\epsilon g_s - g_s \frac{1}{Z_g}\frac{\mathrm{d}Z_g}{\mathrm{d}\ln\mu} = -\epsilon g_s - g_s f(g_s). \tag{G.26}$$

The first term proportional to ϵ vanishes in the limit $D \to 4$. In minimal schemes, the QCD beta function has no explicit dependence on the renormalisation scale μ and is independent of any mass. We proceed by applying (G.18) and write

$$f(g_s)Z_g = f(g_s)\left(1 + \frac{Z_{g,1}}{\epsilon} + \frac{Z_{g,2}}{\epsilon^2} + ...\right). \tag{G.27}$$

On the other hand we have

$$
\begin{aligned}
f(g_s)Z_g &= \frac{\mathrm{d}Z_g}{\mathrm{d}\ln\mu} = \mu\frac{\mathrm{d}Z_g}{\mathrm{d}\mu} = \mu\frac{\mathrm{d}g_s}{\mathrm{d}\mu}\frac{\mathrm{d}Z_g}{\mathrm{d}g_s} \\
&= \beta(g_s,\epsilon)\frac{\mathrm{d}Z_g}{\mathrm{d}g_s} = \beta(g_s,\epsilon)\left(\frac{1}{\epsilon}\frac{\mathrm{d}Z_{g,1}}{\mathrm{d}g_s} + \frac{1}{\epsilon^2}\frac{\mathrm{d}Z_{g,2}}{\mathrm{d}g_s} + ...\right).
\end{aligned} \tag{G.28}
$$

Comparing the non-singular terms of (G.27) and (G.28) leads to

$$f(g_s) = -g_s \frac{\mathrm{d}Z_{g,1}}{\mathrm{d}g_s} \tag{G.29}$$

and thus

$$\beta(g_s) = -g_s f(g_s) = g_s^2 \frac{\mathrm{d}Z_{g,1}}{\mathrm{d}g_s} = 2g_s^3 \frac{\mathrm{d}Z_{g,1}}{\mathrm{d}g_s^2}. \tag{G.30}$$

---

[38]To the knowledge of the author, the highest order considered so far is tenth order [281].

This means that in minimal renormalisation schemes the QCD beta function can be directly obtained from the $1/\epsilon$ coefficient of the renormalisation constant Z_g. Up to NLO, this coefficient is given by (G.17) and we readily obtain

$$\beta(g_s) = -\frac{g_s^3}{16\pi^2}\left(\frac{11}{3}N_C - \frac{2}{3}n_f\right) = -\beta_0\frac{g_s^3}{16\pi^2}. \tag{G.31}$$

Note that the higher order corrections contribute to the $1/\epsilon$ coefficient as well. These corrections have been determined up to fourth order in [282] and extended to fifth order very recently [283]. They can be written as

$$\frac{\beta(g_s)}{g_s} = -\beta_0\frac{\alpha_s}{4\pi} - \beta_1\left(\frac{\alpha_s}{4\pi}\right)^2 - \beta_2\left(\frac{\alpha_s}{4\pi}\right)^3 - \beta_3\left(\frac{\alpha_s}{4\pi}\right)^4 - \beta_4\left(\frac{\alpha_s}{4\pi}\right)^5 \tag{G.32}$$

with β_0 as given in (G.31) and

$$\beta_1 = 102 - \frac{38}{3}n_f. \tag{G.33}$$

$$\beta_2 = \frac{2857}{2} - \frac{5033}{18}n_f + \frac{325}{54}n_f^2. \tag{G.34}$$

$$\beta_3 = \frac{149753}{6} + 3564\zeta(3) - \left(\frac{1078361}{162} + \frac{6508}{27}\zeta(3)\right)n_f$$

$$+ \left(\frac{50065}{162} + \frac{6472}{81}\zeta(3)\right)n_f^2 + \frac{1093}{729}n_f^3. \tag{G.35}$$

$$\beta_4 = \frac{8157455}{16} + \frac{621885}{2}\zeta(3) - \frac{88209}{2}\zeta(4) - 288090\zeta(5)$$

$$+ n_f\left(-\frac{336460813}{1944} - \frac{4811164}{81}\zeta(3) + \frac{33935}{6}\zeta(4) + \frac{1358995}{27}\zeta(5)\right)$$

$$+ n_f^2\left(\frac{25960913}{1944} + \frac{698531}{81}\zeta(3) - \frac{10526}{9}\zeta(4) - \frac{381760}{81}\zeta(5)\right)$$

$$+ n_f^3\left(-\frac{630559}{5832} - \frac{48722}{243}\zeta(3) + \frac{1618}{27}\zeta(4) + \frac{460}{9}\zeta(5)\right)$$

$$+ n_f^4\left(\frac{1205}{2916} - \frac{152}{18}\zeta(3)\right). \tag{G.36}$$

To shorten the expressions above, $N_C = 3$ has been explicitly inserted. Moreover,

$$\zeta(x) = \sum_{n=1}^{\infty}\frac{1}{n^x} \tag{G.37}$$

denotes the Riemann zeta function.

We can use the results collected so far to express the running of the strong coupling α_s as

$$\frac{d\alpha_s}{d\ln\mu} = \frac{d\alpha_s}{dg_s}\frac{dg_s}{d\ln\mu} = \frac{g_s}{4\pi}\beta(g_s,\epsilon). \tag{G.38}$$

Restricting ourselves to NLO and performing the physical limit $D \to 4$ leads to

$$\frac{d\alpha_s}{d\ln\mu} = -2\beta_0\frac{\alpha_s^2}{4\pi}. \tag{G.39}$$

We introduce an auxiliary scale $\bar{\mu}$ and solve this differential equation via

$$
\begin{aligned}
\int_{\alpha_s(\bar{\mu})}^{\alpha_s(\mu)} \frac{\mathrm{d}\alpha_s}{\alpha_s^2} &= \frac{-2\beta_0}{4\pi} \int_{\ln\bar{\mu}}^{\ln\mu} \mathrm{d}\ln\mu' \\
\Leftrightarrow \frac{1}{\alpha_s(\mu)} - \frac{1}{\alpha_s(\bar{\mu})} &= \frac{\beta_0}{4\pi} \ln\left(\frac{\mu^2}{\bar{\mu}^2}\right) \\
\Leftrightarrow \frac{\alpha_s(\mu)}{4\pi} &= \frac{1}{\frac{4\pi}{\alpha_s(\bar{\mu})} + \beta_0 \ln\left(\frac{\mu^2}{\bar{\mu}^2}\right)}.
\end{aligned} \tag{G.40}
$$

This result includes two remarkable properties of QCD. For large energies μ the coupling constant becomes small. The theory is perturbative and quarks behave *asymptotically free*. On the other hand, we observe *confinement* for small energies μ, where the coupling constant increases. Within this non-perturbative regime, quarks can not be observed as free particles. We can introduce a scale Λ_{QCD} to signalise the breakdown of perturbation theory. At $\mu = \Lambda_{\mathrm{QCD}}$ the coupling diverges, i.e. we have

$$
\beta_0 \ln\left(\frac{\Lambda_{\mathrm{QCD}}^2}{\bar{\mu}^2}\right) = -\frac{4\pi}{\alpha_s(\bar{\mu})}. \tag{G.41}
$$

We can reinsert this result into (G.40) to eliminate $\bar{\mu}$ and finally obtain the running of the strong coupling constant α_s at NLO.

$$
\frac{\alpha_s(\mu)}{4\pi} = \frac{1}{\beta_0 \ln\left(\frac{\mu^2}{\Lambda_{\mathrm{QCD}}^2}\right)}. \tag{G.42}
$$

G.4.2. Renormalisation group equation for $m_q(\mu)$

We continue with the derivation of the RGE for the quark mass $m_q(\mu)$. All calculation steps are basically analogous to those of the previous subsection. We start by solving (G.10) for $m_q = m_q(\mu)$ and get

$$
m_q = \frac{m_{q0}}{Z_m}. \tag{G.43}
$$

The bare quark mass is scale-independent. We define the *anomalous dimension of the quark mass* $\gamma(g_s)$ via

$$
\mu\frac{\mathrm{d}m_q}{\mathrm{d}\mu} = \frac{\mathrm{d}m_q}{\mathrm{d}\ln\mu} = -\frac{m_q}{Z_m}\frac{\mathrm{d}Z_m}{\mathrm{d}\ln\mu} = -\gamma(g_s)m_q. \tag{G.44}
$$

Next we apply (G.18) again and write

$$
\gamma(g_s)Z_m = \gamma(g_s)\left(1 + \frac{Z_{m,1}}{\epsilon} + \frac{Z_{m,2}}{\epsilon^2} + ...\right). \tag{G.45}
$$

Alternatively we can express this as

$$
\begin{aligned}
\gamma(g_s)Z_m &= \frac{\mathrm{d}Z_m}{\mathrm{d}\ln\mu} = \mu\frac{\mathrm{d}Z_m}{\mathrm{d}\mu} = \mu\frac{\mathrm{d}g_s}{\mathrm{d}\mu}\frac{\mathrm{d}Z_m}{\mathrm{d}g_s} \\
&= \beta(g_s,\epsilon)\frac{\mathrm{d}Z_m}{\mathrm{d}g_s} = \beta(g_s,\epsilon)\left(\frac{1}{\epsilon}\frac{\mathrm{d}Z_{m,1}}{\mathrm{d}g_s} + \frac{1}{\epsilon^2}\frac{\mathrm{d}Z_{m,2}}{\mathrm{d}g_s} + ...\right). \tag{G.46}
\end{aligned}
$$

Comparing the non-singular terms of (G.45) and (G.46) leads to

$$\gamma(g_s) = -g_s \frac{\mathrm{d}Z_{m,1}}{\mathrm{d}g_s} = -2g_s^2 \frac{\mathrm{d}Z_{m,1}}{\mathrm{d}g_s^2}. \tag{G.47}$$

We insert the divergent part at NLO as given in (G.16) and get

$$\gamma(g_s) = \frac{6g_s^2}{16\pi^2} C_F = \gamma_0 \frac{\alpha_s}{4\pi}. \tag{G.48}$$

As stressed before, the anomalous dimension of the quark mass depends only on the strong coupling constant if we are working in the MS scheme. We also list the available higher order corrections to the anomalous dimension of the quark mass. They can be written as

$$\gamma(g_s) = \gamma_0 \frac{\alpha_s}{4\pi} + \gamma_1 \left(\frac{\alpha_s}{4\pi}\right)^2 + \gamma_2 \left(\frac{\alpha_s}{4\pi}\right)^3 + \gamma_3 \left(\frac{\alpha_s}{4\pi}\right)^4, \tag{G.49}$$

where γ_0 is given by (G.48) and

$$\gamma_1 = \frac{404}{3} - \frac{40}{9} n_f. \tag{G.50}$$

$$\gamma_2 = 2498 - \left(\frac{4432}{27} + \frac{320}{3}\zeta(3)\right) n_f - \frac{280}{81} n_f^2. \tag{G.51}$$

$$\begin{aligned}
\gamma_3 &= \frac{4603055}{81} + \frac{271360}{27}\zeta(3) - 17600\zeta(5) \\
&\quad + \left(-\frac{183446}{27} - \frac{68384}{9}\zeta(3) + 1760\zeta(4) + \frac{36800}{9}\zeta(5)\right) n_f \\
&\quad + \left(\frac{10484}{243} + \frac{1600}{9}\zeta(3) - \frac{320}{3}\zeta(4)\right) n_f^2 + \left(-\frac{664}{243} + \frac{128}{27}\zeta(3)\right) n_f^3. \tag{G.52}
\end{aligned}$$

To shorten the expressions above, $N_C = 3$ and $C_F = 4/3$ have been inserted explicitly. We can finally derive the running of the quark mass from a given scale $\bar{\mu}$ to another scale μ by solving the differential equation

$$\frac{\mathrm{d}m_q}{\mathrm{d}\ln\mu} = \frac{\mathrm{d}m_q}{\mathrm{d}g_s} \frac{\mathrm{d}g_s}{\mathrm{d}\ln\mu} = \frac{\mathrm{d}m_q}{\mathrm{d}g_s} \beta(g_s,\epsilon) = -\gamma(g_s)m_q. \tag{G.53}$$

We restrict ourselves to NLO and $D = 4$, which leads to

$$\begin{aligned}
\int_{m_q(\bar{\mu})}^{m_q(\mu)} \frac{\mathrm{d}m_q}{m_q} &= -\int_{g_s(\bar{\mu})}^{g_s(\mu)} \mathrm{d}g_s' \frac{\gamma(g_s')}{\beta(g_s')} = \int_{g_s(\bar{\mu})}^{g_s(\mu)} \mathrm{d}g_s' \frac{\gamma_0}{\beta_0 g_s'} \\
\Leftrightarrow \ln\left(\frac{m_q(\mu)}{m_q(\bar{\mu})}\right) &= \frac{\gamma_0}{\beta_0} \ln\left(\frac{g_s(\mu)}{g_s(\bar{\mu})}\right) \\
\Leftrightarrow m_q(\mu) &= m_q(\bar{\mu}) \left(\frac{\alpha_s(\mu)}{\alpha_s(\bar{\mu})}\right)^{\frac{\gamma_0}{2\beta_0}}. \tag{G.54}
\end{aligned}$$

Hence, the QCD running of the quark mass is directly linked to the running of the strong coupling constant.

G.5. DM@NLO renormalisation scheme

In this section we describe the renormalisation scheme concretely implemented in DM@NLO, a hybrid on-shell/$\overline{\text{DR}}$ scheme optimised for the treatment of neutralino-stop coannihilation processes, which has proven reliable for many other situations as well. In particular, we stick to this scheme when calculating the neutralino-nucleon cross sections. More details on this scheme can be found in [62, 148, 149].

G.5.1. Quark sector

We start with the discussion of the quark sector, where we have to renormalise two parameters: The quark spinor fields and the quark masses. This is done via multiplicative renormalisation, i.e. by replacing the bare parameters according to

$$m_{q_0} \to Z_m m_q = m_q + \delta m_q \quad \text{and} \quad q_0 \to \sqrt{Z_q} q = (1 + \frac{1}{2} \delta Z_q) q. \tag{G.55}$$

The quark spinor fields are renormalised on-shell. We require the external quark propagators to have unit residue even at one-loop order. In our notation this precisely corresponds to

$$\lim_{p^2 \to m_q^2} \frac{1}{\not{p} - m_q} \Gamma^{\bar{q}q}(p) u(p) \overset{!}{=} i u(p) \tag{G.56}$$

and thus

$$\delta Z_q = -\Pi_V^{\bar{q}q}(p)\Big|_{p^2 = m_q^2} - 2m_q^2 \left(\frac{\partial \Pi_V^{\bar{q}q}(p)}{\partial p^2}\Big|_{p^2 = m_q^2} + \frac{\partial \Pi_S^{\bar{q}q}(p)}{\partial p^2}\Big|_{p^2 = m_q^2} \right). \tag{G.57}$$

The mass of the top quark is directly measurable in experiments. Hence, it seems plausible to use the physical on-shell mass $m_t = m_t^{\text{OS}} = 173.1$ GeV in our calculations and to renormalise the top quark mass in the on-shell scheme via

$$\frac{\delta m_t^{\text{OS}}}{m_t} = \Pi_V^{\bar{q}q}(p)\Big|_{p^2 = m_t^2} + \Pi_S^{\bar{q}q}(p)\Big|_{p^2 = m_t^2}. \tag{G.58}$$

In contrast, all other quarks are rather light and may form bound states. Their masses are not directly measurable. Therefore, we renormalise all other quark masses in the $\overline{\text{DR}}$ scheme. Their counterterms are given by

$$\frac{\delta m_q^{\overline{\text{DR}}}}{m_q^{\overline{\text{DR}}}} = -2 \frac{\alpha_s C_F}{4\pi} \Delta. \tag{G.59}$$

In comparison to (G.16) we have absorbed the whole factor Δ as given in (G.19) in the mass counterterm. Moreover, the prefactor of -3 has turned into -2. The reason is that we have switched from a pure Standard Model to a SUSY calculation, where an additional propagator correction involving a gluino and a squark occurs.

We import the $\overline{\text{DR}}$ masses of the quarks of the first two generations from microMEGAs. In contrast, the $\overline{\text{DR}}$ mass of the bottom quark is calculated by our code. This calculation is performed in three subsequent steps via

$$m_b^{\overline{\text{MS}},\text{SM}}(m_b) \underset{\text{Running}}{\longrightarrow} m_b^{\overline{\text{MS}},\text{SM}}(\mu) \underset{\text{Conversion}}{\longrightarrow} m_b^{\overline{\text{DR}},\text{SM}}(\mu) \underset{\text{Correction}}{\longrightarrow} m_b^{\overline{\text{DR}},\text{MSSM}}(\mu). \tag{G.60}$$
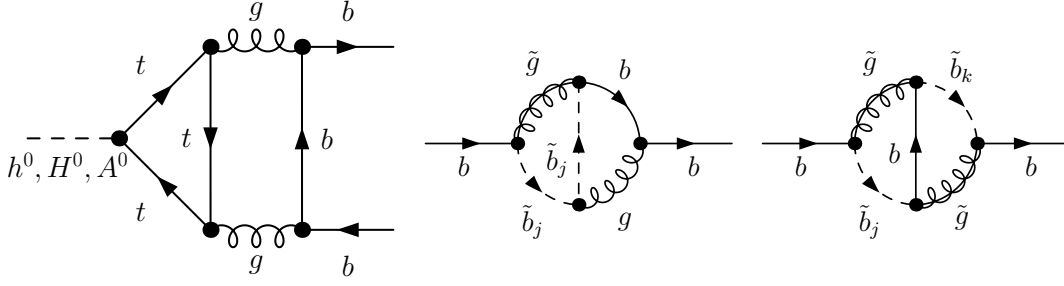
Figure G.3.: Example diagrams contributing to $\Delta_{\phi t}$ (left) and Δ_b (middle and right)

We start with the bottom mass defined at its own scale m_b within the $\overline{\text{MS}}$ scheme and the Standard Model. This parameter is obtained from an analysis of Υ sum rules and transformed to an arbitrary scale μ by RGE running at next-to-next-to-leading order. Afterwards we convert the result from the $\overline{\text{MS}}$ to the $\overline{\text{DR}}$ scheme. In the last step we add so-called threshold corrections which incorporate additional SUSY contributions. More details on the individual steps of this calculation can be found in [284–288].

The bottom quark mass enters the Yukawa coupling to Higgs bosons. This coupling has been studied intensively and Standard Model corrections up to $\mathcal{O}(\alpha_s^4)$ have been determined. We include them by rewriting the Higgs-bottom couplings $g_{\phi bb}$ with $\phi = h^0, H^0, A^0$ as follows:

$$g_{h^0 bb} \rightarrow \frac{g_{h^0 bb}}{1 + \Delta_b} \left(1 - \frac{\Delta_b}{\tan \alpha \tan \beta}\right) \sqrt{1 + \Delta_{\text{QCD}} + \Delta_{h^0 t}}. \tag{G.61}$$

$$g_{H^0 bb} \rightarrow \frac{g_{H^0 bb}}{1 + \Delta_b} \left(1 + \frac{\Delta_b \tan \alpha}{\tan \beta}\right) \sqrt{1 + \Delta_{\text{QCD}} + \Delta_{H^0 t}}. \tag{G.62}$$

$$g_{A^0 bb} \rightarrow \frac{g_{A^0 bb}}{1 + \Delta_b} \left(1 - \frac{\Delta_b}{\tan^2 \beta}\right) \sqrt{1 + \Delta_{\text{QCD}} + \Delta_{A^0 t}}. \tag{G.63}$$

The angles α and β are introduced in subsection 2.4.1 and Δ_{QCD} denotes finite QCD corrections which are not included in the running [289, 290]. They are explicitly given by

$$\begin{aligned} \Delta_{\text{QCD}} &= \frac{\alpha_s}{\pi} \frac{17}{3} + \left(\frac{\alpha_s}{\pi}\right)^2 (35.94 - 1.359 n_f) + \left(\frac{\alpha_s}{\pi}\right)^3 (164.14 - 25.77 n_f + 0.259 n_f^2) \\ &+ \left(\frac{\alpha_s}{\pi}\right)^4 (39.34 - 220.9 n_f + 9.685 n_f^2 - 0.0205 n_f^3). \end{aligned} \tag{G.64}$$

At $\mathcal{O}(\alpha_s^2)$, we encounter additional corrections induced by top quarks as depicted on the left of figure G.3. These scale-dependent corrections have been calculated in [291] and can be casted into the form

$$\Delta_{h^0 t} = \frac{\alpha_s^2}{\pi^2} \frac{1}{\tan \alpha \tan \beta} \left(1.57 - \frac{2}{3} \ln \frac{\mu^2}{m_t^2} + \frac{1}{9} \ln^2 \frac{m_b^2}{\mu^2}\right). \tag{G.65}$$

$$\Delta_{H^0 t} = \frac{\alpha_s^2}{\pi^2} \frac{\tan \alpha}{\tan \beta} \left(1.57 - \frac{2}{3} \ln \frac{\mu^2}{m_t^2} + \frac{1}{9} \ln^2 \frac{m_b^2}{\mu^2}\right). \tag{G.66}$$

$$\Delta_{A^0 t} = \frac{\alpha_s^2}{\pi^2} \frac{1}{\tan^2 \beta} \left(\frac{23}{6} - \ln \frac{\mu^2}{m_t^2} + \frac{1}{6} \ln^2 \frac{m_b^2}{\mu^2}\right). \tag{G.67}$$

Apart from Standard Model corrections, the Higgs-bottom couplings are also subject to SUSY contributions which are particularly relevant for large $\tan \beta$ or large A_b. We denote

the resummable part of this corrections by Δ_b. Two contributing diagrams are exemplarily shown in the middle and on the right of figure G.3. More details on this resummation can be found in [57, 292–294]. We finally stress that we exclude the $\mathcal{O}(\alpha_s)$ part of the effective Higgs-bottom couplings defined via (G.61) to (G.63) as these contributions are already present in our full NLO calculation and would be double counted otherwise.

G.5.2. Squark sector

We continue with the discussion of the squark sector. In contrast to the quark sector, mixing effects can not be neglected here, which complicates the procedure. We start by multiplicatively renormalising the bare squark mass $m_{\tilde{q}_{i,0}}$ and the bare squark wave function $\tilde{q}_{i,0}$ via

$$m_{\tilde{q}_{i,0}}^2 \rightarrow m_{\tilde{q}_i}^2 + \delta m_{\tilde{q}_i}^2 \quad \text{and} \quad \tilde{q}_{i,0} \rightarrow (\delta_{ij} + \frac{1}{2}\delta Z_{\tilde{q}}^{ij})\tilde{q}_j. \tag{G.68}$$

Analogously to (G.15), the one-particle irreducible two-point function $\Gamma^{\tilde{q}_i^* \tilde{q}_j}(p)$ of the squarks at NLO reads

$$\begin{aligned}
\Gamma^{\tilde{q}_i^* \tilde{q}_j}(p) &= i\delta_{ij}(p^2 - m_{\tilde{q}_i}^2) + i\Pi^{\tilde{q}_i^* \tilde{q}_j}(p) \\
&\quad + \frac{i}{2}(p^2 - m_{\tilde{q}_i}^2)\delta Z_{\tilde{q}}^{ij} + \frac{i}{2}(p^2 - m_{\tilde{q}_j}^2)\delta Z_{\tilde{q}}^{*ji} - i\delta_{ij}\delta m_{\tilde{q}_i}^2,
\end{aligned} \tag{G.69}$$

where $\Pi^{\tilde{q}_i^* \tilde{q}_j}(p)$ denotes the squark self-energy. All squarks are renormalised on-shell and the corresponding renormalisation conditions are given by

$$\Gamma^{\tilde{q}_i^* \tilde{q}_j}(p)\Big|_{p^2 = m_{\tilde{q}_j}^2} \stackrel{!}{=} 0 \quad \text{and} \quad \lim_{p^2 \to m_{\tilde{q}_i}^2} \frac{1}{p^2 - m_{\tilde{q}_i}^2}\Gamma^{\tilde{q}_i^* \tilde{q}_i}(p) \stackrel{!}{=} i. \tag{G.70}$$

These conditions fix the squark masses and squark wave function counterterms to

$$(\delta m_{\tilde{q}_i}^2)^{\mathrm{OS}} = \Pi^{\tilde{q}_i^* \tilde{q}_i}(p)\Big|_{p^2 = m_{\tilde{q}_i}^2}. \tag{G.71}$$

$$\delta Z_{\tilde{q}}^{ij} = \frac{2}{m_{\tilde{q}_i}^2 - m_{\tilde{q}_j}^2}\Pi^{\tilde{q}_i^* \tilde{q}_j}(p)\Big|_{p^2 = m_{\tilde{q}_j}^2} \quad \text{for} \quad i \neq j. \tag{G.72}$$

$$\mathrm{Re}\, \delta Z_{\tilde{q}}^{ii} = -\frac{\partial}{\partial p^2}\Pi^{\tilde{q}_i^* \tilde{q}_i}(p)\Big|_{p^2 = m_{\tilde{q}_i}^2}. \tag{G.73}$$

The next step is to renormalise the trilinear couplings A_q. As all squarks are renormalised on-shell, it seems natural to proceed in the same way here. However, trilinear couplings renormalised in the on-shell scheme are subject to large radiative corrections, whereas a definition in the $\overline{\mathrm{DR}}$ scheme leads to improved perturbative stability [295, 296]. Hence, we renormalise all trilinear couplings in the $\overline{\mathrm{DR}}$ scheme. The associated counterterms can be written as

$$\begin{aligned}
\delta A_q^{\overline{\mathrm{DR}}} &= \frac{1}{m_q}\Big(U_{11}^{\tilde{q}}U_{12}^{\tilde{q}}(\delta m_{\tilde{q}_1}^2)^{\overline{\mathrm{DR}}} + U_{21}^{\tilde{q}}U_{22}^{\tilde{q}}(\delta m_{\tilde{q}_2}^2)^{\overline{\mathrm{DR}}} + (U_{21}^{\tilde{q}}U_{12}^{\tilde{q}} + U_{11}^{\tilde{q}}U_{22}^{\tilde{q}})(m_{\tilde{q}_1}^2 - m_{\tilde{q}_2}^2)\delta\theta_{\tilde{q}}^{\overline{\mathrm{DR}}} \\
&\quad - \frac{\delta m_q^{\overline{\mathrm{DR}}}}{m_q}(U_{11}^{\tilde{q}}U_{12}^{\tilde{q}}m_{\tilde{q}_1}^2 + U_{21}^{\tilde{q}}U_{22}^{\tilde{q}}m_{\tilde{q}_2}^2)\Big).
\end{aligned} \tag{G.74}$$

The quark mass counterterm appearing above is given by (G.59). Furthermore, we need the $\overline{\text{DR}}$ squark mass and squark mixing angle counterterms which read

$$
\begin{aligned}
(\delta m_{\tilde{q}_i}^2)^{\overline{\text{DR}}} &= \frac{\alpha_s C_F}{4\pi} \Delta \Bigg(\left((U_{i1}^{\tilde{q}})^2 - (U_{i2}^{\tilde{q}})^2 \right)^2 m_{\tilde{q}_i}^2 - m_{\tilde{q}_i}^2 + (U_{21}^{\tilde{q}} U_{11}^{\tilde{q}} - U_{22}^{\tilde{q}} U_{12}^{\tilde{q}})^2 m_{\tilde{q}_j}^2 \\
&\quad + 8 m_q m_{\tilde{g}} U_{i1}^{\tilde{q}} U_{i2}^{\tilde{q}} - 4 m_{\tilde{g}}^2 - 4 m_q^2 \Bigg) \quad \text{for} \quad j \overset{!}{\neq} i.
\end{aligned}
\tag{G.75}
$$

$$
\begin{aligned}
\delta\theta_{\tilde{q}}^{\overline{\text{DR}}} &= \frac{\alpha_s C_F}{4\pi} \Delta \frac{1}{m_{\tilde{q}_1}^2 - m_{\tilde{q}_2}^2} \Bigg((U_{21}^{\tilde{q}} U_{11}^{\tilde{q}} - U_{22}^{\tilde{q}} U_{12}^{\tilde{q}}) \left(\left((U_{11}^{\tilde{q}})^2 - (U_{12}^{\tilde{q}})^2 \right)^2 m_{\tilde{q}_1}^2 \right. \\
&\quad + \left. \left((U_{21}^{\tilde{q}})^2 - (U_{22}^{\tilde{q}})^2 \right)^2 m_{\tilde{q}_2}^2 \right) + 4 m_{\tilde{g}} m_q (U_{11}^{\tilde{q}} U_{22}^{\tilde{q}} + U_{12}^{\tilde{q}} U_{21}^{\tilde{q}}) \Bigg).
\end{aligned}
\tag{G.76}
$$

We also encounter the squark mixing matrix $U^{\tilde{q}}$ introduced in subsection 2.4.3 and defined by (2.53). Remember that we have included counterterms $\delta U_{ij}^{\tilde{q}}$ in the vertex counterterms VC3 and VC4 (cf. subsection 4.4.4). The individual components $U_{ij}^{\tilde{q}}$ can be considered as functions of other renormalised parameters – in this case $m_{\tilde{q}_1}^2$, $m_{\tilde{q}_2}^2$, m_q and A_q. To obtain the counterterms $\delta U_{ij}^{\tilde{q}}$ we have to perform the expansion

$$
\delta U_{ij}^{\tilde{q}} = \frac{\partial U_{ij}^{\tilde{q}}}{\partial m_{\tilde{q}_1}^2} \delta m_{\tilde{q}_1}^2 + \frac{\partial U_{ij}^{\tilde{q}}}{\partial m_{\tilde{q}_2}^2} \delta m_{\tilde{q}_2}^2 + \frac{\partial U_{ij}^{\tilde{q}}}{\partial m_q} \delta m_q + \frac{\partial U_{ij}^{\tilde{q}}}{\partial A_q} \delta A_q.
\tag{G.77}
$$

A final complication is due to the fact that not all parameters studied so far can be treated independently. This is of particular importance for the third generation involving massive quarks. The associated stop and sbottom sector includes eleven parameters, namely $m_{\tilde{b}_1}^2$, $m_{\tilde{b}_2}^2$, $m_{\tilde{t}_1}^2$, $m_{\tilde{t}_2}^2$, A_b, A_t, $\theta_{\tilde{t}}$, $\theta_{\tilde{b}}$ and the soft SUSY breaking parameters $M_{\tilde{q}_3}^2$, $M_{\tilde{d}_3}^2$, $M_{\tilde{u}_3}^2$ of the third generation (cf. chapter 2). Only five out of these eleven parameters can be chosen freely. We define $(m_{\tilde{t}_1}^2)^{\text{OS}}$, $(m_{\tilde{b}_1}^2)^{\text{OS}}$, $(m_{\tilde{b}_2}^2)^{\text{OS}}$, $A_t^{\overline{\text{DR}}}$ and $A_b^{\overline{\text{DR}}}$ as independent input parameters and $m_{\tilde{t}_2}^2$, $\theta_{\tilde{t}}$, $\theta_{\tilde{b}}$, $M_{\tilde{q}_3}^2$, $M_{\tilde{d}_3}^2$ and $M_{\tilde{u}_3}^2$ as dependent parameters. The counterterms of the independent parameters are given by (G.71) and (G.74), respectively. However, we also need the counterterms of the dependent parameters $m_{\tilde{t}_2}^2$, $\theta_{\tilde{t}}$ and $\theta_{\tilde{b}}$. These can be expressed in terms of already given quantities by

$$
\delta\theta_{\tilde{q}} = \frac{\delta m_q (A_q - \mu(\tan\beta)^{-2I_3}) + m_q \delta A_q - U_{11}^{\tilde{q}} U_{12}^{\tilde{q}} (\delta m_{\tilde{q}_1}^2 - \delta m_{\tilde{q}_2}^2)}{(U_{21}^{\tilde{q}} U_{12}^{\tilde{q}} + U_{11}^{\tilde{q}} U_{22}^{\tilde{q}})(m_{\tilde{q}_1}^2 - m_{\tilde{q}_2}^2)}
\tag{G.78}
$$

and

$$
\begin{aligned}
\delta m_{\tilde{t}_2}^2 &= \frac{1}{U_{21}^{\tilde{t}} U_{12}^{\tilde{t}}} \Bigg((U_{21}^{\tilde{t}} U_{12}^{\tilde{t}} + U_{11}^{\tilde{t}} U_{22}^{\tilde{t}}) \Big((U_{11}^{\tilde{b}})^2 \delta m_{\tilde{b}_1}^2 + (U_{21}^{\tilde{b}})^2 \delta m_{\tilde{b}_2}^2 - 2 m_b \delta m_b \\
&\quad + 2 m_t \delta m_t + 2 U_{11}^{\tilde{b}} U_{21}^{\tilde{b}} (m_{\tilde{b}_1}^2 - m_{\tilde{b}_2}^2) \delta\theta_{\tilde{b}} - (U_{11}^{\tilde{t}})^2 \delta m_{\tilde{t}_1}^2 \Big) \\
&\quad - 2 U_{11}^{\tilde{t}} U_{21}^{\tilde{t}} \Big(\delta m_t (A_t - \mu/\tan\beta) + m_t \delta A_t - U_{11}^{\tilde{t}} U_{12}^{\tilde{t}} \delta m_{\tilde{t}_1}^2 \Big) \Bigg).
\end{aligned}
\tag{G.79}
$$

Note that we use (G.78) only for $\tilde{q} = \tilde{t}, \tilde{b}$. In all other cases we stick to (G.76).

G.5.3. Gluon sector

Our renormalisation scheme includes the renormalisation of the gluon field A^μ and the strong coupling constant g_s as well. The corresponding counterterms are relevant for processes with a gluon in the final state as e.g. $\tilde{\chi}_1^0 \tilde{t}_1 \to tg$ but absent in all calculations presented in this thesis. Hence, we simply refer to [62] for more details on this part of the DM@NLO renormalisation scheme.

All that remains is to detail our implementation of the strong coupling constant and its associated RGE running. The value of α_s defined in the $\overline{\text{DR}}$ scheme and within the MSSM with $n_f = 6$ active flavours at a scale μ is obtained by three subsequent steps which are somewhat similar to (G.60) and read

$$
\alpha_s^{\overline{\text{MS}},\text{SM},n_f=5}(m_{Z^0}) \xrightarrow[\text{Running}]{} \alpha_s^{\overline{\text{MS}},\text{SM},n_f=5}(\mu) \xrightarrow[\text{Conversion}]{} \alpha_s^{\overline{\text{DR}},\text{SM},n_f=5}(\mu)
$$
$$
\xrightarrow[\text{Correction}]{} \alpha_s^{\overline{\text{DR}},\text{MSSM},n_f=6}(\mu). \tag{G.80}
$$

Following the usual convention, we start with α_s defined in the $\overline{\text{MS}}$ scheme and within the Standard Model with $n_f = 5$ active flavours at a scale m_{Z^0}. This value is extracted from experimental data. The first step is to transform this value to an arbitrary scale μ by RGE running at $\mathcal{O}(\alpha_s^3)$, i.e. by applying (G.32). Afterwards we convert α_s from the $\overline{\text{MS}}$ to the $\overline{\text{DR}}$ scheme. This happens at a fixed scale and for a fixed number of flavours. According to [297], the two-loop relation between $\alpha_s^{\overline{\text{MS}}}$ and $\alpha_s^{\overline{\text{DR}}}$ is given by

$$
\alpha_s^{\overline{\text{DR}}} = \alpha_s^{\overline{\text{MS}}} \left(1 + \frac{\alpha_s^{\overline{\text{MS}}}}{4\pi} + \left(\frac{\alpha_s^{\overline{\text{MS}}}}{4\pi} \right)^2 (22 - C_F n_f) \right). \tag{G.81}
$$

The last step is to transfer this result into the MSSM and include the existence of additional heavy coloured particles. We add the effects stemming from the top quark simultaneously, i.e we also shift from $n_f = 5$ to $n_f = 6$ at this place. More details on this last step can be found in [298].

H. Effective field theory

In chapter 4 we have calculated the neutralino direct detection rate within the MSSM including corrections up to $\mathcal{O}(\alpha_s)$ to the leading four-fermion operators. The calculations were performed in a pragmatic and pedagogic fashion. This chapter shall illustrate the underlying *effective field theory* (EFT) formalism itself in more detail. Therein we closely follow the recommendable review [238]. Other mentionable references include the very recent EFT textbook [299] and the more qualitative EFT introductions [300] and [301].

H.1. Basic idea of effective field theory

In contrast to a full theory – which should be valid at any energy scale – the corresponding effective field theory is only valid in a certain regime of energy. This is usually characterised by some scale Λ. If the typical process energy E is much smaller than Λ, we can construct an effective field theory which approximates the full theory in this energy regime.

Let us illustrate this by a concrete example, namely the beta decay. This decay process is depicted in figure H.1. The left diagram corresponds to the modern interpretation in terms of the electroweak Standard Model, the full theory in this example. Here the electroweak force is mediated by a $W^\pm$ gauge boson. The historic predecessor is the Fermi theory, the corresponding effective theory. The diagrammatic interpretation of the beta decay in terms of this theory is depicted on the right of figure H.1. The force mediation is contracted to a point, the $W^\pm$ boson is gone and we are left with a four-fermion interaction. The characteristic scale of the process is given by $\Lambda \sim m_{W^\pm} \sim 80$ GeV, whereas typical mesonic decay energies are around $E \sim 2\text{-}5$ GeV. Hence, we have $E < \Lambda$.

What exactly is happening when contracting the diagram to a point? We say that the heavy mediator gets *integrated out.* The electroweak Standard Model includes all the known elementary particles as degrees of freedom. However, interactions including heavy particles like t, Z^0 or $W^\pm$ are extremely short ranged. In the Fermi theory this range is effectively set to zero. Heavy particles are not degrees of freedom of the theory anymore.

H.2. Operator product expansion

After presenting the general idea of effective field theories in the previous section, we turn to a bit more formal view. Let us begin by writing down the amplitude of the beta decay in the full theory and expand it in the transferred momentum k

$$
\begin{aligned}
i\mathcal{M} &= \left[\frac{ig_w \cos\theta_c}{2\sqrt{2}}\bar{u}\gamma_\mu(\mathbb{1}-\gamma_5)d\right]\frac{-ig^{\mu\nu}}{k^2 - m_{W^\pm}^2}\left[\frac{ig_w}{2\sqrt{2}}\bar{e}\gamma_\nu(\mathbb{1}-\gamma_5)\nu_e\right] \\
\Leftrightarrow \mathcal{M} &= -\frac{G_F}{\sqrt{2}}\cos\theta_c[\bar{u}\gamma_\mu(\mathbb{1}-\gamma_5)d][\bar{e}\gamma^\mu(\mathbb{1}-\gamma_5)\nu_e] + \mathcal{O}(k^2/m_{W^\pm}^2).
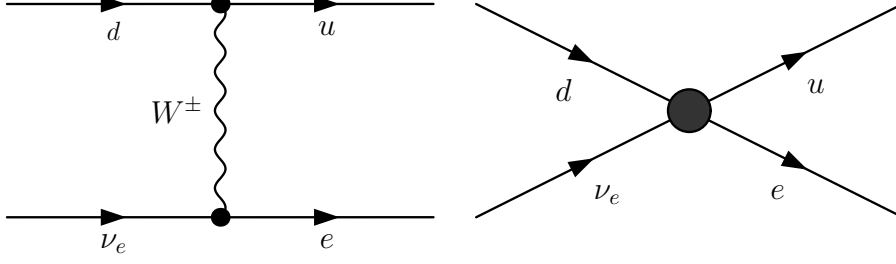\end{aligned} \tag{H.1}
$$

Figure H.1.: Diagrammatic representation of the beta decay within the electroweak Standard Model (left) and the Fermi theory (right)

Here we have introduced the Fermi constant

$$G_F = \frac{\sqrt{2}g_w^2}{8m_{W^\pm}^2} \tag{H.2}$$

and the Cabibbo angle θ_c, which takes into account flavour changing effects. The leading term in this expansion is nothing but the *effective Lagrangian* of the Fermi theory

$$\mathcal{L}_{\text{eff}} = -\frac{G_F}{\sqrt{2}} \cos\theta_c [\bar{u}\gamma_\mu(\mathbb{1} - \gamma_5)d][\bar{e}\gamma^\mu(\mathbb{1} - \gamma_5)\nu_e]. \tag{H.3}$$

We interpret this effective Lagrangian as a product of a coupling constant or so-called *Wilson coefficient C* times a point-like vertex or *effective operator Q*. In this case we have $C = -\frac{G_F}{\sqrt{2}}\cos\theta_c$ and $Q = [\bar{u}\gamma_\mu(\mathbb{1} - \gamma_5)d][\bar{e}\gamma^\mu(\mathbb{1} - \gamma_5)\nu_e]$. Note that the effective operator is non-renormalisable as its mass dimension is six. In general, any effective Lagrangian can be written as a sum of these products which is called an *operator product expansion* (OPE) [302, 303].

$$\mathcal{L}_{\text{eff}} = \sum_i C_i Q_i. \tag{H.4}$$

Neglecting higher order terms in the momentum expansion of the amplitude in (H.1) corresponds to neglecting *higher dimensional operators*, which typically include derivatives, in the effective Lagrangian in (H.3). Hence, the OPE can be understood as a systematic approximation scheme for low energies. The complete, i.e. infinite OPE series including all effective operators corresponding to all orders in $k^2/m_{W^\pm}^2$ is equivalent to the full theory.[39]

It is important to note that the Wilson coefficients contain all the information about the high energy regime and corresponding short distance effects of the full theory, whereas the effective operators are responsible for the low energy regime and corresponding long distance effects. In the example of the beta decay, the Wilson coefficient includes the mass of the heavy mediator as a remnant of the high energy regime. On the other hand, the effective operator consists of spinor fields of light quarks and leptons, which are still degrees of freedom in the low energy regime.

So far we have considered the beta decay only at tree-level. However, one may also calculate electroweak or strong corrections to this process. These corrections lead to more complicated contributions to the Wilson coefficients which – unlike the bare tree-level coefficient – depend on some (renormalisation) scale μ in general. For this reason, we have

---

[39]A formal investigation of this equivalence can be found in [304].

to replace C_i by $C_i(\mu)$, leading to a scale-dependent effective Lagrangian. Now remember that the effective Lagrangian is directly connected to an amplitude of the full theory. This amplitude can be used to compute physical observables like cross sections which have to be scale-independent. Hence, we seem to miss something.

The solution to this dilemma is that the amplitude and therefore the effective Lagrangian as a whole has to be scale-independent but not necessarily its individual components. This is precisely what is happening in effective field theory. Not only the Wilson coefficients but also the effective operators become scale-dependent when including higher order corrections. We have

$$\mathcal{L}_{\text{eff}} = \sum_i C_i(\mu) Q_i(\mu), \tag{H.5}$$

where the scale dependence of the coefficients is inverse to the scale dependence of the effective operators and thus cancels in the product.

The choice of μ corresponds to defining our high and low energy regimes. This is an essential feature of the OPE: We can split the procedure into two distinct parts. The high energy and hence perturbative calculation of the Wilson coefficients on the one hand and the low energy and hence non-perturbative or experimental determination of the effective operators and their matrix elements on the other hand.

H.3. Typical steps of an effective field theory calculation

Having set up the fundamentals in the previous section, we show how a typical calculation in the EFT framework is performed. Such a calculation can usually be divided in four steps. To illustrate these four steps, we refer back to our example of the beta decay.

H.3.1. Setting up the effective field theory

We identify the characteristic scale of the process Λ and choose a lower scale μ_{low} which separates the high and low energy regime. Afterwards we determine the relevant remaining degrees of freedom in the low energy regime and write down the corresponding effective operators accompanied by yet unknown Wilson coefficients. By doing this, we have set up our effective field theory. This first step can be rather simple.

In case of the beta decay, the characteristic scale of the process is given by the mass of the $W^{\pm}$ boson, we have $\Lambda \sim m_{W^{\pm}} \sim 80$ GeV, whereas the low scale should match typical process energies. Hence, we choose $\mu_{\text{low}} \sim E \sim$ 2-5 GeV. The leptons and light quarks remain degrees of freedom in the low energy regime but the $W^{\pm}$ boson does not and we integrate it out. The effective Lagrangian consists of a single term and reads

$$\mathcal{L}_{\text{eff}} = CQ = C[\bar{u}\gamma_\mu(\mathbb{1} - \gamma_5)d][\bar{e}\gamma^\mu(\mathbb{1} - \gamma_5)\nu_e]. \tag{H.6}$$

H.3.2. Matching of full and effective theory

The goal of the second step is to determine the Wilson coefficients. This is done in the *matching* procedure. We require that the effective theory reproduces the full theory at the scale Λ. More precisely, we write down the amplitude of the considered process at the

scale Λ in both the full and the effective theory and require that they equal each other. This so-called matching condition fixes the Wilson coefficients.[40]

$$\mathcal{M}_{\text{full}}(\Lambda) \overset{!}{=} \mathcal{M}_{\text{eff}}(\Lambda). \tag{H.7}$$

In case of the beta decay, the matching calculation is rather trivial. The comparison of the amplitude of the full theory with the amplitude of the effective theory determines the sole Wilson coefficient to $C = -\frac{G_F}{\sqrt{2}}\cos\theta_c$. Usually more than one effective operator and related Wilson coefficient is involved in the matching procedure, but the basic idea remains unchanged.

However, some care is needed when including radiative corrections. The crucial point is that one has to include radiative corrections up to the desired order in perturbation theory also in the effective theory, provided that the respective virtual particles are still degrees of freedom. This means that e.g. a weak correction to the beta decay consisting of an additional Z^0 boson exchange occurs only in the full theory and has no counterpart in the effective theory as the heavy Z^0 boson is not a degree of freedom of the EFT. In contrast to that, a strong correction consisting of an additional gluon exchange occurs also in the effective theory as the massless gluon remains a degree of freedom.

This brings us to another essential feature of the EFT formalism. Processes involving massless virtual particles like the aforementioned gluons may give rise to infrared divergences (cf. section F.1). However, as the EFT has the same degrees of freedom as the full theory in the low energy regime via construction, the very same divergences occur when calculating the corresponding radiative corrections in the EFT. Provided that the infrared divergences are properly regularised in both cases, they cancel in the process of matching. This allows for valuable checks of the matching calculation.

H.3.3. Running of operators and Wilson coefficients

The next step consists of the evolution of the Wilson coefficients from the high scale $\mu_{\text{high}} \sim \Lambda$ down to the low scale $\mu_{\text{low}} \sim E$. The matching procedure described above determines the Wilson coefficients at the high scale Λ. However, we are interested in results valid at typical process energies E. Hence, we have to find and solve the *renormalisation group equations* (cf. section G.4) of the Wilson coefficients. As the scale dependence of the Wilson coefficients has to be inverse to that of the effective operators, this can be done indirectly by calculating the anomalous dimension of the operators, determining their scale dependence and inverting it.

H.3.4. Determination of the matrix elements

The last step is to determine the hadronic matrix element of the operators. We have to determine the expectation values $\langle Q_i \rangle$ at the low scale μ_{low} for the hadron in consideration. This can either be done via non-perturbative calculation methods like e.g. lattice QCD or via experimental measurement. This part of the procedure often constitutes an important source of uncertainty for the whole calculation.[41]

---

[40]We are performing the matching calculation in the standard, diagrammatic approach. Alternatively one may use functional methods to do so. This is illustrated in [305].

[41]Therein the calculation of the neutralino-nucleon cross sections is no exception – cf. section 4.2 and especially the discussion about $f_{T_s}^N$.

We close this chapter with a remark. We are using effective field theory as a tool to approximate the full theory in the low energy regime, where direct detection takes place. The occuring interactions between quarks and neutralinos are effectively described by point-like interactions with Wilson coefficients derived from the given full theory, the MSSM. Analogously we have used the electroweak Standard Model to derive the effective Lagrangian of the Fermi theory in the beginning of this chapter. However, in practice one also uses EFT the other way round. One may write down an effective Lagrangian to parametrise effects from an unknown full theory. Comparing the predictions of this effective Lagrangian with experimental data allows to constrain its Wilson coefficients and in turn the full theory hiding behind it. This is precisely what is done at the LHC at the moment to put constraints on physics beyond the Standard Model [306–313]. Note that this approach is under debate in the context of dark matter production, where the transferred momentum may be comparable to the mediator mass [314–317]. In this situation so-called *simplified models* are more reliable [318, 319].

Bibliography

[1] Zwicky, Fritz: Die Rotverschiebung von extragalaktischen Nebeln. In: *Helvetica Physica Acta* **VI** (1933), p. 110

[2] Rubin, Vera C. ; Ford Jr., W. K.: Rotation of the Andromeda Nebula from a spectroscopic survey of emission regions. In: *The Astrophysical Journal* **159** (1970), p. 379

[3] Rubin, Vera C. ; Ford Jr., W. K. ; Thonnard, N.: Rotational properties of 21 SC galaxies with a large range of luminosities and radii, from NGC 4605 (R = 4 kpc) to UGC 2885 (R = 122 kpc). In: *Astrophysical Journal* **238** (1980), p. 471

[4] WMAP Collaboration: Nine-year Wilkinson Microwave Anisotropy Probe (WMAP) Observations: Final Maps and Results. In: *The Astrophysical Journal Supplement Series* **208** (2013), p. 20

[5] Planck Collaboration: Planck 2013 results. XVI. Cosmological parameters. In: *Astronomy and Astrophysics* **571** (2013), p. A16

[6] Planck Collaboration: *Planck 2015 results. XIII. Cosmological parameters.* 2015. – `http://arxiv.org/abs/1502.01589`

[7] XENON Collaboration: Dark Matter Results from 225 Live Days of XENON100 Data. In: *Physical Review Letters* **109** (2012), p. 181301

[8] LUX Collaboration: First results from the LUX dark matter experiment at the Sanford Underground Research Facility. In: *Physical Review Letters* **112** (2014), p. 091303

[9] `http://dmnlo.hepforge.org/`

[10] Higgs, Peter: Broken symmetries and the masses of gauge bosons. In: *Physical Review Letters* **13** (1964), p. 508

[11] Drees, Manuel ; Godbole, Rohini M. ; Roy, Probir: *Theory and Phenomenology of Sparticles.* World Scientific, 2004

[12] Drees, Manuel: *An Introduction to Supersymmetry.* 1996. – `http://arxiv.org/abs/hep-ph/9611409`

[13] Martin, Stephen P.: *A Supersymmetry Primer.* 1997. – `http://arxiv.org/abs/hep-ph/9709356`

[14] Aitchison, Ian J. R.: *Supersymmetry and the MSSM: An Elementary Introduction.* 2005. – `https://arxiv.org/abs/hep-ph/0505105`

[15] Wess, Julius ; Zumino, Bruno: Supergauge Transformations in four Dimensions. In: *Nuclear Physics B* **70** (1974), p. 39

[16] Wess, Julius ; Zumino, Bruno: A Lagrangian Model invariant under Supergauge Transformations. In: *Physics Letters B* **49** (1974), p. 52

[17] Miyazawa, Hironari: Baryon Number Changing Currents. In: *Progress of Theoretical Physics* **36** (1966), p. 1266

[18] Gervais, Jean-Loup ; Sakita, Bunji: Field theory interpretation of supergauges in dual modes. In: *Nuclear Physics B* **34** (1971), p. 632

[19] Ramond, Pierre: Dual Theory for Free Fermions. In: *Physical Review D* **3** (1971), p. 2415

[20] Weinberg, Steven: Implications of dynamical symmetry breaking. In: *Physical Review D* **13** (1976), p. 974

[21] Gildener, Eldad ; Weinberg, Steven: Symmetry Breaking and Scalar Bosons. In: *Physical Review D* **13** (1976), p. 3333

[22] Gildener, Eldad: Gauge Symmetry Hierarchies. In: *Physical Review D* **14** (1976), p. 1667

[23] ATLAS Collaboration: Observation of a new particle in the search for the Standard Model Higgs boson with the ATLAS detector at the LHC. In: *Physics Letters B* **716** (2012), p. 1

[24] CMS Collaboration: Observation of a new boson at a mass of 125 GeV with the CMS experiment at the LHC. In: *Physics Letters B* **716** (2012), p. 30

[25] Salam, Abdus: Gauge Unification of Fundamental Forces. In: *Reviews of Modern Physics* **52** (1980), p. 525

[26] Weinberg, Steven: Conceptual Foundations of the Unified Theory of Weak and Electromagnetic Interactions. In: *Reviews of Modern Physics* **52** (1979), p. 515

[27] Georgi, Howard ; Glashow, Sheldon L.: Unity of All Elementary-Particle Forces. In: *Physical Review Letters* **32** (1974), p. 438

[28] Buras, Andrzej J. ; Ellis, Johnathan R. ; Gaillard, Mary K. ; Nanopoulos, Dimitri V.: Aspects of the Grand Unification of Strong, Weak and Electromagnetic Interactions. In: *Nuclear Physics B* **135** (1978), p. 66

[29] Haag, Rudolf ; Łopuszański, Jan ; Sohnius, Martin: All possible generators of supersymmetries of the S-matrix. In: *Nuclear Physics B* **88** (1975), p. 257

[30] Coleman, Sidney ; Mandula, Jeffrey: All Possible Symmetries of the S Matrix. In: *Physical Review D* **159** (1967), p. 1251

[31] Haber, Howard E.: The status of the minimal supersymmetric standard model and beyond. In: *Nuclear Physics B – Proceesings Supplements* **62** (1998), p. 469

[32] Chamseddine, Ali H. ; Arnowitt, Richard L. ; Nath, Pran: Locally Supersymmetric Grand Unification. In: *Physical Review Letters* **49** (1982), p. 970

[33] Barbieri, Riccardo ; Ferrara, Sergio ; Savoy, Carlos A.: Gauge Models with Spontaneously Broken Local Supersymmetry. In: *Physics Letters B* **119** (1982), p. 343

[34] Hall, Lawrence J. ; Lykken, Joseph D. ; Weinberg, Steven: Supergravity as the Messenger of Supersymmetry Breaking. In: *Physical Review D* **27** (1983), p. 2359

[35] Dine, Michael ; Fischler, Willy: A Phenomenological Model of Particle Physics Based on Supersymmetry. In: *Physics Letters B* **110** (1982), p. 227

[36] Nappi, Chiara R. ; Ovrut, Burt A.: Supersymmetric Extension of the $SU(3) \times SU(2) \times U(1)$ Model. In: *Physics Letters B* **113** (1982), p. 175

[37] Nilles, Hans P.: Dynamically broken supergravity and the hierarchy problem. In: *Physics Letters B* **115** (1982), p. 193

[38] Barbier, Remi *et al.*: *R*-parity violating supersymmetry. In: *Physics Reports* **420** (2005), p. 1

[39] Jungman, Gerard ; Kamionkowski, Marc ; Griest, Kim: Supersymmetric Dark Matter. In: *Physics Reports* **267** (1996), p. 195

[40] Djouadi, Abdelhak: The anatomy of electroweak symmetry breaking Tome II: The Higgs bosons in the Minimal Supersymmetric Model. In: *Physics Reports* **459** (2008), p. 1

[41] Nambu, Yoichiro: Quasi-Particles and Gauge Invariance in the Theory of Superconductivity. In: *Physical Review* **117** (1960), p. 648

[42] Goldstone, Jeffrey: Field theories with Superconductor solutions. In: *Il Nuovo Cimento* **19** (1961), p. 154

[43] Goldstone, Jeffrey ; Salam, Abdus ; Weinberg, Steven: Broken Symmetries. In: *Physical Review* **127** (1962), p. 965

[44] Kim, Jihn E. ; Nilles, Hans P.: The mu Problem and the Strong CP Problem. In: *Physics Letters B* **138** (1984), p. 150

[45] Guidice, Gian F. ; Masiero, Antonio: A Natural Solution to the mu Problem in Supergravity Theories. In: *Physics Letters B* **206** (1988), p. 480

[46] Dvali, Georgi R. ; Guidice, Gian F. ; Pomarol, Alex: The mu problem in theories with gauge mediated supersymmetry breaking. In: *Nuclear Physics B* **478** (1996), p. 31

[47] Djouadi, Abdelhak *et al.*: *The Minimal Supersymmetric Standard Model: Group Summary Report.* 1999. – https://arxiv.org/abs/hep-ph/9901246

[48] Bertone, Gianfranco ; Hooper, Dan ; Silk, Joseph: Particle Dark Matter: Evidence, Candidates and Constraints. In: *Physics Reports* **405** (2005), p. 279

[49] EINASTO, Jaan: Dark Matter. In: *Brazilian Journal of Physics* **43** (2013), p. 369

[50] CATENA, Riccardo ; COVI, Laura: SUSY dark matter(s). In: *The European Physical Journal C* **74** (2014), p. 1

[51] KLASEN, Michael ; POHL, Martin ; SIGL, Günter: Indirect and direct search for dark matter. In: *Progress in Particle and Nuclear Physics* **85** (2015), p. 1

[52] BERTONE, Gianfranco (Hrsg.): *Particle Dark Matter*. Cambridge University Press, 2010

[53] HOOPER, Dan: *Dunkle Materie: Die kosmische Energielücke*. Spektrum Akademischer Verlag, 2008

[54] PANEK, Richard: *Das 4%-Universum: Dunkle Energie, dunkle Materie und die Geburt einer neuen Physik*. Carl Hanser Verlag, 2011

[55] BERTONE, Gianfranco: *Behind the Scenes of the Universe: From the Higgs to Dark Matter*. Oxford University Press, 2013

[56] SANDERS, Robert H.: *The dark matter problem: a historical perspective*. Cambridge University Press, 2010

[57] STEPPELER, Patrick: *QCD-Korrekturen zur Annihilation von dunkler Materie im Higgs-Funnel*, Westfälische Wilhelms-Universität Münster, Master thesis, 2013

[58] MCCABE, Christopher: *Aspects of Dark Matter Phenomenology*, University of Oxford, PhD thesis, 2011

[59] KAHLHÖFER, Felix: *Complementarity of Searches for Dark Matter*, University of Oxford, PhD thesis, 2014

[60] BALTZ, Edward A.: *Signatures of Dark Matter*, University of California, PhD thesis, 2000

[61] CALORE, Francesca: *Unveiling Dark Matter through Gamma Rays: Spectral Features, Spatial Signatures and Astrophysical Backgrounds*, Universität Hamburg, PhD thesis, 2013

[62] HARZ, Julia: *Supersymmetric QCD Corrections and Phenomenological Studies in Relation to Coannihilation of Dark Matter*, Universität Hamburg, PhD thesis, 2013

[63] MEINECKE, Moritz: *SUSY-QCD Corrections to the (Co)Annihilation of Neutralino Dark Matter within the MSSM*, Westfälische Wilhelms-Universität Münster, PhD thesis, 2015

[64] LE BOULC'H, Quentin: *Neutralino-stop coannihilation in the MSSM: flavor violation, radiative corrections and their impact on the dark matter relic density*, Université de Grenoble, PhD thesis, 2013

[65] KAPTEYN, Jacobus C.: First Attempt at a Theory of the Arrangement and Motion of the Sidereal System. In: *Astrophysical Journal* **55** (1922), p. 302

[66] JEANS, James H.: The Motions of the Stars in a Kapteyn-Universe. In: *Monthly Notices of the Royal Astronomical Society* **82** (1922), p. 122

[67] OORT, Jan H.: The force exerted by the stellar system in the direction perpendicular to the galactic plane and some related problems. In: *Bulletin of the Astronomical Institutes of the Netherlands* **VI** (1932), p. 249

[68] VAN ALBADA, Tjeerd S. ; BAHCALL, John N. ; BEGEMAN, Kor G. ; SANSCISI, Renzo: Distribution of dark matter in the spiral galaxy NGC 3198. In: *The Astrophysical Journal* **295** (1985), p. 305

[69] CLOWE, Douglas ; BRADAČ, Maruša ; GONZALES, Anthony H. ; MARKEVITCH, Maxim ; RANDALL, Scott W. ; JONES, Christine ; ZARITSK, Dennis: A direct empirical proof of the existence of dark matter. In: *The Astrophysical Journal* **648** (2006), p. L109

[70] http://apod.nasa.gov/apod/ap060824.html

[71] SMOOT, George F. *et al.*: Structure in the COBE differential microwave radiometer first year maps. In: *Astrophysical Journal* **396** (1992), p. L1

[72] http://www.esa.int/spaceinimages/Images/2013/03/Planck_CMB

[73] LIDDLE, Andrew: *An Introduction to Modern Cosmology.* Wiley, 2003

[74] HU, Wayne ; SUGIYAMA, Naoshi ; SILK, Joseph: The physics of microwave background anisotropies. In: *Nature* **386** (1997), p. 37

[75] SAMTLEBEN, Dorothea ; STAGGS, Suzanne ; WINSTEIN, Bruce: The Cosmic Microwave Background for Pedestrians: A Review for Particle and Nuclear Physicists. In: *Annual Review of Nuclear and Particle Science* **57** (2007), p. 245

[76] DURRER, Ruth: The theory of CMB anisotropies. In: *Journal of Physical Studies* **5** (2001), p. 177

[77] SPRINGEL, Volker *et al.*: Simulating the joint evolution of quasars, galaxies and their large-scale distribution. In: *Nature* **435** (2005), p. 629

[78] KLYPIN, Anatoly A. ; TRUJILLO-GOMEZ, Sebastian ; PRIMACK, Joel: Dark matter halos in the standard cosmological model: Results from the Bolshoi simulation. In: *The Astrophysical Journal* **740** (2011), p. 102

[79] NAVARRO, Julio F. ; FRENK, Carlos S. ; WHITE, Simon D. M.: The Structure of Cold Dark Matter Halos. In: *Astrophysical Journal* **462** (1996), p. 563

[80] KLYPIN, Anatoly A. ; KRAVTSOV, Andrey V. ; VALENZUELA, Octavio ; PRADA, Francisco: Where Are the Missing Galacting Satellites? In: *The Astrophysical Journal* **522** (1999), p. 82

[81] MILGROM, Mordehai: A modification of the newtonian dynamics as a possible alternative to the hidden mass hypotheses. In: *The Astrophysical Journal* **270** (1983), p. 365

[82] BEKENSTEIN, Jacob D.: Relativistic gravitation theory for the modified Newtonian dynamics paradigm. In: *Physical Review D* **70** (2004), p. 083509

[83] BEKENSTEIN, Jacob D.: The modified Newtonian dynamics—MOND and its implications for new physics. In: *Contemporary Physics* **47** (2006), p. 387

[84] BEKENSTEIN, Jacob D. ; SANDERS, Robert H.: A primer to Relativistic MOND theory. In: *European Astronomical Society Publications Series* **20** (2006), p. 225

[85] ANGUS, Garry W. ; MCGAUGH, Stacy S.: The collision velocity of the bullet cluster in conventional and modified dynamics. In: *Monthly Notices of the Royal Astronomical Society* **383** (2007), p. 417

[86] EROS-2 KOLLABORATION: Limits on the Macho content of the Galactic Halo from the EROS-2 Survey of the Magellanic Clouds. In: *Astronomy and Astrophysics* **469** (2007), p. 387

[87] HAWKINS, Michael R. S.: A new look at microlensing limits on dark matter in the Galactic halo. In: *Astronomy and Astrophysics* **575** (2015), p. A107

[88] ELLIS, Johnathan R. ; HAGELIN, John S. ; NANOPOULOS, Dimitri V. ; OLIVE, Keith A. ; SREDNICKI, Mark A.: Supersymmetric relics from the big bang. In: *Nuclear Physics B* **238** (1984), p. 453

[89] HEMMICK, Thomas Kenneth *et al.*: Search for low-Z nuclei containing massive stable particles. In: *Physical Review D* **41** (1990), p. 2074

[90] PECCEI, Roberto D. ; QUINN, Helen R.: CP Conservation in the Presence of Pseudoparticles. In: *Physical Review Letters* **38** (1977), p. 1440

[91] DUFFY, Leanne D. ; VAN BIBBER, Karl: Axions as dark matter particles. In: *New Journal of Physics* **11** (2009), p. 105008

[92] VISINELLI, Luca ; GONDOLO, Paolo: Dark matter axions revisited. In: *Physical Review D* **80** (2009), p. 035024

[93] COVI, Laura ; KIM, Jihn E. ; ROSZKOWSKI, Leszek: Axinos as Cold Dark Matter. In: *Physical Review Letters* **82** (1999), p. 4180

[94] COVI, Laura ; KIM, Hang B. ; KIM, Jihn E. ; ROSZKOWSKI, Leszek: Axinos as dark matter. In: *Journal of High Energy Physics* **05** (2001), p. 033

[95] BAER, Howard ; LESSA, Andre ; RAJAGOPALAN, Shibi ; SREETHAWONG, Warintorn: Mixed axion/neutralino cold dark matter in supersymmetric models. In: *Journal of Cosmology and Astroparticle Physics* **06** (2011), p. 031

[96] CIRELLI, Marco ; FORNENGO, Nicolao ; STRUMIA, Alessandro: Minimal dark matter. In: *Nuclear Physics B* **753** (2006), p. 178

[97] LOPEZ HONOREZ, Laura ; NEZRI, Emmanuel ; OLIVER, Josep F. ; TYTGAT, Michel H. G.: The Inert Doublet Model: An Archetype for Dark Matter. In: *Journal of Cosmology and Astroparticle Physics* **02** (2007), p. 028

[98] ESCH, Sonja ; KLASEN, Michael ; YAGUNA, Carlos E.: A minimal model for two-component dark matter. In: *Journal of High Energy Physics* **09** (2014), p. 108

[99] ABE, Tomohiro ; SATO, Ryosuke: *Quantum corrections to the spin-independent cross section of the inert doublet dark matter.* 2015. – http://arxiv.org/abs/1501.04161

[100] IBARRA, Alejandro ; WILD, Sebastian: Dirac dark matter with a charged mediator: a comprehensive one-loop analysis of the direct detection phenomenology. In: *Journal of Cosmology and Astroparticle Physics* **05** (2015), p. 047

[101] HAISCH, Ulrich ; KAHLHÖFER, Felix: On the importance of loop-induced spin-independent interactions for dark matter direct detection. In: *Journal of Cosmology and Astroparticle Physics* **04** (2013), p. 050

[102] BRINGMANN, Torsten ; GALEA, Ahmad J. ; WALIA, Parampreet: Leading QCD corrections for indirect dark matter searches: A fresh look. In: *Physical Review D* **93** (2016), p. 043529

[103] KLASEN, Michael ; KOVAŘÍK, Karol ; STEPPELER, Patrick: *SUSY-QCD corrections for the direct detection of neutralino dark matter and correlations with the relic density.* 2016. – http://arxiv.org/abs/1607.06396

[104] GOODMAN, Mark W. ; WITTEN, Edward: Detectability of certain dark-matter candidates. In: *Physical Review D* **31** (1985), p. 3059

[105] HAHN, Thomas: Generating Feynman diagrams and amplitudes with FeynArts 3. In: *Computer Physics Communications* **140** (2001), p. 418

[106] CoGeNT COLLABORATION: Results from a Search for Light-Mass Dark Matter with a P-type Point Contact Germanium Detector. In: *Physical Review Letters* **106** (2011), p. 131301

[107] DAMA COLLABORATION: First results from DAMA/LIBRA and the combined results with DAMA/NaI. In: *The European Physical Journal C* **C56** (2008), p. 333

[108] SCHWETZ, Thomas ; ZUPAN, Jure: Dark matter attempts for CoGeNT and DAMA. In: *Journal of Cosmology and Astroparticle Physics* **08** (2011), p. 008

[109] DEL NOBILE, Eugenio ; GELMINI, Graciela B. ; GEORGESCU, Andreea ; HUH, Ji-Haeng: Reevaluation of spin-dependent WIMP-proton interactions as an explanation of the DAMA data. In: *Journal of Cosmology and Astroparticle Physics* **08** (2015), p. 046

[110] HOOPER, Dan ; COLLAR, Juan I. ; HALL, Jeter ; MCKINSEY, Dan ; KELSO, Chris: Consistent dark matter interpretation for CoGeNT and DAMA/LIBRA. In: *Physical Review D* **82** (2010), p. 123509

[111] CATENA, Riccardo ; IBARRA, Alejandro ; WILD, Sebastian: DAMA confronts null searches in the effectivy theory of dark matter-nucleon interactions. In: *Journal of Cosmology and Astroparticle Physics* **05** (2016), p. 039

[112] Petersen, Michael S. ; Katz, Neal ; Weinberg, Martin D.: *The Dynamical Response of Dark Matter to Galaxy Evolution Affects Direct-Detection Experiments.* 2016. – http://arxiv.org/abs/1609.01307

[113] Del Nobile, Eugenio ; Gelmini, Graciela B. ; Gondolo, Paolo ; Huh, Ji-Haeng: *Update on the Halo-Independent Comparison of Direct Dark Matter Detection Data.* 2014. – http://arxiv.org/abs/1405.5582

[114] Bozorgnia, Nassim ; Herrero-Garcia, Juan ; Schwetz, Thomas ; Zupan, Jure: Halo-independent methods for inelastic dark matter scattering. In: *Journal of Cosmology and Astroparticle Physics* **07** (2013), p. 049

[115] Blennow, Mattias ; Herrero-Garcia, Juan ; Schwetz, Thomas ; Vogl, Stefan: Halo-independent tests of dark matter direct detection signals: local DM density, LHC, and thermal freeze-out. In: *Journal of Cosmology and Astroparticle Physics* **08** (2015), p. 039

[116] Feldstein, Brian ; Kahlhöfer, Felix: A new halo-independent approach to dark matter direct detection analysis. In: *Journal of Cosmology and Astroparticle Physics* **08** (2014), p. 065

[117] Ferrer, Francesc ; Ibarra, Alejandro ; Wild, Sebastian: A novel approach to derive halo-independent limits on dark matter properties. In: *Journal of Cosmology and Astroparticle Physics* **09** (2015), p. 052

[118] Gelmini, Graciela B. ; Gondolo, Paolo ; Soldatenko, Adrian ; Yaguna, Carlos E.: Direct detection of neutralino dark matter in nonstandard cosmologies. In: *Physical Review D* **76** (2007), p. 015010

[119] Popper, Karl R.: *Logik der Forschung.* Julius Springer Verlag, 1934

[120] Sanders, Robert H.: *Reflections on the direct detection of particle dark matter.* 2013. – http://arxiv.org/abs/1311.1744

[121] Babichev, Eugeny ; Marzola, Luca ; Raidal, Martti ; Schmidt-May, Angnis ; Urban, Federico ; Veermäe, Hardi ; von Strauss, Mikael: *Gravitational Origin of Dark Matter.* 2016. – http://arxiv.org/abs/1604.08564

[122] Bergström, Lars ; Gondolo, Paolo: Limits on direct detection of neutralino dark matter from $b \to s\gamma$ decays. In: *Astroparticle Physics* **5** (1996), p. 263

[123] Gondolo, Paolo ; Edsjö, Joakim ; Ullio, Piero ; Bergström, Lars ; Schelke, Mia ; Baltz, Edward A.: DarkSUSY: Computing supersymmetric dark matter properties numerically. In: *Journal of Cosmology and Astroparticle Physics* **07** (2004), p. 008

[124] http://www.darksusy.org/

[125] Bélanger, Geneviève ; Boudjema, Fawzi ; Pukhov, Alexander ; Semenov, Andrei: Dark matter direct detection rate in a generic model with micrOMEGAs_2.2. In: *Computer Physics Communications* **180** (2009), p. 747

[126] https://lapth.cnrs.fr/micromegas/

[127] SMITH, Martin C. *et al.*: The RAVE Survey: Constraining the Local Galactic Escape Speed. In: *Monthly Notices of the Royal Astronomical Society* **379** (2007), p. 755

[128] LAVALLE, Julien ; MAGNI, Stefano: Making sense of the local Galactic escape speed estimates in direct dark matter searches. In: *Physical Review D* **91** (2014), p. 023510

[129] CIRELLI, Marco ; DEL NOBILE, Eugenio ; PANCI, Paolo: Tools for model-independent bounds in direct dark matter searches. In: *Journal of Cosmology and Astroparticle Physics* **10** (2013), p. 019

[130] VOGELSBERGER, Mark ; HELMI, Amina ; SPRINGEL, Volker ; WHITE, Simon D. M. ; WANG, Jie ; FRENK, Carlos S. ; JENKINS, Adrian ; LUDLOW, Aaron ; NAVARRO, Julio F.: Phase-space structure in the local dark matter distribution and its signature in direct detection experiments. In: *Monthly Notices of the Royal Astronomical Society* **395** (2009), p. 797

[131] GREEN, Anne M.: Dependence of direct detection signals on the WIMP velocity distribution. In: *Journal of Cosmology and Astroparticle Physics* **10** (2010), p. 034

[132] MARCOS, Cristina ; PEIRÓ, Miguel ; ROBLES, Sandra: On the importance of direct detection combined limits for spin independent and spin dependent dark matter interactions. In: *Journal of Cosmology and Astroparticle Physics* **03** (2016), p. 019

[133] RUIZ DE AUSTRI, Roberto ; PEREZ DE LOS HEROZ, Carlos: Impact of nucleon matrix element uncertainties on the interpretation of direct and indirect dark matter search results. In: *Journal of Cosmology and Astroparticle Physics* **11** (2013), p. 049

[134] ELLIS, Johnathan R. ; OLIVE, Keith A. ; SAVAGE, Christopher: Hadronic uncertainties in the elastic scattering of supersymmetric dark matter. In: *Physical Review D* **77** (2008), p. 065026

[135] BOTTINO, Allesandro ; DONATO, Fiorenza ; FORNENGO, Nicolao ; SCOPEL, Stefano: Implications for relic neutralinos of the theoretical uncertainties in the neutralino–nucleon cross section. In: *Astroparticle Physics* **13** (2000), p. 215

[136] CRIVELLIN, Andreas ; HOFERICHTER, Martin ; PROCURA, Massimiliano: Accurate evaluation of hadronic uncertainties in spin-independent WIMP-nucleon scattering: Disentangling two- and three-flavor effects. In: *Physical Review D* **89** (2014), p. 054021

[137] HOFERICHTER, Martin ; RUIZ DE ELVIRA, Jacobo ; KUBIS, Bastian ; MEISSNER, Ulf-G.: High-Precision Determination of the Pion-Nucleon σ Term from Roy-Steiner equations. In: *Physical Review Letters* **115** (2015), p. 092301

[138] JUNNARKAR, Parikshit ; WALKER-LOUD, Andre: The Scalar Strange Content of the Nucleon from Lattice QCD. In: *Physical Review D* **87** (2013), p. 114510

[139] BÉLANGER, Geneviève ; BOUDJEMA, Fawzi ; PUKHOV, Alexander ; SEMENOV, Andrei: microOMEGAs: Version 1.3. In: *Computer Physics Communications* **174** (2006), p. 577

[140] BÉLANGER, Geneviève ; BOUDJEMA, Fawzi ; PUKHOV, Alexander ; SEMENOV, Andrei: microOMEGAs 2.0: A program to calculate the relic density of dark matter in a generic model. In: *Computer Physics Communications* **176** (2007), p. 367

[141] SHIFMAN, Mikhail A. ; VAINSHTEIN, Arkady I. ; ZAKHAROV, Valentine I.: Remarks on Higgs-boson interactions with nucleons. In: *Physics Letters B* **78** (1978), p. 443

[142] ENGEL, Jonathan ; VOGEL, Petr: Spin dependent cross sections of weakly interacting massive particles on nuclei. In: *Physical Review D* **40** (1989), p. 3132

[143] ENGEL, Jonathan ; PITTEL, Stuart ; VOGEL, Petr: Nuclear physics of dark matter detection. In: *International Journal of Modern Physics* **E1** (1992), p. 1

[144] LI, Jinmian ; THOMAS, Anthony W.: Bottom quark contribution to spin-dependent dark matter detection. In: *Nuclear Physics B* **906** (2016), p. 60

[145] SMITH, David ; WEINER, Neal: Inelastic dark matter. In: *Physical Review D* **64** (2001), p. 043502

[146] BARELLO, Gregory ; CHANG, Spencer ; NEWBY, Christopher A.: A model independent approach to inelastic dark matter scattering. In: *Physical Review D* **90** (2014), p. 094027

[147] HERRMANN, Björn ; KLASEN, Michael ; KOVAŘÍK, Karol ; MEINECKE, Moritz ; STEPPELER, Patrick: One-loop corrections to gaugino (co)annihilation into quarks in the MSSM. In: *Physical Review D* **89** (2014), p. 114012

[148] HARZ, Julia ; HERRMANN, Björn ; KLASEN, Michael ; KOVAŘÍK, Karol ; LE BOULC'H, Quentin: Neutralino-stop coannihilation into electroweak gauge and Higgs bosons at one loop. In: *Physical Review D* **87** (2013), p. 054031

[149] HARZ, Julia ; HERRMANN, Björn ; KLASEN, Michael ; KOVAŘÍK, Karol: One-loop corrections to neutralino-stop coannihilation revisited. In: *Physical Review D* **91** (2015), p. 034028

[150] HARZ, Julia ; HERRMANN, Björn ; KLASEN, Michael ; KOVAŘÍK, Karol ; MEINECKE, Moritz: SUSY-QCD corrections to stop annihilation into electroweak final states including Coulomb enhancement effects. In: *Physical Review D* **91** (2015), p. 034012

[151] DREES, Manuel ; NOJIRI, Mihoko M.: New contributions to coherent neutralino-nucleus scattering. In: *Physical Review D* **47** (1993), p. 4226

[152] DREES, Manuel ; NOJIRI, Mihoko M.: Neutralino-nucleon scattering reexamined. In: *Physical Review D* **48** (1993), p. 3483

[153] HISANO, Junji ; NAGAI, Ryo ; NAGATA, Natsumi: Effective theories for dark matter nucleon scattering. In: *Journal of High Energy Physics* **05** (2015), p. 037

[154] HISANO, Junji ; ISHIWATA, Koji ; NAGATA, Natsumi: *QCD Effects on Direct Detection of Wino Dark Matter.* 2015. – `http://arxiv.org/abs/1504.00915`

[155] HISANO, Junji ; ISHIWATA, Koji ; NAGATA, Natsumi: Gluon contribution to dark matter direct detection. In: *Physical Review D* **2010** (2010), p. 115007

[156] HISANO, Junji ; MATSUMOTO, Shigeki ; NOJIRI, Mihoko M. ; SAITO, Osamu: Direct detection of the Wino and Higgsino-like neutralino dark matter at one-loop level. In: *Physical Review D* **71** (2005), p. 015007

[157] HISANO, Junji ; ISHIWATA, Koji ; NAGATA, Natsumi ; TAKESAKO, Tomohiro: Direct Detection of Electroweak-Interacting Dark Matter. In: *Journal of High Energy Physics* **07** (2011), p. 005

[158] BERLIN, Asher ; HOOPER, Dan ; MCDERMOTT, Samuel D.: Dark matter elastic scattering through Higgs loops. In: *Physical Review D* **92** (2015), p. 123531

[159] BERLIN, Asher ; ROBERTSON, Denis S. ; SOLON, Mikhail P. ; ZUREK, Kathryn M.: Bino variations: Effective field theory methods for dark matter direct detection. In: *Physical Review D* **93** (2016), p. 095008

[160] HILL, Richard J. ; SOLON, Mikhail P.: Standard model anatomy of WIMP dark matter direct detection. I. Weak-scale matching. In: *Physical Review D* **91** (2015), p. 043504

[161] MCCABE, Christopher: The Astrophysical Uncertainties Of Dark Matter Direct Detection Experiments. In: *Physical Review D* **82** (2010), p. 023530

[162] GRIEST, Kim: Calculations of Rates for Direct Detection of Neutralino Dark Matter. In: *Physical Review Letters* **61** (1988), p. 666

[163] GRIEST, Kim: Cross-Sections, Relic Abundance and Detection Rates for Neutralino Dark Matter. In: *Physical Review D* **38** (1988), p. 2357

[164] GRIEST, Kim: Erratum: Cross sections, relic abundance, and detection rates for neutralino dark matter. In: *Physical Review D* **39** (1989), p. 3802

[165] GONDOLO, Paolo: *Phenomenological Introduction to Direct Dark Matter Detection.* 1996. – http://arxiv.org/abs/hep-ph/9605290

[166] KOVAŘÍK, Karol: *Hitchhiker's Guide to Renormalization.* 2013. – unpublished

[167] KOVAŘÍK, Karol: *Precise predictions for sfermion pair production at a linear collider*, Comenius University Bratislava, PhD thesis, 2005

[168] DIENES, Keith R. ; KUMAR, Jason ; THOMAS, Brooks ; YAYLALI, David: Overcoming velocity suppression in dark-matter direct-detection experiments. In: *Physical Review D* **90** (2014), p. 015012

[169] KAHLHÖFER, Felix: *Sensitivity of Liquid Xenon Detectors for Low Mass Dark Matter*, Ruprecht-Karls-Universität Heidelberg, Diplomarbeit, 2010

[170] FAN, JiJi ; REECE, Matthew ; WANG, Lian-Tao: Non-relativistic effective theory of dark matter direct detection. In: *Journal of Cosmology and Astroparticle Physics* **11** (2010), p. 042

[171] HILL, Richard J. ; SOLON, Mikhail P.: Standard Model anatomy of WIMP dark matter direct detection. II. QCD analysis and hadronic matrix elements. In: *Physical Review D* **91** (2015), p. 043505

[172] AITCHISON, Ian J. R. ; HEY, Anthony J. G.: *Gauge Theories in Particle Physics.* Vol. I From Relativistic Quantum Mechanics to QED. Taylor & Francis Group, 2003

[173] AITCHISON, Ian J. R. ; HEY, Anthony J. G.: *Gauge Theories in Particle Physics.* Vol. II QCD and the Electroweak Theory. Taylor & Francis Group, 2004

[174] SCHWARTZ, Matthew D.: *Quantum Field Theory and the Standard Model.* Cambridge University Press, 2014

[175] CHANG, Spencer ; PIERCE, Aaron ; WEINER, Neal: Momentum Dependent Dark Matter Scattering. In: *Journal of Cosmology and Astroparticle Physics* **01** (2010), p. 006

[176] CRIVELLIN, Andreas ; HOFERICHTER, Martin ; PROCURA, Massimiliano ; TUNSTALL, Lewis C.: Light stops, blind spots, and isospin violation in the MSSM. In: *Journal of High Energy Physics* **07** (2015), p. 129

[177] HISANO, Junji ; ISHIWATA, Koji ; NAGATA, Natsumi: Direct detection of dark matter degenerate with colored particles in mass. In: *Physics Letters B* **706** (2011), p. 208

[178] MERTIG, Rolf ; BÖHM, Manfred ; DENNER, Ansgar: Feyn Calc – Computer-algebraic calculation of Feynman amplitudes. In: *Computer Physics Communications* **64** (1991), p. 345

[179] LARIN, Sergey A.: The renormalization of the axial anomaly in dimensional regularization. In: *Physics Letters B* **303** (1993), p. 113

[180] LARIN, Sergey A.: *Private communication.* 2015

[181] HERRMANN, Björn: *Phenomenology of Dark Matter Annihilation and Non-Minimal Flavour Violation in the MSSM*, Université de Grenoble, PhD thesis, 2008

[182] GONDOLO, Paolo ; GELMINI, Graciela B.: Cosmic abundances of stable particles: improved analysis. In: *Nuclear Physics B* **360** (1991), p. 145

[183] EDSJÖ, Joakim ; GONDOLO, Paolo: Neutralino relic density including coannihilations. In: *Physical Review D* **56** (1997), p. 1879

[184] TURNER, Edward W. ; TURNER, Michael S.: *The Early Universe.* Westview Press, 1994

[185] GRIEST, Kim ; SECKEL, David: Three exceptions in the calculation of relic abundances. In: *Physical Review D* **43** (1991), p. 3191

[186] HAMANN, Jan ; HANNESTAD, Steen ; SLOTH, Martin S. ; WONG, Yvonne Y. Y.: How robust are inflation model and dark matter constraints from cosmological data? In: *Physical Review D* **75** (2007), p. 023522

[187] ARBEY, Alexandre ; MAHMOUDI, Farvah: SUSY constraints from relic density: High sensitivity to pre-BBN expansion rate. In: *Physics Letters B* **669** (2008), p. 46

[188] YAGUNA, Carlos E.: Large contributions to dark matter annihilation from three-body final states. In: *Physical Review D* (**81**), p. 075024

[189] CHATTERJEE, Arindam ; DREES, Manuel ; KULKARNI, Suchita: Radiative corrections to the neutralino dark matter relic density: An effective coupling approach. In: *Physical Review D* **86** (2012), p. 105025

[190] HARZ, Julia ; HERRMANN, Björn ; KLASEN, Michael ; KOVAŘÍK, Karol ; STEPPELER, Patrick: Theoretical uncertainty of the supersymmetric dark matter relic density from scheme and scale variations. In: *Physical Review D* **93** (2016), p. 114023

[191] DAS, Ashok: *Finite Temperature Field Theory.* World Scientific, 1997

[192] MATSUMOTO, Shigeki ; YOSHIMURA, Motohiko: Quantum kinetic equation and cosmic pair annihilation. In: *Physical Review D* **59** (1999), p. 123511

[193] MATSUMOTO, Shigeki ; YOSHIMURA, Motohiko: Temperature power law of equilibrium heavy particle density. In: *Physical Review D* **61** (2000), p. 123508

[194] WIZANSKY, Tommer: Finite temperature corrections to relic density calculations. In: *Physical Review D* **74** (2006), p. 065007

[195] BENEKE, Martin ; DIGHERA, Francesco ; HRYCZUK, Andrzej: *Relic density computations at NLO: infrared finiteness and thermal correction.* 2014. – `http://arxiv.org/abs/1409.3049`

[196] HINDMARSH, Mark ; PHILIPSEN, Owe: Dark matter of weakly interacting massive particles and the QCD equation of state. In: *Physical Review D* **71** (2005), p. 087302

[197] DREES, Manuel ; HAJKARIM, Fazlollah ; SCHMITZ, Ernany R.: The effects of QCD equation of state on the relic density of WIMP dark matter. In: *Journal of Cosmology and Astroparticle Physics* **06** (2015), p. 025

[198] POROD, Werner: SPheno, a program for calculating supersymmetric spectra, SUSY particle decays and SUSY particle production at e^+e^- colliders. In: *Computer Physics Communications* **153** (2003), p. 275

[199] POROD, Werner ; STAUB, Florian: SPheno 3.1: extensions including flavour, CP-phases and models beyond the MSSM. In: *Computer Physics Communications* **183** (2012), p. 2458

[200] ALLANACH, Benjamin C. ; KRAML, Sabine ; POROD, Werner: Theoretical uncertainties in sparticle mass predictions from computational tools. In: *Journal of High Energy Physics* **03** (2003), p. 016

[201] BÉLANGER, Geneviève ; KRAML, Sabine ; PUKHOV, Alexander: Comparison of supersymmetric spectrum calculations and impact on the relic density constraints from WMAP. In: *Physical Review D* **72** (2005), p. 015003

[202] PUKHOV, Alexander: *CalcHEP 2.3: MSSM, structure functions, event generation, batchs, and generation of matrix elements for other packages.* 2009. – `http://arxiv.org/abs/hep-ph/0412191v2`

[203] BELYAEV, Alexander ; CHRISTENSEN, Neil D. ; PUKHOV, Alexander: CalcHEP 3.4 for collider physics within and beyond the Standard Model. In: *Computer Physics Communications* **184** (2013), p. 1729

[204] BLOCH, Felix ; NORDSIECK, Arnold: Note on the Radiation Field of the Electron. In: *Physical Review* **52** (1937), p. 54

[205] KINOSHITA, Toichiro: Mass Singularities of Feynman Amplitudes. In: *Journal of Mathematical Physics* **3** (1962), p. 650

[206] LEE, Tsung-Dao ; NAUENBERG, Michael: Degenerate Systems and Mass Singularities. In: *Physical Review* **133** (1964), p. B1549

[207] HARRIS, Brian W. ; OWENS, Joseph F.: The Two cutoff phase space slicing method. In: *Physical Review D* **65** (2002), p. 094032

[208] CATANI, Stefano ; SEYMOUR, Michael H.: The Dipole formalism for the calculation of QCD jet cross-sections at next-to-leading order. In: *Physics Letters B* **378** (1996), p. 287

[209] CATANI, Stefano ; SEYMOUR, Michael H.: A General algorithm for calculating jet cross-sections in NLO QCD. In: *Nuclear Physics B* **485** (1997), p. 291

[210] DITTMAIER, Stefan: A General approach to photon radiation off fermions. In: *Nuclear Physics B* **565** (2000), p. 69

[211] CATANI, Stefano ; DITTMAIER, Stefan ; SEYMOUR, Michael H. ; TROCSANYI, Zoltan: The Dipole formalism for next-to-leading order QCD calculations with massive partons. In: *Nuclear Physics B* **627** (2002), p. 189

[212] DJOUADI, Abdelhak ; KNEUR, Jean-Loïc ; MOULTAKA, Gilbert: SuSpect: A Fortran code for the Supersymmetric and Higgs particle spectrum in the MSSM. In: *Computer Physics Communications* **176** (2007), p. 426

[213] BAER, Howard ; PAIGE, Frank E. ; PROTOPESCU, Serban D. ; TATA, Xerxes: *ISAJET 7.69: A Monte Carlo Event Generator for pp, $\bar{p}p$, and e^+e^- Reactions.* 2003. – http://arxiv.org/abs/hep-ph/0312045

[214] ALLANACH, Benjamin C.: SOFTSUSY: A program for calculating supersymmetric spectra. In: *Computer Physics Communications* **143** (2002), p. 305

[215] BARO, Nans ; BOUDJEMA, Fawzi ; SEMENOV, Andrei: Full one-loop corrections to the relic density in the MSSM: A few examples. In: *Physics Letters B* **660** (2008), p. 550

[216] BARO, Nans ; BOUDJEMA, Fawzi ; CHALONS, Guillame ; HAO, Sun: Relic density at one-loop with gauge boson pair production. In: *Physical Review D* **81** (2010), p. 015005

[217] HERRMANN, Björn: *(Co-)Annihilation und Detektion dunkler Materie*, Universität Karlsruhe (TH), Diplomarbeit, 2006

[218] HERRMANN, Björn ; KLASEN, Michael: Supersymmetric QCD corrections to dark matter annihilation in the Higgs funnel region. In: *Physical Review D* **76** (2007), p. 117704

[219] HERRMANN, Björn ; KLASEN, Michael ; KOVAŘÍK, Karol: Neutralino annihilation into massive quarks with supersymmetric QCD corrections. In: *Physical Review D* **79** (2009), p. 061710

[220] HERRMANN, Björn ; KLASEN, Michael ; KOVAŘÍK, Karol: Supersymmetric QCD effects on neutralino dark matter annihilation beyond scalar or gaugino mass unification. In: *Physical Review D* **80** (2009), p. 085025

[221] LZ COLLABORATION: *LUX-ZEPLIN (LZ) Conceptual Design Report.* 2015. – http://arxiv.org/abs/1509.02910

[222] DARWIN COLLABORATION: *DARWIN: towards the ultimate dark matter detector.* 2016. – 2016

[223] AGUILAR-SAAVEDRA, Juan Antonio *et al.*: Supersymmetry parameter analysis: SPA convention and project. In: *The European Physical Journal C* **46** (2006), p. 43

[224] ATLAS COLLABORATION ; CMS COLLABORATION: Combined Measurement of the Higgs Boson Mass in pp Collisions at $\sqrt{s} = 7$ and 8 TeV with the ATLAS and CMS Experiments. In: *Physical Review Letters* **114** (2015), p. 191803

[225] BUCHMÜLLER, Oliver *et al.*: Implications of improved Higgs mass calculations for supersymmetric models. In: *The European Physical Journal C* **74** (2014), p. 2809

[226] BAER, Howard ; BRHLIK, Michal ; NO, Diego C. ; TATA, Xerxes: $b \to s\gamma$ constraints on the minimal supergravity model with large $\tan \beta$. In: *Physical Review D* **58** (1998), p. 015007

[227] CARENA, Marcela ; GARCIA, David ; NIERSTE, Ulrich ; WAGNER, Carlos E. M.: $b \to s\gamma$ and supersymmetry with large $\tan \beta$. In: *Physics Letters B* **499** (2001), p. 141

[228] ISHIWATA, Koji ; NAGATA, Natsumi ; YOKOZAKI, Norimi: Natural supersymmetry and $b \to s\gamma$ constraints. In: *Physics Letters B* **710** (2012), p. 145

[229] HEAVY FLAVOR AVERAGING GROUP: *Averages of b-hadron, c-hadron, and tau-lepton properties as of early 2012.* 2012. – https://arxiv.org/abs/1207.1158

[230] MOHR, Peter J. ; TAYLOR, Barry N. ; NEWELL, David B.: CODATA Recommended Values of the Fundamental Physical Constants: 2010. In: *Reviews of Modern Physics* **84** (2012), p. 1527

[231] NARISON, Stephan: *QCD as a Theory of Hadrons.* Cambridge University Press, 2004

[232] ERDÉLYI, Arthur ; WILHELM, Magnus ; OBERHETTINGER, Fritz ; TRICOMI, Francesco G.: *Higher transcendental functions.* Vol. 1. McGraw-Hill Book Company, 1953

[233] ABRAMOWITZ, Milton ; STEGUN, Irene A.: *Handbook of Mathematical Functions with Formulas, Graphs, and Mathematical Tables.* United States National Bureau of Standards, 1964

[234] BJORKEN, James D. ; DRELL, Sidney D.: *Relativistische Quantenmechanik.* Bibliographisches Institut Mannheim, 1966

[235] PESKIN, Michael E. ; SCHROEDER, Daniel V.: *An Introduction to Quantum Field Theory.* Westview Press, 1995

[236] DENNER, Ansgar ; DITTMAIER, Stefan ; WIEDERS, Lars H. ; ROTH, Markus: Electroweak corrections to charged-current $e^+e^- \to 4$ fermion processes – technical details and further results. In: *Nuclear Physics B* **724** (2005), p. 247

[237] COLLINS, John: *Renormalization.* Cambridge University Press, 1984

[238] BURAS, Andrzej J.: *Weak Hamiltonian, CP Violation and Rare Decays.* 1998. – http://arxiv.org/abs/hep-ph/9806471

[239] KÖRNER, Jürgen ; KREIMER, Dirk ; SCHILCHER, Karl: A Practicable γ_5-scheme in dimensional regularization. In: *Zeitschrift für Physik C* **54** (1992), p. 503

[240] SCHUBERT, Christian: The Yukawa model as an example for dimensional renormalization with γ_5. In: *Nuclear Physics B* **323** (1989), p. 478

[241] BONNEAU, Guy: Consistency in dimensional regularization with γ_5. In: *Physics Letters B* **96** (1980), p. 147

[242] CHANOWITZ, Michael S. ; FURMAN, Miguel A. ; HINCHLIFFE, Ian: The axial current in dimensional regularization. In: *Nuclear Physics B* **159** (1979), p. 225

[243] JEGERLEHNER, Fred: Facts of life with γ_5. In: *The European Physical Journal C* **18** (2001), p. 673

[244] FIERZ, Markus: Zur Fermionischen Theorie des β-Zerfalls. In: *Zeitschrift für Physik* **104** (1937), p. 553

[245] ITZYKSON, Claude ; ZUBER, Jean-Bernard: *Quantum Field Theory.* McGraw-Hill Book Company, 1980

[246] OKUN, Lew B.: *Leptons and Quarks.* North Holland Publishing Company, 1982

[247] NISHI, Celso C.: Simple derivation of general Fierz-type identities. In: *American Journal of Physics* **73** (2005), p. 1160

[248] SAULDER, Christoph: *Fierz Identität.* 2008. – unpublished

[249] CHATTOPADHYAY, Utpal ; IBRAHIM, Tarek ; NATH, Pran: Effects of CP violation on Event Rates in the Direct Detection of Dark Matter. In: *Physical Review D* **60** (1999), p. 063505

[250] AVDEEV, Leo V.: Fierz identities in spaces of nonintegral dimensions. In: *Theoretical and Mathematical Physics* **58** (1984), p. 203

[251] BLATTER, Marc: Fierz transformation and Dimensional Regularization. In: *Helvetica Physica Acta* **65** (1992), p. 1011

[252] Stöckinger, Dominik: Regularization by Dimensional Reduction: Consistency, Quantum Action Principle, and Supersymmetry. In: *Journal of High Energy Physics* **03** (2005), p. 076

[253] Mihaila, Luminita: Precision Calculations in Supersymmetric Theories. In: *Advances in High Energy Physics* (2013), p. 607807

[254] Avdeev, Leo V. ; Vladimirov, Alexei A.: Dimensional regularization and supersymmetry. In: *Nuclear Physics B* **219** (1983), p. 262

[255] Dirac, Paul A. M.: The Quantum theory of electron. In: *Proceedings of the Royal Society A* **117** (1928), p. 610

[256] Weyl, Hermann: Electron and gravitation. In: *Zeitschrift für Physik* **56** (1929), p. 330

[257] Kovařík, Karol: *Physik jenseits des Standardmodells.* 2013/2014. – unpublished

[258] Majorana, Ettore: Teoria simmetrica dell'elettrone e del positrone. In: *Il Nuovo Cimento* **14** (1937), p. 171

[259] Passarino, Giampiero ; Veltman, Martinus: One-Loop corrections for e^+e^- annihilation into $\mu^+\mu^-$ in the Weinberg model. In: *Nuclear Physics B* **160** (1979), p. 151

[260] 't Hooft, Gerardus ; Veltman, Martinus: Regularization and Renormalization of Gauge Fields. In: *Nuclear Physics B* **44** (1972), p. 189

[261] 't Hooft, Gerardus ; Veltman, Martinus: Scalar one-loop integrals. In: *Nuclear Physics B* **153** (1979), p. 365

[262] Kilian, Wolfgang: *Übungen zu Strahlungskorrekturen in Eichtheorien.* 2001. – unpublished

[263] Landau, Lew D.: On analytic properties of vertex parts in quantum field theory. In: *Nuclear Physics* **13** (1959), p. 181

[264] Dittmaier, Stefan: Separation of soft and collinear singularities from one-loop N-point integrals. In: *Nuclear Physics B* **675** (2003), p. 447

[265] Denner, Ansgar ; Dittmaier, Stefan: Scalar one-loop 4-point integrals. In: *Nuclear Physics B* **844** (2011), p. 199

[266] Siegel, Warren: Supersymmetric dimensional regularization via dimensional reduction. In: *Physics Letters B* **84** (1979), p. 193

[267] Jones, D. R. T. ; Capper, Derek M. ; van Nieuwenhuizen, Pieter: Regularization by Dimensional Reduction of Supersymmetric and Nonsupersymmetric Gauge Theories. In: *Nuclear Physics B* **167** (1980), p. 479

[268] Siegel, Warren: Inconsistency of supersymmetric dimensional regularization. In: *Physics Letters B* **94** (1980), p. 37

[269] DENNER, Ansgar ; NIERSTE, Ulrich ; SCHARF, Rainer: A compact expression for the scalar one-loop four-point function. In: *Nuclear Physics B* **367** (1991), p. 637

[270] DEVARAJ, Ganesh ; STUART, Robin G.: Reduction of One-loop Tensor Form-Factors to Scalar Integrals: A General Scheme. In: *Nuclear Physics B* **519** (1998), p. 483

[271] STUART, Robin G.: Algebraic reduction of one-loop Feynman diagrams to scalar integrals. In: *Computer Physics Communications* **48** (1988), p. 367

[272] PARK, Kwangwoo: *Reduction of one-loop n-point integrals.* 2010. – http://arxiv.org/abs/0912.0310

[273] DENNER, Ansgar ; DITTMAIER, Stefan: Reduction schemes for one-loop tensor integrals. In: *Nuclear Physics B* **734** (2006), p. 62

[274] CAMPBELL, John M. ; GLOVER, E. W. N. ; MILLER, David J.: One-loop tensor integrals in dimensional regularisation. In: *Nuclear Physics B* **498** (1997), p. 397

[275] BOUDJEMA, Fawzi ; SEMENOV, Andrei ; TEMES, David: Self-annihilation of the neutralino dark matter into two photons or a Z and a photon in the MSSM. In: *Physical Review D* **72** (2005), p. 055024

[276] BINOTH, Thomas ; GUILLET, Jean-Phillipe ; HEINRICH, Gudrun ; PILON, Eric ; SCHUBERT, Christian: An algebraic/numerical formalism for one-loop multi-leg amplitudes. In: *Journal of High Energy Physics* **10** (2005), p. 015

[277] PITTAU, Roberto: A simple method for multi-leg loop calculations. In: *Computer Physics Communications* **104** (1997), p. 23

[278] PITTAU, Roberto: A simple method for multi-leg loop calculations 2: A general algorithm. In: *Computer Physics Communications* **111** (1998), p. 48

[279] BÖHM, Manfred ; DENNER, Ansgar ; JOOS, Hans: *Gauge Theories of the Strong and Electroweak Interaction.* Teubner, 2001

[280] KOVAŘÍK, Karol: *Quantum Chromodynamics.* 2015. – unpublished

[281] AOYAMA, Tatsumi ; HAYAKAWA, Masashi ; KINOSHITA, Toichiro ; NIO, Makiko: Tenth-Order QED Contribution to the Electron $g-2$ and an Improved Value of the Fine Structure Constant. In: *Physical Review Letters* **109** (2012), p. 111807

[282] VAN RITBERGEN, Timo ; VERMASEREN, Jozef Antoon M. ; LARIN, Sergey A.: The four-loop β-function in quantum chromodynamics. In: *Physics Letters B* **400** (1997), p. 379

[283] BAIKOV, Pavel A. ; CHETYRKIN, Konstantin G. ; KÜHN, Johann H.: *Five-Loop Running of QCD coupling constant.* 2016. – http://arxiv.org/abs/1606.08659v1

[284] MELNIKOV, Kirill ; YELKHOVSKY, Alexander: b quark low-scale running mass from Υ sum rules. In: *Physical Review D* **59** (1999), p. 114009

[285] HOANG, Andre H.: $1S$ and $\overline{\text{MS}}$ bottom quark masses from Υ sum rules. In: *Physical Review D* **61** (1999), p. 034005

[286] Beneke, Martin ; Signer, Adrian: The bottom $\overline{\text{MS}}$ quark mass from sum rules at next-to-next-to-leading order. In: *Physics Letters B* **471** (1999), p. 233

[287] Penin, Alexander A. ; Pivovarov, Alexei A.: Bottom quark mass and $|V_{cb}|$ matrix element from $R(e^+e^- \to bb)$ and $\Gamma_{s1}(b \to cl\nu_l)$ in the next-to-next-to-leading order. In: *Nuclear Physics B* **549** (1999), p. 217

[288] Baer, Howard ; Ferrandis, Javier ; Melnikov, Kirill ; Tata, Xerxes: Relating bottom quark mass in $\overline{\text{DR}}$ and $\overline{\text{MS}}$ regularization schemes. In: *Physical Review D* **66** (2002), p. 074007

[289] Chetyrkin, Konstantin G.: Correlator of the quark scalar currents and $\Gamma_{\text{tot}}(H \to \text{hadrons})$ at $O(\alpha_s^3)$ in pQCD. In: *Physics Letters B* **390** (1997), p. 309

[290] Baikov, Pavel A. ; Chetyrkin, Konstantin G. ; Kühn, Johann H.: Scalar Correlator at $\mathcal{O}(\alpha_s^4)$, Higgs Boson Decay into Bottom Quarks, and Bounds on the Light-Quark Masses. In: *Physical Review Letters* **96** (2006), p. 012003

[291] Chetyrkin, Konstantin G. ; Kwiatkowski, A.: Second-order QCD corrections to scalar and pseudoscalar Higgs decays into massive bottom quarks. In: *Nuclear Physics B* **461** (1996), p. 3

[292] Carena, Marcela ; Garcia, David ; Nierste, Ulrich ; Wagner, Carlos E. M.: Effective lagrangian for the $\bar{t}bH^+$ interaction in the MSSM and charged Higgs phenomenology. In: *Nuclear Physics B* **577** (2000), p. 88

[293] Guasch, Jaume ; Häfliger, Petra ; Spira, Michael: MSSM Higgs boson decays to bottom quark pairs reexamined. In: *Physical Review D* **68** (2003), p. 115001

[294] Noth, David ; Spira, Michael: Supersymmetric Higgs Yukawa couplings to bottom quarks at next-to-next-to-leading order. In: *Journal of High Energy Physics* **1106** (2011), p. 084

[295] Heinemeyer, Sven ; Rzehak, Heidi ; Schappacher, Christian: Proposals for bottom quark/squark renormalization in the complex MSSM. In: *Physical Review D* **82** (2010), p. 075010

[296] Heinemeyer, Sven ; Hollik, Wolfgang ; Rzehak, Heidi ; Weiglein, Georg: High precision predictions for the MSSM Higgs sector at $\mathcal{O}(\alpha_b\alpha_s)$. In: *The European Physical Journal C* **39** (2005), p. 465

[297] Harlander, Robert V. ; Mihaila, Luminita ; Steinhauser, Matthias: Two-loop matching coefficients for the strong coupling in the minimal supersymmetric standard model. In: *Physical Review D* **72** (2005), p. 095009

[298] Bauer, Anne H. ; Mihaila, Luminita ; Salomon, Jens: Matching coefficients for α_s and m_b to $\mathcal{O}(\alpha_s^2)$ in the MSSM. In: *Journal of High Energy Physics* **02** (2009), p. 037

[299] Petrov, Alexey A. ; Blechman, Andrew E.: *Effective Field Theories*. World Scientific, 2016

[300] Becher, Thomas: *Effective Field Theories*. 2010. – unpublished

[301] GEORGI, Howard: Effective Field Theory. In: *Annual Review of Nuclear and Particle Science* **43** (1993), p. 209

[302] WILSON, Kenneth G. ; ZIMMERMANN, Wolfhart: Operator Product Expansions and Composite Field Operators in the General Framework of Quantum Field Theory. In: *Communications in Mathematical Physics* **24** (1972), p. 87

[303] WILSON, Kenneth G.: Non-Lagrangian Models of Current Algebra. In: *Physical Review* **179** (1969), p. 1499

[304] FRÖB, Markus B. ; HOLLAND, Jan: *All-order existence of and recursion relations for the operator product expansion in Yang-Mills theory.* 2016. – `http://arxiv.org/abs/1603.08012`

[305] HENNING, Brian ; LU, Xiaochuan ; MURAYAMA, Hitoshi: *One-loop Matching and Running with Covariant Derivative Expansion.* 2016. – `http://arxiv.org/abs/1604.01019`

[306] WILLENBROCK, Scott ; ZHANG, Cen: Effective Field Theory Beyond the Standard Model. In: *Annual Review of Nuclear and Particle Science* **64** (2014), p. 83

[307] CONTINO, Roberto ; FALKOWSKI, Adam ; GOERTZ, Florian ; GROJEAN, Christophe ; RIVA, Francesco: On the Validity of the Effective Field Theory Approach to SM Precision Tests. In: *Journal of High Energy Physics* **07** (2016), p. 144

[308] FALKOWSKI, Adam ; GONZÁLEZ-ALONSO, Martín ; GRELJO, Admir ; MARZOCCA, David: Global constraints on anomalous triple gauge couplings in effective field theory approach. In: *Physical Review Letters* **116** (2016), p. 011801

[309] ALLOUL, Adam ; FUKS, Benjamin ; SANZ, Verónica: Phenomenology of the Higgs Effective Lagrangian via `FeynRules`. In: *Journal of High Energy Physics* **04** (2014), p. 110

[310] GRAZZINI, Massimiliano ; ILNICKA, Agnieszka ; SPIRA, Michael ; WIESEMANN, Marius: *BSM effects on the Higgs transverse-momentum spectrum in an EFT approach.* 2015. – `http://arxiv.org/abs/1511.08059`

[311] AZATOV, Aleksandr ; CONTINO, Roberto ; PANICO, Giuliano ; SON, Minho: Effective field theory analysis of double Higgs boson production via gluon fusion. In: *Physical Review D* **92** (2015), p. 035001

[312] BALÁZS, Csaba ; LI, Tong ; NEWSTEAD, Jayden L.: Thermal dark matter implies new physics not far above the weak scale. In: *Journal of High Energy Physics* **08** (2014), p. 061

[313] LIEM, Sebastian ; BERTONE, Gianfranco ; CALORE, Francesca ; RUIZ DE AUSTRI, Roberto ; TAIT, Tim M. P. ; TROTTA, Roberto ; WENIGER, Christoph: *Effective Field Theory of Dark Matter: a Global Analysis.* 2016. – `http://arxiv.org/abs/1603.05994`

[314] BUCHMÜLLER, Oliver ; DOLAN, Matthew J. ; MCCABE, Christopher: Beyond effective field theory for dark matter searches at the LHC. In: *Journal of High Energy Physics* **01** (2014), p. 025

[315] Busoni, Giorgio ; De Simone, Andrea ; Morgante, Enrico ; Riotto, Antonio: On the validity of the effective field theory for dark matter searches at the LHC. In: *Physics Letters B* **728** (2014), p. 412

[316] Busoni, Giorgio ; De Simone, Andrea ; Gramling, Johanna ; Morgante, Enrico ; Riotto, Antonio: On the validity of the effective field theory for dark matter searches at the LHC, part II: complete analysis for the s-channel. In: *Journal of Cosmology and Astroparticle Physics* **06** (2014), p. 060

[317] Busoni, Giorgio ; De Simone, Andrea ; Jacques, Thomas ; Morgante, Enrico ; Riotto, Antonio: On the validity of the effective field theory for dark matter searches at the LHC part III: analysis for the t-channel. In: *Journal of Cosmology and Astroparticle Physics* **09** (2014), p. 022

[318] De Simone, Andrea ; Jacques, Thomas: Simplified models vs. effective field theory approaches in dark matter searches. In: *The European Physical Journal C* **76** (2016), p. 367

[319] Matsumoto, Shigeki ; Mukhopadhyay, Satyanarayan ; Tsai, Yue-Lin S.: *Effective Theory of WIMP Dark Matter supplemented by Simplified Models: Singlet-like Majorana fermion case*. 2016. – `http://arxiv.org/abs/1604.02230`

[320] Musil, Robert: *Die Verwirrungen des Zöglings Törleß*. Wiener Verlag, 1906

Patrick Norbert Steppeler

Angaben zur Person

Geburtsdatum und -ort	29. April 1988 in Gütersloh
Staatsangehörigkeit	Deutsch

Schul- und Hochschulbildung

seit Mai 2013	**Westfälische Wilhelms-Universität Münster**. Promotionsstudium zur Erlangung des Grades Dr. rer. nat.
Okt 2010 - März 2013	**Westfälische Wilhelms-Universität Münster**. Hauptstudium der Physik mit Nebenfach Wirtschaftswissenschaften. Abschluss: Master of Science mit der Abschlussarbeit *QCD-Korrekturen zur Annihilation von dunkler Materie im Higgs-Funnel*
Okt 2007 - Aug 2010	**Westfälische Wilhelms-Universität Münster**. Grundstudium der Physik mit Nebenfach Informatik. Abschluss: Bachelor of Science mit der Abschlussarbeit *Untersuchungen der Transmission durch Modellpotentiale*
Aug 2004 – Juni 2007	**Augustin-Wibbelt-Gymnasium**, Warendorf. Abschluss: Abitur mit den Leistungskursen Physik und Mathematik
Aug 1998 – Juni 2004	**Städtische Realschule**, Harsewinkel.

Praktika, Berufs- und Lehrerfahrung

seit Feb 2014	**Ravati Seminare**, Düsseldorf, Marburg und Halle. Dozent für Physik in Repetitorien für Pharmazeuten
Mai 2013 - Juni 2016	**Westfälische Wilhelms-Universität Münster**. Wissenschaftlicher Mitarbeiter am Institut für Theoretische Physik
seit April 2013	**Fachhochschule für Ökonomie und Management**, Essen. Dozent für Mathematik und Physik
Sep 2011	**Hochschule Bochum**. Dozent für Mathematik
Aug 2008	**Struwig Eco Reservat**, Hoedspruit, Südafrika. Mitarbeit als Volontär beim Aufbau eines Ökotourismus-Camps im Krüger-Nationalpark
Aug 2007	**Deutsches Zentrum für Luft- und Raumfahrt**, Köln. Mitarbeit als Praktikant bei der Auswertung der Daten des *Matroschka*-Experiments

Danksagung